

THE UNIVERSITY
of EDINBURGH

This thesis has been submitted in fulfilment of the requirements for a postgraduate degree (e.g. PhD, MPhil, DClinPsychol) at the University of Edinburgh. Please note the following terms and conditions of use:

This work is protected by copyright and other intellectual property rights, which are retained by the thesis author, unless otherwise stated.
A copy can be downloaded for personal non-commercial research or study, without prior permission or charge.
This thesis cannot be reproduced or quoted extensively from without first obtaining permission in writing from the author.
The content must not be changed in any way or sold commercially in any format or medium without the formal permission of the author.
When referring to this work, full bibliographic details including the author, title, awarding institution and date of the thesis must be given.

Design and Fabrication of Soft Circuit Elements and Integrated Soft Electronic Systems

Lijun Teng



The University of Edinburgh
School of Engineering
Institute for Integrated Micro and Nano Systems

Supervised by:
Dr. Adam A. Stokes

A Thesis submitted for the Degree of
Doctor of Philosophy

2019

Lijun Teng:

Design and Fabrication of Soft Circuit Elements and Integrated Soft Electronic Systems

Doctor of Philosophy, 2019 ©

SUPERVISOR:

Dr. Adam A. Stokes

LOCATION:

Edinburgh, United Kingdom

Lay Summary of Thesis

THE UNIVERSITY of EDINBURGH

The lay summary is a brief summary intended to facilitate knowledge transfer and enhance accessibility, therefore the language used should be non-technical and suitable for a general audience. (See the Degree Regulations and Programmes of Study, General Postgraduate Degree Programme Regulations. These regulations are available via: www.drps.ed.ac.uk.)

Name of student:	Lijun Teng	UUN	S1426523
University email:	L.Teng@ed.ac.uk		
Degree sought:	Doctorate	No. of words in the main text of thesis:	30000
Title of thesis:	Design and Fabrication of Soft Circuit Elements and Integrated Soft Electronic Systems		

Insert the lay summary text here - the space will expand as you type.

My Ph.D. study focuses on developing fully integrated soft electronic systems by making electronic components and soft materials have better integration and creating unique flexible and stretchable electronic circuit components (by using liquid metal and silicone materials) that can contribute to forming fully integrated soft electronic systems. I design and fabricate soft electronic components with unique repeatable approaches that I developed and provide methods to integrate electronic components into integrated soft electronic systems. My studies could contribute to many cutting-edge research fields, such as soft robotics, wearable devices, microfluidics, prosthetics, etc.

Document control

K:\AAPS\D-AcademicAdministration\02-CodesOfPractice,Guidelines&Regulations\24-MainReferencesCopiesPolicies\01-Current\Assessment BOE SCC & Feedback\Forms\ThesisLaySummary	
If you require this document in an alternative format please email Academic.Services@ed.ac.uk or telephone 0131 651 4990.	Date last reviewed: 31.05.16

ABSTRACT

Soft systems are machines that are chiefly fabricated with soft (highly compliant) materials. These soft machines often take inspiration from biology, mimicking the softness and flexibility of organisms, like the octopus, to acclimate to unstructured environments, or mimicking the elasticity of skin to provide harmonious human-machine interface. Since soft systems improve the biocompatibility and versatility of conventional hard systems, they can make up for the shortfalls of hard systems and have great potential in plenty of applications, such as: physical assistive robotics; wearable computing; health monitoring; and human-machine interaction.

Electronic components can provide crucial and fundamental functionalities, such as data acquisition (sensors), data processing (microprocessors), data transmission (antennas), and data visualisation (displays), for the systems they serve. Integrating electronics into soft systems will inevitably enrich the capabilities of these systems, enabling them to detect the surrounding environment and transmit information to the real world.

Integrating electronics into soft structures introduces unique challenges which arise from materials compatibility and integration in fabrication and interfacing. The majority of integrated electronic circuits are made from rigid materials that are difficult to bend or stretch, while the production material of soft systems has given priority to flexible and stretchable materials, such as hydrogels and silicones. When solid-state electronic components are embedded in soft materials, delamination tends to occur at the interface between the soft and the hard materials when the devices deform.

My Ph.D. study focuses on developing fully integrated soft electronic systems by improving the integration between electronic components and soft materials, and by creating unique flexible and stretchable electronic circuit components (using liquid metal and silicone materials). These developments enable fully integrated soft electronic systems with the functionalities of data acquisition, data processing, data transmission, and data visualisation.

This thesis includes: (i) a systematic review of previous research on soft systems and stretchable soft electronics; (ii) the development of a rapid-prototyping technique for soft-lithography masters; (iii) the development of a high resolution pressure-sensor soft system that can transduce normal force into a digital output; (iv) the development of a new passive wireless soft sensor, which benefits from a combination of radio-frequency identification (RFID) tag design and microfluidic sensor fabrication technologies. (v) the development of a method, which has potential to be mass-manufacturable, to fabricate soft printed circuit boards.

In summary, I describe the design and fabrication of soft electronic components with unique repeatable approaches that I developed and I provide methods to integrate electronic components into integrated soft electronic systems. My studies contribute to many cutting-edge research fields, such as soft robotics, wearable devices, microfluidics, and prosthetics.

摘要

软体系统是指主要由软体的（即高柔软度的）材料制作而成的机器。这些软体系统通常从生物学中获取灵感，模仿有机体（如章鱼）的柔软性和柔韧性去适应结构复杂的环境，或者模仿皮肤弹性以提供更好的人机交互功能。由于软体系统提高了传统系统的生物相容性和多功能性，它们可以弥补传统系统的不足并在很多新兴应用中具有很大的潜力，例如：医学辅助机器人、可穿戴计算设备和健康监测仪器。

电子元件可为其所服务的系统实现一些至关重要的功能，例如：数据采集（传感器）、数据处理（微处理器）、数据传输（天线）和数据可视化（显示）。将电子设备集成到软体系统中可以丰富这些软体系统的功能，从而使这些系统能够获取并传输周围环境中的信息。

大多数集成电子电路由难以弯曲或拉伸的刚性材料制成，而软体系统的生产材料以柔韧、可拉伸的材料为主，例如：水凝胶和硅树脂。将电子器件集成到软体系统中是有一些难度的，这些难度主要在于软体材料和刚性材料之间的不兼容性。如果将硬质的电子元件嵌入软体系统中，当系统发生形变时，软体材料和硬质材料之间的交界处会发生分离。

博士在读期间，我的研究的重点是：通过改进电子元件和软体材料之间的兼容性、以及设计独特的可拉伸软体电子电路元件（使用液态金属和硅胶材料）来开发多功能的软体集成电子系统。这些研究可以使软体系统具有数据采集、数据处理、数据传输和数据可视化的功能。我的研究为许多前沿研究领域做出了贡献，例如：软机器人，可穿戴设备和微流体设备等领域。

本论文的主要内容包括：1. 系统回顾关于软体系统和可拉伸软体电子（柔性电子）器件的文献；2. 一种新型的制作软刻模具的方法；3. 可以将压力信号输入转化为数字信号输出的高分辨率压力传感器系统的设计和生产方法；4. 一种无线软体传感器的设计和生产方法；5. 一种有大规模制造潜力的柔性印刷电路板的制作方法。

DECLARATION

I declare that this thesis was composed by myself, that the work contained herein is my own except where explicitly stated otherwise in the text, and that this work has not been submitted for any other degree or professional qualification except as specified.

Edinburgh, United Kingdom, 2019

Lijun Teng

May 1, 2020

ACKNOWLEDGEMENTS

Firstly, I would like to express my gratitude and thanks to my parents Fang Li and Jianqing Teng for their financial and emotional support. I would also like to express my sincere appreciation to supervisor Dr. Adam A. Stokes for providing this opportunity and the continuous support, for his patience, motivation, and immense knowledge.

Secondly, I would like to thank all the brilliant colleagues and collaborators who I have worked with over the past four years, namely Rui Song, Cong Chao, Karina Jeronimo, Markus P. Nemitz, Mohammed E. Sayed, Stephen Mahon, Simona Aracri, Alistair McConnell, Anthony Buchoux, Jamie Roberts, Derek Chun, Jennifer Dodoo, Ross McKenzie, Constantine Talalaev, Thomas W. Barraclough, Kewen Pan, and Geng Lyu for their support and friendship.

Finally, but by no means the least, I would like to express my special thanks to Rui Song, Yichen Du, Qianqian Shen, Yiming Yang, Ruiqiu Wang, Yang Luo, and Li Deng for their priceless friendship and making the past four years of my Ph.D a pleasant memory.

To my parents Jianqing Teng and Fang Li.

致我的父母滕建青和李芳。

ABBREVIATIONS

ADC Analogue-to-digital Converter.

BCD Binary-Coded Decimal.

CMOS Complementary Metal Oxide Semiconductor.

CNC Computerised Numerical Control.

CNT Carbon Nanotube.

DI water Deionized water.

eGaIn Eutectic Gallium Indium.

FET Field-effect transistor.

FR4 Flame Retardant 4.

HCl Hydrochloride.

IMNS Integrated Micro and Nano Systems.

IoT Internet of Things.

IC Integrated Circuit.

LCE Liquid Crystal Elastomer.

LM Liquid Metal.

MCU Micro-controller Unit.

NEMA National Electrical Manufacturers Association.

NaOH Sodium Hydroxide.

PEDOT-PSS Poly(3, 4-ethylenedioxythiophene)-poly(styrenesulfonate)

PDMS Polydimethyl-siloxane.

PCB Printed Circuit Board.

PN Pneumatic-net.

PANI polyaniline.

QR Quick Response.

RFID Radio-frequency Identification.

SPCB Soft Printed Circuit Board.

UV Ultra-violet.

VQFP Very thin Quad Flat Package.

CONTENTS

Abstract iv
Declaration vii
Acknowledgments viii
Dedication ix
Abbreviations x
List of Figures xv
List of Tables xviii
1 INTRODUCTION 1
1.1 Motivation . . . 1
1.2 Aims and Objectives . . . 3
1.3 Preview of Contributions . . . 4
1.4 Publications . . . 6
1.5 2D Barcodes . . . 7
1.6 Thesis Structure . . . 9
2 BACKGROUND AND LITERATURE SURVEY 11
2.1 Soft Systems . . . 11
2.1.1 Soft Robotics . . . 14
2.1.2 Wearable Devices . . . 17
2.2 Soft Electronics . . . 21
2.2.1 Flexible Electronics . . . 22
2.2.2 Stretchable Electronics . . . 24
2.3 Liquid Metal Devices . . . 33
2.4 Integration of Electronics and Soft Systems . . . 39
3 MATERIALS AND METHODS 43
3.1 Eutectic Liquid Metal: Galinstan . . . 44
3.2 Elastomer: PDMS and Ecoflex . . . 47
3.3 Soft-lithography Master Fabrication . . . 49
3.3.1 Materials and Equipment . . . 52
3.3.2 Fabrication Process . . . 53
3.3.3 Applications . . . 55
3.4 Conclusion . . . 61
4 INTEGRATED SOFT PRESSURE SENSING SYSTEM 62

4.1 Introduction . . . 63
4.2 Methods . . . 65
4.2.1 New Interconnect Material: Conductive Thread . . . 65
4.2.2 An Integrated Soft System with Conductive Thread Interconnects 67
4.2.3 Design and Fabrication of the Microfluidic Pressure Sensor . . . 68
4.2.4 Design of the Electronic System . . . 69
4.2.5 Design of the Experimental Systems and Tests . . . 71
4.3 Experiments and Results . . . 72
4.4 Discussion . . . 77
4.5 Conclusion . . . 78
5 WIRELESS SOFT STRAIN SENSORS FOR SOFT ROBOTIC SYSTEMS 80
5.1 Introduction . . . 81
5.2 Principles and Implementations . . . 82
5.2.1 RFID Technology . . . 82
5.2.2 Sensor Constitution and Working Principles . . . 83
5.2.3 Implementation in Soft Robotics . . . 85
5.3 Antenna Design . . . 86
5.3.1 Selection and Design of the Antenna . . . 86
5.3.2 Antenna Matching . . . 87
5.4 Materials and Fabrication Methods . . . 89
5.5 Experimental Design . . . 90
5.6 Results . . . 93
5.6.1 Permittivity of Ecoflex 00-50 . . . 93
5.6.2 Simulation of Antenna Efficiency . . . 93
5.6.3 Resonant Frequency upon Strain . . . 96
5.6.4 Repeatability and Reliability Test . . . 98
5.6.5 Radiation Pattern . . . 99
5.7 Discussion . . . 100
5.8 Conclusion . . . 101
6 INTEGRATING ELECTRONIC SYSTEMS ON A SOFT PRINTED CIRCUIT BOARD 103
6.1 Introduction . . . 103
6.2 Materials and Methods . . . 105
6.3 Circuit and Implementation . . . 107
6.4 Discussion . . . 108
6.5 Conclusion . . . 110
7 CONCLUSION AND FUTURE DIRECTIONS 111
7.1 Vinyl Soft-lithography Masters . . . 111
7.2 Integrated Pressure-sensor Soft System . . . 113

7.3 Wireless Soft Strain Sensor 114
7.4 Soft Printed Circuit Board 116

REFERENCES 118

Appendices 143

A POSTER: TOWARDS HARD AND SOFT PACKAGING FOR DIE-SCALE ICS 144

B FLEXIBLE AND STRETCHABLE SOFT ELECTRONIC SYSTEMS 146

C PRESENTATION: FROM HARD TO SOFT SYSTEMS: USING SOFT MATERIALS TO ENCAPSULATE OFF-THE-SHELF ELECTRONIC COMPONENTS 148

D INTEGRATING SOFT SENSOR SYSTEMS USING CONDUCTIVE THREAD 150

E SOFT RFID SENSORS: WIRELESS LONG-RANGE STRAIN SENSORS USING RADIO-FREQUENCY IDENTIFICATION 164

F SOFT WIRELESS BATTERY-FREE UHF RFID STRETCHABLE SENSOR BASED ON MICROFLUIDIC TECHNOLOGY 181

G COPYRIGHT 190

LIST OF FIGURES

Figure 1.1 Thesis structure layout. . . . 8
Figure 2.1 Introduction of Young's modulus . . . 12
Figure 2.2 Soft systems are the bridge between world of hard things and soft things . . . 13
Figure 2.3 Pneu-net (PN) architecture . . . 15
Figure 2.4 Previous work on soft robotics . . . 16
Figure 2.5 Wearable devices in different forms–1 . . . 17
Figure 2.6 Wearable devices in different forms–2 . . . 18
Figure 2.7 Wearable sensors in monitoring human activities and personal care . . . 20
Figure 2.8 Non-elastic, elastic, and hyper-elastic materials . . . 21
Figure 2.9 Flexible electronics . . . 22
Figure 2.10 Stretchable electronics with deterministic geometries . . . 25
Figure 2.11 Stretchable electronics made of composites . . . 26
Figure 2.12 The curve of conductivity versus carbon black filler concentration. (Data from: Brigandi et al. [2014]) . . . 27
Figure 2.13 Intrinsically stretchable electronics . . . 29
Figure 2.14 Liquid conductors are "softer" than many electrical and biological materials. . . . 30
Figure 2.15 Electrical conductivity and strain limits of common stretchable conductors. . . . 31
Figure 2.16 Liquid metal stretchable electrical connections . . . 34
Figure 2.17 Liquid metal stretchable antennas . . . 35
Figure 2.18 Intrinsically soft circuit elements created with liquid metal . . . 36
Figure 2.19 Intrinsically soft strain sensors . . . 37
Figure 2.20 Design concept of a liquid metal strain sensor . . . 38
Figure 2.21 Intrinsically soft pressure and tactile sensors . . . 39
Figure 2.22 Untethered soft electronic systems . . . 40
Figure 2.23 Conception of a future soft robot . . . 42
Figure 3.1 Galinstan and ultrastretchable conductive fibre . . . 44
Figure 3.2 Process of fabricating an SU-8 soft-lithography master and patterning PDMS . . . 50

Figure 3.3 Soft sensors and soft-lithography masters . . . 51
Figure 3.4 Photograph of LPKF Protolaster U3 laser micro-machining system . . . 52
Figure 3.5 Fabrication Process of a vinyl soft-lithography master . . . 53
Figure 3.6 Example fabrication process of a liquid metal microfluidic device 54
Figure 3.7 Soft packaging for conventional IC chips . . . 55
Figure 3.8 Intrinsically soft electronic components . . . 57
Figure 3.9 Integrating soft sensors into a maggot robot . . . 58
Figure 3.10 Photograph of a PDMS device with micro-channels inside . . . 59
Figure 3.11 Vinyl mask for metal depositing . . . 60
Figure 3.12 Vinyl mask for graphene ink printing . . . 61
Figure 4.1 Comparison of conventional copper wire and conductive thread 64
Figure 4.2 Photographs showing the withdrawal of conductive thread and copper wire . . . 66
Figure 4.3 Top view of the integrated soft pressure sensing system . . . 67
Figure 4.4 Fabrication process of the soft pressure sensor . . . 68
Figure 4.5 Circuit schematic of the system on the flexible PCB . . . 69
Figure 4.6 Experimental set-up . . . 71
Figure 4.7 Stress versus strain curves . . . 73
Figure 4.8 Results of four experiments to characterise the pressure sensor 75
Figure 4.9 Demonstrating the sensitivity of the integrated soft system . . . 76
Figure 5.1 Schematic diagram of the stretchable microfluidic sensor . . . 83
Figure 5.2 The electronic system for measuring data from a pneumatic soft robot that contains four embedded microfluidic strain sensors . . . 85
Figure 5.3 Equivalent circuit of the RFID chip and the transporter antenna 87
Figure 5.4 Fabrication process and prototype of the stretchable microfluidic sensor (RFID tag antenna) . . . 89
Figure 5.5 Experimental design . . . 91
Figure 5.6 Radiation pattern measurement in an anechoic room . . . 92
Figure 5.7 Permittivity of Ecoflex type 00-50 in the frequency range of 200MHz 1.2GHz . . . 93
Figure 5.8 Finite elements simulation results . . . 95
Figure 5.9 Results: Resonant frequency upon stra in-1 . . . 97
Figure 5.10 Results: Resonant frequency upon strain-2 . . . 98
Figure 5.11 Theoretical reading range of the antenna in H-plane and E-plane 100
Figure 6.1 Fabrication process of a soft printed circuit board . . . 105
Figure 6.2 Effect of HCl treatment on contact interface . . . 107
Figure 6.3 Schematic diagram of a soft seven-segment display system . . . 108

Figure 6.4 Photograph of a soft seven-segment display system 109
Figure 7.1 Soft sensors and soft-lithography masters 111
Figure 7.2 Fabrication of PDMS half semi-sphere with integrated liquid metal sensor 112
Figure 7.3 Top view of the integrated soft pressure sensing system 114
Figure 7.4 Photograph of the stretchable microfluidic sensor (RFID tag antenna) 115
Figure 7.5 The electronic system for measuring data from a pneumatic soft robot that contains four embedded microfluidic strain sensors 116
Figure 7.6 Photograph of a soft seven-segment display system 117
Figure D.1 Ecoflex pressure sensor under tensile test 162
Figure D.2 Samples used to test mechanical robustness of the connection . 163
Figure E.1 Dimensional drawing of the meander line antenna 178
Figure E.2 Photographs of the fabrication process 178
Figure E.3 Demonstration of three different test conditions in the twisting experiment 179
Figure E.4 A prototype was tested under three different twist angles: 0°, 45°, and 90° 180

LIST OF TABLES

Table 3.1 Physical properties of common liquid metals. 45
Table 3.2 Mechanical properties of PDMS and Ecoflex. 48
Table 4.1 Values of minimum load required to lose connection 74

LIST OF QR CODES



p.7 - QRcode 1.1.: Test your camera.
Website of Soft System Group.

p.14 - QRcode 2.1.: Soft robot
walking and crawling.





p.54 - QRcode 3.1.: Fabrication of
a vinyl soft-lithography master.

p.76 - QRcode 4.1.: Demonstrating the sensitivity
of the integrated soft system.





p.106 - QRcode 6.1.: Galinstan selectively
wets to copper.

p.108 - QRcode 6.2.: Soft seven-segment
display system.



1

INTRODUCTION

In this thesis, I present my research work undertaken in the Institute of Integrated Micro and Nano System (IMNS). This work, which reflects a combination of micro-fabrication, electronic engineering and soft materials science, focusses on designing and fabricating soft systems with integrated soft electronic circuit components (such as sensors and antennas), and manufacturing printed circuit boards with soft substrates and liquid conductors. In this chapter, the motivation of this research work is detailed, followed by aims and objectives of the project, a preview of contributions, a publication list, and an overview of the thesis structure.

1.1 MOTIVATION

In recent decades, researchers have paid increasing amounts of attention to the development of soft systems. Soft systems here refer to the machines which are chiefly fabricated with soft materials. These soft machines usually take inspiration from biology, mimicking the softness and flexibility of organisms like the octopus to adopt to unstructured environments, or mimicking the elasticity of skin to provide harmonious human-machine interface. Soft systems can improve the biocompatibility and versatility of conventional hard systems, therefore can making up for the shortages of hard systems and having great potential in a variety of applications, such as: physical assistive robotics; wearable computing; health monitoring; and human-machine interaction.

Our lives are brimming with systems which contain electronic components. Electronic components can provide crucial and fundamental functionalities, such as data acquisition (sensors), data processing (microprocessors), data transmission (antennas), and data visualisation (displays), for the systems they serve. It can be said that electronic components are the basis for a system to interact with the real world. Integrating electronics in current soft systems such as soft robotic systems (Tolley et al. [2014], Marchese et al. [2015], Wehner et al. [2016]), will inevitably enrich the capabilities of these systems for detecting the surrounding environment and transmitting information to the outside world.

Nevertheless, there are some difficulties in integrating current electronic components into the current soft systems. Key challenges arise from issues in materials compatibility and integration. Integrating electronics into soft structures introduces unique challenges in fabrication and interfacing. The bulk of chip packaging materials are plastic or ceramic and the majority of integrated electronic circuits are based on insulating substrates (such as silicon and FR4) and metal conductors (such as aluminium and copper). "FR" stands for flame retardant, FR4 is a NEMA (National Electrical Manufacturers Association) grade designation for glass-reinforced epoxy laminate material. All the materials mentioned above are difficult to bend or stretch, while the production material of soft systems has given priority to flexible and stretchable materials, such as hydrogels and silicones. When solid-state electronic components are embedded in soft materials, delamination tends to happen at the interface between the soft and the hard materials when the devices deform.

Producing electronic components with high compliance or incorporating current electronic components into soft structures is therefore the key demand in developing fully integrated soft electronic systems. This challenge can be addressed by many methods, such as: (i) Reducing the thickness of stiff materials (such as copper) and arranging them into elastically deformable structures; (ii) Embedding soft materials with conductive nanofilms or percolating networks of conductive nano/micro particles; (iii) Filling hydrogels with ionic solutions; and (iv) Embedding liquid metals (such as eutectic gallium-indium) in flexible and stretchable elastomer substrate.

1.2 AIMS AND OBJECTIVES

The aim of this research is to develop soft electronic circuit components and to develop the methods to integrate electronics into soft systems. The overall development was step-wise, the steps include: (i) development of fundamental fabrication technologies, such as soft-lithography master fabrication and soft encapsulation for conventional IC chips; (ii) design and fabrication of flexible and stretchable soft electronic circuit components, such as sensors and antennas, (iii) development of methods for integrating the developed soft electronic components into soft electronic systems. The list below briefly summarises the main objectives in this work:

- Review literature and study related previous work.
- Develop a reliable way to fabricate soft-lithography masters for casting silicone based on the available experimental equipment.
- Develop methods to make soft encapsulation for conventional IC chips.
- Design and manufacture soft sensors with silicone and liquid metal materials. The soft sensor here is aimed at sensing of physical shape variables such as stretch and pressure. The ability to fabricate them in the lab is a foundation of the follow-up study of the whole system.
- Develop methods to form connections between the soft sensors and the soft electronic systems.
- Design and manufacture wireless soft sensors which can be integrated into electronic systems remotely.
- Develop a method to fabricate flexible and stretchable printed circuit boards and make the fabrication process have potential to be mass manufacturable.

1.3 PREVIEW OF CONTRIBUTIONS

The main contributions of this thesis include:

- A systematic review of previous research on flexible and stretchable soft electronics. Teng et al. [2018a], Teng et al. [2018b]

- Development of a rapid-prototyping technique for soft-lithography masters using laser-cutting systems and self-adhesive materials. (Poster presentation in *MicroTech 2016*, Appendix A)

- Development of soft sensors using elastic silicone materials and a conductive eutectic liquid alloy. The soft sensors here were designed based on resistance change of the liquid alloy and aimed at sensing of physical shape variables such as stretch and pressure. Teng et al. [2018a]

- Development of a high resolution pressure-sensor soft system that can transduce normal force into a digital output. In this system, a microfluidic soft pressure sensor was integrated with a flexible printed circuit board. Conductive thread was used in this system as the interconnect to alleviate electrical connection problems arising due to the mechanical mismatch between conventional metal wires and soft or liquid materials. Teng et al. [2018a]

- Development of a new wireless soft sensor, which benefits from a combination of radio-frequency identification (RFID) tag design and microfluidic sensor fabrication technologies. This new microfluidic sensor is intrinsically stretchable and can be reversibly strained. This sensor is a passive and wireless device, and as such, it does not require a power supply and is capable of transporting data without a wired connection. Teng et al. [2018b], Teng et al. [2019] (Poster

presentation in *The University of Edinburgh Research Conference 2017*, Appendix B)

- Development of methods to make soft package and connections for conventional chips and other electronic components by using flexible conductors and soft substrates as substitutes for copper and plastic in conventional printed circuit boards. (Technical presentation in *ASME IMECE 2017*, Appendix C)

- Development of a method, which has potential to be mass-manufacturable, to fabricate soft printed circuit boards. This method involves metal depositing on silicone materials, liquid metal wetting, and HCl vapour 'soldering'.

- Development of a flexible and stretchable 7-segment display system and a soft printed circuit board fabrication method.

1.4 PUBLICATIONS

Some ideas and figures in this thesis have been published in the following journal [J] and conference [C] articles:

[J1] **L. Teng**, K. Jeronimo, T. Wei, M. P. Nemitz, G. Lyu, and A. A. Stokes. Integrating soft sensor systems using conductive thread. In *Journal of Micromechanics and Microengineering*, 2018.

[J2] **L. Teng***, K. Pan*, M. P. Nemitz, R. Song, Z. Hu, and A. A. Stokes. Soft RFID sensors: Wireless Long-range Strain Sensors Using Radio-frequency Identification. In *Soft Robotics*, 2018.

[J3] **L. Teng***, K. Pan*, L. Ting, X. Zhou, Z. Hu, and A. A. Stokes. Soft Wireless Battery-free UHF RFID Stretchable Sensor based on Microfluidic Technology. In *IEEE Journal of Radio Frequency Identification*, 2019.

[J4] C. Chao, X. Jin, **L. Teng**, A. A. Stokes, and X. Fan. Bubble dislodgment in a capillary network with microscopic multi-channel and multi-bifurcation features. In *Langmuir*, 2019.

[J5] R. Song, G. Richard, C. Cheng, **L. Teng**, Y. Qiu, M. Lavery, S. Trolier-McKinstry, S. Cochran, and I. Underwood. Multi-Channel Signal Generator ASIC for Acoustic Holograms. In *IEEE Transactions on Ultrasonics, Ferroelectrics, and Frequency Control*, 2019.

[J6] G. Lyu, X. Shen, T. Komura, K. Subr, and **L. Teng**. Widening Viewing Angles of Automultiscopic Displays Using Refractive Inserts. In *IEEE Transactions on Visualization and Computer Graphics*, 2018.

[J7] M. P. Nemitz, M. E. Sayed, J. Mamish, G. Ferrer, **L. Teng**, R. M. McKenzie, A. O. Hero, E. Olson, and A. A. Stokes. HoverBots: Precise Locomotion Using Robots That Are Designed for Manufacturability. In *Frontiers in Robotics and Artificial Intelligence*, 2017.

[C1] S. T. Mahon, A. Buchoux, M. E. Sayed, **L. Teng**, and A. A. Stokes Soft robots for extreme environments: Removing electronic control. In *RoboSoft 2019 - IEEE International Conference on Soft Robotics*, 2019.

1.5 2D BARCODES

Throughout this thesis, I use QR codes (Quick Response code, a type of 2D barcode) to direct the reader towards important videos that help understand the context and thesis relevant videos (such as the videos of manufacturing process or device performance). I use the *qrcode* package in Latex to encode data such as html links into the QR codes. There is a list of all the QR codes at the beginning of this thesis on page xix. Most mobile phones such as the iPhone series are able to read the QR codes. Please open the standard camera application on you phone, aim for the QR code, and open the link that pops up. Otherwise I refer to *QR Reader for iPhone* in the AppStore or *QR Code Reader* in the Google Play Store; both applications are freeware.

QRcode 1.1.: Test your camera.

Link to the webpage of Soft Systems Group.

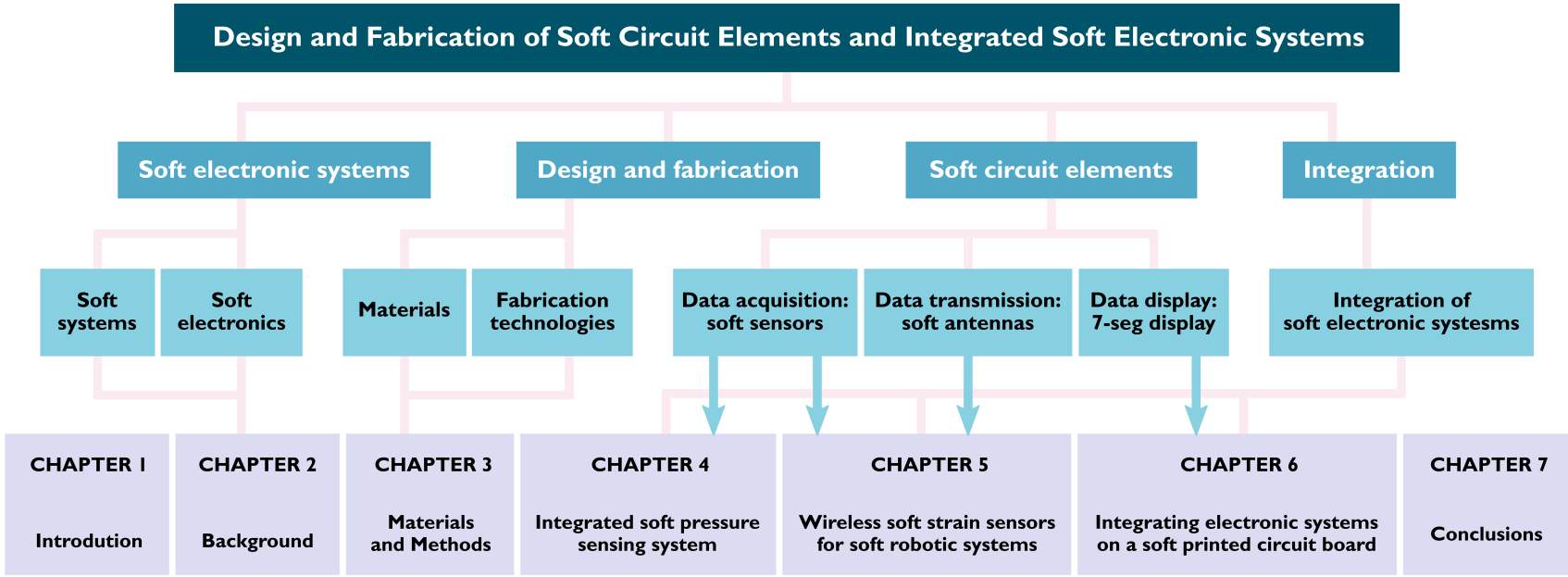

Figure 1.1.: *Thesis structure layout.* Chapter 1, 2, and 3 contain the general introduction, literature background, and fundamental materials and fabrication technologies of this Ph.D work. Chapter 4, 5, and 6 present the integrated soft electronic systems I created during the period of Ph.D. Each of the system includes one soft circuit element that I originally designed and manufactured. The soft antenna proposed in Chapter 5 is also a wireless strain sensor, that is why both 'soft sensors' and 'soft antennas' are pointed to Chapter 5.

1.6 THESIS STRUCTURE

The overall structure of my thesis takes the form of seven chapters, including this introductory chapter. The second chapter introduces background knowledge of this study while the third chapter deals with the fundamental materials and fabrication technologies used in all the follow-up work. Chapter 4, 5, and 6 present, respectively, three integrated soft electronic systems that I designed and manufactured in my Ph.D work. Each of the integrated system involves an originally designed soft electronic device. Figure 1.1 on page 8 shows the overall layout of this thesis. A summary of the content of each part and chapter is given below:

- **Chaper 2: Background**

  The background knowledge of existing soft systems (such as soft robotic systems), and soft electronic devices is introduced in this chapter to help readers understand the follow-up chapters.

- **Chaper 3: Materials and Methods**

  The third chapter is concerned with properties of the basic materials which are used to make soft electronic devices in my Ph.D work and the development of a rapid-prototyping technique for soft-lithography masters using laser-cutting systems and self-adhesive materials.

- **Chaper 4: Integrated Soft Pressure Sensing system**

  This chapter introduces the development of a high resolution pressure-sensor soft system that can transduce normal force into a digital output. In this system, I integrated a microfluidic soft pressure sensor with a flexible printed circuit board and used conductive thread in this system as the interconnect to alleviate electrical connection problems arising due to the mechanical mismatch between conventional metal wires and soft or liquid materials.

- **Chaper 5: Wireless Soft Strain Sensors for Soft Robotic Systems**

  The fifth chapter presents the development of a new wireless soft sensor, which benefits from a combination of radio-frequency identification (RFID) tag design and microfluidic sensor fabrication technologies. This new microfluidic sensor is intrinsically stretchable and can be reversibly strained. This sensor is a passive and wireless device, and as such, it does not require a power supply and is capable of transporting data without a wired connection.

- **Chaper 6: Integrating Electronic Systems on a Soft Printed Circuit Board**

  The sixth chapter presents the development of a method, which has potential to be mass-manufacturable, to fabricate soft printed circuit boards. This method involves metal depositing on silicone materials, liquid metal wetting, and HCl vapour 'soldering'. This chapter also presents the development of a flexible and stretchable 7-segment display system and a soft printed circuit board fabrication method.

- **Chaper 7: Conclusion and Future Work**

  The last chapter includes conclusions of my work, evaluation of my contributions, and a wide range of future work.

2

BACKGROUND AND LITERATURE SURVEY

As introduced in Chapter 1, the main purpose of this study is to develop flexible and stretchable soft electronic circuit components, and to study the methods to integrate electronic components into soft systems. In order to provide the reader with sufficient background knowledge, this chapter presents a review of some critical previous work on soft systems and soft electronics.

2.1 SOFT SYSTEMS

Before talking about 'soft' and 'hard', I would like to introduce the definition of Young's modulus. Young's modulus is a mechanical property that measures the stiffness of a solid material. It defines the relationship between stress (force per unit area) and strain (proportional deformation) in a material in the linear elasticity regime of a uniaxial deformation. (Linear elasticity assumes infinitesimal strain and linear relationships between the components of stress and strain. These assumptions are reasonable for many engineering materials, so it is used extensively in structural analysis and engineering design.) Young's modulus Y, can be calculated by

$$Y = \frac{\sigma}{\varepsilon} = \frac{F/A}{\Delta L/L_0} = \frac{FL_0}{A\Delta L} \tag{2.1}$$

where σ (stress) is uniaxial force per unit surface (in Pa), ϵ (strain) is proportional deformation (change in length divided by original length), F is the uniaxial force, A is the cross-section area perpendicular to the force, L_0 and ΔL are the original length

and the change in length respectively. In practice, Young's modulus is usually given in MPa (N/mm^2) or GPa (kN/mm^2).

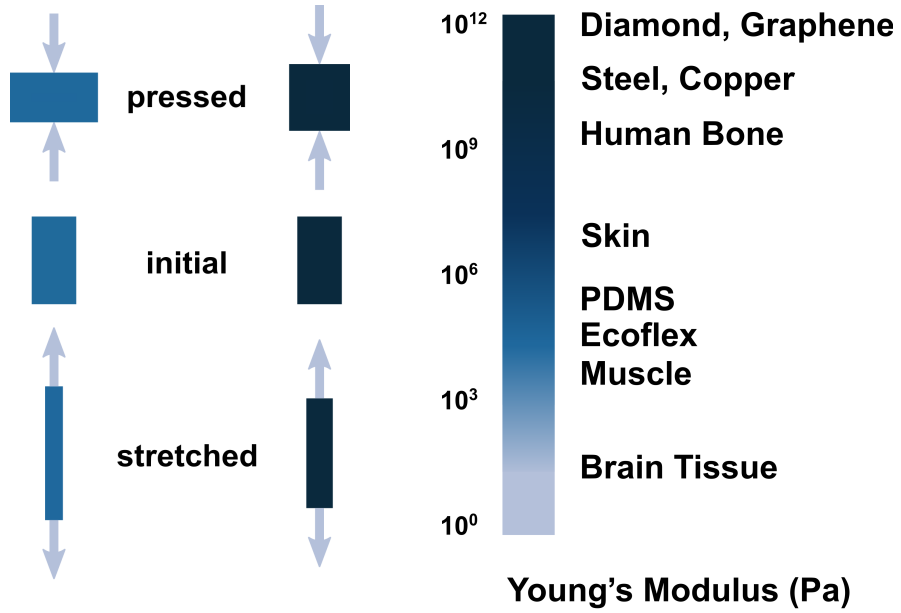

(a) (b)

Figure 2.1.: *Introduction of Young's modulus.* **(a).** Young's modulus is a measure of stiffness, the larger the Young's modulus, the stiffer the material. A given tensile (extension) or compressive (compression) uniaxial stress creates more deformation in a material with low stiffness (left) than with a high stiffness (right). **(b).** Young's modulus comparison of various common materials.

The larger the Young's modulus, the stiffer the material. In Figure 2.1a, the left material has a smaller Young's modulus than the right one. A given tensile or compressive uniaxial stress causes more deformation in the material with lower Young's modulus. In general, Young's modulus of the hard materials that we are familiar with (such as diamond, steel, copper, and human bone) are in GPa scale while of the soft materials (such as skin, muscle, silicone) are in MPa scale. Figure 2.1b shows a Young's modulus comparison of various common materials.

As shown in Figure 2.2 on page 13, there are multiple mechanical, biological, economic, and manufacturing mismatches between the world of biological things (soft) and the world of made-things (hard). These mismatches limit the utility, and restrict the uptake, of diagnostics, therapeutics, and robotics in human-robot interaction and healthcare technologies. Soft system can help us eliminate the

mismatches between soft and hard things. Soft systems that possess functions of hard systems (like electronic functions) have potential to provide better adaption to the world of soft things, therefore contribute to a plenty of cutting-edge applications, such as human-machine interaction, prosthetics, medical instrument, and in-body health monitoring.

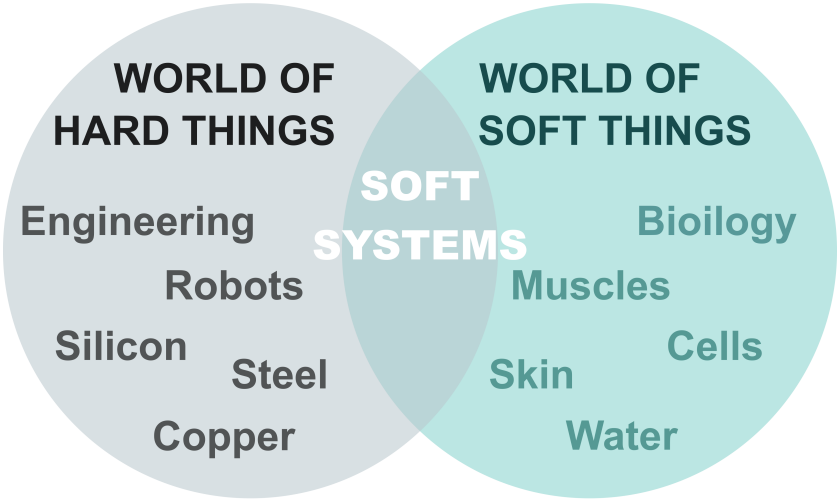

Figure 2.2.: *Soft systems are bridges between world of hard things and soft things.* There are multiple mechanical, biological, economic, and manufacturing mismatches between the world of biological things and the world of made-things. These mismatches limit the utility, and restrict the uptake, of diagnostics, therapeutics, and robotics in human-robot interaction and healthcare technologies.

Soft machines containing compliant actuators, with sample collection, and drug delivery, have potential to be a step change in medical device technology for use in surgery, biopsy, and treatment. These systems are inherently soft - they have lower mechanical compliance than the materials they are being used to explore. This property makes them intrinsically safe.

As a radical change in the materials and processes used to make robotics and healthcare technologies, the field of soft systems has developed sharply in recent years. These developments are benefit from a large and growing body of literature that is reported on an abundance of novel soft materials, such as silicones (e.g. PDMS (polydimethyl-siloxane) and Ecoflex), hydrogels, etc. Research in soft matter engineering has bought in new approaches in creating soft systems, especially, soft robotics and wearable devices. The following content in this section introduces

previous research on soft robotics and wearable devices in the last ten years and discuss why the integration of electronics is essential to the development of these soft systems.

2.1.1 *Soft Robotics*

Soft robotics, which deals with constructing robots from highly compliant materials (with MPa Young's modulus), is a specific sub-field of robotics. The mainstream of conventional robotic systems are built from hard and non-compliant components. These 'hard' robots, that are fabricated as rigid branches connected at discrete joints, loaded with electronic instruments and components, can carry heavy objects, build cars, and even dismantle bombs. However, in some special circumstance, it is essential to have robots with soft structures - soft robots.

Most soft robots take inspiration from the creatures that don't have hard bones, such as earthworms, octopuses, squids, jellyfish, etc. We expect the soft robots to have great flexibility and adaptability, so that they can enter spaces with narrow entrance, crawl through curved pipe, move on broken, rocky, and uneven surfaces, and also improve safety when working around humans. The QR code below links to a video of a soft robot walking and crawling. (Soft robot in this video is pneumatically actuated.) From our point of view, soft robots have the potential to make up for some shortages of conventional hard robots. These robots with soft bodies can find their utilities in the applications of human-robot interaction, disaster area rescue, battle field reconnaissance, etc.

QRcode 2.1.: Soft robot walking and crawling.



Conventional robotic systems usually contains many motors to actuate subsections in the system. In contrast to traditional rigid robots, actuation of soft robotic systems has been tackled with a wide variety of methods. Among these soft actuation

methods, pneumatic actuators have long been popular, due to their relatively large actuation force, large strains, and fast response time. Figure 2.4a on page 16 shows a pneumatic soft robot (Shepherd et al. [2011]) presented by Whitesides research group. This soft robotic system uses five actuators and a valving system operates at low pressure (< 10 psi). These types of robots can cross difficult obstacles and benefit from a combination of crawling and undulation gaits.

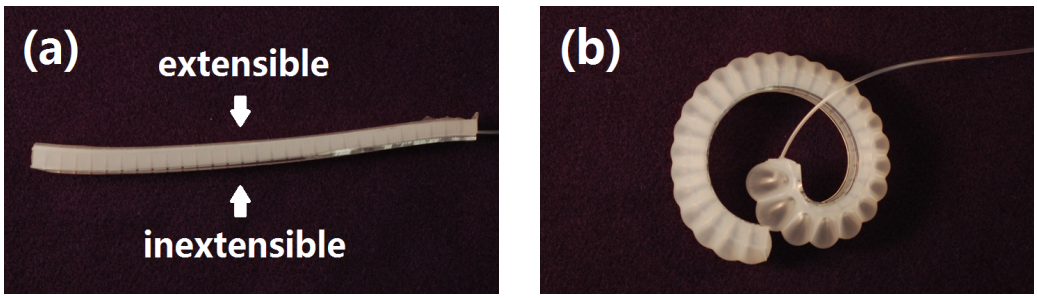

Figure 2.3.: *Pneu-net (PN) architecture.* **(a).** A PN architecture contains a series of chambers embedded in a extensible layer and bond to an inextensible layer. **(b).** Compressed air inflates pneumatic network and induces strain. Different strain on the extensible and inextensible materials induces curvature deformation. Material stiffness and thickness affect degree of bending. In this presented work, the high strain (extensible) material is Ecoflex, while the low strain (inextensible) material is PDMS (Sylgard 184). Reproduced from: Shepherd et al. [2011]

Channel design of the pneumatic soft robot follows the pneu-net (PN) architecture (Ilievski et al. [2011]) which contains a series of chambers embedded in a layer of extensible elastomer (usually fabricated with the soft-lithography technology) and bond to an inextensible layer. Figure 2.3 shows a PN architecture that was manufactured with a high strain (extensible) material Ecoflex (silicone elastomer) and a low strain (inextensible) material PDMS (Sylgard 184). When actuated, the embedded chambers inflate like balloons, the PN structure bends when pressurised because of the difference in strain between the extensible layer and the inextensible layer. Besides the mentioned work, there is a plenty of other research on soft robotics used similar pneumatic actuators, such as Yang et al. [2016], Wei et al. [2016], Wirekoh and Park [2017], McKenzie et al. [2017], etc.

Figure 2.4 shows part of the representative work in the field of soft robotics. In addition to pneumatic actuation, there are many other ways to actuate soft robots,

such as ionic actuation (Cho et al. [2007], Wei and Guo [2010], Bahramzadeh and Shahinpoor [2014]), combustion (Loepfe et al. [2015], Bartlett et al. [2015], Wehner et al. [2016] in Figure 2.4b), light actuation (Rogoz et al. [2016], Palagi et al. [2016], Zeng et al. [2018] in Figure 2.4d), thermal or photo-actuation(Yuan et al. [2017] in Figure 2.4e, Rodrigue et al. [2017]), electrical actuation (Godaba et al. [2016], Li et al. [2017]), electromagnetic actuation (Nemitz et al. [2016]) to just name a few. All of these soft actuation method have performance trade-offs between speed, force, deformation, displacement, flexibility, reliability, and ancillary equipment requirements (Rus and Tolley [2015], Rich et al. [2018]). These actuation methods each have their own best-fit situations. To date, none of the listed actuation methods has become a principal method of soft robotic actuation.

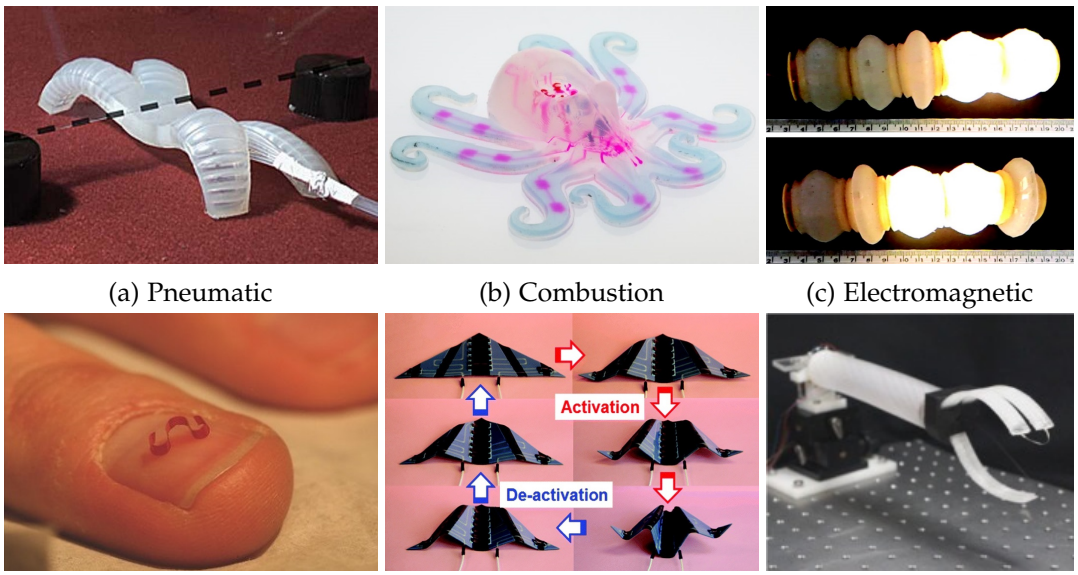

(a) Pneumatic (b) Combustion (c) Electromagnetic

(d) Light sensitive (e) Heat sensitive (f) Shape memory

Figure 2.4.: *Previous work on soft robotics with different actuators.* **(a).** A pneumatic actuated silicone soft robot (∼160 mm long). Reproduced from: Shepherd et al. [2011]. **(b).** Octopus robot (∼55 mm) powered by combustion and controlled by fluidic logic. Reproduced from: Wehner et al. [2016]. **(c).** A pneumatic worm-robot (∼180 mm long) with electromagnetic actuators. Reproduced from: Nemitz et al. [2016]. **(d).** A miniature LCE (liquid crystal elastomer) crawler (∼13 mm long) that moves in response to light. Reproduced from: Zeng et al. [2018]. **(e).** Origami robot (∼110 mm side length) actuated by resistive heating in LCE hinges. Reproduced from: Yuan et al. [2017]. **(f).** Gripper (∼100 mm long) actuated by resistive heating in a shape-memory alloy. Reproduced from: Rodrigue et al. [2017].

No matter which actuation method we use to drive soft robots, the aim that we design and fabricate soft robots is to make them perform the actions we need, and acquire and transmit information from the environment to us. These functions require soft robots to have a lot of electronic components, such as sensors, microcontrollers, antennas, and batteries, with no mechanical mismatch.

2.1.2 *Wearable Devices*

In recent decades, the field of wearable devices has experienced a spectacular growth due to breakthroughs in biotechnology, nanotechnology, and material science. Wearable devices are of special interest because of their widespread applications in consumer electronics (Zhang et al. [2015]), healthcare (Wang et al. [2013], Bandodkar and Wang [2014]), personalised Internet of Things (IoT) (Zhu et al. [2015], Parrilla et al. [2016], Trung and Lee [2016]), security fields (O'Mahony and Wang [2013], Sekhar and Wignes [2016]), etc.

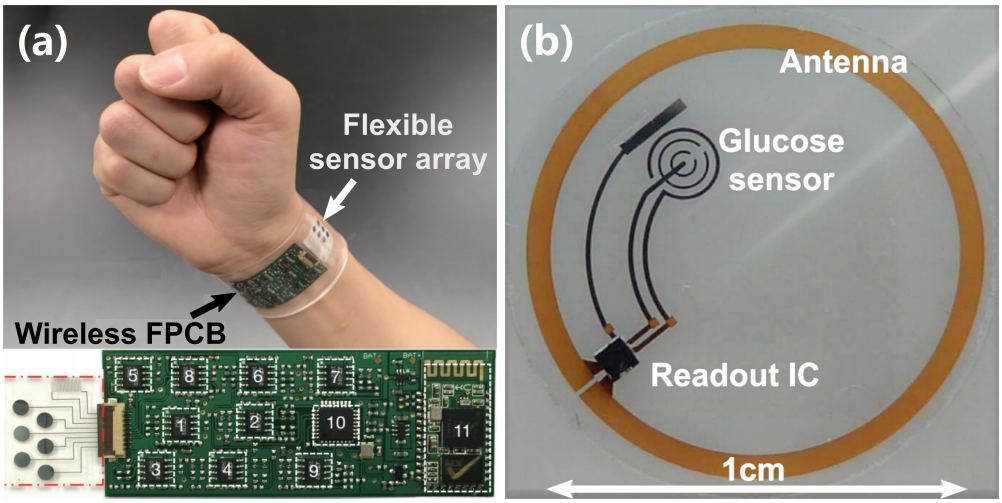

Figure 2.5.: *Wearable devices in different forms–1.* **(a).** A smart wristband for measuring sweat profile of human subject engaged in prolonged physical activities. Reproduced from: Gao et al. [2016b]. **(b).** A soft contact lens for measuring glucose levels in the wearer's eye fluids. Reproduced from: Liao et al. [2012].

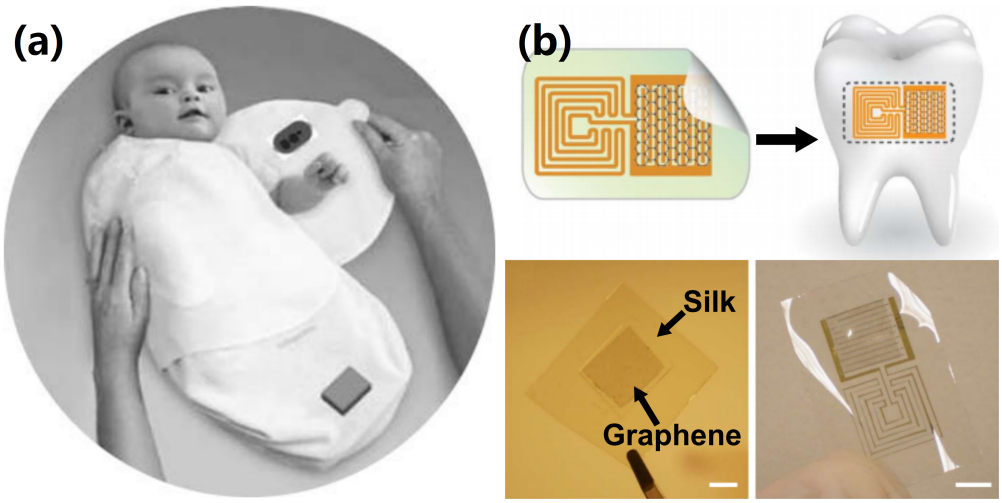

Figure 2.6.: *Wearable devices in different forms–2.* **(a).** A swaddling baby wrap contains integrated health monitoring devices for measuring temperature, hydration, and pulse rate of the baby. Reproduced from: Baker et al. [2007]. **(b).** A wireless tattoo-based resistive sensor for bacteria detection on tooth enamel. Reproduced from: Mannoor et al. [2012].

Wearable devices come in a variety of forms, such as wrist-supported watches, straps, and gloves; foot-supported shoes and socks; head-supported glasses, helmet, and headbands; lenses, clothing, school bags, crutches, and accessories. Figure 2.5 and Figure 2.6 shows some wearable devices with different forms. The smart wristband in Figure 2.5 (a) is a wearable sensing system that can measure the detailed sweat profile of human subject engaged in prolonged indoor and outdoor physical activities, and make a real-time assessment of the physiological state of the subject (Gao et al. [2016b]). Figure 2.5 (b) demonstrates a soft contact lens that can measure glucose levels in the wearer's eye fluids. Figure 2.6 (a) represents an integrated health monitoring device that contained within a swaddling baby wrap. This baby glove provides a comfortable method of securing the baby, while continuously monitoring temperature, hydration, and pulse rate, which are three main health considerations of the baby (Baker et al. [2007]). Figure 2.5 (b) shows a wireless sensor fabricated by printing graphene onto a bioabsorbable silk film. This sensor can detect bacteria (staphylococcus aureus) on tooth enamel (Mannoor et al. [2012]).

To monitor human activity and personal care, flexible and stretchable sensors that can provide data acquisition function are core of the wearable devices. These sensors are capable of measuring many physical parameters that generated by human activities, such as skin temperature, pressure, and strain. Figure 2.7 provides a list of several flexible and stretchable physical sensors in the form of wearable pads, bands, patches, and straps that can be attached or laminated to various position of the human body (Trung and Lee [2016]). To date, most of physical sensors in wearable devices are temperature sensors, pressure sensors, strain sensors, and integrated sensing systems. Temperature sensors are useful in body temperature detection (Webb et al. [2013], Kim et al. [2015]), wound-healing monitoring (Hattori et al. [2014]), etc. Pressure sensors can realise pulse rate monitoring (Kang et al. [2014], Pang et al. [2015]) and voice monitoring (Wang et al. [2014a]). Strain sensors are useful in monitoring human motions (Yamada et al. [2011]), muscle movements (Wang et al. [2014b]), and human emotion (Roh et al. [2015]) to just name a few.

Since most customers demand wearable devices to be soft, thin, light, stretchable, have good skin compliance and adhere well to the complex three dimensional curvature of the human body, the size, quality, performance, and packaging materials of the components can intensely affect user experience of the wearable products. In previous research, the dominant technologies utilised for fabricating wearable electronic devices are lithographic (Gao et al. [2016a], Gao et al. [2016c]) and three-dimensional printing (Malzahn et al. [2011], Jost et al. [2013], Imani et al. [2016]) methods. Lithographic methodologies, such as soft-lithography, photo-lithography, e-beam and ion-beam lithography, produce high performance devices but have high financial cost. Inexpensive printing techniques can significantly reduce the fabrication costs when one is fabricating devices at large scale with desired precision and accuracy.

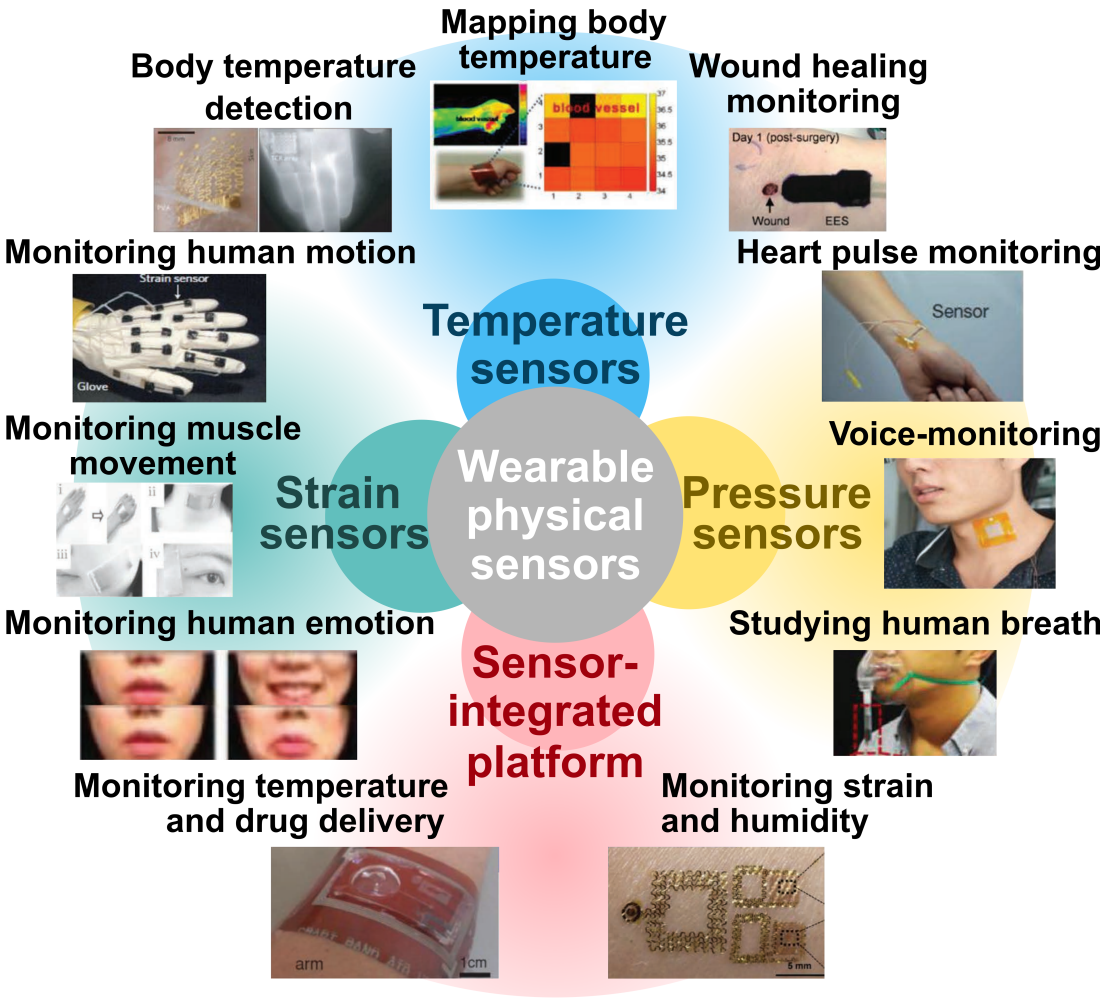

Figure 2.7.: *Wearable sensors in monitoring human activities and personal care.* **Temperature sensors:** Body temperature detection. Reproduced from: Webb et al. [2013]. Mapping of body temperature. Reproduced from: Kim et al. [2015]. Wound-healing monitoring. Reproduced from: Hattori et al. [2014]. **Pressure sensors:** Heart pulse monitoring. Reproduced from: Kang et al. [2014]. Voice monitoring. Reproduced from: Wang et al. [2014a]. Pulse rate detection. Reproduced from: Pang et al. [2015]. Studying human breath. Reproduced from: Park et al. [2014]. **Strain sensors:** Monitoring human motions. Reproduced from: Yamada et al. [2011]. Monitoring muscle movements. Reproduced from: Wang et al. [2014b]. Monitoring human emotion. Reproduced from: Roh et al. [2015]. **Sensor-integrated platform:** Monitoring temperature and drug delivery. Reproduced from: Honda et al. [2014]. Monitoring strain and humidity. Reproduced from: Huang et al. [2014].

2.2 SOFT ELECTRONICS

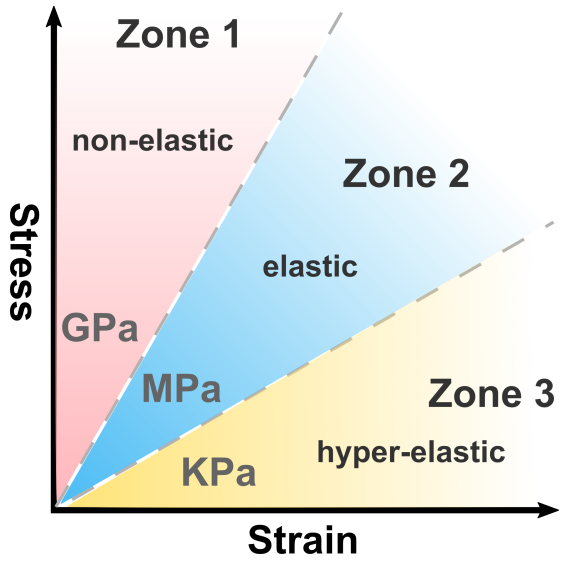

Figure 2.8.: *Non-elastic, elastic, and hyper-elastic materials.* Solid materials can be divided in three zones by the Young's modulus of them. Materials in Zone 1 that has GPa Young's modulus are defined as non-elastic, while materials in Zone 2 that has MPa Young's modulus are defined as elastic, and materials in Zone 3 that has KPa Young's modulus are defined as hyper-elastic.

As introduced in Section 2.1, Young's modulus that equals to stress upon strain is a mechanical property that measures the stiffness of a material. Figure 2.8 divides solid materials in three zones. Materials that has GPa Young's modulus are in Zone 1 and defined as non-elastic, while materials that has MPa and KPa Young's modulus are in Zone 2 and Zone 3 respectively and defined as elastic and hyper-elastic.

Historically, there has been a trade-off between conductivity and compliance. Usually, materials with high conductivity, such as metals, are in Zone 1, whereas compliant materials in Zone 2 and Zone 3, such as silicones, have low conductivity. Researchers have therefore paid much attention to the challenge that to develop soft structures with high compliance and conductive electrical properties. This challenge has been addressed by many of the methods described below.

2.2.1 *Flexible Electronics*

Traditional electronics are generally built on thick inflexible substrates. Instead, flexible electronics - built on substrates like plastics, polymers or metallic foils - can be bent, wrapped, rolled, twisted, and folded with negligible effect on its electronic function. Intrinsically stiff materials with GPa Young's modulus (Zone 1 in Figure 2.8) can be rendered flexible by making them sufficiently thin. For example, a bulk sample of tin is rigid, but thin foil is flexible. Even silicon (serves as the substrates for chips in modern computers and mobile phones), an extremely rigid and brittle material, can be flexible if it is thin enough (Crabb and Treble [1967]). This concept has been known for many years and is used commercially to build flexible conductors and transistors on polymeric substrates (Brody [1984]).

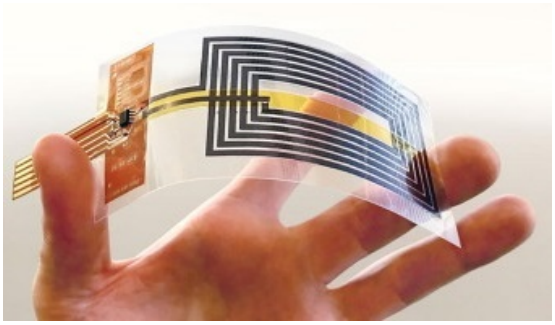

(a) Flexible graphene antenna

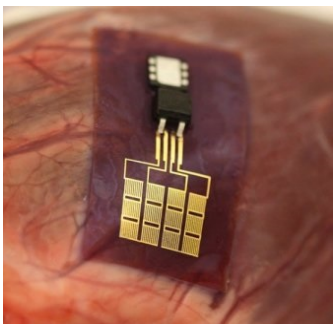

(b) Flexible PZT system

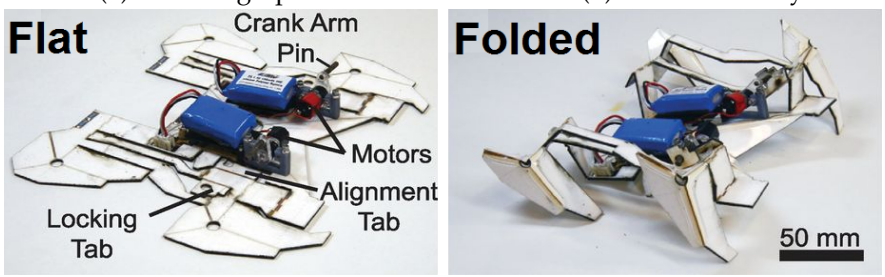

(c) Self-folding machines

Figure 2.9.: *Flexible electronics.* **(a).** A flexible graphene antenna. Reproduced from: Scidà et al. [2018]. **(b).** A flexible and integrated system that is fabricated with a gold film on top of a multilayer stack of PZT (Lead Zirconate Titanate) ribbons. This system is capable of harvesting and storing energy from the natural contractile and relaxation motions of the heart, lung, and diaphragm. Reproduced from: Dagdeviren et al. [2014]. **(c).** A method for building self-folding machines based on the principles of kirigami and origami. Reproduced from: Felton et al. [2014].

Flexible electronic is typically composed of a thin passive substrate (e.g. plastic, textile, etc.) topped with a second layer of active electronic components. The functional layer of flexible electronics may be composed of electronic and optoelectronic components, such as sensors (Vilela et al. [2016], Nag et al. [2017]), antennas (Dagdeviren et al. [2014] in Figure 2.9a), Thin film transistors (TFTs) (Sekitani et al. [2010], Franklin [2015]), OLEDs (Li et al. [2016]), batteries (Tan et al. [2017]), and energy harvest systems (Scidà et al. [2018] in Figure 2.9b). Flexible sensors have great potential in health monitoring applications, such as the monitoring of glucose (Wang et al. [2011]Zhang et al. [2015]), pH (Gou et al. [2014]), and cholesterol (Ji et al. [2015]).

In addition, flat and thin rigid materials can form complex three-dimensional structures by using the principles of the Japanese art of paper cutting, kirigami ('kiru', cut; 'kami', paper) and origami ('ori', fold), these principles are often used in pop-up books. With the inspiration from pop-up books, researchers at Harvard University fabricated the Monolithic Bee (Sreetharan et al. [2012]) which is a millimetre-scale flapping wing robotic insect produced using PC-MEMS (Printed Circuit Microelectromechanical Systems) techniques. Engineers at Harvard SEAS (School of Engineering and Applied Sciences), Wyss Institute, and MIT (Massachusetts Institute of Technology) have developed a robot that assembles itself into a complex shape in four minutes, then folds up and crawls away (in Figure 2.9c, Felton et al. [2014]). With the similar ideas, researchers in the US have made a stretchable and bendable transistor (Reynolds et al. [2016]) by applying the principles of kirigami.

The ability to make rigid conductive materials thin creates flexible electronic devices, but the devices are not stretchable. Krigami and origami make rigid materials flexible in three-dimensional structures and stretchable in some measure, but the durability, flexibility and stretchability of the devices are considerably limited.

2.2.2 *Stretchable Electronics*

Comparing with flexible electronics, stretchable electronics can be used in wider application space since they can not only be bent, but also be elongated. There are a number of ways to make stretchable conductors. Lorussi *et al.* have developed strain sensing fabric composites for detecting hand posture and gesture using an electrically conductive elastomer (Lorussi et al. [2005]). Cheung *et al.* have presented an ionic fluid soft sensor for measuring strains (Cheung et al. [2008]). Researchers have also used polymer structures with embedded conductive material in making soft sensors, such as conductive polymer-based sensors (Nambiar and Yeow [2011]), solid-state organic field-effect transistor (FET) circuits (Kawaguchi et al. [2005]), silicone robot fingers with embedded conductive liquid (Wettels et al. [2008]), and fibre optic strain sensors in a plastic robotic finger for force sensing and contact localisation (Park et al. [2007]), (Park et al. [2009]). Figure 2.10, Figure 2.11, and Figure 2.14 respectively present three general strategies of making stretchable electronics: deterministic geometries, random composites, and intrinsically stretchable structures (Dickey [2017]), which are summarized briefly below.

Deterministic Geometries: Some materials are inherently rigid, but they can be arranged to be stretchable using strategic geometries (Rogers et al. [2010]). A classic example is a metallic spring can be stretched and compressed despite being rigid against other modes of deformation. It is possible to make conductive but stiff materials flexible and stretchable by reducing thickness of the materials and patterning them with "deterministic geometries". Figure 2.10 presents some design principle of the deterministic geometries and some typical previous work designed based on this concept.

Using designs based on deterministic geometries, researchers have created many soft electronic devices with various structures, such as wavy structures (Gray et al. [2004], Sun et al. [2006]), filamentary and serpentine meshes (Brosteaux et al. [2007], Kim et al. [2008], Guo et al. [2014]), intentionally fractured thin films (Lacour et al.

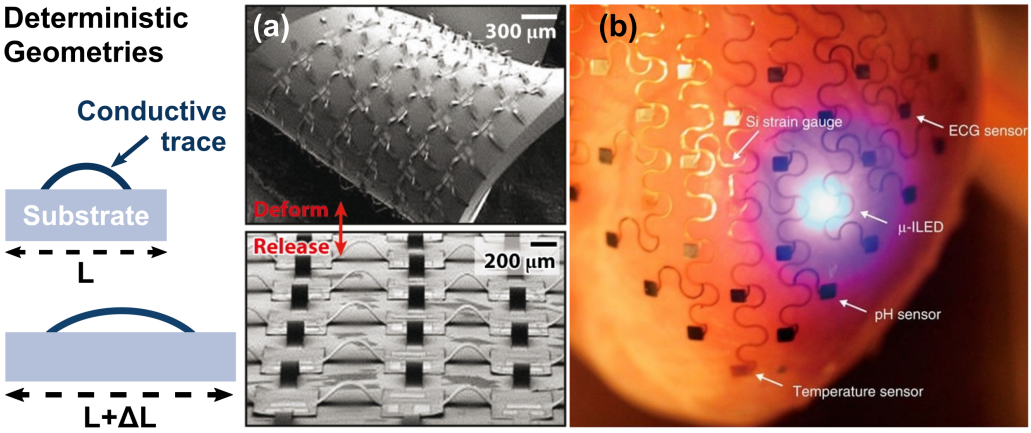

Figure 2.10.: *Stretchable electronics with deterministic geometries.* Solid thin conductive traces in deterministic geometries can flex when stretched. Many stretchable electronic devices were designed based on this principle, such as: **(a).** An array of stretchable CMOS inverters. Reproduced from: Kim et al. [2008]; and **(b).** A stretchable electronic device designed with serpentine structure integrated on a Langendorff-perfused rabbit heart. Reproduced from: Xu et al. [2014].

[2003], Lacour et al. [2005]), and fractal and kirigami structures (Blees et al. [2015], Shyu et al. [2015], Fan et al. [2014]).

A very attractive advantage of deterministic design is that it is generally compatible with conventional microfabrication techniques (can be fabricated in the same process flow) to pattern a wide variety of materials, including silicon. Limitations of this technique are (i) rigidity of the embedded conductive materials limit the ultimate strain at failure; (ii) Wavy and serpentine geometries lower the density of components since the indirect paths increase the areal footprint; (iii) Fabrication of these structures often requires the use of expensive clean room facilities; (iv) The resulting filaments need to be thin (so they flex easily) but this limits the electrical conduction.

Composites: Dispersing conductive particles in elastomers provides another method for making stretchable electronic devices. Figure 2.11 shows principle of this fabrication method and some representative work designed based on this concept.

There are various options for the conductive particles, such as metallic (Ag (Chun et al. [2010], Xu and Zhu [2012]) and Cu (Ding et al. [2016]) and carbonaceous (carbon black (Brigandi et al. [2014]), carbon nanotubes (Shin et al. [2010]), graphene (Lin et al.

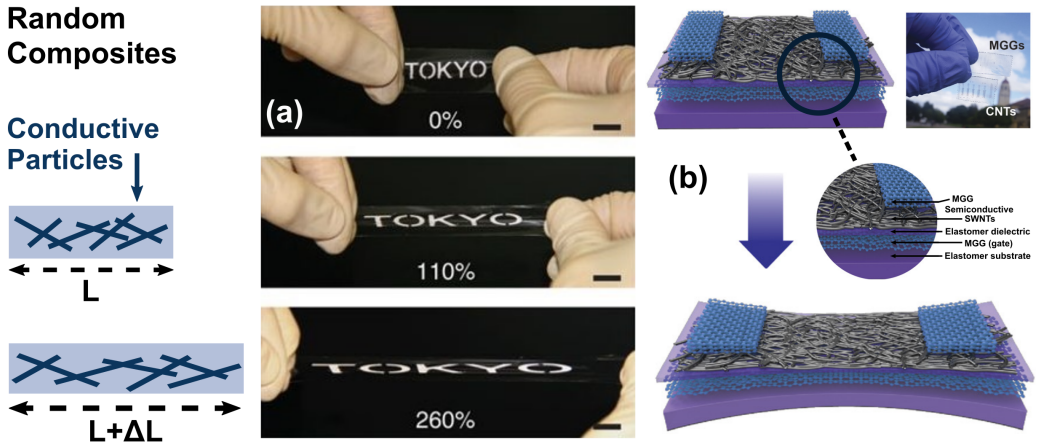

Figure 2.11.: *Stretchable electronics made of composites.* Dispersing conductive particles in elastomer offers another method for creating stretchable conductors. For examples: **(a).** Printed elastic conductor and demonstration of the stretchability. Reproduced from: Matsuhisa et al. [2015]; and **(b).** Scheme of a graphene-based stretchable transistor and photo of stretchable transistors arrays (top right). SWNTs in the figure means single-walled carbon nanotubes. Reproduced from: Liu et al. [2017].

[2016], and carbon fibres Liu et al. [2015]). Silver nanowires are popular fillers due to their high electrical conductivity. Previous work has presented incorporating silver nanowires into elastomers to form stretchable electrodes (You et al. [2017], Shuai et al. [2017], Ma et al. [2017]) and LEDs (You et al. [2017]). Graphene nanoscrolls and graphene sheets can also enable conductivity in elastomers and keep functional under high strain (Liu et al. [2017]). Some of these filled conductive elastomers show great optical properties, such as high transparency, so they are possible to be useful in optical applications (You et al. [2017], Liu et al. [2017] (in Figure 2.11), Pyo et al. [2018]).

The most popular filler material is carbon black (Brigandi et al. [2014]), which is produced by the incomplete combustion of heavy petroleum products. Figure 2.12 shows the relationship between electric conductivity and filler concentration of carbon black particles. As shown in the figure, the curve of conductivity versus filler concentration is S-shaped. Adding a conductive filler above a critical concentration to insulating polymers can make them electrically conductive. The critical concentration

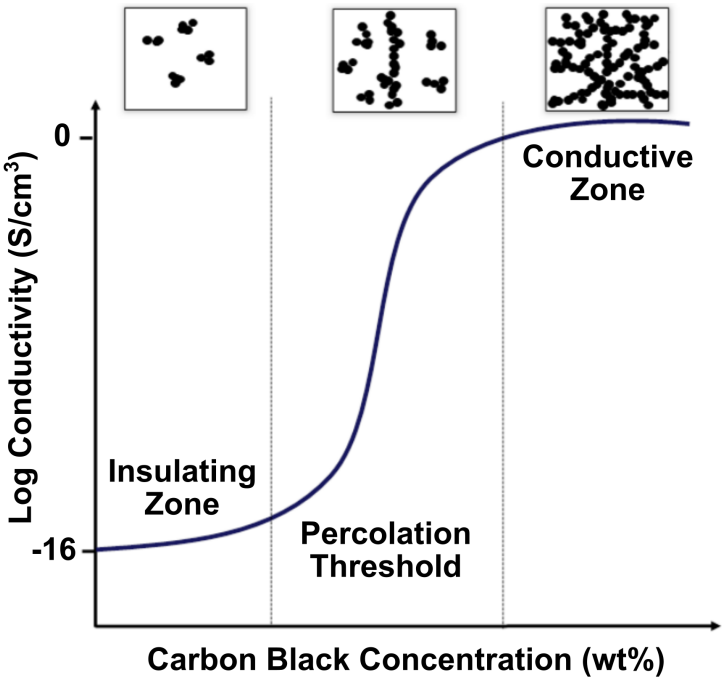

Figure 2.12.: The curve of conductivity versus carbon black filler concentration. (Data from: Brigandi et al. [2014])

is called the percolation threshold, where the polymer composite makes a transition from the insulating zone to the conductive zone.

If the percolated polymers are used well above the percolation threshold, and for modest elongations, they can be used as stretchable or flexible conductors, with high conductivity close to that of the filler particles (e.g. conductive inks). These conductive composites are useful for electrical interconnects and electrodes. If the percolated polymers are used close to the percolation threshold, they can be used as extremely sensitive pressure or strain sensors with very large conductivity changes (Bloor et al. [2005]). By utilising this property, researchers have produced robust resistive strain and pressure sensors, such as (Mitrakos et al. [2018]), (Miyamoto et al. [2017]), (Varga et al. [2017]), (Xu et al. [2017]), and (Luo et al. [2017]). These soft sensors are often well-suited for the applications of soft robots and wearable devices. However, that close to percolation threshold, they can suffer from sensitivity to temperature and humidity (and indeed can even engineered as thermal and / or chemical vapour sensors to take advantage of this effect). Researchers have also

created capacitive pressure sensors by deforming a dielectric layer between electrodes made from these filler materials (Shuai et al. [2017], Pyo et al. [2018]).

The resistive and capacitive sensors mentioned above usually have very simple structures, the fabrication of these simple sensors is both robust and scalable. Previous literature has presented a variety of fabrication techniques, such as spray deposition (Sencadas et al. [2017]), screen printing (Yuen et al. [2017], White et al. [2017]), direct writing (Muth et al. [2014], White et al. [2017]), and ink-jet printing (Kholghi Eshkalak et al. [2017]). Ink-jet printing is used for nanoscale filler particles only to avoid clogging of jet nozzles. Inks of these filler materials can be patterned without a clean room environment. Screen printing and stencil lithography are inexpensive processes but have low resolution. Commercial inks that are elastomeric and conductive are being developed.

A recent review uses the term "intrinsically stretchable" to define the elastic materials that contains conductive particles (Trung and Lee [2016]). Here I define that these materials are not intrinsically stretchable since the components in these composites are intrinsically stiff and only rendered stretchable by dispersing them in an elastomeric matrix. Therefore, in this thesis, I sort the materials dispersed with conductive particles as "composites" and use the term "intrinsically stretchable" to define other structures that are more stretchable and involve intrinsically stretchable components.

Intrinsically Stretchable: Figure 2.13 shows stretchable electronics created by utilising conductive conductors that are intrinsically stretchable. There are few types of intrinsically stretchable conductive materials that can meet both electrical and mechanical requirements of stretchable electronics. Examples include ionic conductors, conducting polymers, and liquid metals.

Ionic conductors are conductive materials that can transport current by ions (and possibly electrons and holes, too) moving around. Electrical current transport via ions or electrons or holes, can be found in ionic liquids and ion conducting solids. Both ionic liquids and ion conducting solids can be called as electrolytes. Hydrogels

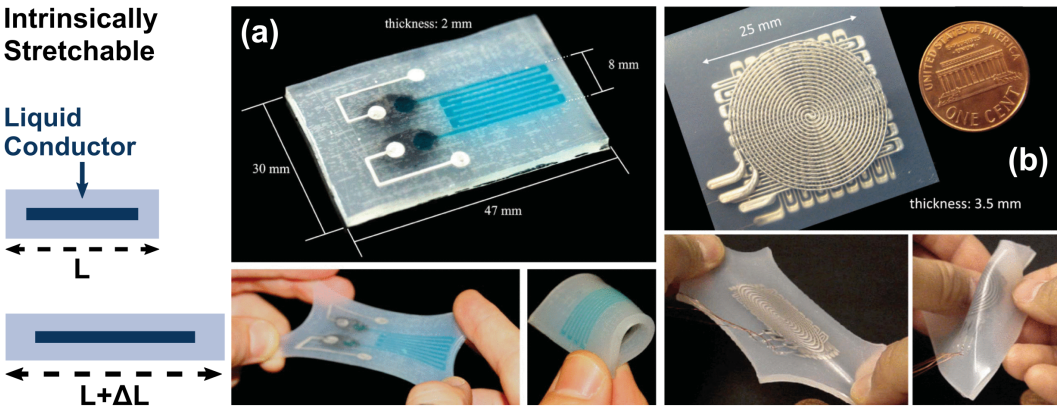

Figure 2.13.: *Intrinsically stretchable electronics.* Filling liquid conductors in elastomeric substrate creates intrinsically stretchable electronic devices that maintain bulk conductivity during deformation. Examples include: **(a).** A soft strain sensor based on ionic and metal liquids. Reproduced from: Chossat et al. [2013]. **(b).** A highly compliant artificial skin sensor consists of multilayered mircochannels in an elastomer matrix filled with liquid metal, capable of detecting multiaxis strains and contact pressure. Reproduced from: Park et al. [2012b].

that are made with ions or ionic liquids are widely used in stretchable electronics. These gels usually have high transparency and excellent stretchability (>600%) while deformation on the gel has negligible effect on the conduction of ions (Matsuhisa et al. [2019]). Applications of ionic conductors include: stretchable electrodes (Chen et al. [2014]), actuators (Keplinger et al. [2013], Yang and Suo [2018]), mechanical sensors (Chossat et al. [2013], Yang and Suo [2018], Sun et al. [2014]), capacitors (Keplinger et al. [2013], Sun et al. [2014]), and light-emitters (Larson et al. [2016], Wang et al. [2016]). The major challenges of ionic conductors are raised by bonding with the other components (e.g. elastomers and electrodes), and preventing them from drying out. Researchers have worked on methods to alleviate problems caused by the two challenges. In recent years, Wirthl *et al.* and Yuk *et al.* have proposed solutions to the material bonding issue by chemically adhering energy-dissipative tough hydrogels (Wirthl et al. [2017], Yuk et al. [2016]). The problem of dehydration has been resolved by incorporation of hygroscopic salts (Chen et al. [2018]), encapsulation with elastomer (Sun et al. [2014]), or use of gels based on nonvolatile ionic liquids (Chen et al. [2014]).

Conducting polymers, which have a mixed transport of ions and electrons (Rivnay et al. [2016]), are molecular-level stretchable materials. These materials are especially useful for constructing electronic devices which require smooth interfaces (O'Connor et al. [2016]) and reducing the interfacial impedance for applications in electrophysiology (Khodagholy et al. [2015]), actuators, and batteries (Snook et al. [2011]). Poly(3, 4-ethylenedioxythiophene)-poly(styrenesulfonate) (PEDOT-PSS) that consists of conjugated PEDOT polymer doped by acidic PSS is representative in conducting polymers. This conducting polymer exhibits a high conductivity at 10^3 S/cm level. However, since both PEDOT and PSS are semicrystalline in nature, the intrinsic stretchability of PEDOT-PSS has a strain limitation of ∼5%. In recent years, researchers have proposed numerous methods to use plasticiser to improve the stretchability of PEDOT-PSS (Savagatrup et al. [2015], Oh et al. [2016]). To date, the maximum strain PEDOT-PSS has reached with plasticiser is 100% (Wang et al. [2017], Teo et al. [2017]). Blending PEDOT-PSS with other soft polymers is another approach to render it stretchable, though there is a trade off between the stretchability and the conductivity. With this approach, a stretchability of 200% was obtained with a maintaining conductivity of ∼30 S/cm (Hansen et al. [2007]). In addition to PEDOT-PSS, polyaniline (PANI) is another class of conducting polymers that can be utilised as stretchable conductors. The maximum strain of PANI can be enhanced to ∼200% with an initial conductivity of ∼100 S/cm (Dufour et al. [2003]).

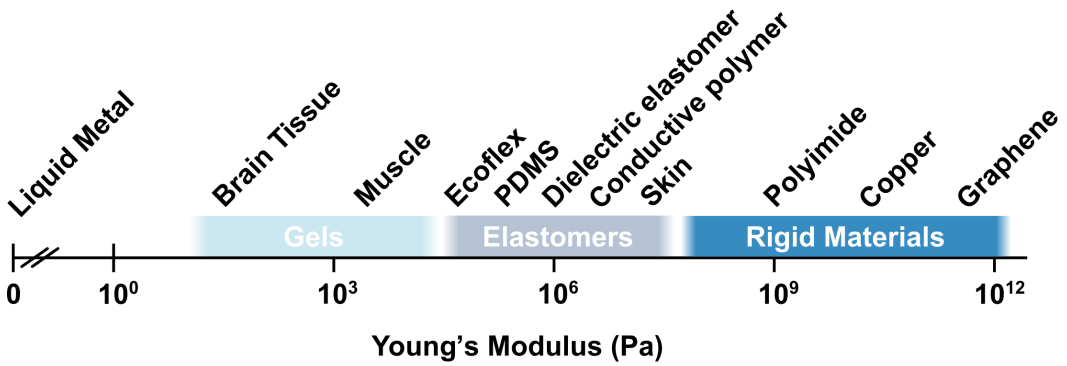

Figure 2.14.: *Liquid metals are "softer" than many electrical and biological materials.*Liquid metals are softer (in tension) than materials employed in flexible and stretchable electronics and materials found in human body.

Liquid metals are widely used in stretchable electronics. Dickey (Dickey [2017]) suggested that liquid metals can only be categorised as "intrinsically stretchable" if they are encased in an elastomer, as they do not store mechanical energy even when deformed significantly. Here I define liquid metals as intrinsically stretchable conductors since liquid metals are "softer" (in tension) than common materials used for flexible and stretchable electronics and materials found in human body (as shown in Figure 2.14). Figure 2.15 compares electrical conductivity and strain limits of some common stretchable conductors with copper as a reference. As seen in the figure, to date, no stretchable conductor offers the combination of excellent stretchability and high conductivity as liquid metal does.

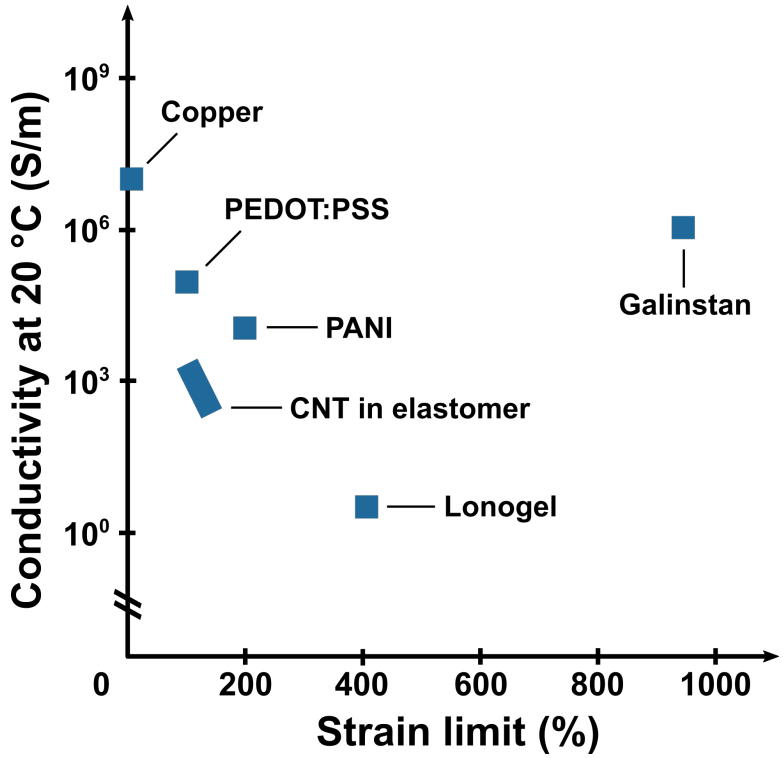

Figure 2.15.: *Electrical conductivity and strain limits of common stretchable conductors.* CNT (Carbon nanotube) in elastomer is a composite. The conductivity of the composite has an obvious change when the strain on it changes. Data from: Sekitani et al. [2008]. Lonogel is an ionic conductor. This gel has good stretchability but low conductivity. Data from: Chen et al. [2014]. PEDOT-PSS and PANI are conducting polymers that have excellent conductivity and good stretchability. Data from: Wang et al. [2017], Dufour et al. [2003]. Galinstan is a liquid metal. to date, the known strain limit of Galinstan (encapsulated in a fibre tube) is 1000%. (Zhu et al. [2013]) This liquid metal has both excellent conductivity and stretchability. Data from: Liu et al. [2012].

Instead of stiff conductive materials, liquid metals such as mercury can form conductive pathways in soft elastomers. Some non-toxic eutectic gallium alloys also have excellent electrical conductivity and form a liquid at room temperature; Galinstan and eGaIn are representative among them. The typical eutectic composition of Galinstan is 68 wt% Gallium (Ga), 22 wt% Indium (In) and 10 wt% Tin (Sn); Typical melting point of this alloy is -19 °C (Surmann and Zeyat [2005]). The conductivity of Galinstan is found to be $(3.83 \pm 0.16) \times 10^6$ S/m (Liu et al. [2009]). The other alloy eGaIn is made of 75% Ga and 25% In by weight. It has a melting point at $\sim$15.5 °C (Dickey et al. [2008]).

These gallium-based liquid metals are easy to be filled in a micro-size channel and will try to keep in the channel after filling without letting bubbles leak in. Previous work has presented using liquid metal to form an electric interconnect for ICs soft packaging (Zhang et al. [2013]), thereby avoiding some of the conventional IC packaging challenges which are not compatible with current soft robotic technologies such as wire bonding and flip-chip bonding.

Eutectic liquid alloys are also ideal materials for soft sensors and have increasing applications in stretchable electronics (Kramer et al. [2011a], Paik et al. [2011]) and flexible sensors (Majidi et al. [2011], Park et al. [2012b]). The basic principle of liquid alloy sensors is when the liquid alloy channels are deformed, the electrical resistance of the channels changes because of the changes of their cross-sectional areas and channel lengths. A challenge is to make the sensors compact ($\sim$10 Ω in 4 cm^2 area). The gallium alloys have a conductivity of 10^6 S/m; The high conductivity gives the channel size of soft sensors a critical requirement. To make the sensors compact, the channel width and thickness of the channels need to be reduced to micro-scale.

At present, the stretchability and resolution limits of gallium liquid metals (ie., how far liquid metal wires can be stretched and how small liquid metals can be patterned) and what defines the limits are out of our knowledge. To date, some groups have demonstrated liquid metal wires that can be stretched to 800$\sim$1000% strain (Zhu et al. [2013], Mineart et al. [2013]) and this limitation is mainly caused by the strain limits of the encasing materials. With large pressures, gallium liquid metal has been

injected into ∼150 nm capillaries (Lin et al. [2016]). Although the extreme limits are still unknown, the current achievable stretchability and pattern resolution (microns to hundreds micron length scale) are excellent enough to the overwhelming majority of soft electronic devices.

2.3 LIQUID METAL DEVICES

Section 2.2 (Soft Electronics) introduces a variety of methods to develop soft electronic devices. During my Ph.D study, I designed and fabricated a couple of soft electronic devices. All these devices have Galinstan (a eutectic liquid alloy) filler embedded in a polydimethylsiloxane (PDMS) or Ecoflex (two highly stretchable silicone elastomers) substrate. In recent years, combining liquid metal and elastomer is one of the most common methods of creating soft electronic devices. I chose this method because it produces intrinsically stretchable and soft devices, it takes short fabrication time, and all the equipment it requires is easily accessible to me in my workspace. With this method, usually I can a device from scratch in one day.

The method of using liquid metal mercury to make stretchable strain sensors was proposed as early as 1953 (Whitney [1953]), but possibly due to the toxicity of mercury, similar studies were rare at that time. In the last 20 years, researchers have found that some alloys of the metal gallium, which has a low melting point at 30 °C, can maintain liquid state at room temperature and have high electrical conductivity (such as eGaIn and Galinstan). These alloys became excellent low-toxic alternatives of mercury, thereby the research on soft electronic devices based on liquid metal has flourished in the past two decades.

To make soft electronic devices with gallium liquid metal, we need to pattern and embed the liquid metal within a highly elastic substrate. There are various options for the elastic substrate, such as fibres (Zhu et al. [2013]) and silicones (Khoshmanesh et al. [2017]). The substrate materials I used in my Ph.D work are PDMS and Ecoflex. Most of examples in the literature are implemented by embedding liquid metal in a

PDMS substrate with designed microfluidic structures. PDMS is frequently used in these studies because it is commercially available, inexpensive, easy to use, familiar within the microfluidic community, as well as it has a transparent appearance.

Although PDMS has the above advantages, it also has some shortcomings, such as easy to tear, unable to cure when contacted with some materials (such as some 3D printing materials), and PDMS substrates in the literature usually have a stretchable limitation under 200% (Dickey [2017]). Another highly elastic material, Ecoflex, can make up for some of the shortcomings of PDMS. Ecoflex is also a commercially available and inexpensive material, and it's not as easy to tear as PDMS. There are a variety types of Ecoflex, most of them have a stretchability over 800% and some even up to 1000%. However, Ecoflex is translucent, whether to use PDMS or Ecoflex for substrate should depend on the need of the devices.

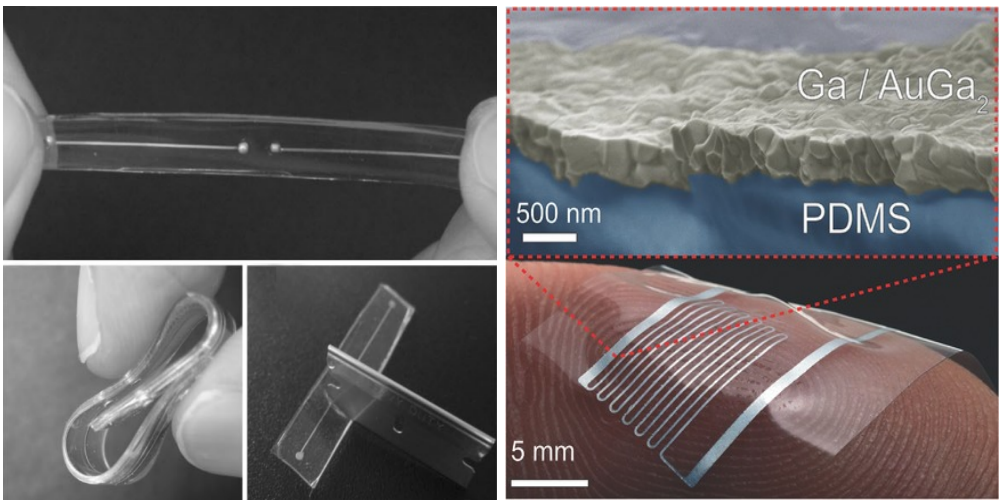

(a) Self-healing electrical wire (b) Stretchable interconnects

Figure 2.16.: *Liquid metal stretchable electrical connections.* **(a).** A prototype of an antenna that self-heals in response to sharp cuts. Reproduced from: So et al. [2009]. **(b).** A biphasic gold-gallium film patterned by photolithography with critical dimension of 100 μm on a 40 μm thick PDMS elastomer membrane. Reproduced from: Hirsch et al. [2016].

As shown in Figure 2.16, utilising the excellent conductivity and stretchability of gallium liquid metal, researchers presented stretchable conductors (Park et al. [2012b]), self-healing electrical wires (So et al. [2009] in Figure 2.16a, Li et al. [2016]),

as well as superior stretchable interconnects for circuits (Jeong et al. [2012], Lazarus et al. [2015], Hirsch et al. [2016]) in Figure 2.16b.

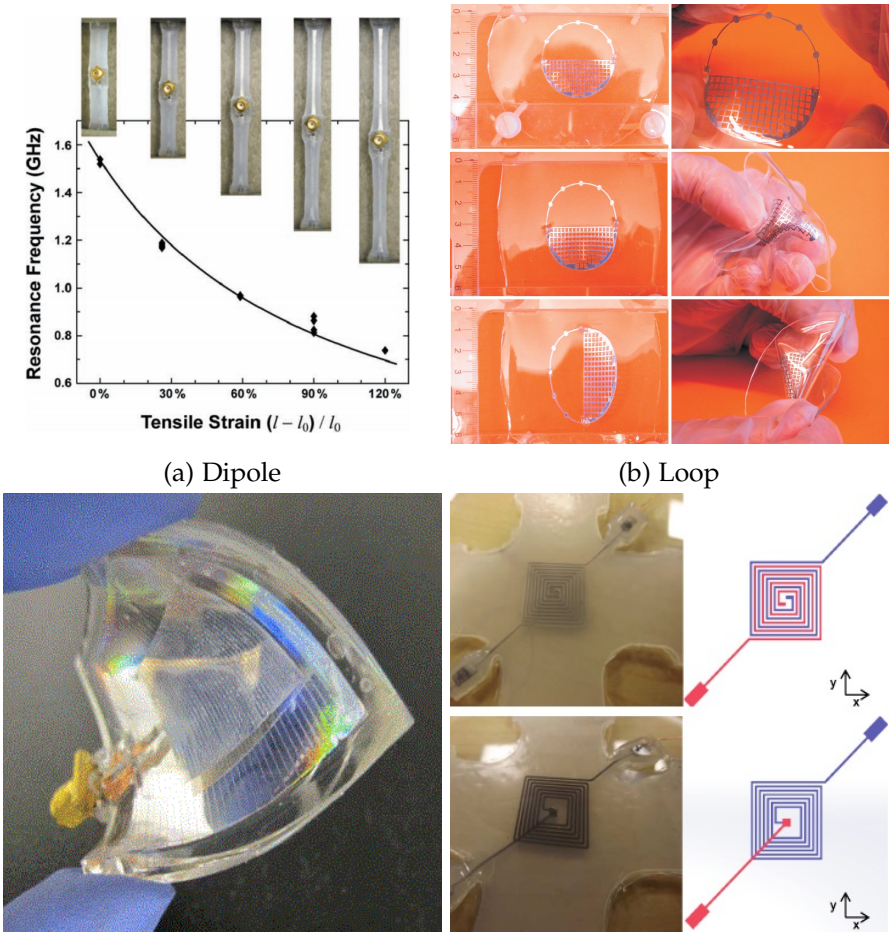

(a) Dipole (b) Loop

(c) Patch (d) Inductor

Figure 2.17.: *Liquid metal stretchable antennas.* **(a).** A half-wave dipole antenna that is made of eGaIn embedded in microfluidic channels composed of PDMS and Ecoflex. Reproduced from: Kubo et al. [2010]. **(b).** Photographs of a stretchable unbalanced loop antenna. Reproduced from: Cheng et al. [2009]. **(c).** Photographs of a multi-layer, stretchable microstrip patch antenna composed of liquid metal encased in elastomer. Reproduced from: Hayes et al. [2012]. **(d).** Top down view of a square planar spiral inductor. The inductor has a coil in one plane and a bridge that spans over the coil in a separate plane. Fassler and Majidi [2013].

Since gallium liquid alloys are great conductors, we can also employ them in efficient antennas. Figure 2.17 shows some representative work in the literature. The spectral properties of an antenna are related to its shape, so antennas produced by embedding liquid metal into PDMS or Ecoflex microfluidic channels have tunable

and reconfigurable characteristics. Based on this idea, in recent years, researchers have presented many types of gallium liquid metal antenna, such as diople antennas (So et al. [2009], Kubo et al. [2010] in Figure 2.17a), loop antennas (Cheng et al. [2009] in Figure 2.17b), patch antennas (Hayes et al. [2012] in Figure 2.17c, Aïssa et al. [2013]), coils and inductors (Fassler and Majidi [2013] in Figure 2.17d, Qusba et al. [2014], Lazarus et al. [2014]), radio-frequency antennas (Teng et al. [2018b]), to just name a few. Moreover, these liquid antennas have considerable potential to be harnessed as soft sensors since the resonant frequency of the antennas change upon strain or curvature.

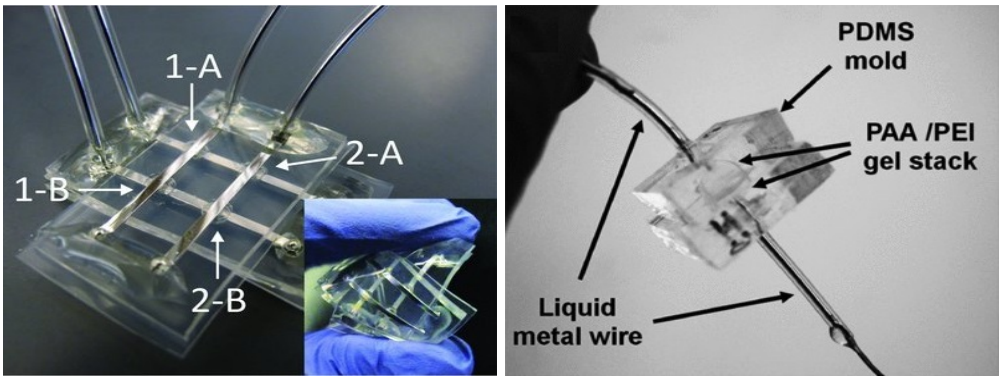

(a) Memory (b) Diode

Figure 2.18.: *Intrinsically soft circuit elements created with liquid metal.* **(a).** A memristor device composed of hydrogels between liquid metal cross-bar juctions. Reproduced from: Koo et al. [2011]. **(b).** A soft diode composed of elastomer, gel, and liquid metal. Reproduced from: So et al. [2012].

Apart from being adopted as conductive elements in soft wires, antennas and interconnects, galllium liquid metal can also form functional electronic components in soft devices beyond conductors. Liu *et al.* have created soft capacitors by injecting liquid metal into microchannels separated by a gap filled with an isolating liquid (Liu et al. [2015]). With the ability to electrochemically deposit or remove the surface oxide that forms on the gallium liquid metal, So *et al.* have demonstrated a soft diode composed of PDMS, gel, and gallium liquid metal (So et al. [2012] in Figure 2.18b). With similar principle of liquid metal diodes, Koo *et al.* have used gallium liquid metal to form memristor-like devices (Koo et al. [2011] in Figure 2.18a) (Memristor means memory resistor which stores binary information (i.e., 1's and 0's) by either being in a conductive or resistive state).

When liquid metal in a microchannel deforms, the related resistance and capacitance of it will change as well. These features have offered researchers new opportunities in soft sensors. Some previous work has presented strain sensors designed base on resistance change, such as Park et al. [2010] and Overvelde et al. [2014] (in Figure 2.19a). These sensors have low Young's modulus (0.1 $\sim$ 10 MPa) and high stretchability (100 $\sim$ 1000% strain at failure) (Dickey [2017]), so that can be useful in activating human gait without limiting the natural kinematics (Mengüç et al. [2014] in Figure 2.19b), measuring joint motion (Kramer et al. [2011a], Majidi et al. [2011]), and detecting deformation in soft robots (Teng et al. [2018b]), etc. There are also some commercial products for stretch sensing, such as StretchSense based on dielectric elastomer and similar products from Danfoss Polypower.

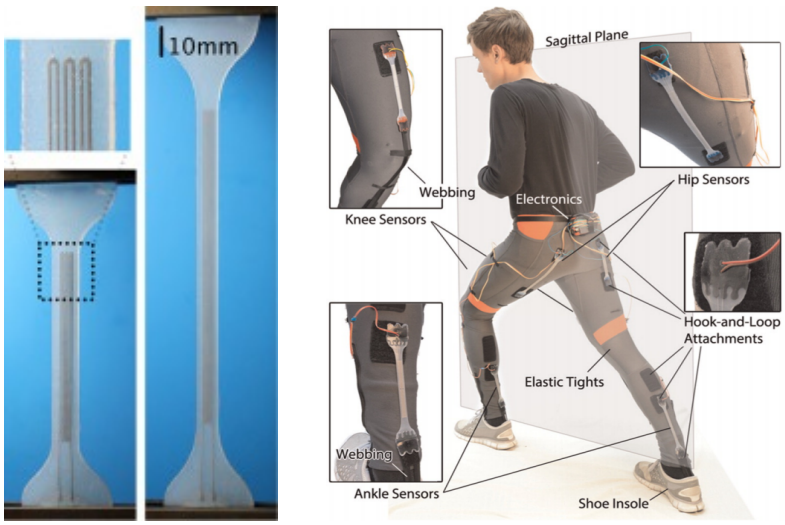

(a) Strain sensor (b) Strains sensors for detecting gait

Figure 2.19.: *Intrinsically soft strain sensors.* **(a).** A soft strain sensor fabricated with liquid metal and Ecoflex. Reproduced from: Overvelde et al. [2014]. **(b).** Detecting gait in soft wearable sensors. Reproduced from: Mengüç et al. [2014].

Figure 2.20 explains the design concept of a resistance based liquid metal strain sensor. When the liquid metal strips encapsulated in elastomer experience strain in the axial direction of the channels, the channel length increases from L to $L + \Delta L$ and the cross-section areas of the channels decrease from A to $A + \Delta A$. The theoretical

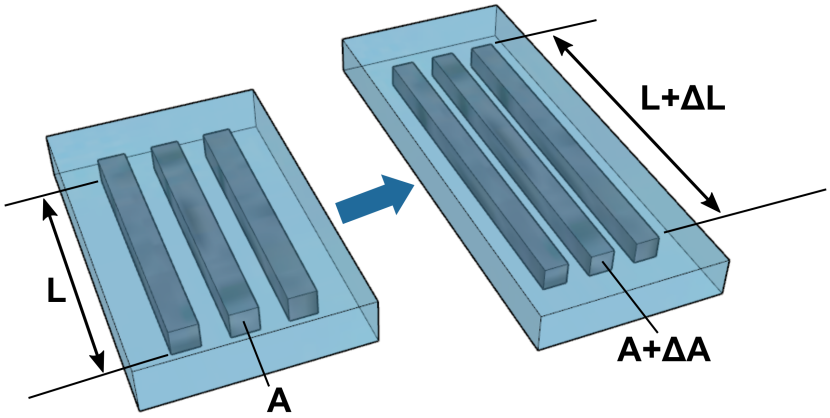

Figure 2.20.: Design concept of a liquid metal strain sensor.

relationship between the resistance change (ΔR) and strain (ϵ) can be easily found as follows (Park et al. [2012b]):

$$\Delta R = R - R_0 = \rho \frac{L + \Delta L}{(w + \Delta w)(h + \Delta h)} - \rho \frac{L}{wh},$$

where R and R_0 are respectively the resistance of the liquid metal channel when stretched by ΔL and not stretched, ρ is the electrical resistivity of the liquid metal in channels, L is the length of the channels, and w and h are the width and height of the cross-section of the channels, respectively.

By replacing Δw and Δh respectively with $-v\epsilon w$ and $-v\epsilon h$, and since $\epsilon = \Delta L / L$,

$$\Delta R = \frac{\rho L}{wh} \left\{ \frac{(1 + 2v)\epsilon - v^2\epsilon^2}{(1 - v\epsilon)^2} \right\},$$

where v is the Poisson's ratio of the elastomer material. For an elastomer material ($v = 0.5$), we can further simplify the above equation to

$$\Delta R = \frac{\rho \epsilon L (8 - \epsilon)}{wh(2 - \epsilon)^2}.$$

It is also possible to use liquid metal encased in elastomer to sense touch and pressure according to the resistance and capacitance change caused by deforming. I have developed a high resolution pressure sensing system consists of a liquid metal soft sensor and a bridge circuit. (Teng et al. [2018a]). As shown in Figure 2.21,

Anderson *et al.* have presented space-suits for detecting pressures as low as 5 kPa (Anderson et al. [2015] in Figure 2.21b), Kramer *et al.* have demonstrated tactile keyboards that completely made of soft materials (Kramer et al. [2011b] in Figure 2.21a). Park *et al.* have designed and fabricated sensors with multilayer microchannel structures that can sense pressure, and strain in two directions (Park et al. [2012b]).

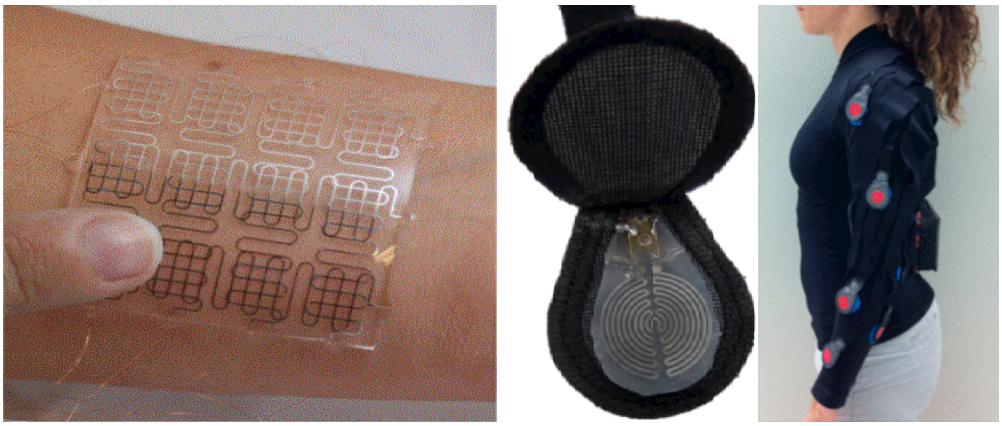

(a) Tactile keyboards (b) Pressure sensors in space-suit

Figure 2.21.: *Intrinsically soft pressure and tactile sensors.* **(a).** Soft tactile pads that can be applied on skin. Reproduced from: Kramer et al. [2011b]. **(b).** Soft pressure sensors integrated in space-suit. Reproduced from: Anderson et al. [2015].

2.4 INTEGRATION OF ELECTRONICS AND SOFT SYSTEMS

For a soft system to be useful in robotics or wearable devices, essential electronic components (for actuation, sensing, processing, etc.) need to be integrated in the system. The integration of electronics and soft systems can improve the biocompatibility and versatility of conventional robots in unstructured environments and provide intrinsic safety and comfort to the users. Research on soft electronic systems is, therefore, particularly important for the applications of physically assertive robotics, human-machine interaction,wearable computing, health monitoring, etc.

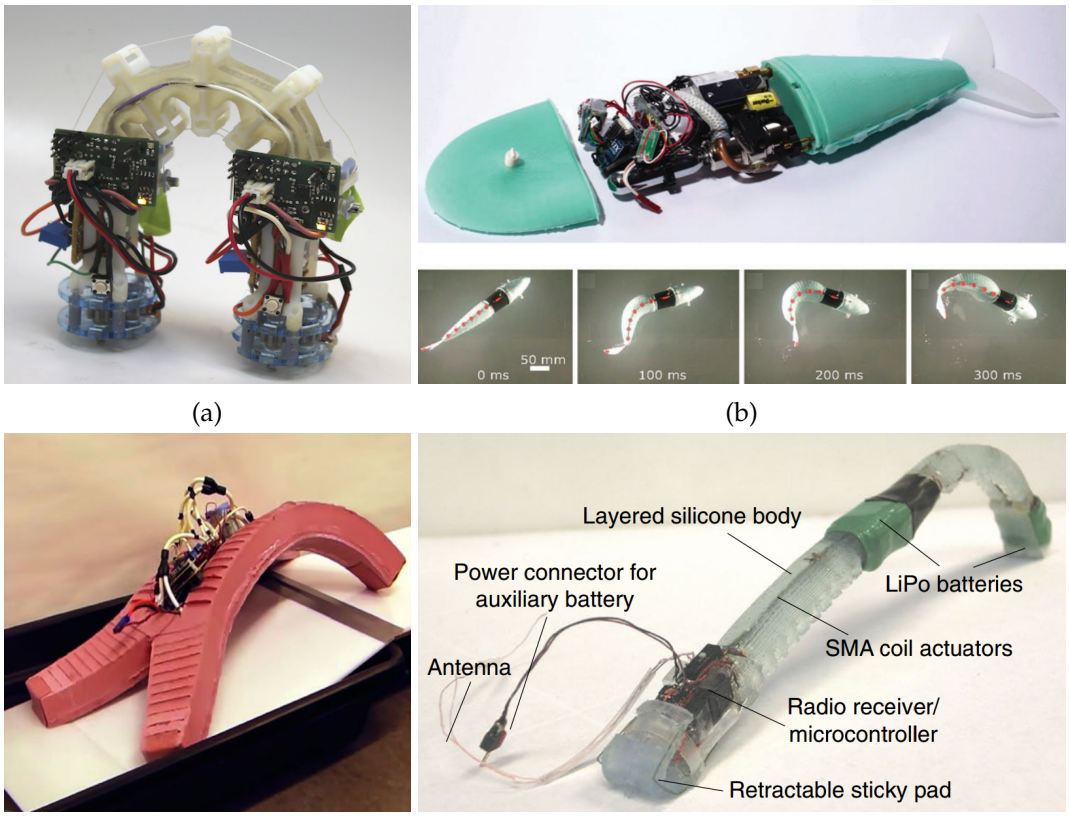

Figure 2.22.: *Untethered soft electronic systems.* **(a).** Climbing robot powered by a motor-cable system. Reproduced from: Malley et al.. **(b).** Biomimetic swimming robot powered by a hydraulic actuation system (35 cm long). Reproduced from: Marchese et al. [2015]. **(c).** Robust walking robot powered by on-board pneumatics (65 cm long). Reproduced from: Tolley et al. [2014]. **(d).** Caterpillar-inspired multi-gait robot powered by SMAs (10 cm long). Reproduced from: Lin et al..

To date, attempts at integration of electronics and soft systems have shown obvious trade-offs: fully soft systems often require a tethered connection to support pneumatic or electrical hardware, while untethered systems typically depend on bulky on-board components such as sensors, microprocessors, pumps and motors (Rich et al. [2018]). Figure 2.22 shows some recent work on untethered integrated soft electronic systems. Figure 2.22a presents an untethered flipping soft robot that could climb Velcro surface (Malley et al.), while Figure 2.22c shows a 0.65-m-long pneumatic robot that is able to carry batteries, compressors, valves and microprocessors (Tolley et al. [2014]). Figure 2.22b demonstrates an autonomous soft robotic fish (65 cm long) that encapsulates hydraulic actuators and power within its body cavity (Marchese

et al. [2015]). This robot takes advantage of marine environments to circumvent static friction and offload the mass of its auxiliary components, thereby improving the system efficiency. Figure 2.22d shows a caterpillar-inspired multi-gait robot powered by SMA coil actuators. SMA is a direct activation method that can minimise weight of the robot since it requires notably less auxiliary equipment. (Marchese et al. [2015]).

In the previous work presented in Figure 2.22, though researchers have endeavoured to reduce amount and weight of the electronic devices, the conventional electronic components and printed circuit boards still have obvious impact on size, weight, and flexibility of the soft robotic systems. The conventional hard electronic components and circuit boards in these work bring unique challenges arise from material mechanical mismatch in fabrication and interfacing of the integrated soft electronic systems. Since the electronics are difficult to bend or stretch, delamination tends to happen at the interface between the soft and the hard materials when the devices deform.

Several groups have put effort into improving integration by unifying the fabrication of actuators and sensors (Yang et al. [2017]), while others have investigated the transitions in material stiffness that diminish the stress caused by the impedance mismatches between stiff and soft components (Park et al. [2016], Naserifar et al. [2016], Naserifar et al. [2017]). Some groups have created untethered sensor systems by dispensing with the need for on-board power entirely, thus circumventing the challenge of shrinking their electrical components. This comes either in the form of electronics-free, microfluidic sensors (Koh et al. [2016], Choi et al. [2017a], Choi et al. [2017b]), or NFC induction coils that can briefly power wearable devices with electromagnetic waves in order to allow sensor readings to be taken (Kim et al. [2016], Varga et al. [2017]).

I deem that eventually an ideal fully integrated soft electronic system should have electronic components embedded within the own structure of the soft system itself, just like the artist's conception of an octopus-robot shown in Figure 2.23. This kind of ideal soft systems require further research on advanced soft actuators and better integration methods of electronics and soft systems. Therefore, the aim of my Ph.D is

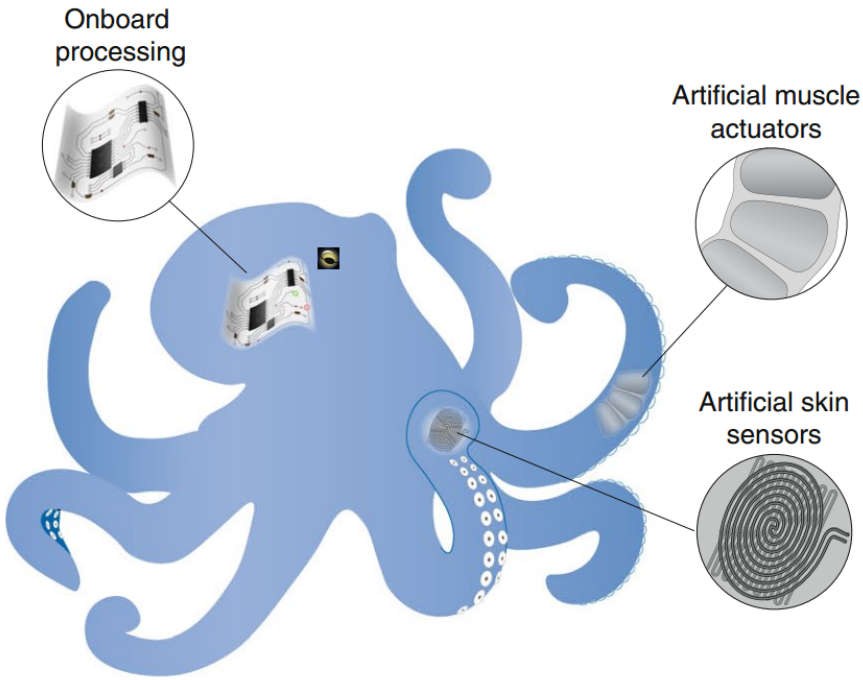

Figure 2.23.: *Conception of a future soft robot* with embedded soft electronic components. This concept figure is inspired by current state-of-the-art octopus-inspired robots (Sfakiotakis et al. [2015], Calisti et al. [2015]). Reproduced from: Rich et al. [2018].

to create unique flexible and stretchable electronic components with high compliance and incorporate current electronic components into soft structures (i.e. develop soft printed circuit boards) to form fully integrated soft electronic systems that have the functionalities of data acquisition, data processing, data transmission, and data visualisation.

3

MATERIALS AND METHODS

Section 2.2 (Soft Electronics) in the last chapter introduces a variety of methods to develop soft electronic devices. During my Ph.D study, I designed and fabricated a couple of soft electronic devices. All these devices have Galinstan (a eutectic liquid alloy) filler embedded in a PDMS or Ecoflex (two highly stretchable silicone elastomer) substrate. As mentioned in Section 2.3 (Liquid Metal Devices), combining liquid metal and elastomer is one of the most common methods of creating soft electronic devices. I chose this method because it produces intrinsically stretchable and soft devices, it takes short fabrication time (I usually can fabricate a device from scratch in one day), and all the equipment it requires is easily accessible to me in my workspace.

In this chapter, I introduce the properties (mechanical and electrical properties) of Galinstan (in Section 3.1 Eutectic Liquid Alloy: Galinstan) and PDMS and Ecoflex (in Section 3.2 Elastomer: PMDS and Ecoflex). Then I introduce the method I used to fabricate soft-lithography moulds for casting silicone materials in Section 3.3 (Soft-lithography Master Fabrication). Chapter 4, 5, and 6 each introduces one soft electronic system I designed and manufactured in my Ph.D study. The systems have different fabrication methods and experimental set-ups that are introduced in the corresponding chapters. I only introduce the soft-lithography mould fabrication method that I used in all my Ph.D work in this chapter as a fundamental fabrication method.

3.1 EUTECTIC LIQUID METAL: GALINSTAN

Galinstan (Liu et al. [2012]), as shown in Figure 3.1a, is a family of room temperature liquid eutectic alloys consisting of gallium (Ga), indium (In), and tin (Sn, Stannum in Latin). A typical eutectic mixture of Galinstan is 68 wt% Ga, 22 wt% In, and 10 wt% Sn. Similar to Galinstan, eGaIn is another gallium liquid alloy which has a typical mixture of 75 wt% Ga and 25 wt% In. These two liquid metals are both commercially available and have been widely utilised in literature.

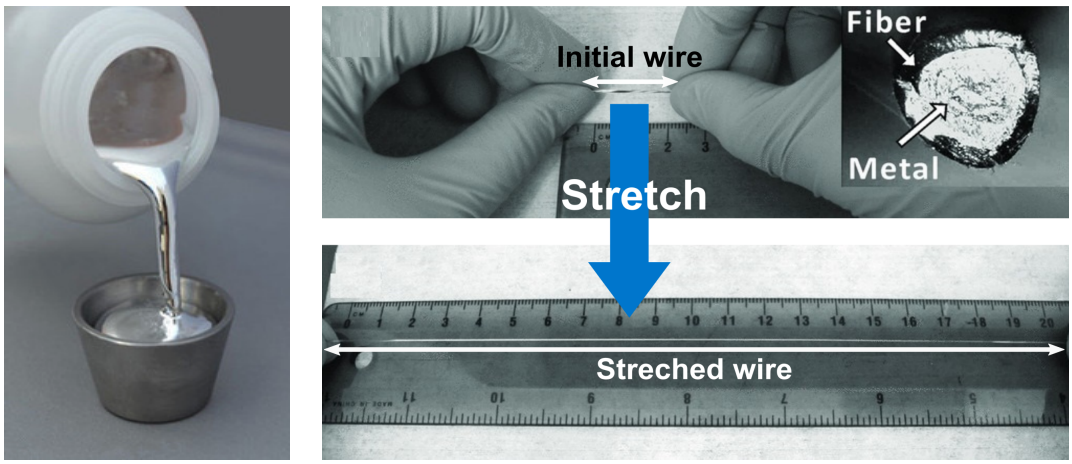

(a) (b)

Figure 3.1.: *Galinstan and ultrastretchable conductive fibre.* **(a).** Flowing Galinstan. **(b).** A conductive fibre (2 cm) that can be stretched to 20 cm and the liquid metal inside appears to uniformly fill the stretched fibre. Reproduced from: Zhu et al. [2013]

At present, the stretchability and resolution limits of gallium liquid metals (i.e., how far liquid metal wires can be stretched and how small liquid metals can be patterned) and what defines the limits are out of our knowledge. To date, some groups have demonstrated liquid metal wires that can be stretched to 800 $\sim$ 1000% strain (Zhu et al. [2013] in Figure 3.1b, Mineart et al. [2013]) and this limitation is mainly caused by the strain limits of the encasing materials. With large pressures, gallium liquid metal has been injected into $\sim$150 nm capillaries (Lin et al. [2016]). Although the extreme limits are still unknown, the current achievable stretchability and pattern resolution (microns to hundreds micron length scale) are excellent enough to the overwhelming majority of soft electronic devices.

Table 3.1 summarises some physical properties of Galinstan and eGaIn, with mercury and water included as reference materials. In my Ph.D study, I fabricated all the devices with Galinstan since it has the same conductivity but obviously lower melting point than eGaIn. Comparing as a 'liquid', Galinstan is ~6.5 times denser, ~2.4 times more viscous, and extraordinarily ~10 times more cohesive (cohesion depends on the surface tension) than water. Comparing as a 'metal', Galinstan is surprisingly ~8 orders of magnitude more conductive than tap water (0.05 that of copper) and ~27.5 times more thermally conductive than water (0.06 that of copper).

Table 3.1.: Physical properties of Galinstan, eGaIn, mercury, and DI water. (Data from: Dickey et al. [2008], Liu et al. [2012])

Property	Galinstan	EGaIn	Mercury	DI water (25 °C)
Density (kg m^{-3})	6440	6280	13533	998
Viscosity (Pa s)	2.4×10^{-3}	1.99×10^{-3}	1.526×10^{-3}	1×10^{-3}
Surface tension (N m^{-1})	718×10^{-3}	624×10^{-3}	487×10^{-3}	72×10^{-3}
Electrical conductivity (S m^{-1})	3.46×10^{6}	3.4×10^{6}	1.04×10^{6}	$< 5 \times 10^{-4}$
Thermal conductivity (W m^{-1} $^{-1}$)	16.5	26.6	8.5	0.6
Vapour pressure (Pa)	$< 1.33 \times 10^{-6}$ (at 500 °C)	N/A	1 (at 42 °C)	3169 (at 25 °C)
Melting point (°C)	−19	15.5	−38.8	0
Boiling point (°C)	> 1300	2000	356	100

Although the melting point of Galinstan (−19 °C) is ~20 °C higher than mercury, it doesn't have significant impact on soft electronic devices operating at room temperature. Beyond that, Galinstan has a many advantages than mercury, such as 0.5 time denser and ~3.5 times more conductive. Most of all, compared with mercury, gallium alloys are much less toxic. Some gallium salts (e.g. gallium nitrate) have therapeutic potentials (Bernstein [1998]) and have been approved to be used as contrast agents for magnetic resonance imaging (MRI) by the United States Food and Drug Administration (FDA). Neurons, which are notably delicate, grow safely in the presence of eGaIn (Hallfors et al. [2013]). More recently, Lu *et al.* showed that

gallium-based liquid metals can be used as an effective carrier for anti-cancer drugs (Lu et al. [2015]).

Furthermore, unlike mercury, the vapour pressure of Galinstan is absolutely neglectable ($< 1.33 \times 10^{-6}$ Pa). (Vapour pressure is the pressure exerted by a vapour in thermodynamic equilibrium with its condensed phases (solid or liquid) at a given temperature in a closed system.) Like most metals, Galinstan is almost completely insoluble in water. These features limit the ways for Galinstan to get into the body, therefore we can process Galinstan outside the chemical hood, with no need to consider the issue of inhalation. However, being a liquid, Galinstan could enter the body easier than solid metals. When handling Galinstan, we must take care and wear lab coats, protection glasses and glovces.

Another feature of gallium liquid alloys is that they are almost always covered with an oxidation film. The surface of Galinstan and eGaIn reacts rapidly with oxygen to form a film of oxides with a main component of gallium oxide (Dickey et al. [2008]). This oxide film forms nearly immediately even in an environment with only ppm oxygen concentration (Liu et al. [2012]), thereby it is hard to avoid. The oxidation film is usually 3 nm thick in ambient conditions (or 1 nm thick in a controlled environment (Regan et al. [1997])). Researchers have reported that the most stable form of the oxide is β-Ga_2O_3, which is a semiconductor that has a wide bandgap (Passlack et al. [1995]). In a humid environment, the oxide can change to gallium oxide monohydroxide, then become mechanically weaker and less passivating than the original gallium oxide (Khan et al. [2014]).

The oxidation film is crucial to gallium liquid metals in microfluidic devices (including a large amount of soft electronic devices) because it increases surface tension of the liquid metals and allows the metals to adhere to the channels it is embedded in. Since it is very thin, it does not have an obvious impact on performance of the liquid metal in soft electronic devices. However, some researchers have reported the oxidation film may affect stability of a connection between liquid metal and an external wire when linking the soft devices with other equipment. (I discussed this problem in one of my papers (Teng et al. [2018a])). Others have reported the

oxide skin can interfere with sensitive electrochemical measurements, adhere to many surfaces, and change the rheological properties of the liquid metal (Larsen et al. [2010]). When manufacturing gallium liquid metal devices, the challenge we face is how to minimize the impact of drawbacks while making the most of advantages of the oxide film.

Except the applications in soft electronic devices, gallium liquid alloys also have great potential for fabricating a variety of other microfluidic devices, including channels (Parekh et al. [2016]), pumps (O'Mullane et al. [2014]), valves (Pekas et al. [2012]), mixers (Tang et al. [2014]), and heaters (Je and Lee [2014]). The details and principles of these applications are not the focus of this chapter, therefore, not discussed in depth here.

In terms of cost, gallium is expensive, the price of gallium is about 1 dollar per gram. Therefore, the cost of Galinstan is high, around $700 per kilogram (price on Alibaba). In addition, the mining cost of gallium is high and seems unlikely to drop since gallium is a by-product of aluminium mining and can not be mined separately. However, as a filler of microfluidic devices, only a small volume of Galinstan is required, so the price is not a significant problem in my work.

The Galinstan I used has the typical eutectic mixture of 68 wt% Ga, 22 wt% In, and 10 wt% Sn. I ordered the Galinstan from Wuhan Dongxin Mill Import And Export Trade Co., Ltd on Alibaba website.

3.2 ELASTOMER: PDMS AND ECOFLEX

The full name of PDMS is poly-di-methyl-siloxane. This material, sometimes also called dimethicone, is a polymer widely used in microfluidic devices. Apart from microfluidic devices, PDMS has also been used in shampoos, food additives, beverages and lubricating oils (as anti-foaming agent). PDMS is a mineral-organic polymer since the structure of it contains carbon and silicon, and belongs to siloxane

family. (Siloxane is a name derived from silicon, oxygen, and alkane.) Two types of PDMS are commonly used in the literature: PDMS RTV-615 and PDMS Sylgard-184. To fabricate microfluidic devices, we usually mix PDMS (liquid) with a cross-linking agent (or called curing agent) and pour the liquid into a microstructured mould and heat it at ∼65 °C to achieve an elastomeric replica of the mould.

Ecoflex is a series of translucent rubbers produced by 'Smooth-on' company. These rubbers are platinum-catalysed silicones that are versatile and easy to handle. Usually the Ecoflex products come with two parts of viscous liquid (part A and part B). We mix part A and part B 1:1 by weight and leave the mixed liquid in an convection oven at ∼65 °C for 20 mins to 1 hour (depends on what type the Exoflex is). Then the Ecoflex cures and becomes a very soft, strong, and stretchable material.

Table 3.2.: Mechanical properties of PDMS and Ecoflex. (Data from: datasheet of Sylgard-184 and datasheet of Ecoflex series)

	Elongation at break (%)	Shore hardness	Tear strength (pli)	Pot life (hours)	Cure time (hours)
Sylgard-184	160	A-48	15	1.5 (25 °C)	48 (25 °C)
Ecoflex-0010	800	00-10	22	0.5 (23 °C)	4 (23 °C)
Ecoflex-0030	900	00-30	38	0.75 (23 °C)	4 (23 °C)
Ecoflex-0050	980	00-50	50	0.3 (23 °C)	3 (23 °C)

Table 3.2 shows some mechanical properties of PDMS and Ecoflex which are crucial to the fabrication of soft electronic devices. Elongation at break means the strain on a sample when it breaks. Shore hardness is a measure of the hardness of a material, typically used for polymers, elastomers, and rubbers. All the Ecoflex materials are measured in Shore 00 scale, which means Ecoflex materials are much softer than PDMS measured in Shore A scale. Tear strength is the minimum tensile force required to tear a pre-slit sample film of unit thickness, measured in pli or pounds per linear inch. Pot life is the time it takes when the viscosity of the mixed liquid doubles.

As shown in Table 3.2, Ecoflex materials are softer, stronger, more stretchable, and have much shorter cure time than PDMS Sylgard-184. These advantages make Ecoflex a better substrate material than PDMS in some situations. However, to date, PDMS

is still chosen to make microfluidic devices primarily. The possible reasons are: (i) PDMS is transparent at optical frequencies, so researchers can observe contents in the microchannels visually or using a microscope; (ii) PDMS has low autofluorescence (Piruska et al. [2005]); (iii) PDMS is a bio-compatible material (Ecoflex 00-33 has been certified as a skin safe material); (iv) With a simple plasma treatment, PDMS can bond tightly to another PDMS layer or glass. (v) PDMS is inexpensive (£166 for 1.1 kg, price on Farnell) compared to some previously used substrate materials, such as silicon; (vi) PDMS is easy to mould and can mould structures at surprisingly high resolution, even in nano-scale (Hua et al. [2004]); (vii) PDMS is gas permeable.

In my Ph.D study, the PDMS I used is Sylgard-184 (Dow Corning) and the Ecoflex I used is Exoflex 00-50 (Smooth-on).

3.3 SOFT-LITHOGRAPHY MASTER FABRICATION

Soft-lithography is well suited for a wide range of elastomeric materials, such as polymers, gels, and organic monolayers. These materials are mechanically soft, that is why the term 'soft' is used. Soft-lithography can be taken for a complementary extension of photolithography. In the past, industries developed photolithography mainly to deal with semiconductors in microelectronics. To date, most microfluidic devices still rely on photolithography for fabricating photoresist masters to pattern micro-structures. SU-8 is the most commonly used photoresist material. Figure 3.2 shows the process of (a-d) fabricating a rigid SU-8 master with photolithography and (e-f) patterning PDMS with the SU-8 master.

As shown in part (d) of Figure 3.2, SU-8 master can achieve extremely high resolution. The minimum height and width of the micro-structures can even reach 500 nm. However, the SU-8 photolithography requires an expensive direct-write maskless lithography system, or conventional lithography equipment and a mask that usually cost £200 - £300 and need weeks to be manufactured. Once the mask is manufactured, it is nearly impossible to change the design on it.

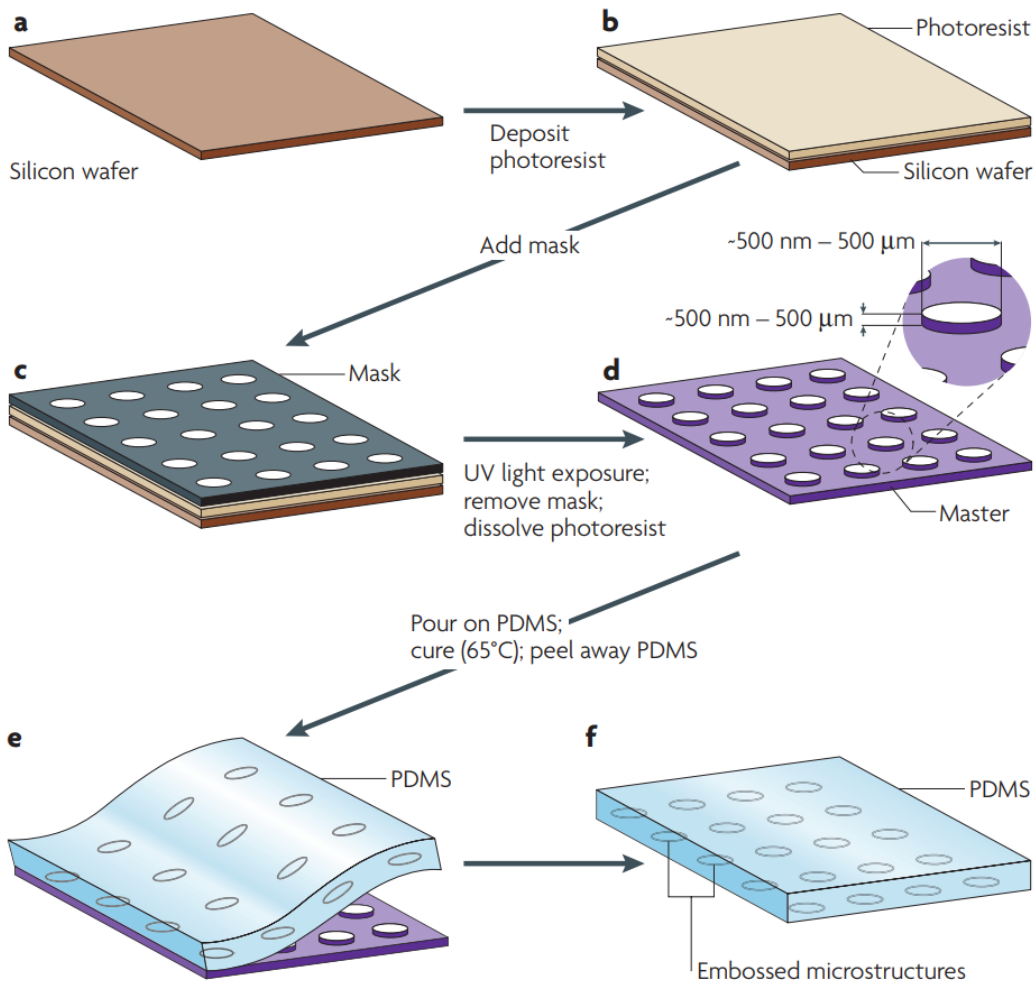

Figure 3.2.: *Process of fabricating an SU-8 soft-lithography master and patterning PDMS.* **(a-b).** A photoresist layer is spin-coated on a silicon wafer. **(c).** A mask is placed on top of the photoresist layer. **(d).** The photoresist is exposed under UV (ultraviolet) light. An organic solvent dissolves and removes the part of photoresist that is not covered by the mask. **(e).** PDMS is poured on the master, cured at around 65 °C and peeled away. **(f).** The resulting layer of PDMS has micro-structures embossed in its surface. Reproduced from: Weibel et al. [2007]

To eliminate the costs of consumables and time, I developed a novel, rapid, and reliable way of making soft-lithography masters. This method employs vinyl (a self-adhesive material) and laser-cutting as alternatives of photoresists and photolithography. Figure 3.3a presents such a master that I made with vinyl and acrylic substrate. Figure 3.3c shows the resulting microfluidic device fabricated with this vinyl master.

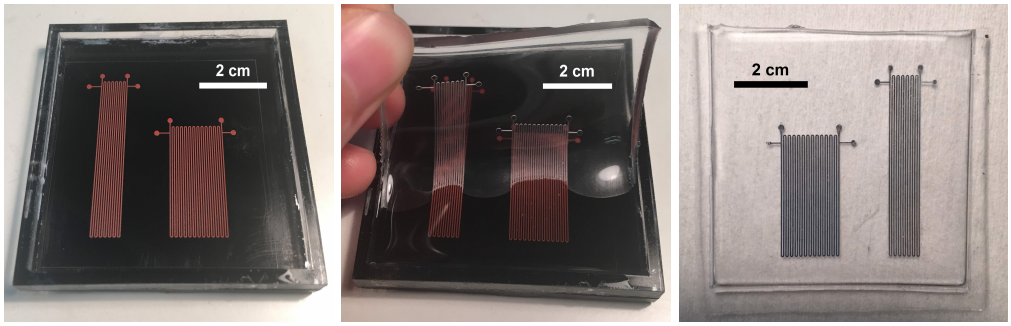

(a) (b) (c)

Figure 3.3.: *Soft sensors and soft-lithography masters.* **(a-b).** A soft-lithography master that I made with vinyl and acrylic substrate for patterning PDMS. **(c).** The resulting microfluidic device fabricated with this vinyl master.

Using this new method, I can fabricate the master in Figure 3.3 in half an hour with consumables cost less than £1. The smallest channel-width that I achieved using this method is 100 μm. Theoretically, I can fabricate any 2D structure with the fabrication procedure I proposed, as long as size of the design can fit the laser machine.

The minimum cutting width that the laser micro-machining system can produce is 30 μm and the minimum distance between lines is 70 μm. When I produce a soft-lithography master with vinyl, I tend to get stable and reliable production results when the line width and space width are both equal or greater than 200 μm. This limit of 200 μm is limited by the physical removal of the vinyl, not the resolution of the laser system. This type of soft-lithography master I fabricated can be used approximately 10 times before the vinyl loses adhesion to the substrate. This method is rapid and convenient for microfluidics and soft-systems researchers.

Though the resolution of this new master fabrication method is not as good as that of SU-8 photolithography, it is good enough for most of the microfluidic devices.

It benefits from a short fabrication time and low consumables cost. I can also make changes in my design easily whenever I need. This master fabrication method is a foundation of all my Ph.D work.

3.3.1 *Materials and Equipment*

The vinyl I used to fabricate the soft-lithography masters is a self-adhesive material that is designed to be removed without leaving any residue on the surface (Brand: d-c-fx®, model number: CRAFTPK20). The laser equipment I used is LPKF Protolaster U3 (in Figure 3.4), which is an ultra-fast, advanced ultraviolet laser micro-machining system. I performed experiments to compare the ideal and actual cutting width of some microstructures in the range of 100 μm to 300 μm, and the experimental and theoretical values agreed with a deviation of less than 5%.



Figure 3.4.: *Photograph of LPKF Protolaster U3 laser micro-machining system.*

In the machine head of the laser system, a CNC (computer numerical control) and laser optics are used to direct the generated laser beam to the material. When the laser beam is directed at the material, the material will melt, burn, and vaporise away, then

it will be blown away by a jet of gas to achieve a high-quality edge surface. This laser micro-machining system works straight from CAD data to process boards. Ideally, circuit traces as small as 50 μm can be achieved, along with spacing of 25 μm.

3.3.2 *Fabrication Process*

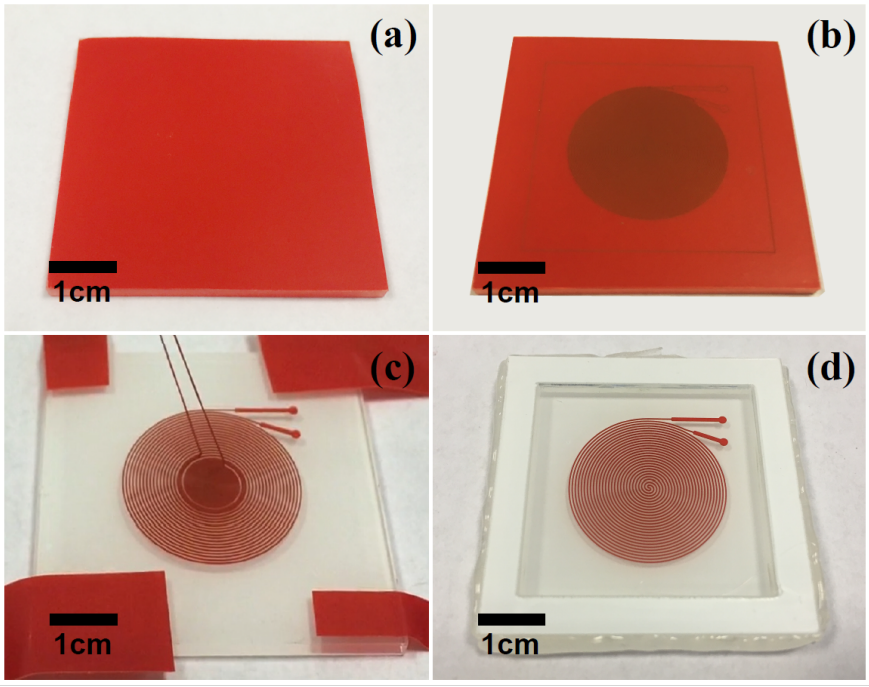

Figure 3.5.: *Fabrication Process of a vinyl soft-lithography master.* **(a).** I stuck a piece of 0.15 mm thick self-adhesive vinyl onto an acrylic substrate; **(b).** I cut the vinyl using a laser micro-machining system. The channel width and the gap-width between channels are both 200 μm; **(c).** I weeded out the unwanted vinyl; **(d).** finally I glued a 2 mm-think acrylic frame onto the substrate to form a mould for soft-lithography.

Figure 3.5 illustrates the fabrication process of a soft-lithography master: (a) I applied a piece of self-adhesive vinyl onto the surface of a 2 mm-thick acrylic board (2 mm Acrylic Cast, AMARI), and removed bubbles using a roller; (b) I used an LPKF Protolaser U3 laser micromachining to cut out the designed channel profle on vinyl. The profile of the channels can be cut precisely since the laser system has an error rate less than 5%; (c) I weeded out the unwanted parts of vinyl and no residue remained on the surface as this vinyl is designed to be removed without leaving residue; (d) I

glued another 2 mm-think acrylic frame onto the acrylic substrate as the final step of making a master for soft-lithography. The QR code below links to a video I took when removing the unwanted vinyl (corresponding to part (c) in Figure 3.5).

QRcode 3.1.: Fabrication of a vinyl soft-lithography master.

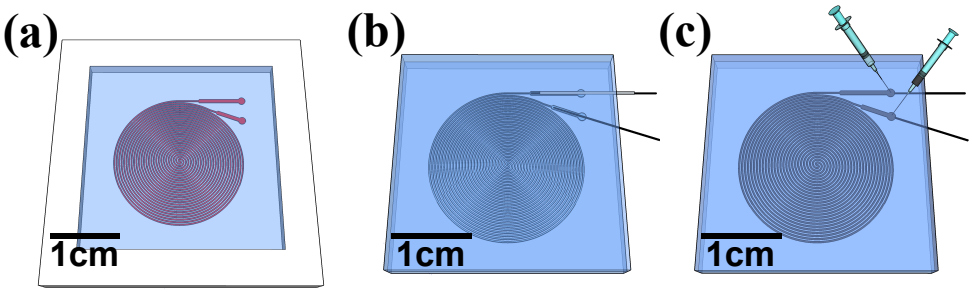

Figure 3.6.: *Example fabrication process of a liquid metal microfluidic device.* **(a).** I cured a piece of silicone material in the soft-lithography master to get the designed channels pattern on its surface. **(b).** I sealed the channels by bonding another piece of silicone material with flat surfaces and inserted connection wires into the channels. **(c).** I injected liquid metal into the channels with two needles, one to fill the liquid metal and one to vent the air. (The syringes are not shown to scale).

With the soft-lithography masters that fabricated with vinyl and acrylic, I can fabricate microfluidic devices consist of liquid metal and silicone substrates. Figure 3.6 illustrates an example fabrication process of a liquid metal microfluidic device: (a) I cured a piece of silicone material (PDMS or Ecoflex) in the soft-lithography master to pattern the designed channels on its surface; (b) I sealed the channels by bonding another piece of silicone material with flat surfaces and inserted connection wires into the channels; (c) I injected liquid metal into the channels with two needles, one to fill the liquid metal and one to vent the air. To bond two pieces of PDMS, I usually treat the surfaces to be bond (one flat surface and one pattered surface) with an oxygen plasma oven, then gently attach the flat surface to the patterned surface. Applying plasma treatment can provide an effective pretreatment of surface activation before bonding and result in a strong adhesion between the bonded surfaces. To bond two pieces of Ecoflex, I usually spin coat a thin layer of uncured Ecoflex on the flat surface

at a spin speed of 2000 rpm/s. I apply the patterned surface on the flat surface which is covered by the spin coated uncured Ecoflex and then put the whole device in a convection oven at 65 °C for 20 minutes to complete the bonding.

3.3.3 *Applications*

Figure 3.7 ∼ Figure 3.12 present some prototypes I fabricated with the vinyl soft-lithography masters. These prototypes were designed for a variety of applications, such as soft packaging, soft electronics, and microfluidics, which are summarised below. (In this section I show the prototypes for introducing the applications of the vinyl masters. Details of the key prototypes are introduced in the following chapters.)

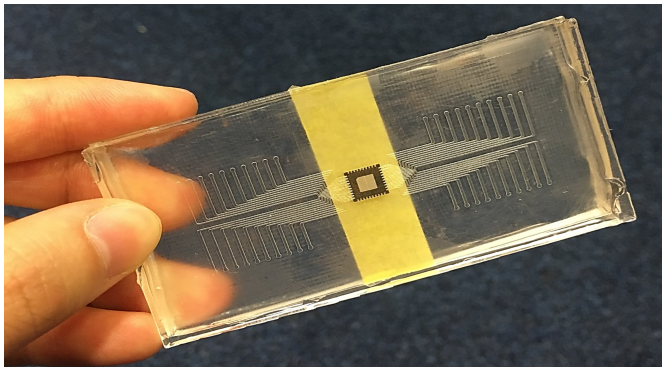

(a)

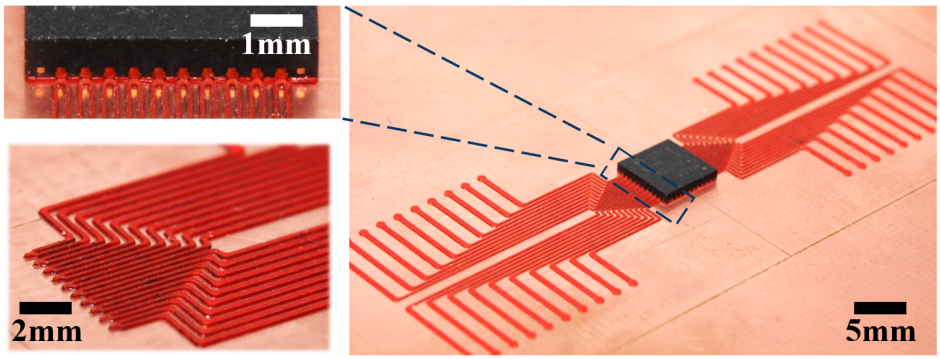

(b)

Figure 3.7.: *Soft packaging for conventional IC chips.* **(a).** Soft packaging for a VQFP microprocessor chip. **(b).** The vinyl soft-lithography master in detail.

Soft Packaging for Conventional IC Chips: Figure 3.7 shows that I can fabricate vinyl masters for making breakout connections for VQFP (Very Thin Quad Flat Package) chips. The yellow part in Figure 3.7a is apiece of paper that I embedded in the structure to stiffen the PDMS in the vicinity of the chip. When the sample is under strain, the paper works as a mechanical stiffness-gradient. PDMS near the chip will not sustain obvious deformation since the piece of paper is nearly unstretchable, so that can prevent voids opening between the PDMS substrate and the VQFP chip. Combining two silicone materials with different stretchability could be a replacement solution to this problem. The chip I embedded in this sample is MSP430FR5739 (an ultra-low-power microcontroller), with dimensions of $6.15 \times 6.15 \times 0.95$ mm and a pad size of 0.3×0.18 mm. The smallest channel-width in the master is 100 μm. As it shows in Figure 3.7b, removing the unwanted part of vinyl leaves a clean and neat surface (the substrate of this vinyl master is copper). I presented details of this work in the international conference *MicroTech 2016*. The poster is attached in Appendix A.

Soft Electronic Components: With the vinyl soft-lithography masters, I can also fabricate intrinsically soft electronic components. Figure 3.8 shows (a) two strain sensors, (b) a pressure sensor, and (c) a half-dipole antenna that I designed and fabricated. I observed that Galinstan holds uniform distribution in the channels and remains electrical connection despite extreme twisting, stretching, and folding.

Galinstan is a deformable conductive material, the length (L) and cross-sectional area (A) of the Galinstan in the channel change when the sensors are stretched or compressed. Since $R = \rho \frac{L}{A}$, resistance of the sensors will change when the sensors are deformed. For example, forcing a current I_{in} through the left sensor in Figure 3.8 (a) will create a voltage drop V_{out} between the test electrodes, and $V_{out} = I_{in} \times R_{sensor}$. When I_{in} is fixed, V_{out} changes based on the change of R_{sensor}, which is the resistance value of the sensor under test. Measuring V_{out} can help us calculate the value of R_{sensor} and then deduce the deformation situation on the sensor. We can also use a microcontroller chip to measure the value of V_{out}. The analogue-to-digital converter in a microcontroller can convert the analogue signal V_{out} to a digital output that can be read and recorded, thereby the sensor can be integrated into an electronic system

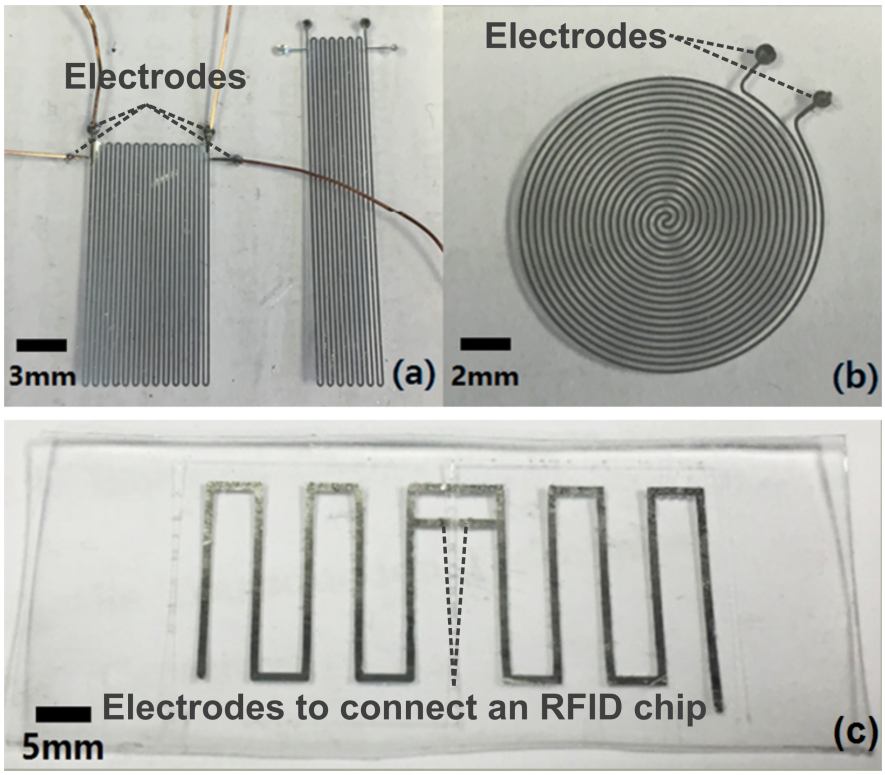

Figure 3.8.: *Intrinsically soft electronic components.* **(a).** Two strain sensors; **(b).** A pressure sensor; **(c).** A half-dipole antenna for wireless strain sensing.

as an input device. In Chapter 4 and Chapter 5, I introduce more details of these sensors and their measurement and assistant electronic systems.

Soft Electronics Integrated in Soft Robots: The vinyl soft-lithography masters can also contribute to integrating soft electronics into soft robots. I collaborated with Tianqi Wei to integrate stretchable strain sensors into a maggot robot (Wei et al. [2016]). The maggot robot shown in Figure 3.9 (a) is made of Ecoflex. It is a soft bionic robot that the EU Minimal project proposed for studying the neurons and exercise habits of larvae. This soft robot contains 24 pneumatic chambers connecting with air pumps though tubes. In this collaboration work, Tianqi designed and 3D printed the master for casting the pneumatic chambers. I designed and fabricated the vinyl masters with a piece of acetate as the substrate. We used this vinyl-acetate master to cover the 3D printed master to form a mould for curing Ecoflex. We can glue two piece of Ecoflex which are casted in the mould in Figure 3.9 (b) and wrap the whole piece of Ecoflex up to achieve the maggot robot shown in Figure 3.9 (a).

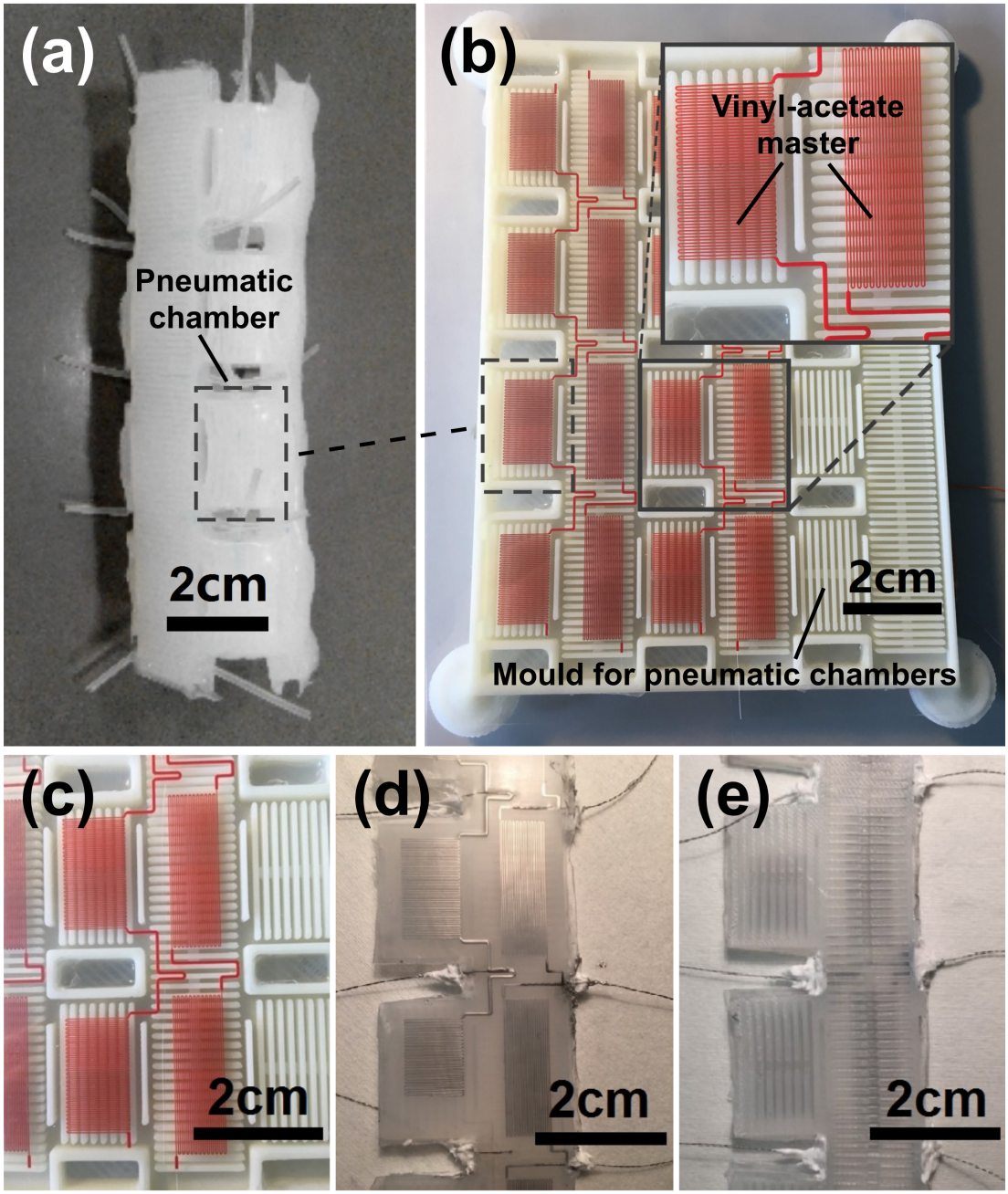

Figure 3.9.: *Integrating soft sensors into a maggot robot.* **(a).** The Ecoflex pneumatic actuated maggot robot. Reproduced from: Wei et al. [2016]. **(b-c).** The mould consists of a vinyl master and a 3D printed master for preparing the Ecoflex. **(d).** The sensors side and the **(e).** pneumatic channels side of part of the maggot robot.

Figure 3.9 (c) is a close-up look photo of the mould to show details of the pneumatic channels and the sensors channels. Figure 3.9 (d) and Figure 3.9 (e) respectively present the strain sensors side and the pneumatic channels side of part of the maggot robot. Strain sensors on surface of the maggot robot can reflect the dynamic driven data when the robot is moving. With the help of the strain sensors, we can have a instant deformation feedback when the robot is moving. This feedback can help us realise a preciser control of the air flow rate of the pumps. Tianqi and I attempted to fully integrate 24 strain sensors into the robot with each of the strain sensor corresponding to a pneumatic chamber. However, when we use this fabrication method, there are sometimes small air bubbles mixed in the uncured Ecoflex. These small bubbles may gradually float to the surface and then affect the pattern of the strain sensors channels. This means, to manually fabricate a pneumatic chamber with an integrated strain sensor, the manufacturing yield is not high. It is thereby difficult to successfully fabricate the maggot robot with 24 functional strain sensors. Due to the limited time of the project, the project leader Tianqi decided to suspend the project. That is why Figure 3.9 (d-e) only show an incomplete part of the maggot robot. A possible solution to the future work is to manufacture the 24 strain sensors separately and then stick them on the surface of the moggot robot, as long as the strain sensors are fabricated thin enough to not obviously affect the flexibility of the pneumatic chambers.

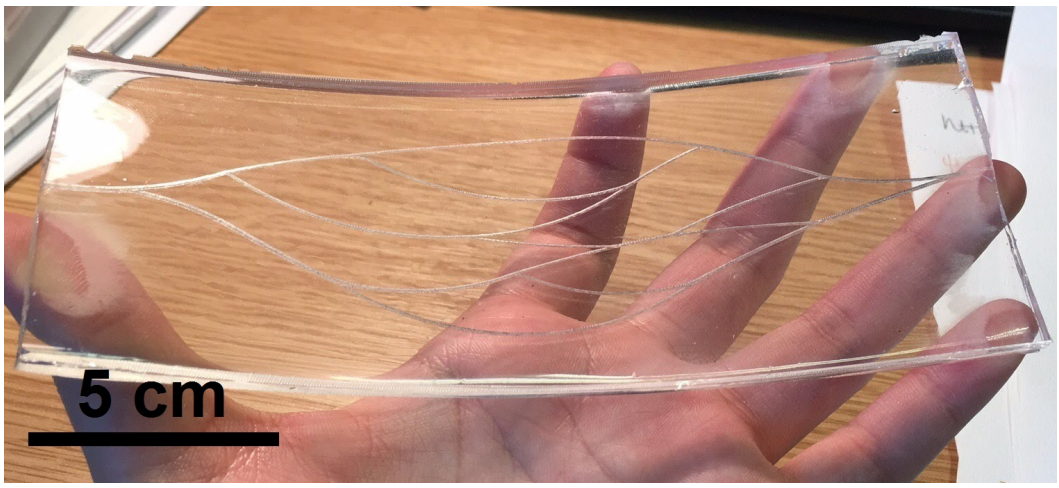

Figure 3.10.: *Photograph of a PDMS device with micro-channels inside* for investigating bubble lodgement and dislodgement in a capillary network.

Microfluidics: Figure 3.10 shows a PDMS device with micro-channels inside for investigating bubble lodgement and dislodgement in a capillary network. This device is created for a collaboration work that lead by Cong Chao in the University of Edinburgh. Bubble lodgement and dislodgement is a common issue in many industrial and biological process. Addressing this issue can contribute to many applications such as petroleum extraction and drug delivery in capillary networks. We published a paper (Chao et al. [2019]) to discuss the pressure required to dislodge single bubbles from a microscopic capillary network. In the collaboration work, Cong Chao designed structure of the channel network. I fabricated the test device based on Cong's design with the vinyl-master soft-lithography method I developed. Cong did experiments with this device, built model, and analysed data to investigate the pressure required to dislodge single bubbles from the microscopic capillary network and the factors affecting the dislodging pressure to facilitate the precise control of bubble flows in porous media.

Mask for Metal Depositing and Ink Printing: Besides being used as masters, vinyl can be used as masks with a very similar fabrication method. Figure 3.11a shows a vinyl mask that I made for depositing Tin and Copper on PDMS with the pattern of a designed circuitry. Figure 3.11b presents the resulting PDMS substrate with deposited copper tracks on top of it. With the help of the metal depositing mask, I managed to fabricate soft printed circuit boards (I introduce the details of this work in Chapter 6).

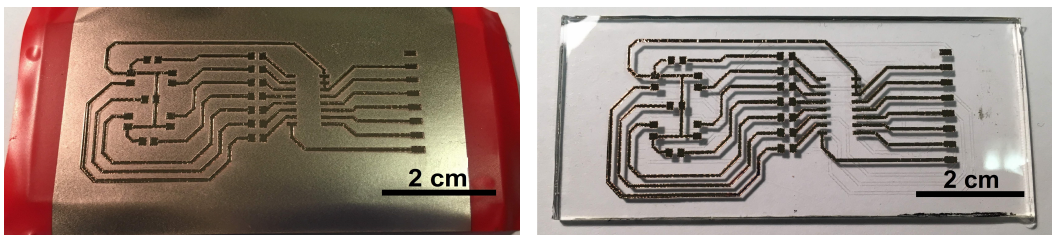

(a) (b)

Figure 3.11.: *A vinyl mask for metal depositing.* **(a).** A vinyl mask that I made for depositing tin and copper on PDMS with the pattern of a designed circuitry. **(b).** The resulting PDMS substrate with deposited copper tracks on top of it.

Figure 3.12a shows a vinyl mask I made for graphene ink printing (colour of the vinyl mask is golden). This is a collaboration work with Kewen Pan in the University of Manchester. Figure 3.12b shows a resulting prototype (graphene printed on a piece of paper) that can be used as a flexible field antenna. In this collaboration work, Kewen designed shape and dimensions of the antenna. I fabricated the mask that can stick on the piece of paper with vinyl. Kewen did ink printing on the paper covered by vinyl mask and eventually remove the vinyl mask to achieve the final prototype of a flexible graphene antenna when the ink is dry.

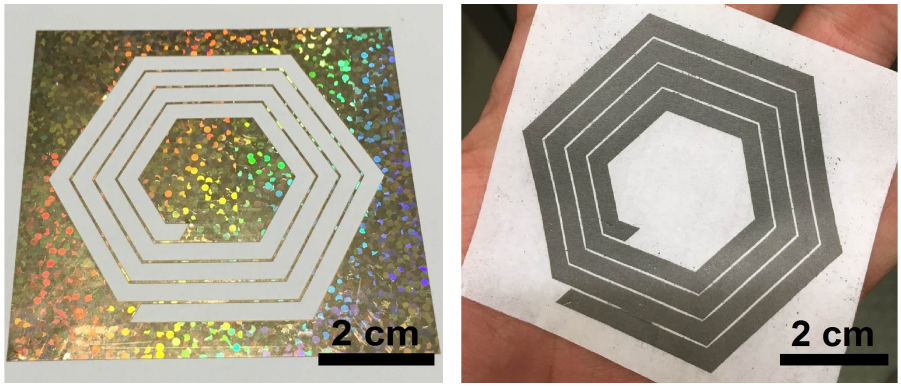

(a) (b)

Figure 3.12.: *Vinyl mask for graphene ink printing.* **(a).** A vinyl mask applied on a piece of paper for graphene ink printing. **(b).** The resulting flexible graphene antenna.

3.4 CONCLUSION

In this chapter, I introduced the materials that I used in all my Ph.D projects: Galinstan, PDMS and Ecoflex. I detailed physical properties of these materials, especially mechanical properties and electrical properties, and discussed the applications of these materials in the field of soft electronics. In addition, I introduced a vinyl master/mask fabrication method that is crucial to all the projects presented in the subsequent chapters. With this master/mask fabrication method, I am able to fabricate the soft electronic devices I designed in a short period of time. This soft-lithography master fabrication method is the cornerstone of all my Ph.D research.

4

INTEGRATED SOFT PRESSURE SENSING SYSTEM

In this chapter, I present the design and fabrication of a high-resolution pressure-sensor soft system that can transduce normal force into a digital output. In this soft system, which is built on a monolithic silicone substrate, a Galinstan-based microfluidic pressure sensor is integrated with a flexible printed circuit board. In addition to presenting the sensor system, I propose a method to alleviate problems arising due to the mechanical mismatch between metal connection wires and soft or liquid materials.

Some text and figures in this chapter are reproduced from my paper *Integrating soft sensor systems using conductive thread* with permission. The published version of this paper is attached in Appendix D. As the first author of this journal paper, I led this project, designed and fabricated the whole pressure-sensor soft system, completed all the experiments, and took charge of more than 90% of paper writing. Except me and my supervisor Adam A Stokes, the other authors of this paper are: Karina Jeronimo, Tianqi Wei, Markus P Nemitz, and Geng Lyu. Karina and Tianqi helped me think of ideas, setup the experiments, and write around 5% of the paper respectively. Markus and Geng gave me advice on paper writing and helped me revise and polish the paper.

4.1 INTRODUCTION

To develop fully integrated soft machines — which include power, communications, and control sub-systems — the research community requires methods for interconnecting between soft and hard electronics. Most of the current Gallium-based microfluidic devices can not work individually, they need to be connected with some other hard electronic devices, such as power supplies and data processors (Park et al. [2012b], Tabatabai et al. [2013], Majidi et al. [2011], and Kubo et al. [2010], Zhang et al. [2013]). This means we need to use wires to connect electrodes of the Gallium-based microfluidic devices to some other hard electronic devices. Since the conductive component in Gallium-based microfluidic devices is liquid, it is impossible to solder the connection wire on the electrodes. We have to insert the connection wires into the channels, as shown in Figure 4.1 (In order to show the wires in the channels clearly, there is no liquid metal filled in the channels in Figure 4.1 (a-b)).

Conventional copper wires, which are commonly used to connect sub components in hard electronic devices by soldering, are not suitable for interconnecting eutectic liquid-metal microfluidic devices. As shown in Figure 4.1 (a), copper wires have a high bending moment, meaning that any mechanical reaction force acting upon the surrounding soft material can cause delamination, and device failure. Figure 4.1 (a) provides a schematic of the mechanical displacement of a copper wire inside the fluidic channel. Due to the high-bending moment and rigidity of the copper wire, when the external part of the copper wire moves it causes movement inside the channel. This movement can lead to leakage of the liquid metal or instability of the contact resistance.

As introduced in Section 3.1, gallium-based liquid alloys are covered by a thin film of gallium-oxide. This oxide forms a solid oxide 'skin' which affects the wetting dynamic of this complex fluid. Gallium-oxide film is a semiconducting material which means if a wire does not connect to the bulk-liquid, but is in-contact with the surface of the liquid, it is likely to form a rectifying junction. Figure 4.1 (d) shows the

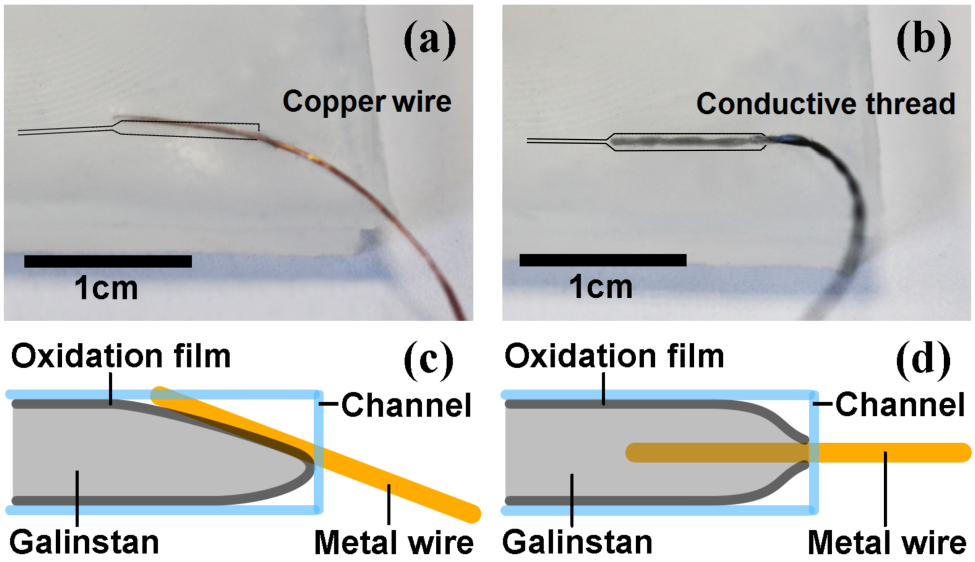

Figure 4.1.: *Comparison of conventional copper wire and conductive thread.* **(a).** A single-core copper wire inserted into a microfluidic channel in an Ecoflex substrate. **(b).** When conductive thread is inserted into a microfluidic channel in an Ecoflex substrate then external movement does not affect the position of the wire inside the channel. **(c).** Schematic showing a poor connection between the wire and the liquid metal. The copper wire has moved out of the bulk-liquid and only touches the semi-conducting gallium-oxide film. **(d).** Schematic showing a good connection between the liquid-metal and a wire. The wire is wetted by the eutectic, and makes an electrical connection to the conductive bulk-liquid.

condition when a metal wire is inserted into a micro-channel and is wetted by highly conductive Galinstan, this configuration results in a stable connection. Figure 4.1 (c) shows an unstable connection between the metal wire and the Galinstan, where the displaced wire only makes electrical-contact with the gallium-oxide skin.

In recent years, several studies have been focused on making soft microfluidic sensors, but little work has been conducted into finding suitable materials for making robust interconnect. Park *et al.* designed a soft artificial skin which uses multiple layers of microfluidic channels embedded in an elastomeric substrate ((Park et al. [2012b])). These channels are filled with eutectic gallium indium (eGaIn). The system is used to detect multi-axial strain and normal pressure. The researchers used thin single-core copper wire as interconnect to an external datalogger. Similar connection methods have also been used in other research work, such as (Tabatabai et al. [2013]), (Majidi et al. [2011]), and (Kubo et al. [2010]). (Zhang et al. [2013]) reported on a

novel method for integrating solid state ICs directly with eGaIn microfluidics in an elastomer package, by including the package at the casting-step. They used steel needles to inject the eGaIn into the microchannels and then left these needles in-place to act as the external electrical-connection. Each of these systems has drawbacks in the interconnection to other devices. The connection wires or needles they used may cause leakage of the liquid metal and instability of the contact resistance. These limitations hinder the uptake of the soft-sensor devices into integrated systems.

In summary, integrating sensors based upon eutectic gallium alloys in microfluidic channels into systems of heterogeneous Young's modulus is difficult due the complexity of finding a material which is electrically conductive, mechanically flexible, and stable over prolonged periods of time. Single-core copper-wire is a poor material for making strong-and-stable connections between printed circuit boards and eutectic liquid-metal sub-systems. There is a need of a material used for connections with both high conductivity and mechanical flexibility.

4.2 METHODS

4.2.1 *New Interconnect Material: Conductive Thread*

My approach to solve the interconnection-problem is to use conductive thread. This thread is a low-cost commodity material made of steel fibre which is commonly used to make electrically conductive smart-textiles. As shown in Figure 4.1 (b), conductive thread produces little bending moment into the microfluidic channel, which means moving the external part of the conductive thread will not cause movement inside the channel. Since conductive thread has both high conductivity and mechanical flexibility, it shows better performance than conventional single-core copper wire when used as connection material for microfluidic devices based on eutectic gallium alloys.

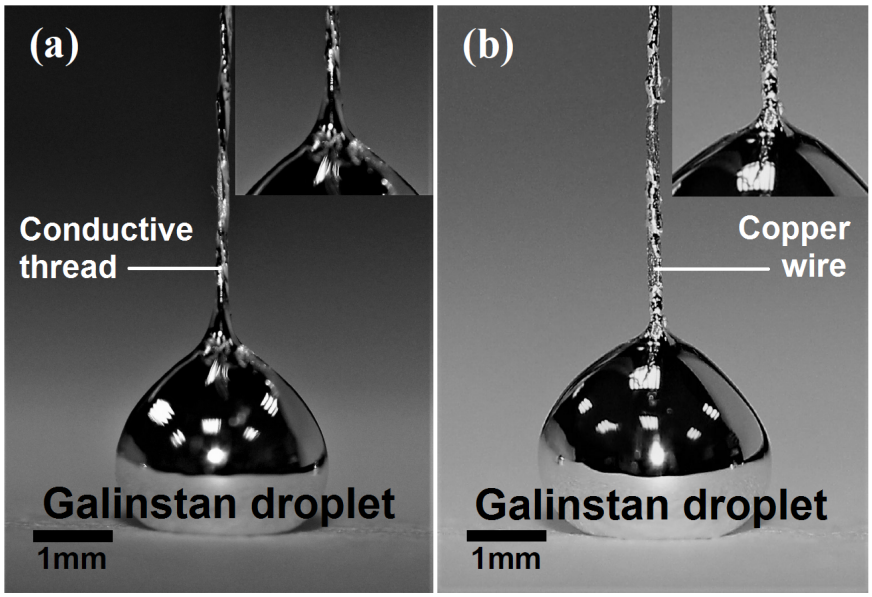

Figure 4.2.: Photographs showing the withdrawal of **(a).** conductive thread and **(b).** copper wire from a Galinstan droplet. The Galinstan wets more onto the conductive thread than the copper wire.

Figure 4.2 shows that Galinstan has better adhesion to conductive thread than copper wire. To take these photos, I inserted one piece of conductive thread and one piece of copper wire (each of the same diameter) into two equal volume droplets of Galinstan. I observed the deformation of the complex-liquid surface as I withdrew the wires from the droplets. Figure 4.2 provides photographs taken immediately before the wires detached from the droplets. This figure shows conductive thread is wetted more than the copper.

It is worth mentioning that resistivity of the conductive thread I used is 0.27 Ω per centimetre. As a connection wire, this resistivity is not as small as copper, but can meet the requirement in many electronic systems. This resistivity offers conductive thread the possibility to be used to make a soft sensor. In 2015, researchers have presented a shape sensor by wrapping a long strip of such conductive thread around an elastic strap to form a conductive yarn (Wurdemann et al. [2015]). This soft sensor is protected in a stretchable pipe and able to measure bending behaviour as well as elongation.

4.2.2 *An Integrated Soft System with Conductive Thread Interconnects*

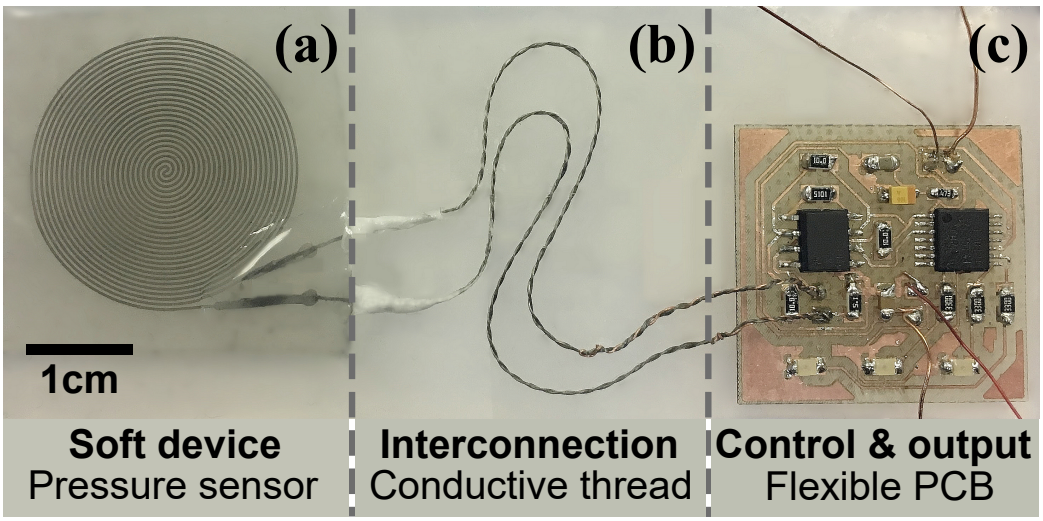

Figure 4.3.: *Top view of the integrated soft pressure sensing system.* **(a).** Normal-force pressure sensor made with a Galinstan-filled microfluidic-channel encapsulated in an Ecoflex substrate. **(b).** Conductive thread is used as interconnection between the pressure sensor and the flexible PCB. The serpentine shape provides strain-relief. **(c).** A flexible PCB consisting of hard electronic components, including a bridge circuit, an amplifier, a microcontroller, and LEDs.

I used conductive thread to fabricate interconnects for an integrated electronics system. Figure 4.3 shows the integrated system which contains a sensor, interconnect, and a flexible printed circuit board. The printed circuit board provides a bridge, an amplifier, a microcontroller and LED outputs. The conductive thread lies in a serpentine shape (shown by Figure 4.3 (b)) and forms a mechanically, and electrically, robust connection between the soft microfluidic pressure sensor and the flexible printed circuit board (PCB). I made the pressure sensor via soft-lithography using a silicone substrate (Ecoflex 00-50), and I filled the channel with Galinstan that contains 68.5 wt% gallium, 21.5 wt% indium, and 10 wt% tin. I made this alloy from the constituent metals, and I chose the proportions to ensure that the eutectic was liquid at room temperature. The PCB is 18 μm (0.5 oz) copper based on a 200 μm flexible FR4 substrate.

4.2.3 *Design and Fabrication of the Microfluidic Pressure Sensor*

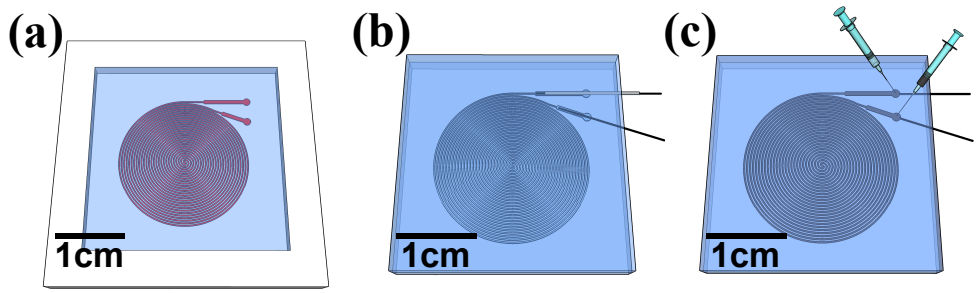

Figure 4.4.: *Fabrication process of the soft pressure sensor.* **(a).** I cured Ecoflex in the vinyl master. **(b).** I bonded another 2 mm blank piece of Ecoflex on to the patterned Ecoflex to seal the channel. I inserted the conductive thread into the channels with a cannula. **(c).** I injected Galinstan into the channel with two needles, one to fill the Galinstan and one to vent the air. (The syringes are not shown to scale).

Figure 4.4 shows the fabrication process of the microfluidic pressure sensor. **(i)** I mixed Part A and Part B of Ecoflex 00-50 (Reynolds Advanced materials) with a volume ratio of 1:1, degassed the pre-polymer, poured the liquid into in the soft-lithography master (fabrication process of this vinyl master is introduced in Section 3.3, and then placed the filled master into a convection oven at 65 °C for 20 min. **(ii)** I bonded another 2 mm-thick blank piece of Ecoflex to the casted piece of Ecoflex. I used a cannula to insert the conductive thread into the channels in the Ecoflex substrate. The resistance of the conductive thread is 27 Ω m^{-1} (Smooth conductive stainless-steel thread bobbin, Sparkfun Electronics). **(iii)** I injected Galinstan into the channels using a syringe and a needle, and I inserted a second needle into the outlet of the channel to vent air. To ensure that the conductive thread is fully wetted, I injected the Galinstan 1 cm further into the channel than the protrusion of the embedded conductive thread. Finally, I used silicone epoxy to seal the holes that I created during the injection process. This seal prevents the wire being pulled out and prevents liquid metal-alloy leaks when the sensor is pressed.

4.2.4 *Design of the Electronic System*

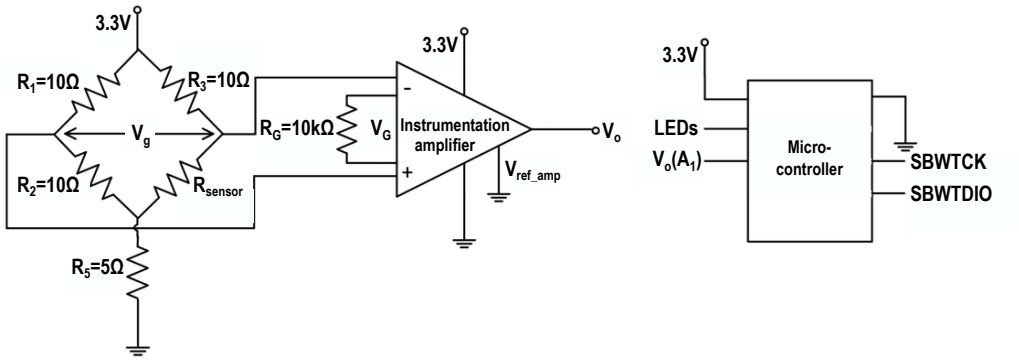

Figure 4.5.: *Circuit schematic of the system on the flexible PCB.* The pressure sensor is a variable-resistance in the Wheatstone bridge network. The voltage output (V_0) from the instrumentation amplifer is the voltage input to the analog-to-digital (ADC) converter in the microcontroller (12-bit ADC on the Atmel SAM3X8E ARM Cortex-M3 or 10-bit ADC on the MSP430F2012 MCU). The MCU is programmed using 2-wire JTAG via SBWTCK (Spy-Bi-Wire Test Clock) and SBWTDIO (Spy-Bi-Wire Test Digital IO). The MCU outputs to three LEDs which light in-proportion to the applied normal pressure.

Figure 4.3 shows a top view of PCB in the integrated soft electronic system. In this flexible PCB, there is a Wheatstone bridge, an instrumentation amplifier, a microcontroller, and three LEDs as output. Figure 4.5 shows the circuit design of the flexible PCB. The Wheatstone bridge is used to measure the variable resistance of the pressure sensor, and the instrumentation amplifier (INA 128, Texas Instruments) is used to amplify the voltage difference from the bridge circuit.

The output from the instrumentation amplifier is fed to the 10-bit analogue-to-digital converter (ADC) in the microcontroller. In electronics, an analog-to-digital converter is a system that converts an analogue signal into a digital signal. In the system presented in Figure 4.5, the 10-bit ADC in the microcontroller converts the input analogue voltage on pin A1 of the microcontroller to a digital number representing the magnitude of the voltage. Here, I use 'ADC value' to represent the digital number output from the ADC. The relationship between the resistance of the microfluidic sensor and the ADC value is shown by Equations 4.1 $\sim$ 4.4. In these equations, v_{ADC} is the ADC value (digital number output of ADC) in the

microcontroller and V_{A1} is the voltage on pin A1 of the microcontroller, N is the number of bits in the ADC, and $V_{\text{ref_MCU}}$ is the reference voltage of the ADC (3.3 V in this circuit).

$$V_{A1} = \frac{v_{\text{ADC}}}{2^N} \times V_{\text{ref_MCU}} \tag{4.1}$$

$$V_{A1} = V_{\text{g}} \times G \tag{4.2}$$

$$V_{\text{g}} = \left(\frac{R_x}{R_3 + R_x} - \frac{R_2}{R_1 + R_2} \right) \times V_{\text{s}} \tag{4.3}$$

$$G = 1 + \frac{50\ \text{k}\Omega}{R_{\text{G}}} \tag{4.4}$$

The bridge circuit consists of four resistors, R_1, R_2, R_3, and R_x, which is resistance of the microfluidic sensor. When the sensor is pressed, the cross-sectional area of the channel changes accordingly, and so does the value of R_x. The gain of the instrumentation amplifier is G, and this value depends on R_G in the circuit. Increasing the value of R_G can enhance the measurement sensitivity of the system while decreasing the value of R_G can improve measurement range of the system.

Many of the previously reported soft-sensors have been evaluated using external instrumentation such as a digital multimeter, an LCR meter or four-point probes (Park et al. [2012a], Hirsch et al. [2016], Chossat et al. [2013]). Including the Wheatstone bridge as an integral part of the system offers the following benefits: (i) The system can be powered with a low-voltage supply or even a 3.3 V button battery. (ii) The Wheatstone bridge is based on the concept of a differential measurement which can be extremely accurate (Giordano [1997]) and provides robustness to thermal-drift.

I used the MSP430F2012 microcontroller in this system as it offers a 10-bit ADC and is capable of low-power modes. I used three LEDs to visually demonstrate compression of the pressure sensor.

4.2.5 *Design of the Experimental Systems and Tests*

To test the physical limitation of the pressure sensor and the mechanical robustness of the proposed conductive thread connection, I performed: (i) A tensile test on three batches of samples at a strain rate of 100 mm min^{-1} using an INSTRON 3367. (ii) A tensile test on two batches of samples with copper and conductive thread connections at a strain rate of 100 mm min^{-1} using an INSTRON 3367. Figure 4.6 shows a photograph of the system I used to apply pressure for the pressure sensing system. In order to apply pressure uniformly, I made a flat clip with a pressure-plate which fully overlapped the sensor.

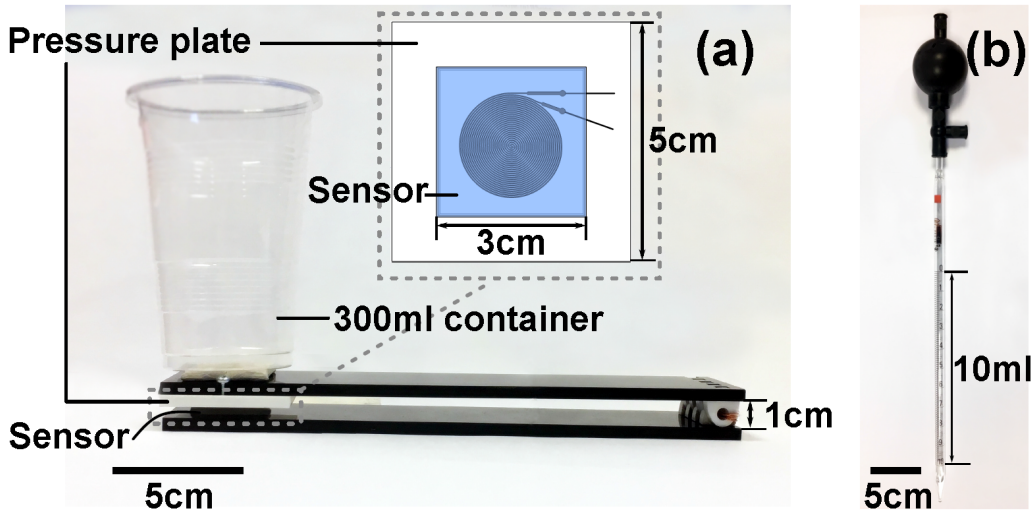

Figure 4.6.: *Experimental set-up.* **(a).** A system for applying uniform pressure over the surface of the pressure sensor. The thickness of the pressure-plate is 6 mm and the thickness of the sensor is 4 mm, by designing the hinge to be 1 cm the plates are kept parallel. **(b).** I used a 10 ml-size pipette to dispense accurate volumes of water into the container shown in (a). I found this volumetric approach to be a convenient way to refine the increments of weight applied to the sensor.

As shown in Figure 4.6 (a), I placed the sensor at the centre of a pressure plate. I placed a 300 ml container on the top of the indenter. I used a pipette as shown in Figure 4.6 (b) to fill the container, and this volumetric approach allowed me to refine the applied weight in varying increments. At 25 °C, 10 ml water results in a weight of 10 g, i.e. about 9.8 N on the pressure sensor. The distance between the parallel-

plates of the clip is 1 cm, which is the sum of thickness of the pressure plate and the pressure sensor. The area of the pressure-plate is 5×5 cm^2, and the area of the sensor is 3×3 cm^2, which is the effective pressing area.

I designed five experiments using this system, to improve the resolution when characterising the pressure sensor we used a 12-bit ADC on an Atmel SAM3X8E ARM Cortex-M3 rather than the 10-bit ADC on the final integrated device, which used an MSP430F2012 MCU.

- **Experiment (1):** To test the sensitivity and resolution of the pressure sensing system, I measured the change in the ADC value ($\triangle$ADC) when I varied the weight on the sensor from 0 g to 300 g with a step-size of 10 g.
- **Experiment (2):** To test the hysteresis properties of the pressure sensor I increased the weight from 0 g to 300 g and then back from 300 g to 0 g.
- **Experiment (3):** To measure the full-range, and get a calibration curve we increased the weight from 0 g to 1080 g using weights.
- **Experiment (4):** To test the reliability of the sensing system we powered on the sensing system at zero-applied load and recorded the change in the ADC value.
- **Demonstration:** To visually display the high resolution of our pressure sensing system we used coins as weights to press the sensor. The LEDs on the PCB were used to visually display the number of coins on the sensor.

4.3 EXPERIMENTS AND RESULTS

In order to investigate the mechanical properties of this system, a tensile testing was carried out using an INSTRON3367 fitted with a 250 N load cell at a strain rate of 100 mm min^{-1}. We fabricated three sets of samples with the following dimensions: $50 \times 30 \times 4$ mm. Each set of samples were tested up to a strain of 500%, including

neat Ecoflex, Ecoflex with empty microchannels and Ecoflex with microchannels filled of Galinstan. Figure D.1 in Appendix D shows photographs in process of this experiment. Figure 4.7 plots stress and strain curves of the three sets of samples.

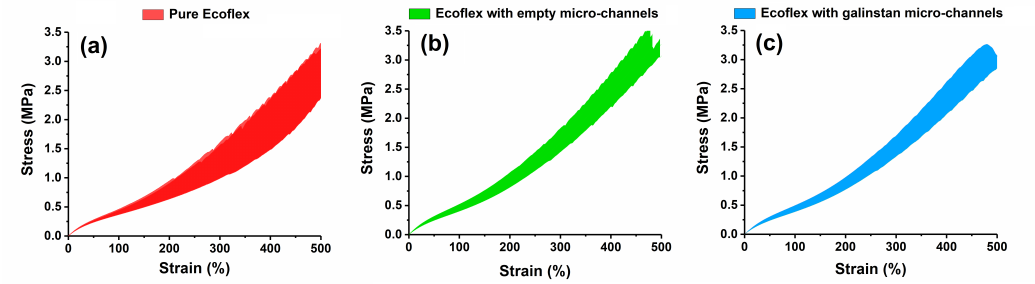

Figure 4.7.: Stress versus strain curves of **(a).** pure Ecoflex; **(b).** Ecoflex with empty micro-channels; and **(c.)** Ecoflex with micro-channels filled with galinsran. The red, green, and blue areas represent range of stress versus strain curves of four samples in each batch.

In the results, the stress and strain curves of the three batches of samples do not show meaningful difference. The micro-channel and the Galinstan does not affect the overall mechanical behaviour in comparison to the pure Ecoflex. This might be due to the small size of the microchannel comparing to the thickness of the samples as well as the small amount of conductive-liquid within. In addition, each sample can be stretched to a strain up to 500% without failure. When the strain was higher than 500%, the samples slipped out from the clamps during the test. However, according to the datasheet of Ecoflex, elongation at breakage of Ecoflex 00-50 is 980% (tested with ASTM D-412). Therefore, the stretchability of the sensor is enough for the pressure sensing system.

An additional test was carried out in order to evaluate the mechanical robustness of the proposed connection. I fabricated two sets of samples. In each sample, copper wire or conductive thread was inserted into Ecoflex with a dimension of $30 \times 20 \times 4$ mm and then sealed with sil-epoxy, as shown in Figure D.2. In this experiment, the Ecoflex were clamped from the bottom and the thread or copper wire was clamped from the top. I used INSTRON 3367 fitted with a 250 N load cell to stretch the thread or copper wire at a strain rate of 100 mm min^{-1} until it detached. The minimum load and extension required to detach the thread and the wire are shown in Table 4.1.

Table 4.1.: Values of minimum load required to lose connection (to detach wire and thread from the channel).

	Threads		Copper	
	Extension (mm)	Load (N)	Extension (mm)	Load (N)
1	Sylgard-10.00323	1.50569	8.67000	1.12497
2	Ecoflex-10.17000	1.34725	7.83669	1.00257
3	Ecoflex-14.16996	1.81460	9.5003	1.10632
4	Ecoflex-7.17011	0.93495	9.83657	1.30265

As shown in Table 4.1, although fabrication errors may affect the experimental results, the conductive thread needs more load and extension to be pulled out of Ecoflex substrate than copper wire in general. An average minimum load of 1.40 ± 0.37 N and 1.13 ± 0.12 N is needed in order to detach the conductive thread and copper wire connections from the channel respectively. This test demonstrates that the conductive thread exhibits a higher mechanical robustness than using a copper wire for the system.

Results from the four experiments that were carried out with the pressure applying system are shown by Figure 4.8. From the perspective of an electronic system, it is the most intuitive to show the relationship between the value of the ADC read by the microprocessor and the pressure on the sensor. Therefore, ΔADC was used in our results instead of ΔR.

Figure 4.8 shows the sensitivity and resolution of the system by tracking the variation of the 12-bit ADC output — ΔADC — in the 0 Pa - 300 Pa pressure range, with a step of $\sim$100 Pa. Good linearity is observed when the load above 500 Pa and when the pressure is spread evenly. In the measured range, the value of the 12-bit ADC increased by 143 units. This experiment was conducted three times and the standard deviation of each point on the curve is less than 4. Figure 4.8 (b) shows the result of the hysteresis test. In this experiment, I increased (in $\sim$100 Pa increments) the pressure on the pressure sensor from 0 Pa to 3500 Pa and then decreased it back to 0 Pa. The results show that the sensor is has little to zero hysteresis.

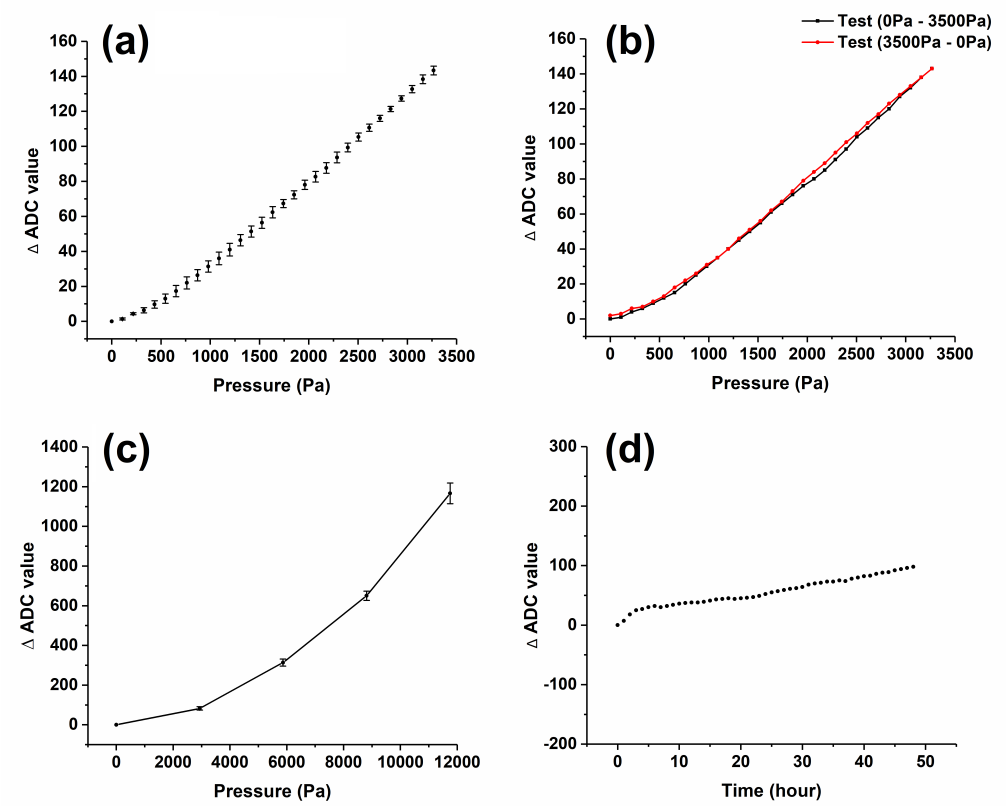

Figure 4.8.: *Results of four experiments to characterise the pressure sensor:* **(a).** sensitivity and resolution test over a pressure range of 0 Pa - 3500 Pa, with an increment of around 100 Pa. Points show the mean values of ΔADC and the error bar on the Y-axis shows one standard deviation (n = 7); **(b).** hysteresis test. I increased the pressure on the sensor from 0 Pa to 3500 Pa (black curve) then decreased it from 3500 Pa to 0 Pa (red curve); **(c.)** calibration curve of ΔADC when I increased the weight over a large range from 0 Pa to 12 kPa, using multiple 270 g weights; **(d).** reliability test. This curve shows the baseline change of the ADC from sample 1 at t = 0 to 48 h. This drift can be corrected by tracking the baseline value and taking the instantaneous ΔADC.

I tested a high-load range from 0 Pa to 12 kPa and the results are shown by Figure 4.8 (c). We conducted this experiment seven times. In the measured range, the value of the 12-bit ADC increased by around 1166 units. The results show that the larger loads give more spread in the data; the largest standard deviation is 52 at the last data point. The sensor shows a quadratic relationship between applied force and electronic output. The sensitivity increases as more pressure is added and this may warrant future investigation for a design with enhanced sensitivity. I conducted an investigation into baseline-drift over along period of time. Figure 4.8 (d) shows the reliability test that I conducted for 48 h. The 12-bit ADC value in the no-load sensing

system increased by 100 units in a linear fashion, but this drift is mitigated in the measurement system by taking instantaneous differential measurements.

To show, visually, the high sensitivity of our integrated pressure sensing system using the MSP430F2012 MCU: we used coins (UK £1) to weigh down the sensor. Figure 4.9 (a)-(d) illustrate that when there was no weight on the sensor, no LED lights up, two coins light one LED and four coins light two LEDs. The weight of a one pound coin is 9.5 g, the diameter of the coin is 22.55 mm. Two coins, therefore, create 0.18 N force and ∼200 Pa on the sensor.

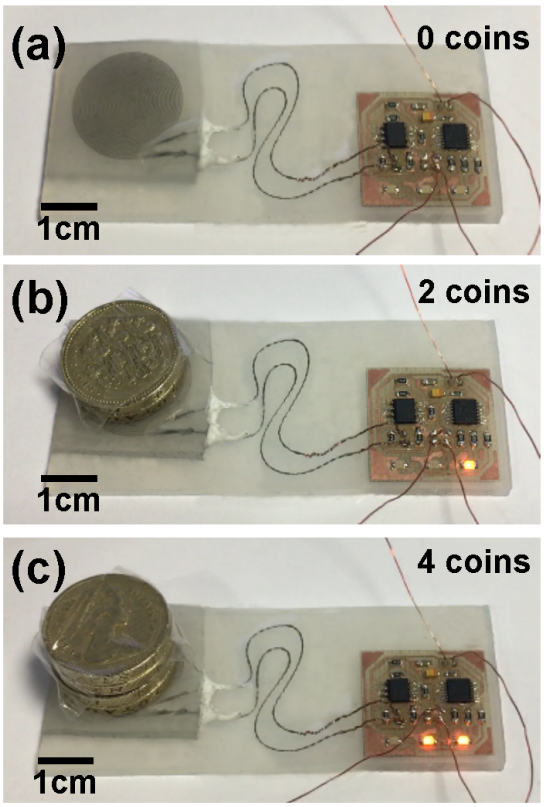

Figure 4.9.: *Demonstrating the sensitivity of the integrated soft system.* I programmed the system to light LEDs in proportion to the applied force **(a).** no coins applied; **(b).** two coins applied; **(c).** four coins applied. The QR code below links to video of this demonstration.

QRcode 4.1.: Demonstrate the sensitivity of the integrated soft system.

4.4 DISCUSSION

The results clearly show that the proposed pressure sensing system has a high sensitivity in the low-Newtons of force range. Within the pressure range of 500-3500 Pa, the relationship between the 12-bit ADC value in the system and the weight on the sensor shows a linear relationship. Every 100 Pa increment in pressure causes an increment of five units in the 12-bit ADC value. After repeating three times the hysteresis experiment, I found out that the largest standard deviation is not higher than four (with a maximum 12-bit ADC variation of 143). However, when applying a high load (12 kPa), the largest standard deviation goes up to 52 (with a maximum 12-bit ADC value of 1166). In 7 repeats of the high-load (12 kPa) experiment (with a maximum 12-bit ADC value of 1166) then the largest standard deviation is 52. These results show a good reliability and feasibility of the soft system. As shown in Figure 4.8 (b), this pressure sensing system exhibits a low hysteresis. The test in Figrue 4.8 (b) has proved this pressure sensing system has low hysteresis.

In summary, I used conductive thread to integrate, robustly, a microfluidic sensor into an electronic system. This integration means that the resulting soft electronic system benefits from the functionality of conventional solid-state electronic system and exhibits the mechanical properties of soft and flexible materials.

I used a Wheatstone bridge and instrumentation amplifier in this system, the voltage that is measured by the microcontroller depends on both the voltage output of the Wheatstone bridge, and on the gain of the instrumentation amplifier. The gain of the amplifier depends on the choice of R_G. I do not discuss the influence of R_G to the sensing system as this is basic background electronics theory; increasing the gain of the instrumentation amplifier can give the sensing system higher resolution but will reduce the corresponding measurement range, and vice versa. The system I presented in this chapter is supplied by 3.3 V, which means the instrument amplifier that connected to the bridge circuit has a maximum output of 3.3 V. When output voltage of the instrument amplifier reaches 3.3 V, even resistance of the sensor keeps

increasing, the voltage output will not change. In conclusion, ADC value which can represent voltage at the analogue I/O port in the microcontroller, will increase when the sensor is pressed, then remain the same at its maximum value when the pressure reaches a boundary.

In the 48 h stability test, the ADC value in the system slightly and gradually increased. This increment indicates that the resistance of the microfluidic sensor was increasing. The resistance increase may be a result of temperature increase due to joule-heating or may be due to further oxidation of Galinstan in the channel. To mitigate this drift, in future work, I could use a resistor which has ten or hundred times higher resistance than the microfluidic sensor before matching the Wheatstone bridge. This method will reduce the resolution in the system as it will reduce the current passing though the Galinstan microfluidic pressure sensor.

4.5 CONCLUSION

In this chapter, I raise an issue that has not received enough attention at present– most of current Gallium-based microfluidic devices need to be connected to hard electronic devices during use and these Gallium-based microfluidic devices require unique methods for interconnecting between soft and hard electronics. Conventional copper wires, which are commonly used to connect sub components in hard electronic devices by soldering, are not suitable for interconnecting eutectic liquid-metal microfluidic devices due to its high-bending moment and rigidity. I put forward a solution for this problem– conductive thread is a good replacement for conventional metal wires to be used as interconnects in soft systems that contains Gallium-based microfluidic devices.

In this chapter, I also present the design and fabrication of a high-resolution pressure-sensor soft system that can transduce normal force into a digital output. In this soft system, which is built on a monolithic silicone substrate, a Galinstan-based microfluidic pressure sensor is integrated with a flexible printed circuit board.

I used conductive thread to connect the Galinstan-based pressure sensor and the flexible printed circuit board. Since conductive thread is electrically conductive and mechanically flexible, it provided stable connection over prolonged periods of time. On the printed circuit board, I built a bridge-system to provide stable readings from the Galinstan pressure sensor. I investigated the relationship between the digital output and the applied pressure in the pressure range of 0 Pa to 12 kPa. This system gives linear measurement results between 500–3500 Pa of applied pressure.

Many current Gallium-based microfluidic devices mentioned in Section 4.1, which were designed and tested individually, have the potential to be prolonged integrated into an electronic system with the help of proper connection wires. These soft devices can play greater role when they are integrated in an electronic system. Compared with the four-probe resistance measurement method which was commonly used in the previous work, the bridge circuit I connected to the pressure sensor enhanced the resolution of the system and make the system can be independently powered by a 3.3V battery instead of a current source.

Compared with conventional copper-wire, conductive thread has better integration with Gallium-based microfluidic electronic devices and is able to provide long-term stability of the connection. However, the resistivity of conductive thread is larger than that of copper. For an electronic system with long wiring requirement, the resistance of conductive thread is not negligible.

By using conductive thread connection we can design systems which overcome the bulk-mechanical mismatches between soft biological systems and hard engineered components and develop fully integrated soft machines, which include power, communications, and control sub-systems. By enabling strong-and-stable electrical connections I hope to enable the community to be one-step-closer to developing fully integrated soft robotic, or wearable systems. I anticipate that integrated systems of this type will find utility in soft-robotic systems as used for wearable technologies like virtual reality, or in soft-medical devices such as exoskeletal rehabilitation robots.

5

WIRELESS SOFT STRAIN SENSORS FOR SOFT ROBOTIC SYSTEMS

In this chapter, I introduce the design and fabrication of a stretchable strain sensor and present the tested results of its characteristics. Some text and figures in this chapter are reproduced from my paper *Soft RFID Sensors: Wireless Long-range Strain Sensors Using Radio-frequency Identification* and *Soft Wireless Battery-free UHF RFID Stretchable Sensor based on Microfluidic Technology* with permissions. The published version of these papers are in Appendix E and Appendix F.

Kewen and I published these joint papers together. Kewen is a Ph.D student of Microwave and Communication Systems Group in the University of Manchester. In this work, Kewen and I designed structure of the sensors together. Based on the Galinstan-based microfluidic devices fabrication method I introduced in Chapter 3, I individually fabricated samples of the designed sensors. Kewen performed an finite element simulation to simulate characteristic of the soft sensors under a variety of strains. Then I did all the experiments with Kewen in the University of Manchester. In the paper *Soft RFID Sensors: Wireless Long-range Strain Sensors Using Radio-frequency Identification*, I took charge of 90% paper writing, Kewen took charge of 10%. In the paper *Soft Wireless Battery-free UHF RFID Stretchable Sensor based on Microfluidic Technology*, Kewen did most of writing while I provided figures and descriptions of the fabrication process. In author list of the two papers, Adam A. Stokes is my supervisor and Zhirun Hu is Kewen's supervisor, they provided workspace, equipment, and guidance of our work. The other authors provided advice and help to our experimental setup and paper writing process to some extent.

5.1 INTRODUCTION

In the last chapter, I raise an issue that most of current Gallium-based microfluidic sensors need to be connected to hard electronic devices but conventional copper wires are not suitable for interconnecting eutectic liquid-metal microfluidic devices due to its high-bending moment and rigidity. In the last chapter, I put forward a solution for this problem — conductive thread is a good replacement for conventional metal wires. In this chapter, I present another solution to the connection problem — a wireless Galinstan-based sensor that does not need any external wire connection to other hard electronic devices.

The wireless soft strain sensor was primarily designed for the applications in pneumatic soft robotics. In recent years, increasing amounts of attention are being paid to the study of *Soft Sensors* and Soft Robotic Systems. One motivating factor for using *Soft Robotics* is the fact that the materials of the robots are *softer* than the environments with which they interact, and this compliance makes them ideal for applications involving human-robot interaction (Shademan et al. [2016], Polygerinos et al. [2015], Alspach et al. [2015]).

Soft Robotic Systems require input from advances in the field of *Soft Sensors*. Soft sensors can help a soft robot to perceive and to act upon its immediate environment. Sensor research impacts a robots' sensor modalities, sensor accuracy or measurement range besides others. The concept of integrating sensing capabilities at low cost has also become increasingly important, especially for certain subgroups in robotics, namely soft robotics, modular robotics and swarm robotics. In such cases, lower cost systems are motivated by *design for manufacturability* allowing one to commercialise or to scale a robot system.

In this work, I intend to develop untethered soft sensors which can work wirelessly by dispensing, entirely, with the need for onboard power and processors. The proposed sensor can be fully embedded into soft robots without adding any other devices or additional electrical tethers, so that one can eliminate the wire and weight

pressures on soft robotic systems. The relatively long measurement working range can allow the soft robots to move freely in a reasonably large area.

5.2 PRINCIPLES AND IMPLEMENTATIONS

5.2.1 *RFID Technology*

The proposed soft strain sensor is also a configurable RFID tag antenna. Radio Frequency Identification (RFID) is a low-cost technology that allows the passive wireless communication of data. In recent decades, RFIDs have been used in many projects such as in robot motion sensors (Liu et al. [2014]), indoor localization (Sanpechuda and Kovavisaruch [2008]), and distributed sensor networks (Choi et al. [2011]).

An RFID system usually consists of a transponder (sometimes called RFID tag) and the reader. The reader transmits electromagnetic waves to reach out to the RFID tag; if the RFID tag is within the operating range, it utilizes the energy of the incoming electromagnetic wave to transmit a new electromagnetic wave that contains RFID tag specific information. The information usually contains a unique serial number. The reader receives and visualizes the information. RFIDs can be operated in different frequency bands. While the LF (125 - 134 KHz) and HF (13.56 MHz) bands use magnetic flux coupling, the UHF (300 MHz - 3 GHz) band uses electromagnetic wave coupling. The communication distance of the UHF band is over 16 m, which outperforms the LF and HF bands. In this work, the proposed antenna operates in the UHF band.

5.2.2 *Sensor Constitution and Working Principles*

Figure 5.1 (a) depicts a stretchable meandered half-wave dipole antenna. I embedded an RFID chip into the antenna design. Figure E.1 in the Supplemental Information in Appendix E indicates specific antenna dimensions.

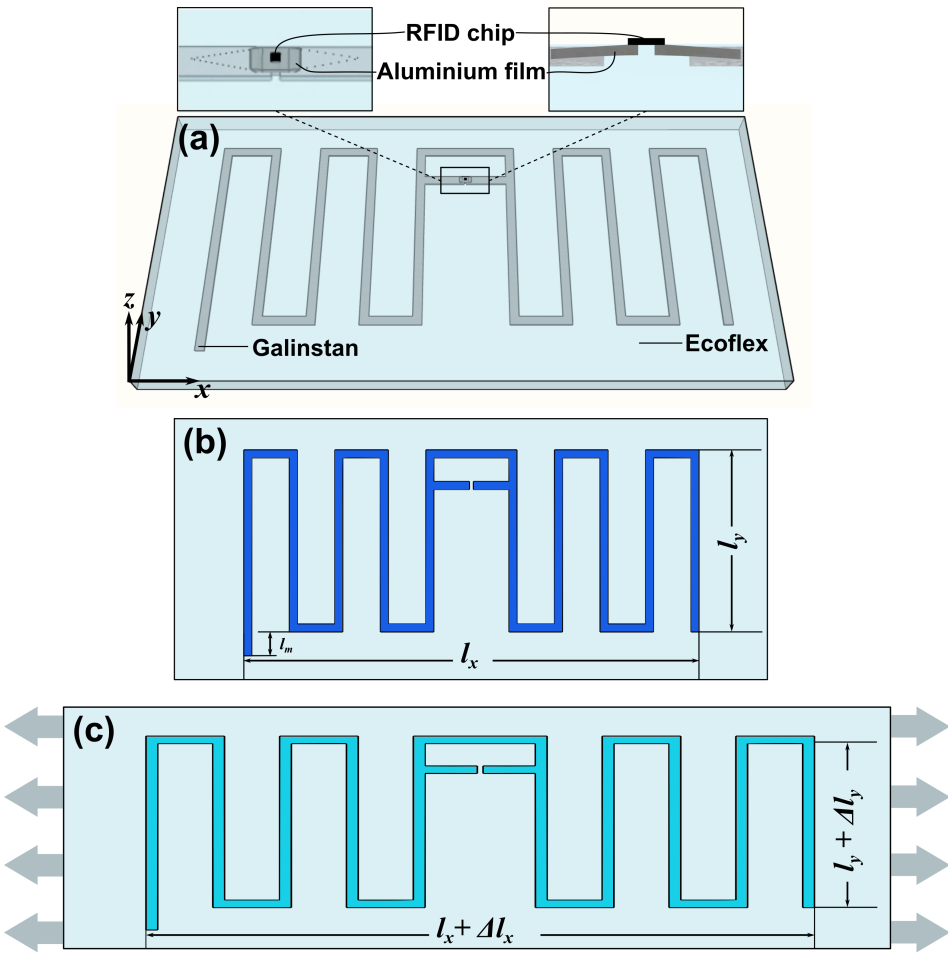

Figure 5.1.: *Schematic diagram of the stretchable microfluidic sensor.* **(a).** Galinstan is enclosed in Ecoflex substrate while an RFID chip is bonded on a piece of aluminium foil which is inserted in the channels. Detailed and cross-section figures of the part near RFID chip are presented. Directions of x, y, and z axis are indicated; **(b).** Initial state of the antenna when it's not stretched. The effective antenna length on x-direction and y-direction is defined as l_x and l_y respectively. Notice: The electrical length of the entire antenna is $l_x + 10l_y + l_m$. The non-symmetric part, l_m is used for fine impedance matching between the antenna and the RFID chip; **(c).** When the soft antenna is stretched, the effective antenna length on x-direction and y-direction is defined as $l_x + \Delta l_x$ and $l_y + \Delta l_y$.

The sensor I present in this work consists of an RFID chip and a half-dipole antenna. The antenna consists of eutectic liquid alloy filled microfluidic channels in an elastic silicone substrate. The eutectic alloy I used is Galinstan. As introduced in Section 3.1, Galinstan can be easily injected into channels of soft structures. The resistance of a channel can be approximated by $R = \frac{\rho}{A} * l$, (ρ is resistivity of the liquid metal, A and l are cross-section area and length of the channel respectively); so the channel resistance changes through deformation. The Galinstan I made consists of 68.5 wt% Ga, 21.5 wt% In, and 10 wt% Sn; its melting temperature is -19 °C; and its electrical conductivity is 3.46×10^6 S m^{-1}. Galinstan indicates favourable properties as channel conductor. I observed reliable liquid distributions in the antenna channels despite extreme twisting, stretching and folding.

I used Ecoflex as the elastic silicone substrate. This silicone material has a Young's modulus of $\sim$69 kPa. As introduced in Section 3.2, I chose Ecoflex to be the substrate due to its favourable properties, it is: easy to synthesise, easy to handle, low cost, and biocompatible. In tensile tests with the ASTM D412 system, the maximum elongation of Ecoflex 00-50 (type 00-50) is 980% (defined as the percentage change in length or $((l - l_0)/l_0) \times 100\%$).

In Figure 5.1 (a), the RFID chip is bonded on aluminium pads and inserted in between two Galinstan channels. The RFID chip consumes power from received signals and backscatters them without requiring an external power supply depicting a wireless passive soft sensor. Figure 5.1 (b) and Figure 5.1 (c) indicate how deformation of an antenna can change its dimensions. If the channel dimensions change, the channel resistances change and therefore the entire antenna and its parameters change. The RFID chip backscatters signals with varying amplitude and phase based on the degree of stretching.

5.2.3 *Implementation in Soft Robotics*

Figure 5.2 shows the schematic diagram of the soft RFID sensor implementation. The implementation comprises a pneumatic soft robot with four embedded soft RFID tags, one tag on each robot leg, and the electronic circuitry to transceiver data.

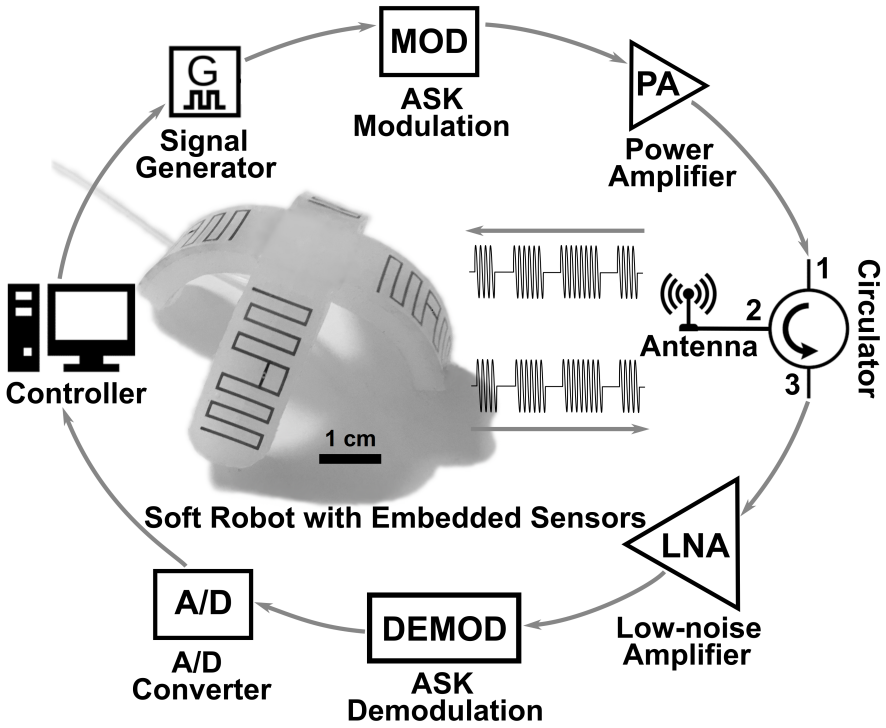

Figure 5.2.: *The electronic system for measuring data from a pneumatic soft robot that contains four embedded microfluidic strain sensors.*

In Figure 5.2, the Controller uses the Signal Generator to generate a high frequency carrier signal. An Amplitude Shift Keying (ASK) module modulates the amplitude of the carrier signal to decode information. A binary "one" consists of a fixed amplitude and frequency; a binary "zero" is a zero-voltage output. The modulated signal is passed through a power amplifier preparing the signal for transmission. The signal lies on port 1 of a circulator circuit. Port 2 of the circulator outputs the signal to an antenna, therefore broadcasting the signal. The soft RFID tags receive the signal, utilize its energy and transmit a new signal that incorporates their unique IDs. The antenna receives the signals from the soft RFID tags and outputs them to port 3 of the

circulator. The circulator ensures that outgoing and incoming signals do not interfere with one another. The incoming signals from the soft RFID tags pass a low-noise filter, an ASK demodulator and are ultimately inserted into an analogue-to-digital converter. The controller analyses the various signals (distinguishable through their IDs) with regard to their amplitude and phase.

5.3 ANTENNA DESIGN

5.3.1 *Selection and Design of the Antenna*

The antenna design of the soft RFID sensor is different from other antenna designs because of power and size requirements. The antenna powers the RFID chip with incoming signals; It does not require a power supply. I decided to design the soft RFID sensor as small as possible to attach the RFID tags to even small objects making our sensor more applicable. Since the soft RFID sensors can be attached in any arbitrary orientation, I ensured 360 degree or *omnidirectional* readouts by using a half-wave dipole antenna design. The effective electrical length of a half-wave dipole antenna is half the wavelength of the operating frequency of the system. This antenna design is commonly used in Radio Frequency (RF) systems with omnidirectional radiation patterns perpendicular to the antenna axis.

In previous work, small antenna sizes were accomplished by using micro-strips (Ukkonen et al. [2006]). However, they suffered directional read-out constraints and low efficiency. My design uses a Meander Line Antenna (MDA) to achieve long reading ranges and small antenna size. MDA is a derivative of the dipole antenna and achieves high efficiencies (Takiguchi and Yamada [2003]) for small antenna sizes (Hu et al. [2009]).

Stretching the soft half-wave dipole antenna as illustrated in Figure 5.1 (b) causes a change in the dimensions if the antenna in both the x- and y-directions. An increase

in strain in the x-direction decreases the thickness of the soft polymer, due to the Poisson effect, and also decreases its height by Δl_y. Therefore, stretching the soft RFID tag changes the electric length of the antenna; each infinitely small change in electric length shifts the resonant frequency. Now, if we send signals to RFID tags, the frequency of the carrier signal can be changed to the specific resonant frequency of current electric length of the antenna. The backscattered signals from the RFID tags will indicate phase and amplitude changes due to the resonant frequency.

5.3.2 *Antenna Matching*

As mentioned in the previous section, the RFID antenna utilizes power from the incoming electromagnetic waves to supply power to the RFID chip. Impedance matching between the RFID chip and the antenna is paramount in RFID antenna design because it affects how much power the antenna is able to reflect, hence determines the antenna's operational range.

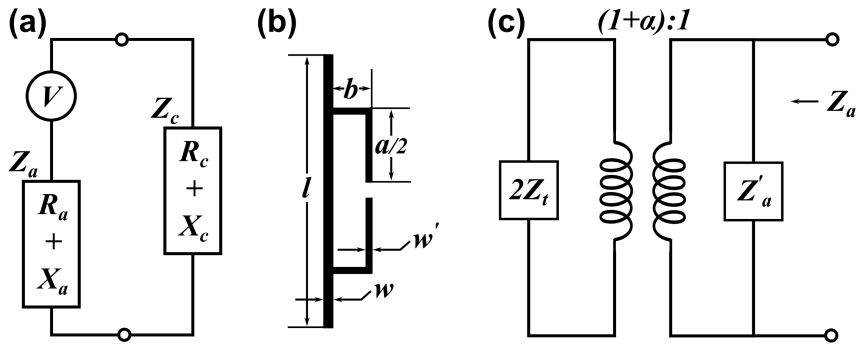

Figure 5.3.: *Equivalent circuit of the RFID chip and the transporter antenna.* **(a).** Z_a is the total impedance of the transport antenna whereas Z_c is impedance of the RFID chip; **(b).** Schematic diagram of T-matching for a dipole antenna. The l represents length of the original dipole antenna. This antenna is connected at the centre to a short second dipole. The close distance between matching stub and the original antenna is b, whereas w and w' are the widths of the original dipole antenna and the mating stub respectively; **(c).** Equivalent circuit at the source point of the dipole antenna after T-matching. Z'_a is the impedance of the first dipole antenna without T-matching while Z_t is the impedance that the matching stub created. The α in the ratio is the current division factor between the two connectors.

Figure 5.3 indicates how to match impedances; The best impedance matching for maximum power transmission to is conjugate impedance matching, which means $R_a = R_c$ while $X_a =$ -X_c. The RFID chip we used (Monza R6, Impinj) possesses an impedance of $Z_c = (13.5 - j126)\ \Omega$ at 860 MHz. Therefore, we designed the transporter antenna to match the impedance of this RFID chip.

The theoretical impedance of a half wave dipole antenna in free space is $73 + j42.5$ Ohms (Bansal [2013]) which makes it impossible to match the impedance of the RFID chip. Therefore, we used the T-match method to match the impedance between transporter antenna and RFID chip. Figure 5.3 (b) and (c) indicate that a half-wave dipole antenna can be changed through a centred short-circuit stub. The antenna source is connected to a small dipole of length $a \leq l$ and is placed at a close distance b from the first and larger dipole. The electric current distributes along the two main radiators according to the size of their transverse sections. The impedance Z_a at the source points is given by Equation 5.1 (Marrocco [2008]):

$$Z_a = \frac{2Z_t(1+\alpha)^2 z'_a}{2Z_t + (1+\alpha)^2 Z'_a}. \tag{5.1}$$

In Equation 5.1, Z'_a is the original dipole impedance taken at its centre in the absence of a T-match connection, whereas Z_t is the impedance created by the matching stubs. α is the current division factor between the two connectors, re and re' are the equivalent radii of the initial dipole and the matching stub, $\alpha = \ln(b/re') \,/\, \ln(b/re)$.

We performed impedance calculation with finite element method (FEM) simulations with Computer Simulation Technology Microwave Studio (CST Microwave Studio). FEM includes the use of mesh generation techniques for dividing a complex structure into a large number of small elements. Calculations are made for every single element and combining the individual results can give us the conclusive results of the structure. We modified the edge of the antenna to be asymmetric, so that created l_m in Figure 5.1 (a), for a final fine matching step.

5.4 MATERIALS AND FABRICATION METHODS

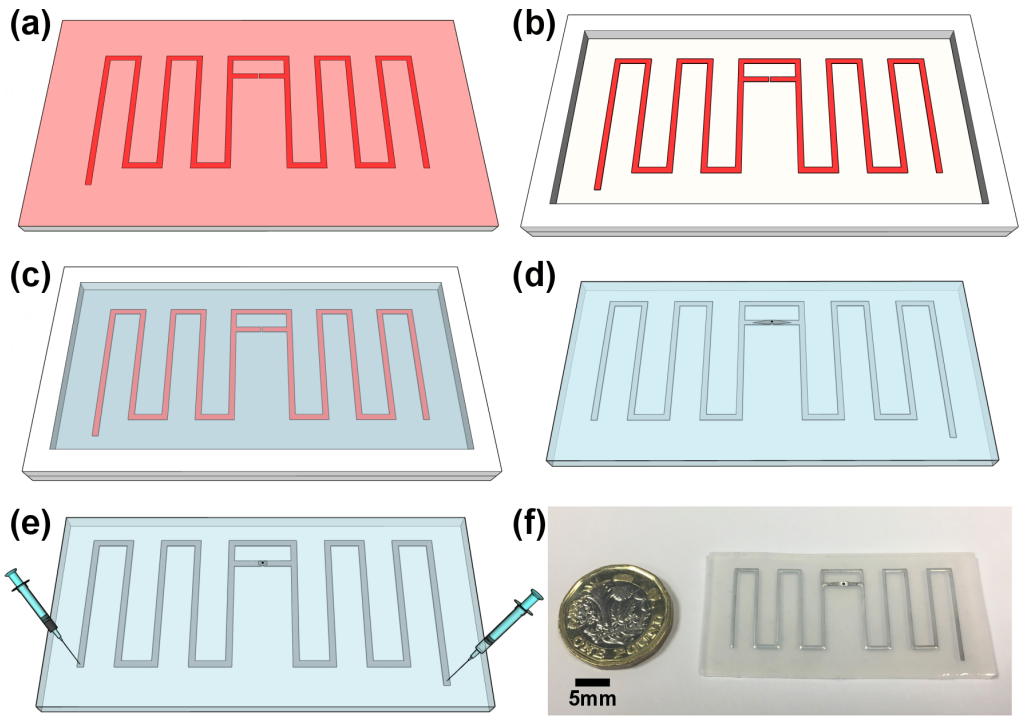

Figure 5.4.: *Fabrication process and prototype of the stretchable microfluidic sensor (RFID tag antenna).* **(a).** cut the sensor profile on a piece of self-adhesive vinyl attached on an Acrylic substrate. Notice: the red and pink parts are a same piece of vinyl. Two different colours are used here to show the laser-cut profile clearer; **(b).** the unwanted part of vinyl was peel off, a 2 mm-thick Acrylic frame was stuck on the substrate to form a soft-lithography mould; **(c).** uncured Ecoflex with a controlled height of 2 mm was poured into the soft-lithography mould; **(d).** the casted piece of Ecoflex was sealed with another 0.15 mm Ecoflex film and the RFID chip bonded on aluminium film was inserted into the channels; **(e).** two needles were used to inject Galinstan into the channel; **(f).** Photograph of the final prototype.

Figure 5.4 shows the soft-lithography fabrication process of the stretchable antenna (photographs of the fabrication process are shown in Figure E.2 in Appendix E). I designed and fabricated an antenna master with a laser micro-machining system (Protolaser U3, LPKF) and a self-adhesive vinyl film (CRAFTRKZO, d-c-fix®) as shown in Figure 5.4 (a). A piece of vinyl film was attached to an Acrylic substrate (2 mm Acrylic Cast, AMARI). The channel profiles were cut with the LPKF laser system. I peeled the vinyl residuals (negative) from the substrate and laid a 2 mm-thick acrylic frame along the master edges as indicated in Figure 5.4 (b).

I synthesized Ecoflex 00-50 (Reynolds Advanced Materials, 1:1 ratio), degassed it in a vacuum chamber and poured the soft polymer into the mould as illustrated in Figure 5.4 (c). I put the master into a convection oven at 65 °C for 20 minutes, then removed the soft structure from the mould and flipped it over. A 150 μm thin Ecoflex 00-50 layer were fabricated with spin coater to seal the unfolded channels in Figure 5.4 (d). I made small incisions in the centre of the thin Ecoflex layer to embed the RFID chip; the RFID chip (Monza R6, Impinj) was bonded on an Aluminium film with a bonding machine (FB-300 manual RFID wrapping machine) and inserted in the channels. During the bonding process, the chip was aligned to the substrate with a vacuum sucker, microscopes and cameras in the bonding machine, an adhesive material was dispensed between the chip and the aluminium film, then the chip was firmly bonded on the aluminium film with hot-pressing for 10 seconds.

I inserted two injection needles into the soft structure as illustrated in Figure 5.4 (e). One needle was used to inject the Galinstan into the channel, the other needle was used to release air pressure. The Galinstan made contact with the aluminium pads of the RFID chip without leaking to the surface. At the end, I applied a thin film of uncured Ecoflex on top of the device to seal the open holes created by chip insert and liquid metal injection.

5.5 EXPERIMENTAL DESIGN

Figure 5.5 presents experimental setup of this work. The permittivity of Ecoflex 00-50 and the resistivity of Galinstan are parameters that are required to simulate S_{11}; S_{11} is the input reflection coefficient or input return loss. S_{11} indicates the radiation efficiency of the antenna and reaches its maximum value at resonant frequency. We used an Agilent 85070E dielectric probe kit to measure the permittivity variations of Ecoflex 00-50 in a frequency range from 200 MHz to 1.2 GHz as shown in Figure 5.5 (b). We simulated changes in resonant frequency and radiation efficiency under strain variations between 0% to 50% and a step size of 5%.

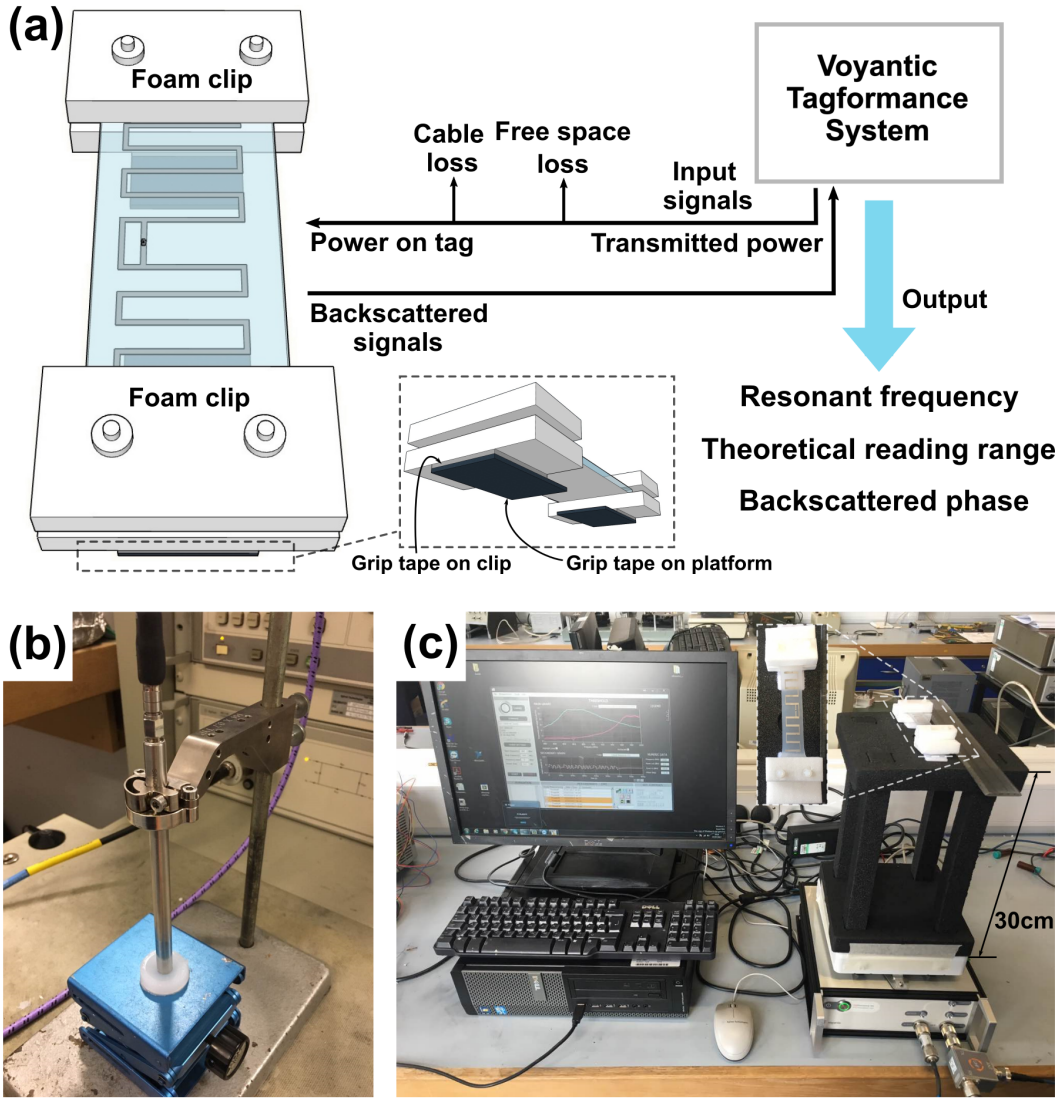

Figure 5.5.: *Experimental design.* **(a).** We used Voyantic Tagformance system to measure characteristics of the proposed antenna. This measurement system sends input signals to the tag antenna with transmitted power. The power received on tag is the transmitted power minus cable loss and free space loss. RFID chip in the tag antenna receives the input signals, absorbs energy in the signals, and then sends backscattered signals back to the measurement system. According to the results of the measurement system, we can know the resonant frequency and the theoretical reading range of the tag antenna, as well as the phase of the backscattered signals. We affixed the two edges of the tag antenna with clips made of rigid foam. In order to stretch the tag antenna and hold its position for measurement, we stuck grip tape on the surface of the foam clips, and on the measurement platform. **(b).** Experimental setup for measurement of the permittivity of Ecoflex 00-50 with the Agilent 85070E dielectric probe kit system. **(c)**. Photograph of the experimental setup of the soft antenna and the Voyantic Tagformance system.

I used a Voyantic Tagformance system to measure the characteristics of our antenna design; namely, the frequency modulation of our soft RFID sensor due to strain variations as indicated in Figures 5.5 (a) and (c). This setup allowed us to determine the resonant frequency, the theoretical RFID reading range, and the phase changes of the backscattered signals for every applied strain in the range from 0% to 50% with a step size of 5%. I repeated each measurement seven times to indicate the soft polymer's reversibility. I fabricated three sensor samples to enable us to evaluate the repeatability of our fabrication process. I did a cyclic stretching test to prove the reliability of the proposed sensor when it is stretched to 50% for 240 times. It is worth mentioning that we calculated the strain value in all the experiments with $\left(\left(\frac{\Delta l_x}{l_x}\right) \times 100\%\right)$, l_x and Δl_x are as shown in Figure 5.1. The length I used in calculation is the effective antenna length in x-direction, not the distance between the foam clips. I also tested the soft RFID sensors when applied twists of 0°, 45°, and 90°.

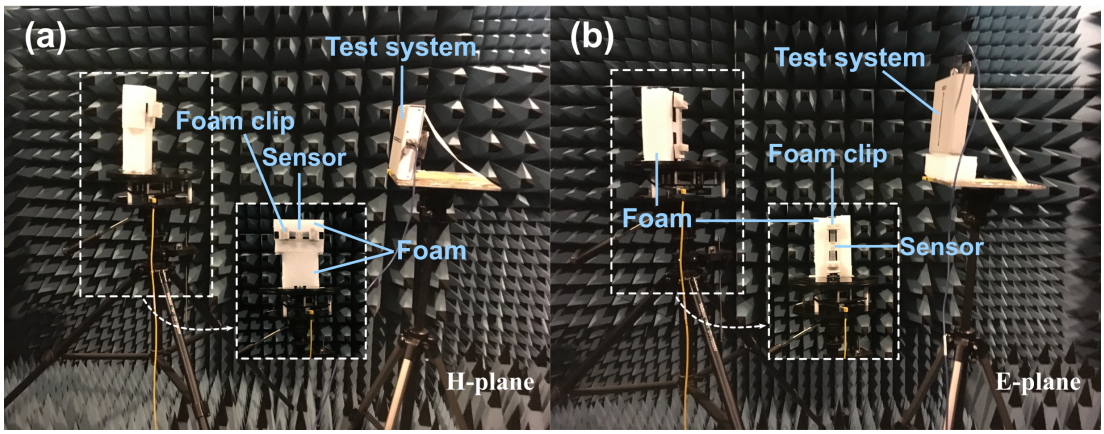

Figure 5.6.: *Radiation pattern measurement in H-plane and E-plane in an anechoic room* with Diamond Engineering Automated measurement system and an automatic turntable. In the measurement, the reader antenna holds its position while the strain sensor (transporter antenna) turn with the turntable.

Figure 5.6 shows that I used a diamond engineering automated measurement system and an automatic turning table in an anechoic room to measure the radiation patterns of our soft RFID sensor in the H- and E-plane. An anechoic room absorbs reflections from acoustic and electromagnetic waves. I analysed the directivity of the antenna (in the H- and E-planes) when subjected to strains of 0%, 25%, and 50%.

5.6 RESULTS

5.6.1 *Permittivity of Ecoflex 00-50*

The relative permittivity (ε_r) of Ecoflex 00-50 is nearly stable at 3 in the range of 500 MHz $\sim$ 1.2 GHz as shown in Figure 5.7. The operating frequency range of our sensor is 800 MHz to 860 MHz, which is covered in this stable range; Thus, we can take ε_r of Ecoflex as a constant in calculation and simulation.

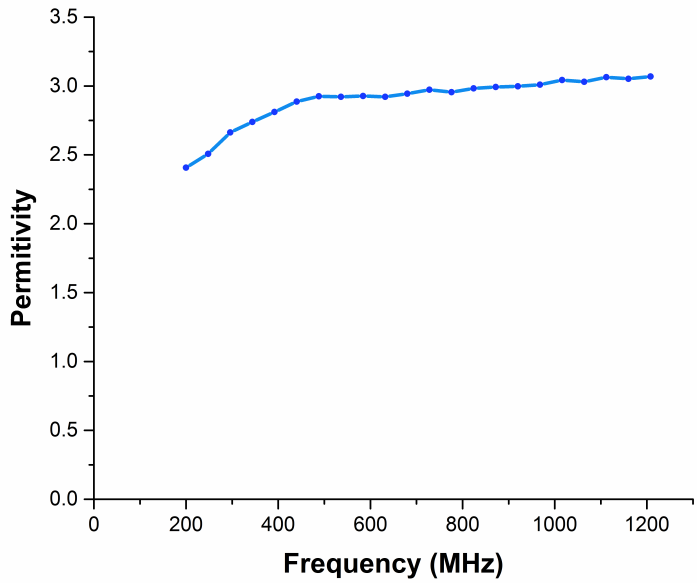

Figure 5.7.: *Permittivity of Ecoflex type* 00-50 *in the frequency range of* 200 *MHz* $\sim$ 1.2 *GHz.* Measured with Agilent 85070E dielectric probe kit system.

5.6.2 *Simulation of Antenna Efficiency*

When the soft RFID sensor is stretched, its antenna parameters such as resonant frequency and radiation efficiency change. Below I analyse, analytically, the antenna

parameters due to strain variations and we apply an ideal folded half-wave dipole antenna model.

The resonant frequency of a half-wave dipole antenna is given by

$$f_r = \frac{c}{2l_e\sqrt{\varepsilon_e}} \times r, \tag{5.2}$$

l_ε is the effective electrical length of the antenna; f_r is the resonant frequency; ε_e is the effective permittivity of the antenna substrate; and r is the correction factor of a folded half-wave dipole antenna. We can estimate the effective relative permittivity through

$$\varepsilon_e = 1 + \left(\frac{\varepsilon_r - 1}{2}\right)\frac{K_1}{K_2}, \tag{5.3}$$

ε_r is the relative permittivity of Ecoflex, which is considered as a constant here; $K_1 = \frac{K(k_1)}{K'(k_1)}$ and $K_2 = \frac{K(k_2)}{K'(k_2)}$ while $K(k)$ is a complete elliptic function of the first kind and $K(k')$ is its complimentary function. In the K function, $k_1 = \frac{l_e}{l_e+2s}$ and $k_2 = e^{-\frac{\pi s}{2h}}$ whereas l_e is effective electrical length of the antenna, s is the gap at the feed point, and h is height of substrate of the antenna. Equation 5.2 shows the resonant frequency of a half-wave dipole antenna changes with its effective electrical length, while Equation 5.3 indicates that the resonant frequency also changes with the substrate height of the antenna.

Rigid antennas possess a fixed effective electrical length, whereas our soft antenna's effective electrical length changes due to strain. Due to the Poisson effect, our antenna physically changes according to

$$\frac{\Delta l_y}{l_y} = 1 - \left(1 + \frac{\Delta l_x}{l_x}\right)^{-v}, \tag{5.4}$$

l_x is the antenna length; Δl_x describes a change in antenna length; l_y is the antenna width; Δl_y describes a change in antenna width; and the initial (not stretched) electrical length of our antenna is $l_x + 10l_y + l_m$. Since $l_m \ll l_x + 10l_y$, we neglect the effect of l_m here. Figure 5.1 complements Equation 5.4.

I insert Equations 5.3 and 5.4 in Equation 5.2 and receive a new equation for the resonant frequency for the soft antenna I proposed:

$$f_r = \frac{c}{2\left(l_x\left(1+\frac{\Delta l_x}{l_x}\right)+10l_y\left(2-\left(1+\frac{\Delta l_x}{l_x}\right)^{-v}\right)\times\sqrt{1+\left(\frac{\varepsilon_r-1}{2}\right)\frac{K_1}{K_2}}\right.} \times k, \tag{5.5}$$

v is the Poisson ratio of Ecoflex type 00-50.

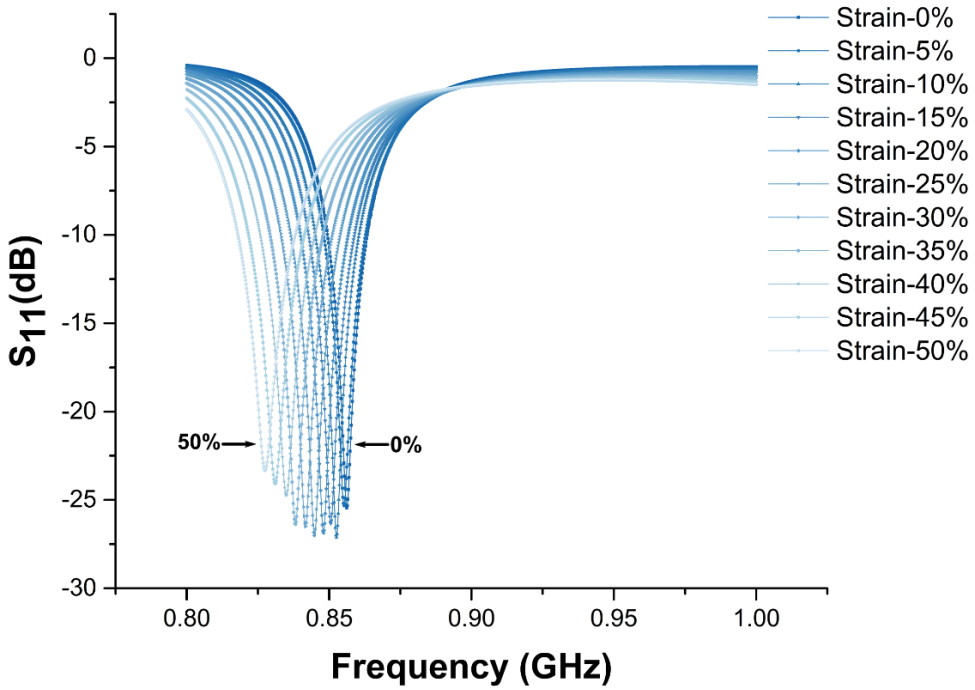

Figure 5.8.: *Finite elements simulation results.* Under 0% strain condition, simulated resonant frequency of the antenna is 856 MHz. The simulated resonant frequency continuously goes down to 827 MHz when the antenna is under 50% strain.

We performed an electromagnetic finite element simulation using Computer Simulation Technology (CST) to determine S_{11}, the input return loss, under a variety of strains. The maximum of S_{11} indicates resonant frequency of the antenna. Figure 5.8 indicates the simulation results; the soft antenna has been strained from 0% to 50% with a step size of 5%; the S_{11} peak values are all below -20 dB at resonance frequency for each strain condition indicating that 99% of the power from the input signal is scattered back from the soft RFID sensor. We successfully matched antenna to RFID chip resistance.

5.6.3 *Resonant Frequency upon Strain*

The Voyantic Tagformance measurement system controls the power of the signal that we transmit to the soft RFID sensor. First, we set the initial signal power to 25 dB. Second, we gradually decreased the signal power until we could not detect the backscattered signal from the soft RFID sensor anymore. Power of the input signal was recorded as Transmitted Power (P_t). We repeated this process for each sampling frequency in the frequency band of 800 MHz - 880 MHz, with a step of 1 MHz.

As indicated in Figure 4.6 (a), the power received by the soft RFID tag antenna (P_{tag}) can be calculated as

$$P_{\text{tag}} = P_t - L_c + G_t - FSPL, \tag{5.6}$$

L_c are cable losses; G_t is the Gain of the Voyantic Tagformance's transmitter antenna; and FSPL are losses due to free space transmissions. L_c, G_t, FSPL can be determined by calibrating the Voyantic Tagformance.

Figure 5.9 (a) shows the minimum transmitted power (P_t) for each sample frequency to result in a detectable backscattered signal from the soft RFID sensor. Figure 5.9 (b) indicates the power received on tag antenna (Power on tag, P_tag) corresponding to the minimum P_t for each sample frequency. The theoretical measurement reading range of the soft RFID sensor is frequency dependent and can be calculated by

$$R_r = \sqrt{\frac{P_{\text{max},BIRP}}{P_{\text{tag}}}} \times \frac{c}{4\pi f}, \tag{5.7}$$

$P_{max,EIRP}$ is the maximum signal power of the Voyantic Tagformance (default: 3.28 W). P_{tag} in this equation is related to the minimum transmitted power. Figure 5.9 (c) depicts the reading ranges calculated with Equation 5.7 for the various frequencies; our soft RFID sensor has a reading range of approximately 7.5 meters, whereas this range increases if the soft sensor is under strain. The reading range of the sensor increases to 10 meters under a strain of 50%. The resonant frequency decreases from

862 MHz in idle state (no strain) to around 802 MHz under 50% strain. Figure 5.9 (d) illustrates the backscattered signals from the soft RFID sensor under different strain conditions.

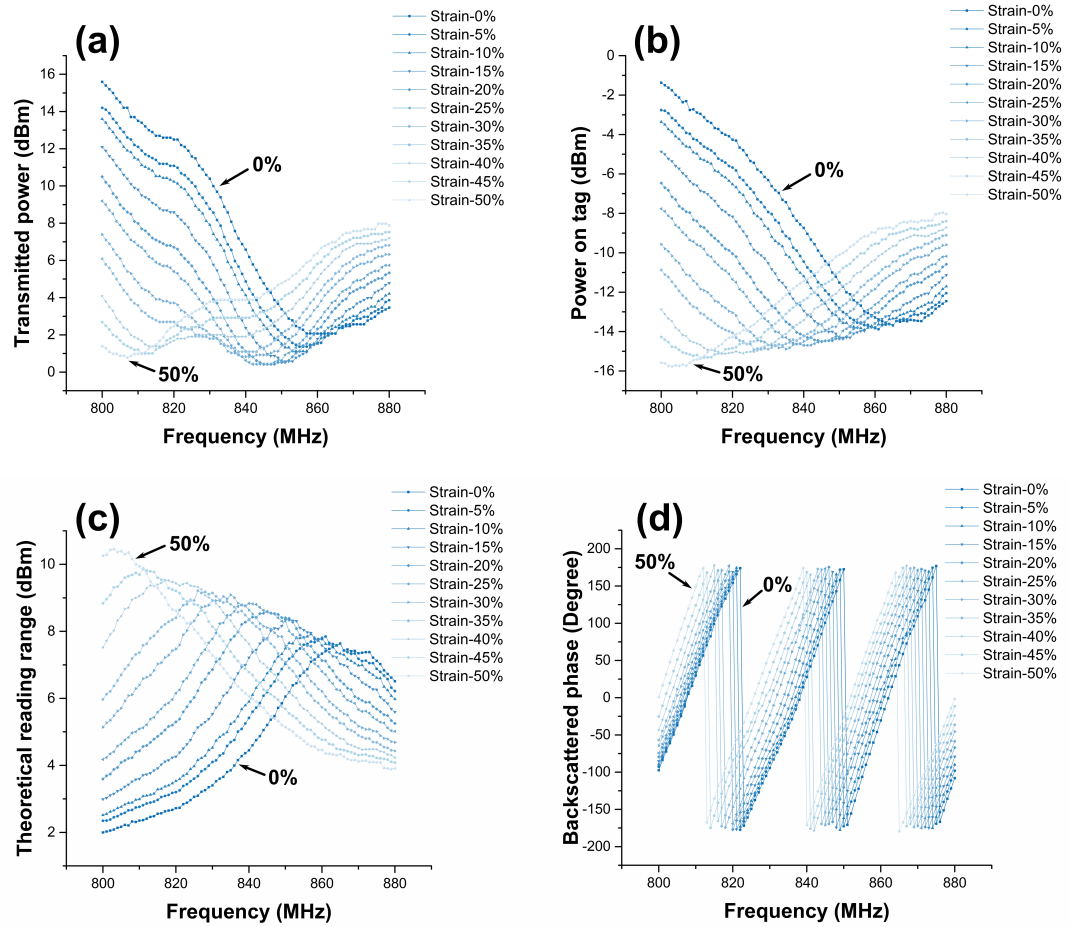

Figure 5.9.: *Results: Resonant frequency upon strain-1.* **(a).** Transmitted power. The minimum transmitted power recorded for the sensor under 0% - 50% strain, with a step of 5%. **(b).** The power received on tag, which was calculated based on the transmitted power and cable and free space loss. **(c).** Theoretical reading range forward, which was calculated based on the power received on tag. **(d).** Backscattered phase in the frequency band of 800 MHz - 880 MHz (with a step of 1 MHz) when the sensor was under 0% - 50% strain, with a step of 5%.

5.6.4 *Repeatability and Reliability Test*

We tested the reliability of our soft RFID sensor by performing seven strain experiments. We measured the resonant frequency under 0% to 50% strain with a step size of 5%. Figure 5.10 (a) shows the average value and standard deviation of the resonant frequency for each strain. The resonant frequency dropped approximately 61 MHz (from 86 MHz to 827 MHz) from 0% to 50% strain, whereas the maximum standard deviation did not exceed 2.6 MHz.

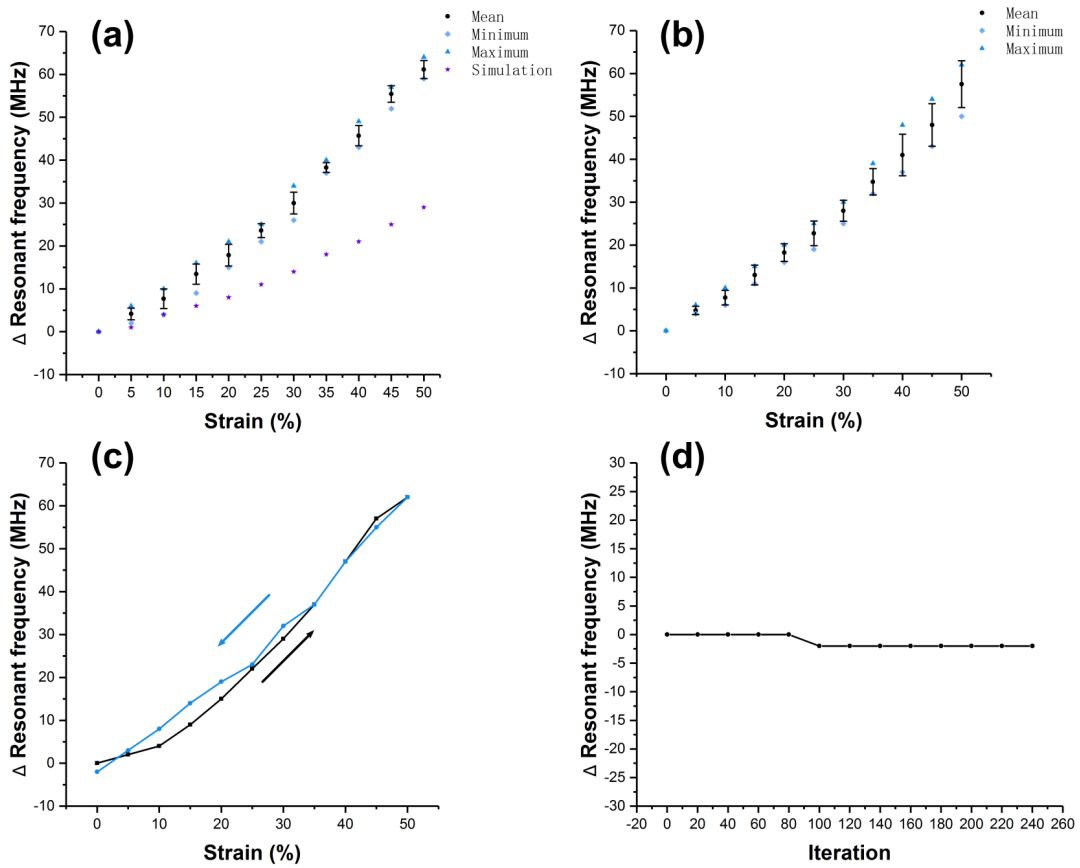

Figure 5.10.: *Results: Resonant frequency upon strain-2.* **(a).** Resonant frequency change upon different strain conditions. In the experiment, we did 7 tests on the same prototype. Error bars represent standard deviation. **(b).** Resonant frequency change upon different strain conditions. In the experiment, we did one test on 3 different prototypes with same design and same fabrication method. Error bars represent standard deviation. **(c).** Hysteresis test. A prototype was tested from 0% to 50% of strain, leave for 24 hours, then from 50% back to 0%. **(d).** Cyclic stretching test. The sample was stretched to 50% of strain then back to 0% for 240 times. Resonant frequency of the sample was measured 20 times of stretching.

We performed a similar experiment in Figure 5.10 (c); once we reached 50% strain we left the device stretched for 24 hours in the laboratory before we gradually released the device to 0% strain. We also involved the simulation results of resonant frequency upon strain in Figure 5.10 (a) as a comparison with the measurement results. In the simulation, the resonant frequency changed 29 MHz (from 856 MHz to 800 MHz) from 0% to 50% strain, which is smaller than the measurement results.

We fabricated another three prototypes of the same sensor design and again performed strain-resonant-frequency tests. Average value and standard deviation of the resonant frequency for each prototype are shown by Figure 5.10 (b). Figure 5.10 (b) shows similar results than Figure 5.10 (a). Figure 5.10 (d) depicts a cyclic s stretching test to prove the reliability of the proposed sensor when it is stretched 240 times. As shown in the results, resonant frequency of the sensor remains stable in the test (only dropped 2 MHz between 80 and 100 of iteration). We also measured resonant frequency response of a soft RFID sensor due to twist rather than strain and put the results in the supplemental information. As shown in Figure E.3 and Figure E.4, three different twist angles were tested. According to the results, the electrical characteristics of our soft RFID sensor at frequency of operation are highly sensitive to mechanical strain while having no response to twisting.

5.6.5 *Radiation Pattern*

We measured the theoretical reading range from our soft RFID sensor in the H- and E-plane with an antenna measurement system consisting of antenna measurement studio 5.5 and Diamond Engineering. The right subfigure of Figure 5.11 shows that omnidirectional radiation patterns were measured in the H-plane. The left subfigure of Figure 5.11 indicates that the antenna is constrained in directions that are parallel to the sensor's x-axis ($60^\circ + n\pi < \theta < 120^\circ + n\pi$; n is an arbitrary integer). This constraint might have to be considered in certain applications. The different strain

conditions have an impact on our soft RFID sensor's reading range radius; if strain is applied, the reading range radius increases.

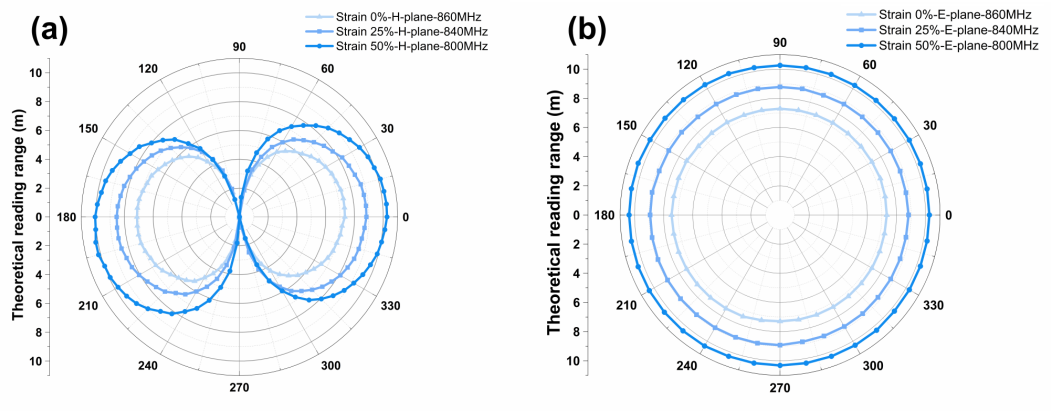

Figure 5.11.: *Theoretical reading range of the antenna in H-plane (left) and E-plane (right)* with 0%, 25% and 50% length stretching in x-direction. The data were recorded for every 5-degree rotation in H-plane and every 10-degree rotation in E-plane.

5.7 DISCUSSION

The results show that our soft RFID sensor changes its resonant frequency and the phase of its backscattered signal as function of strain. Our measurements correlate with our simulations, the initial resonant frequency of all our sensor prototypes lies in the region of 860 MHz. In our simulation, the resonant frequency did not decrease as much under strain as in our experiments. This mismatch could be caused by the simplified model that we used for the Poisson effect or a potentially emerging resistance between the Galinstan channels and the RFID chip that might occur under strain.

We matched the resistances of the RFID chip and the antenna under 0% strain. Once we apply strain, the resistance of the antenna changes, hence the resistances of the RFID chip and antenna do not perfectly match any more. Therefore, we expected a decrease in the measurement reading range with an increase in strain. However, the measurement reading range increased with an increase of strain. One explanation

could be that a folded dipole antenna consists of conductors with opposite current flows; the opposing magnetic fields that are evoked through the currents might cancel each other out. Now, if we stretch the soft antenna, the conductors are being further separated and the magnetic fields might be too far away to interfere with one another enhancing the antenna's radiation efficiency. An increase of the radiation efficiency might outperform an imperfectly matched antenna-RFID chip.

In this study we investigated the resonant frequency response of stretchable soft RFID sensors due to strain. Future work might focus on the design of soft RFID sensors based on phase shift differences that occur in backscattered signals. We also want to increase the initial resonant frequency of our soft RFID sensors to increase the strain range. RFIDs usually operate in the range of 800 MHz to 1 GHz; whereas, currently, our system operates in the 800 MHz - 860 MHz range.

5.8 CONCLUSION

In this chapter I design, fabricate, and characterise a new soft sensor which benefits from a combination of RFID tag design and microfluidic sensor fabrication technologies. I designed this sensor using the working principle of an RFID transporter antenna, but one whose resonant frequency changes in response to an applied strain. This new microfluidic sensor is *intrinsically stretchable* and can be reversibly strained. This sensor is a *passive* and *wireless device* and as such, it does not require a power supply, and is capable of transporting data without a wired connection.

This strain sensor is best understood as an RFID tag antenna; it shows a resonant frequency change from 860 MHz to 800 MHz upon an applied strain change from 0% to 50%. Within the operating frequency, the sensor shows a stand-off reading range of over 7.5 metres (at the resonant frequency). This sensor can withstand repeated mechanical strain whilst retaining electrical functionality, and can return to its original state after stretching. I characterise, experimentally, the electrical

performance and the reliability of the fabrication process. I demonstrate a pneumatic soft robot that has four microfluidic sensors embedded in four of its legs, and I describe the implementation circuit to show that I can obtain movement information from the soft robot using our wireless soft sensors. With the fully integrated soft sensors, the pneumatic actuators in the soft robot can get instant deformation feedbacks. The feedbacks are conducive to precise control of the actuation system.

In comparison to other existing stretchable sensors, the sensor I present in this chapter is a completely passive and wireless device. This RFID sensor can be embedded into soft robots without requiring any power consumption from the original robotic device. The feature of wireless power extends the lifetime of the device, removing the need for changing batteries, or integrating an energy harvesting system. Additionally, most of the existing soft sensors have a requirement to be hardwired to power supplies or to signal-processing equipment. This dependence on electrical tethers limits the practical use of soft sensors in many promising applications in real-world conditions. Also, most of existing gallium-based liquid alloy sensors were designed based on measuring the resistance change of the liquid metal, but the long-time stability of these sensors will be affected by the oxidation of gallium (gallium-based liquid alloy is easily oxidized). The RFID strain sensor I propose here was designed based on resonant frequency change upon strain. Benefiting from the high electrical conductivity of Galinstan, the skin depth (a measure of how closely electric current flows along the surface of a material) of Galinstan under 800 MHz - 865 MHz is only a few micrometres. Even though the Galinstan in the channels has a thin oxide layer at the surface, the oxide won't have a large effect on the resonant frequency of the sensor.

6

INTEGRATING ELECTRONIC SYSTEMS ON A SOFT PRINTED CIRCUIT BOARD

6.1 INTRODUCTION

In Chapter 4 and Chapter 5, I introduce the soft sensor and soft antenna I designed and fabricated. Besides these intrinsically soft electronic components, I also studied on developing soft printed circuit boards (PCBs). In this chapter, I present a method of integrating small-size surface mount electronic components into a soft printed circuit board with liquid metal microfluidic traces and soft elastomer PCB substrates.

Soft-matter circuits that can sustain large amounts of bending, stretching, and other modes of deformation are desired in a wide range of cutting-edge applications, such as wearable computing and soft robotics. Although current research on soft-electronic components is booming, existing soft electronic components are far less functional, condensed, and cost-effective than solid-state current electronic components. An ideal soft circuit board should be constitutive of substrate, tracks, and electronic components which are all purely soft. However, due to the limitation of current soft electronic components, currently this research field is far from achieving the ideal soft printed circuit boards.

The current printed circuit boards consist of stiff substrate material (such as FR4, a composite material composed of woven fibreglass cloth with an epoxy resin binder) and solid metal tracks (such as copper). These non-bendable and non-stretchable composites are the principal components of a conventional printed circuit board, so they primarily limit the flexibility and stretchability of the board. If we use flexible

and stretchable substrate materials instead of FR4, replace copper tracks with liquid metal tracks, and choose small-size surface mount electronic components and IC chips in PCB fabrication, the resulting circuit boards will have a certain degree of flexibility and stretchability.

In Chapters 4 and 5, the method I used to produce soft electronic components is to first make micro-channels using soft-lithography, and then fill liquid metal into the channels. Since this method requires two ports at both ends of the channel (one for injection and one for vent), components produced with this method require a special channel design. It is difficult to connect the solid-state surface mount resistors, capacitors and IC chips to the liquid metal channels by using positive pressure injection while preventing liquid metal from leaking during the injection process. Therefore, I need to study new fabrication methods to make soft printed circuit boards.

To create functional soft and stretchable electronics, I need to achieve scalable fabrication approaches and effective electromechanical interfaces between liquid metal traces and microelectronics. To date, researchers have presented many methods for EGaIn and Galinstan circuit fabrication, including direct-writing (Wang et al. [2015], Gannarapu and Gozen [2016]), injection (Park et al. [2010], Fassler and Majidi [2013]), ink-jet printing (Li et al. [2016]), laser patterning (Lu et al. [2014]), contact printing (Tabatabai et al. [2013]), imprinting (Gozen et al. [2014]), selective wetting (Kim et al. [2017]). Screening printing (Jeong et al. [2012]), spray printing (Jeong et al. [2015]). And reductive patterning (Khan et al. [2016]).

In 2018, Ozutemiz *et al.* presented a unique approach to interface liquid metal with IC chips and other microelectronic components by using HCl-vapour assistance to "solder" the metal pins of the surface-mount microelectronic devices (SMD) with EGaIn interconnects on a soft elastomer substrate (Ozutemiz et al. [2018]). In their work, the LM circuits were produced based on the selectively wetting property of EGaIn. Ga-based alloys, including EGaIn and Galinstan, selectively wet to metals, such as copper (Wissman et al. [2017], Tang et al. [2017]) and gold (Hirsch et al. [2016], Jeong et al. [2017]), rather than soft elastomer substrates.

I reproduced and made some adjustments to the method Ozutemiz *et al.* proposed for soft PCBs fabrication in my workspace (Scottish Microelectronics Centre). This chapter describes the equipment and fabrication process I used to produce a soft PCB in SMC and demonstrates a novel seven-segment display system that I manufactured with this fabrication method.

6.2 MATERIALS AND METHODS

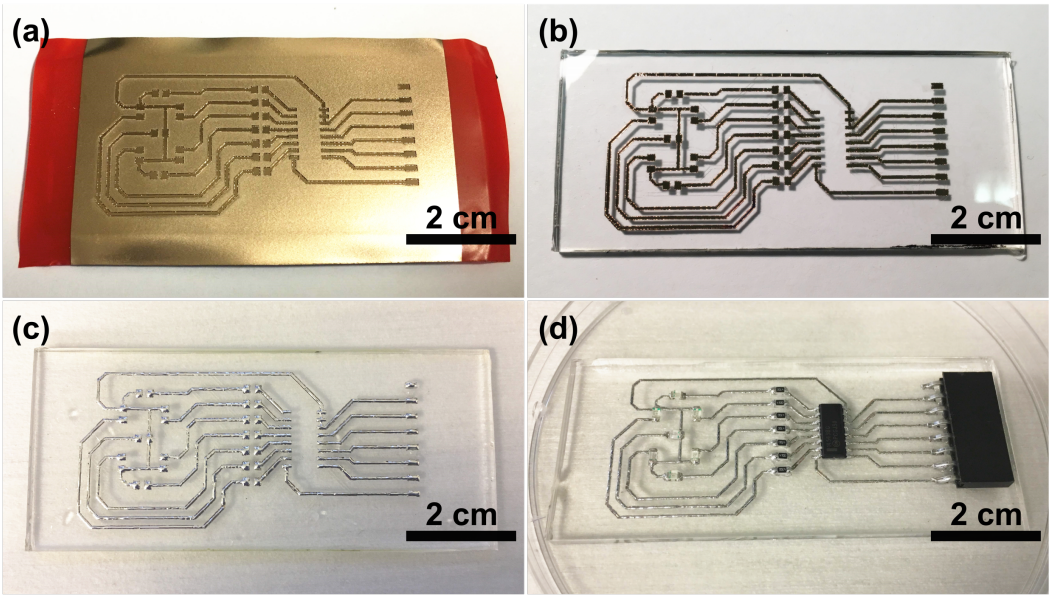

Figure 6.1.: Fabrication process of a soft printed circuit board: **(a).** A vinyl mask is applied on a 2 mm-thick PDMS substate. A Cu layer is sputter deposited on the PDMS substrate with a Cr adhesion layer. **(b).** The vinyl mask is removed and resulted the patterned circuit geometry. **(c).** Galinstan was applied on the PDMS substrate inside a 3% NaOH bath and selectively wets on the copper traces. **(d).** Microelectronics components are placed on designated locations. Then HCl vapour is applied to the components to "solder" the component pins and the liquid metal. Finally the circuit is sealed by curing another layer of PDMS on the surface.

In Figure 6.1, I outline the steps for the fabrication of soft and stretchable circuits composed of LM traces and packaged microelectronics embedded in PDMS. Figure 6.1 (a) shows I applied a vinyl mask on a piece of 2 mm-thick PDMS, then deposit 20 μm Tin and 200 μm Copper on the PDMS substrate with an OPT Plasma Lab 400 system in

the cleanroom of SMC. The 20 μm Chromium here is an adhesion layer between Cu and PDMS. In Section 3.3 I introduced how I fabricated the vinyl mask. Figure 6.1 (b) shows the resulting PDMS substrate with desired circuit geometry after I peeled off the vinyl mask.

I deposited liquid metal Galinstan to the Cu wetting layer while immersing the PDMS substrate in to 3% NaOH bath and applying Galinstan inside the bath. Then I immersed the PDMS substrate into DI water to remove the NaOH solution that remains on the PDMS surface. Figure 6.1 (c) shows a photo of the resulted Galinstan traces geometry. The QR code here links to a video I took when applying Galinstan on a PCB with FR4 substrate in a 3% NaOH bath.

QRcode 6.1.: Galinstan selectively wets to copper.

Figure 6.1 (d) shows photograph of the completed soft circuit board. First, I placed the microelectronics components on designated locations. Then, I applied HCl vapour to the components for one second (at a speed of ~10 ml per second) to "solder" the component pins and the liquid metal. HCl vapour can immediately remove the thin gallium oxidation film of Galinstan so that improves electrical connection between the component pins and the liquid metal traces. Figure 6.2 shows the interface between a component pin and a Galinstan trace before and after HCl vapour treatment. Before HCl treatment, the component pin only *touches* oxidation film of the LM. Electrical connection at the LM-component interface is not stable due to the high surface tension of the semi-conductive oxidation film. During HCl treatment, LM wraps the component pin and forms a robust electrical connection since the HCl vapour removes the oxidation film instantly. After HCl treatment, new gallium oxidation film forms and helps LM and components stay in the right place.

Finally, I immersed the circuit in DI water to remove HCl that remains on the surface and then dried the device on a hot plate at 50 °C for 10 minutes. I sealed the circuit by curing another layer of PDMS on top of the surface. Due to the high surface

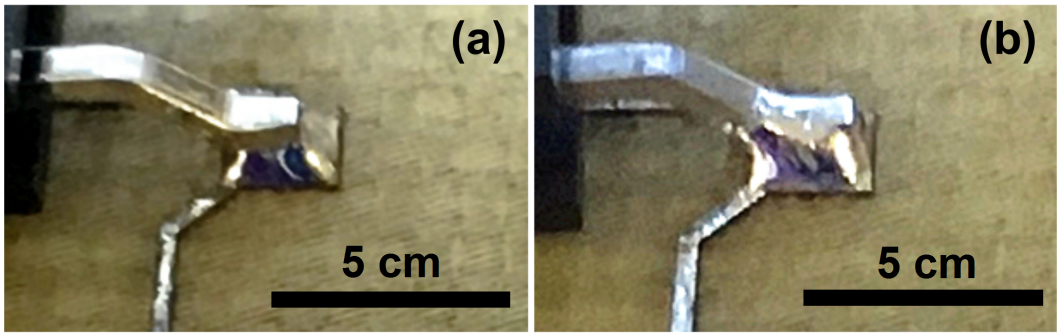

Figure 6.2.: *Effect of HCl treatment on contact interface.* The interface between a component pin and a Galinstan trace **(a).** before and **(b).** after HCl vapour treatment

tension of Galinstan, gently putting the device into DI water and pouring uncured PDMS on the surface will not move the components and traces on it.

Ozutemiz et. al (Ozutemiz et al. [2018]) reported that without HCl treatment, it is difficult to achieve robust LM-component interfaces (in the their test, 9 of 20 samples did not work). With HCl treatment, LM-component interfaces of the 20 samples become conductive immediately and maintain a stable contact resistance at $\sim$50 mΩ, with nearly no variability over 10 days. In strain limit test, the LM-component interfaces maintain conductivity when the strain is under 80%. When loaded to beyond 80%, the loss of conductivity is primarily caused by mechanical failure due to tearing occurs at the LM-component interface, rather than electrical failure of the LM leads or LM-pin connections. In cyclic loading test, three HCl treated samples completed 2000-cycle test between 5 and 40% strain without failure while three nontreated samples all failed within the first 20 cycles.

6.3 CIRCUIT AND IMPLEMENTATION

Figure 6.3 shows the schematic diagram of a soft seven-segment display system. This system mainly contains seven ultra-violet (UV) LEDs with 395 nm peak wavelength and a Binary-Coded Decimal (BCD) to seven segment decoder (MC14543B). Figure 6.4 shows photograph of this display system. With a CNC milling machine, I

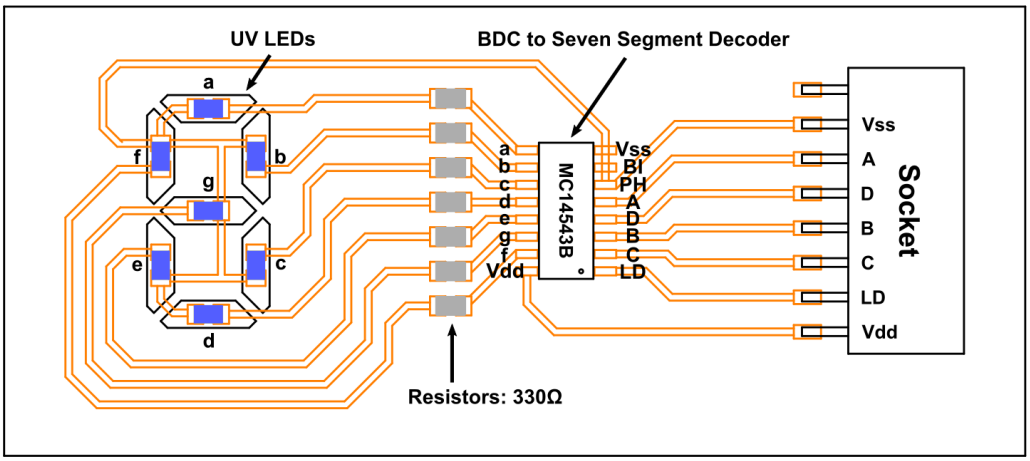

Figure 6.3.: *Schematic diagram of a soft seven-segment display system.* This system mainly contains seven ultra-violet (UV) LEDs and a BCD to seven segment decoder (MC14543B).

made an acrylic master with seven segment structures. Then I mixed PDMS with UV activated luminescent paint, cured it in the acrylic master, and bonded the UV-PDMS segments on top of the corresponding seven UV LEDs. These flexible and stretchable UV-PDMS segments illuminate under UV light, so that change the light source from LED spots to stretchable strips. Therefore, the numbers illustrated on the seven-segment display system are clear and deformable. The QR code here links to a video that demonstrates performance of the soft 7-segment display system.

QRcode 6.2.: Soft seven-segment display system

6.4 DISCUSSION

Using vinyl as the mask in soft printed circuit board (SPCB) fabrication process is a rapid and cost-effective method. Comparing with non-adhesive mask materials (such as thin acetate films), adhesive vinyl can stick on the surface of PDMS during the metal depositing process. The deposited metal is impossible to be sputtered between

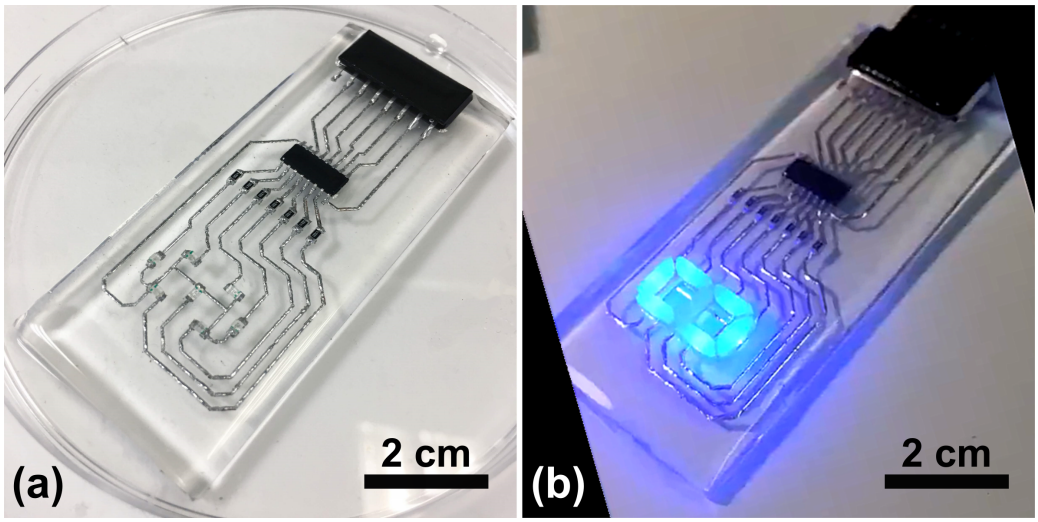

Figure 6.4.: *Photograph of a soft seven-segment display system.* **(a).** The system consists of a socket, a BCD to seven segment decoder, surface mount resistors, and seven UV LEDs. **(b).** PDMS strips mixed with UV paint were bonded on top of the UV LEDs.

mask and PDMS substrate, therefore vinyl mask gives us metal traces with clear edges. The adhesion between the sputtered copper and the PDMS substrate is week, so we need an adhesive layer between copper and PDMS to keep the copper traces in place during the fabrication process. This adhesive layer can be chromium and tin.

Ozutemiz et. al reported that the reason to use the 3% NaOH bath is to reduce oxide that forms on top of the copper wetting layer, and remove the oxide skin on the liquid metal surface, thus exposing the bulk EGaIn or Galinstan to copper. During the fabrication process, I found the NaOH solution has the ability to keep PDMS surface clean. If I do not apply Galinstan to the copper wetting layer in the NaOH bath, Galinstan will not only wet to copper but also leave residual on the surface of PDMS. I also found that when the Galinstan wetting step is done, if I do not move the substrate out of the NaOH bath in time, the Galinstan and the copper will gradually delaminate from the PDMS substrate, then the circuit pattern "disappear" in the end. Therefore, when using this SPCB fabrication method manually, it would be better to apply Galinstan to the wetting layer as quick as possible and then immerse the PDMS substrate into DI water immediately to remove the NaOH solution.

HCl-vapour treatment is crucial in this SPCB fabrication process since it tremendously improve the electromechanical interface between component pins and LM interconnects. After HCl-vapour treatment, it is also important to immerse the PDMS substrate into DI water to remove te HCl vapour residual on the surface.

6.5 CONCLUSION

In this chapter I introduced a method to manufacture fully functional stretchable electronic circuits. In the fabrication process, I used HCl vapour treatment to enhance the electromechanical interfacing of liquid metal interconnects with IC chips and other microelectronics. With this SPCB fabrication method, I demonstrated a soft seven-segment display system with UV LEDs. I included a video to show that this soft display system remains functional under mechanical deformation.

Compared with the pin-Galinstan interfaces without HCl vapour treatment, the fabrication method introduced in this chapter can obviously improve electrical connection of the interfaces. New oxidation films form after the HCl treatment can protect the interfaces between the pins and the Galinstan traces when the devices is under strain. Even so, the mechanical mismatch between the soft materials and the conventional packaged microelectronics still exists. This mismatch limits the stretchability of the SPCBs. However, currently, hard-packaged electronic components are far more functional than soft electronic components. In this condition, the SPCB fabrication method presented in this chapter is crucial in the transition process from hard to soft electronics. This method can accelerate the development of many cutting-edge research fields such as soft robotics and wearable devices.

Currently the fabrication method is limited to single layer circuit layouts. Due to the use of HCl vapour during the fabrication process, packaged components that can not sustain corrosive vapours in short term should not be used. In future work, we could consider using Galinstan or other stretchable conductive materials to make vias for the PCBs.With stretchable vias, we should be able to make double-sided SPCBs.

7

CONCLUSION AND FUTURE DIRECTIONS

In summary, the aim of my Ph.D research is to develop soft electronic circuit components and to develop the methods to integrate electronics into soft systems. The development was step-wise, (i) starting with those objectives which are related to the fundamental fabrication technologies, such as soft-lithography master fabrication and soft encapsulation for conventional IC chips. (ii) Then the development moved to design and fabrication of flexible and stretchable soft electronic circuit components, such as sensors and antennas. (iii) The final development was making integrated soft electronic systems with the developed soft electronic components. Main findings of this work include:

7.1 VINYL SOFT-LITHOGRAPHY MASTERS

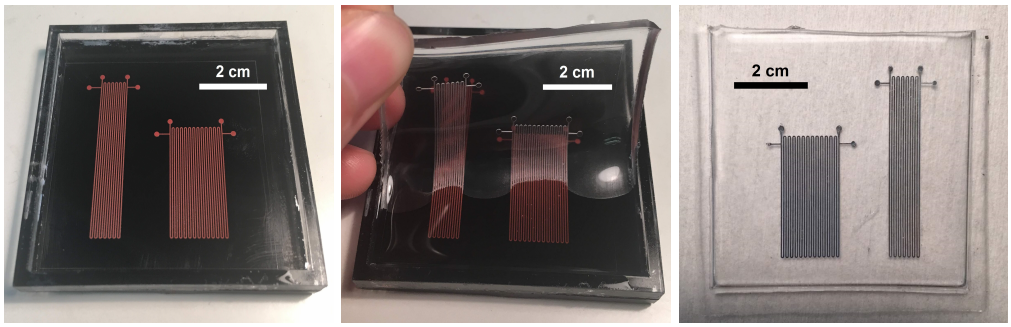

(a) (b) (c)

Figure 7.1.: *Soft sensors and soft-lithography masters.* **(a-b).** A soft-lithography master that I made with vinyl and acrylic substrate for patterning PDMS. **(c).** The resulting microfluidic device fabricated with this vinyl master.

In Chapter 3, I introduce the development of a rapid-prototyping technique for soft-lithography masters using laser-cutting systems and self-adhesive materials, as shown in Figure 7.1 (a-b). With this type of soft-lithography masters I can fabricate Galinstan-based soft sensors, as shown in Figure 7.1 (c).

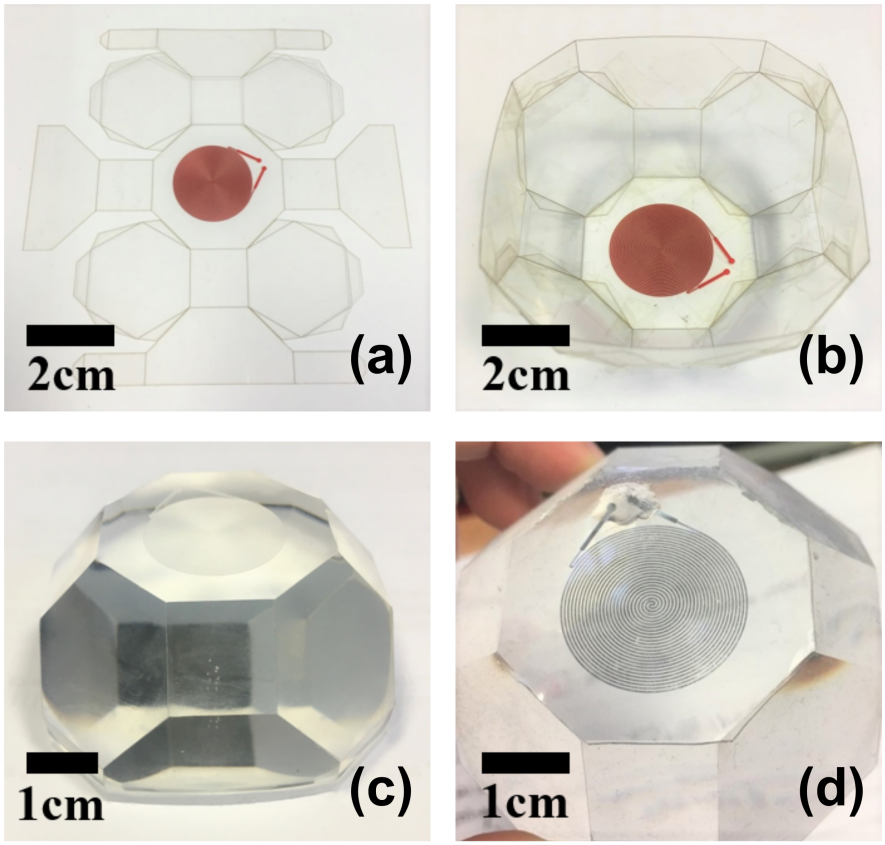

Figure 7.2.: *Fabrication of PDMS half semi-sphere with integrated liquid metal sensor.* **(a).** I used a laser system to cut and half cut the acetate film to give it an origami design. **(b).** I made a soft-lithography master with 3D structure by folding up the acetate film. **(c-d).** PDMS semi-sphere with liquid metal pressure sensor on its surface cured in this acetate master.

The advantage of this master fabrication method is that the production time is short and the price of consumable materials is low. This method saved me huge amount of time fabricating the soft electronic circuits and components that I designed. The disadvantage of this method is that it is not suitable to deal with channel-with less than 100 μm and the usage count of each master is limited. Therefore, this master fabrication method is excellent for laboratory research but not suitable for industrial

production. To further reduce size of the soft electronic devices I designed, we have to use master fabrication methods with higher resolution, such as photolithography.

Future work directions: The vinyl soft-lithography master fabrication method can work on many different substrate materials, such as: silicon wafer, copper, and acetate. Figure 7.2 (a-b) shows a 3D-structured half semi-sphere soft-lithography master I made with acetate (a plastic sheet) as substrate. Figure 7.2 (c-d) shows the resulting PDMS semi-sphere with liquid metal sensor on it. This sensing device holds potential in many research areas. For instance, enough duplicates of this device can form semi-spheres with pressure sensors on their surfaces, these semi-spheres can be a solution of force distribution problem of granular materials in civil engineering.

7.2 INTEGRATED PRESSURE-SENSOR SOFT SYSTEM

In Chapter 4, I present the development of a high resolution pressure-sensor soft system that can transduce normal force into a digital output, using elastic silicone materials and a conductive eutectic liquid alloy, as shown in Figure 7.3. In this system, I integrated a microfluidic soft pressure sensor with a flexible printed circuit board, and used conductive thread as the interconnect to alleviate electrical connection problems arising due to the mechanical mismatch between conventional metal wires and soft or liquid materials.Teng et al. [2018a]

By using conductive thread connection we can design systems which overcome the bulk-mechanical mismatches between soft biological systems and hard engineered components and develop fully integrated soft machines, which include power, communications, and control sub-systems. By enabling strong-and-stable electrical connections I hope to enable the community to be one-step-closer to developing fully integrated soft robotic, or wearable systems. I anticipate that integrated systems of this type will find utility in soft-robotic systems as used for wearable technologies like virtual reality, or in soft-medical devices such as exoskeletal rehabilitation robots.

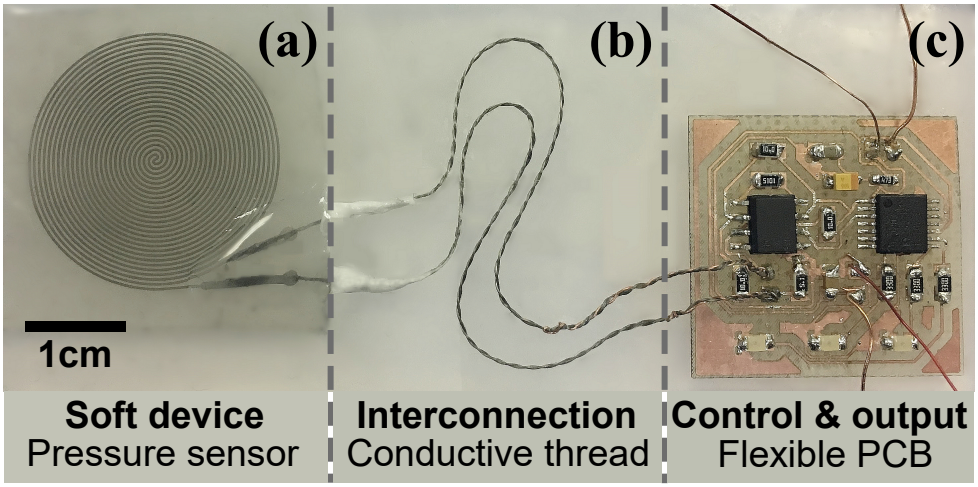

Figure 7.3.: *Top view of the integrated soft pressure sensing system.* **(a).** Normal-force pressure sensor made with a Galinstan-filled microfluidic-channel encapsulated in an Ecoflex substrate. **(b).** Conductive thread is used as interconnection between the pressure sensor and the flexible PCB. The serpentine shape provides strain-relief. **(c).** A flexible PCB consisting of hard electronic components, including a bridge circuit, an amplifier, a microcontroller, and LEDs.

Future work directions: This soft pressure-sensor system is an early work in my Ph.D study. The Galinstan pressure sensor and the flexible printed circuit board are actually two separated parts and they need to be connected with conductive thread. In the future work, we could consider how to combine the fabrication method of the soft sensors and the production method of soft printed circuit board that I introduced in Chapter 6 to directly integrate the soft sensor into the SPCB.

7.3 WIRELESS SOFT STRAIN SENSOR

In Chapter 5, I introduce the development of a new wireless soft sensor, which benefits from a combination of radio-frequency identification (RFID) tag design and microfluidic sensor fabrication technologies, as shown in Figure 7.4. This new microfluidic sensor is intrinsically stretchable and can be reversibly strained. Teng et al. [2018b]

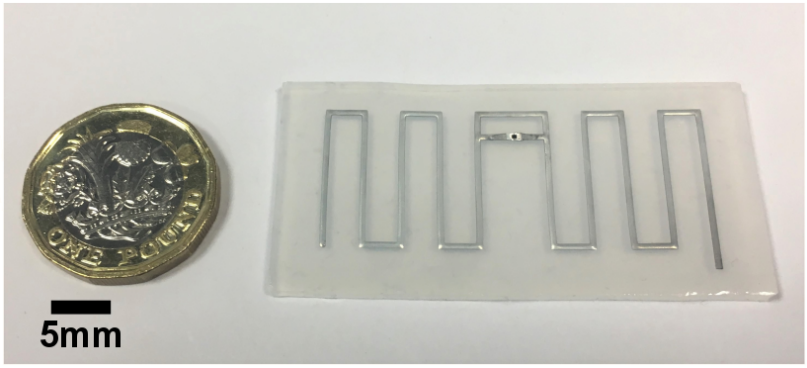

Figure 7.4.: Photograph of the stretchable microfluidic sensor (RFID tag antenna).

In comparison to other existing stretchable sensors, the sensor I presented is a completely passive and wireless device. This RFID sensor can be embedded into soft robots without requiring any power consumption from the original robotic device. Most of the existing soft sensors have a requirement to be hardwired to power supplies or to signal-processing equipment. This dependence on electrical tethers limits the practical use of soft sensors in many promising applications in real-world conditions. The feature of wireless power extends the lifetime of the soft sensor I present, removing the need for changing batteries, or integrating an energy harvesting system.

Although the RFID soft strain sensor has many advantages benefit from working wirelessly, compared with many resistance-based soft sensors that need wire connections, the wireless RFID sensor needs more complicated and more expensive electronic system to receive signals from the sensor. In addition, the wireless sensor is essentially a configurable RFID tag antenna. Except strain, resonant frequency of this antenna will also be affected by permittivity of the substrate material and water in the environment. Therefore, this RFID sensor is not suitable to be applied on skin and organs, not suitable for hydraulic actuated soft robots, or other underwater applications.

Future work directions: Currently, the sensors operate in the range of 800 MHz - 860 MHz. Future work might focus on the design of soft RFID sensors based on phase shift differences that occur in backscattered signals, and increase the initial resonant

frequency of the soft RFID sensors to increase the strain range (RFIDs usually operate in the range of 800 MHz to 1 GHz). Additionally, in Chapter 5 I provide a schematic diagram of the soft RFID sensor implementation, as shown in Figure 7.5. The implementation comprises a pneumatic soft robot with four embedded soft RFID tags, one tag on each robot leg, and the electronic circuitry to transceiver data. Future work could focus on realising this conceptual electronic system and utilise the system in soft robotic applications.

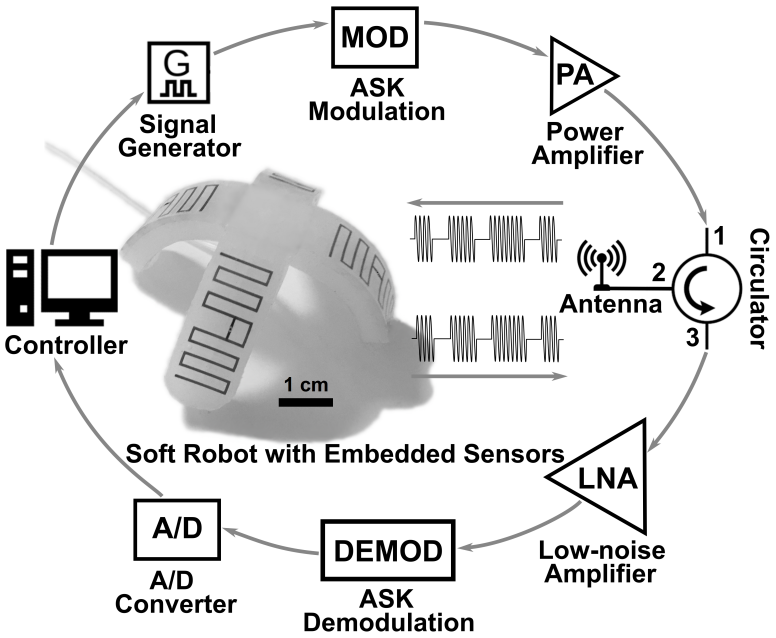

Figure 7.5.: *The electronic system for measuring data from a pneumatic soft robot that contains four embedded microfluidic strain sensors.*

7.4 SOFT PRINTED CIRCUIT BOARD

In chapter 6 I introduced the development of a method to manufacture fully functional stretchable printed circuit board. In the fabrication process, I used HCl vapour treatment to enhance the electromechanical interfacing of liquid metal interconnects with IC chips and other microelectronics. Compared with the pin-Galinstan interfaces without HCl vapour treatment, the fabrication method introduced in this chapter can

obviously improve electrical connection of the interfaces. New oxidation films form after the HCl treatment can protect the interfaces between the pins and the Galinstan traces when the devices is under strain. Even so, the mechanical mismatch between the soft materials and the conventional packaged microelectronics still exists. This mismatch limits the stretchability of the SPCBs. However, currently, hard-packaged electronic components are far more functional than soft electronic components. In this condition, the SPCB fabrication method presented in this chapter is crucial in the transition process from hard to soft electronics. This method can accelerate the development of many cutting-edge research fields such as soft robotics and wearable devices.With this SPCB fabrication method, I demonstrated a soft seven-segment display system with UV LEDs, as shown in Figure 7.6.

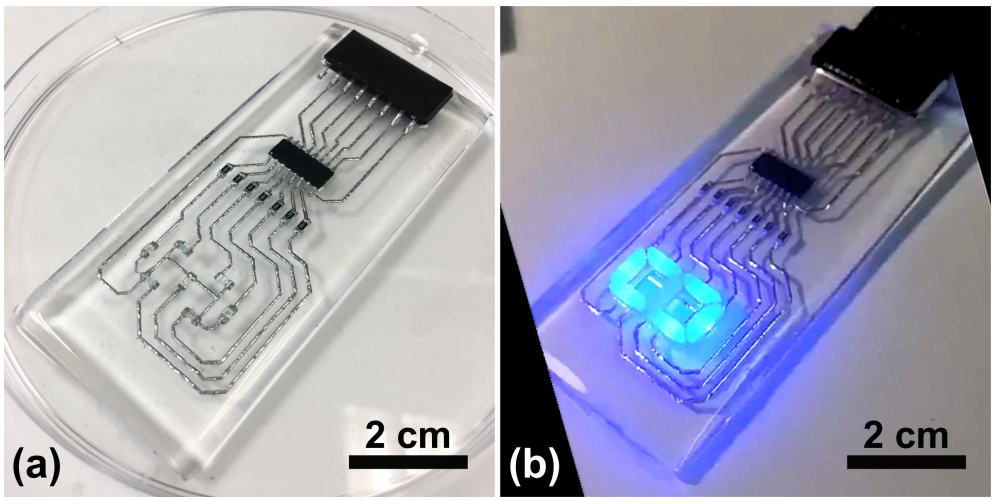

Figure 7.6.: *Photograph of a soft seven-segment display system.* **(a).** The system consists of a socket, a BCD to seven segment decoder, surface mount resistors, and seven UV LEDs. **(b).** PDMS strips mixed with UV paint were bonded on top of the UV LEDs.

Future work directions: Currently the fabrication method is limited to single layer circuit layouts. Due to the use of HCl vapour during the fabrication process, packaged components that can not sustain corrosive vapours in short term should not be used. In future work, we could consider using Galinstan or other stretchable conductive materials to make vias for the PCBs.With stretchable vias, we should be able to make double-sided SPCBs.

REFERENCES

B. Aïssa, M. Nedil, M. A. Habib, E. Haddad, W. Jamroz, D. Therriault, Y. Coulibaly, and F. Rosei. Fluidic patch antenna based on liquid metal alloy/single-wall carbon-nanotubes operating at the S-band frequency. *Applied Physics Letters*, 2013. (Cited on page 36.)

A. Alspach, J. Kim, and K. Yamane. Design of a soft upper body robot for physical human-robot interaction. In *IEEE-RAS International Conference on Humanoid Robots*, 2015. (Cited on page 81.)

A. Anderson, Y. Menguc, R. J. Wood, and D. Newman. Development of the polipo pressure sensing system for dynamic space-suited motion. *IEEE Sensors Journal*, 2015. (Cited on page 39.)

Y. Bahramzadeh and M. Shahinpoor. A review of ionic polymeric soft actuators and sensors. *Soft Robotics*, 2014. (Cited on page 16.)

C. R. Baker, K. Armijo, S. Belka, M. Benhabib, V. Bhargava, N. Burkhart, A. Der Minassians, G. Dervisoglu, L. Gutnik, M. B. Haick, C. Ho, M. Koplow, J. Mangold, S. Robinson, M. Rosa, M. Schwartz, C. Sims, H. Stoffregen, A. Waterbury, E. S. Leland, T. Pering, and P. K. Wright. Wireless sensor networks for home health care. In *Proceedings - 21st International Conference on Advanced Information Networking and Applications Workshops*, 2007. (Cited on page 18.)

A. J. Bandodkar and J. Wang. Non-invasive wearable electrochemical sensors: a review. *Trends in Biotechnology*, 2014. (Cited on page 17.)

R. Bansal. Antenna theory. *IEEE Antennas and Propagation Society Newsletter*, 2013. (Cited on page 88.)

N. W. Bartlett, M. T. Tolley, J. T. B. Overvelde, J. C. Weaver, B. Mosadegh, K. Bertoldi, G. M. Whitesides, and R. J. Wood. A 3D-printed, functionally graded soft robot powered by combustion. *Science*, 2015. (Cited on page 16.)

L. R. Bernstein. Mechanisms of therapeutic activity for gallium. *Pharmacological reviews*, 1998. (Cited on page 45.)

M. K. Blees, A. W. Barnard, P. A. Rose, S. P. Roberts, K. L. McGill, P. Y. Huang, A. R. Ruyack, J. W. Kevek, B. Kobrin, D. A. Muller, and P. L. McEuen. Graphene kirigami. *Nature*, 2015. (Cited on page 25.)

D. Bloor, K. Donnelly, P. J. Hands, P. Laughlin, and D. Lussey. A metal-polymer composite with unusual properties. *Journal of Physics D: Applied Physics*, 2005. (Cited on page 27.)

P. J. Brigandi, J. M. Cogen, and R. A. Pearson. Electrically conductive multiphase polymer blend carbon-based composites, 2014. (Cited on pages xv, 25, 26, and 27.)

T. P. Brody. The Thin Film Transistor—A Late Flowering Bloom. *IEEE Transactions on Electron Devices*, 1984. (Cited on page 22.)

D. Brosteaux, F. Axisa, M. Gonzalez, and J. Vanfleteren. Design and fabrication of elastic interconnections for stretchable electronic circuits. *IEEE Electron Device Letters*, 2007. (Cited on page 24.)

M. Calisti, F. Corucci, A. Arienti, and C. Laschi. Dynamics of underwater legged locomotion: Modeling and experiments on an octopus-inspired robot. *Bioinspiration and Biomimetics*, 2015. (Cited on page 42.)

C. Chao, X. Jin, L. Teng, A. A. Stokes, and X. Fan. Bubble dislodgment in a capillary network with microscopic multi-channel and multi-bifurcation features. *Langmuir*, 2019. (Cited on page 60.)

B. Chen, J. J. Lu, C. H. Yang, J. H. Yang, J. Zhou, Y. M. Chen, and Z. Suo. Highly stretchable and transparent ionogels as nonvolatile conductors for dielectric elastomer transducers. *ACS Applied Materials and Interfaces*, 2014. (Cited on pages 29 and 31.)

G. Chen, N. Matsuhisa, Z. Liu, D. Qi, P. Cai, Y. Jiang, C. Wan, Y. Cui, W. R. Leow, Z. Liu, S. Gong, K. Q. Zhang, Y. Cheng, and X. Chen. Plasticizing Silk Protein for On-Skin Stretchable Electrodes. *Advanced Materials*, 2018. (Cited on page 29.)

A. Cheng, S.and Rydberg, K. Hjort, and Z. Wu. Liquid metal stretchable unbalanced loop antenna. *Applied Physics Letters*, 2009. (Cited on pages 35 and 36.)

Y. N. Cheung, Y. Zhu, C. H. Cheng, C. Chao, and W. W. F. Leung. A novel fluidic strain sensor for large strain measurement. *Sensors and Actuators, A: Physical*, 2008. (Cited on page 24.)

M. S. Cho, H. J. Seo, J. D. Nam, H. R. Choi, J. C. Koo, and Y. Lee. An electroactive conducting polymer actuator based on NBR/RTIL solid polymer electrolyte. *Smart Materials and Structures*, 2007. (Cited on page 16.)

B. Choi, J. Lee, J. Lee, and K. Park. Distributed Sensor Network Based on RFID System for Localization of Multiple Mobile Agents. *Wireless Sensor Network*, 2011. (Cited on page 82.)

J. Choi, D. Kang, S. Han, S. B. Kim, and J. A. Rogers. Thin, Soft, Skin-Mounted Microfluidic Networks with Capillary Bursting Valves for Chrono-Sampling of Sweat. *Advanced Healthcare Materials*, 2017a. (Cited on page 41.)

J. Choi, Y. Xue, W. Xia, T. R. Ray, J. T. Reeder, A. J. Bandodkar, D. Kang, S. Xu, Y. Huang, and J. A. Rogers. Soft, skin-mounted microfluidic systems for measuring secretory fluidic pressures generated at the surface of the skin by eccrine sweat glands. *Lab on a Chip*, 2017b. (Cited on page 41.)

J. B. Chossat, Y. L. Park, R. J. Wood, and V. Duchaine. A soft strain sensor based on ionic and metal liquids. *IEEE Sensors Journal*, 2013. (Cited on pages 29 and 70.)

K. Y. Chun, Y. Oh, J. Rho, J. H. Ahn, Y. J. Kim, H. R. Choi, and S. Baik. Highly conductive, printable and stretchable composite films of carbon nanotubes and silver. *Nature Nanotechnology*, 2010. (Cited on page 25.)

R. L. Crabb and F. C. Treble. Thin silicon solar cells for large flexible arrays. *Nature*, 1967. (Cited on page 22.)

C. Dagdeviren, B. D. Yang, Y. Su, P. L. Tran, P. Joe, E. Anderson, J. Xia, V. Doraiswamy, B. Dehdashti, X. Feng, B. Lu, R. Poston, Z. Khalpey, R. Ghaffari, Y. Huang, M. J. Slepian, and J. A. Rogers. Conformal piezoelectric energy harvesting and storage from motions of the heart, lung, and diaphragm. *Proceedings of the National Academy of Sciences*, 2014. (Cited on pages 22 and 23.)

M. D. Dickey. Stretchable and Soft Electronics using Liquid Metals, 2017. (Cited on pages 24, 31, 34, and 37.)

M. D. Dickey, R. C. Chiechi, R. J. Larsen, E. A. Weiss, D. A. Weitz, and G. M. Whitesides. Eutectic Gallium-Indium (EGaIn): A Liquid Metal Alloy for the Formation of Stable Structures in Microchannels at Room Temperature. *Advanced Functional Materials*, 2008. (Cited on pages 32, 45, and 46.)

S. Ding, J. Jiu, Y. Gao, Y. Tian, T. Araki, T. Sugahara, S. Nagao, M. Nogi, H. Koga, K. Suganuma, and H. Uchida. One-Step Fabrication of Stretchable Copper Nanowire Conductors by a Fast Photonic Sintering Technique and Its Application in Wearable Devices. *ACS Applied Materials and Interfaces*, 2016. (Cited on page 25.)

B. Dufour, P. Rannou, D. Djurado, H. Janeczek, M. Zagorska, A. De Geyer, J. P. Travers, and A. Pron. Low Tg, stretchable polyaniline of metallic-type conductivity: Role of dopant engineering in the control of polymer supramolecular organization and in the tuning of its properties. *Chemistry of Materials*, 2003. (Cited on pages 30 and 31.)

J. A. Fan, W. H. Yeo, Y. Su, Y. Hattori, W. Lee, S. Y. Jung, Y. Zhang, Z. Liu, H. Cheng, L. Falgout, M. Bajema, T. Coleman, D. Gregoire, R. J. Larsen, Y. Huang, and J. A. Rogers. Fractal design concepts for stretchable electronics. *Nature Communications*, 2014. (Cited on page 25.)

A. Fassler and C. Majidi. Soft-matter capacitors and inductors for hyperelastic strain sensing and stretchable electronics. *Smart Materials and Structures*, 2013. (Cited on pages 35, 36, and 104.)

S. Felton, M. Tolley, E. Demaine, D. Rus, and R. J. Wood. A method for building self-folding machines. *Science*, 2014. (Cited on pages 22 and 23.)

A. D. Franklin. Nanomaterials in transistors: From high-performance to thin-film applications, 2015. (Cited on page 23.)

A. Gannarapu and B. A. Gozen. Freeze-Printing of Liquid Metal Alloys for Manufacturing of 3D, Conductive, and Flexible Networks. *Advanced Materials Technologies*, 2016. (Cited on page 104.)

W. Gao, S. Emaminejad, H. Y. Y. Nyein, S. Challa, K. Chen, A. Peck, H. M. Fahad, H. Ota, H. Shiraki, D. Kiriya, D. H. Lien, G. A. Brooks, R. W. Daivs, and A. Javey. Fully integrated wearable sensor arrays for multiplexed in situ perspiration analysis. *Nature*, 2016a. (Cited on page 19.)

W. Gao, S. Emaminejad, H. Y. Y. Nyein, S. Challa, K. Chen, A. Peck, H. M. Fahad, H. Ota, H. Shiraki, D. Kiriya, D. H. Lien, G. A. Brooks, R. W. Davis, and A. Javey. Fully integrated wearable sensor arrays for multiplexed in situ perspiration analysis. *Nature*, 2016b. (Cited on pages 17 and 18.)

W. Gao, H. Y. Y. Nyein, Z. Shahpar, H. M. Fahad, K. Chen, S. Emaminejad, Y. Gao, L. C. Tai, H. Ota, E. Wu, J. Bullock, Y. Zeng, D. H. Lien, and Ali. Javey. Wearable Microsensor Array for Multiplexed Heavy Metal Monitoring of Body Fluids. *ACS Sensors*, 2016c. (Cited on page 19.)

José Luis Giordano. On the sensitivity, precision and resolution in DC Wheatstone bridges. *European Journal of Physics*, 1997. (Cited on page 70.)

H. Godaba, J. Li, Y. Wang, and J. Zhu. A Soft Jellyfish Robot Driven by a Dielectric Elastomer Actuator. *IEEE Robotics and Automation Letters*, 2016. (Cited on page 16.)

P. Gou, N. D. Kraut, I. M. Feigel, H. Bai, G. J. Morgan, Y. Chen, Y. Tang, K. Bocan, J. Stachel, L. Berger, M. Mickle, E. SejdiĆ, and A. Star. Carbon nanotube chemiresistor for wireless pH sensing. *Scientific Reports*, 2014. (Cited on page 23.)

B. A. Gozen, A. Tabatabai, O. B. Ozdoganlar, and C. Majidi. High-density soft-matter electronics with micron-scale line width. *Advanced Materials*, 2014. (Cited on page 104.)

D. S. Gray, J. Tien, and C. S. Chen. High-Conductivity Elastomeric Electronics. *Advanced Materials*, 2004. (Cited on page 24.)

C. F. Guo, T. Sun, Q. Liu, Z. Suo, and Z. Ren. Highly stretchable and transparent nanomesh electrodes made by grain boundary lithography. *Nature Communications*, 2014. (Cited on page 24.)

N. Hallfors, A. Khan, M. D. Dickey, and A. M. Taylor. Integration of pre-aligned liquid metal electrodes for neural stimulation within a user-friendly microfluidic platform. *Lab on a Chip*, 2013. (Cited on page 45.)

T. S. Hansen, K. West, O. Hassager, and N. B. Larsen. Highly stretchable and conductive polymer material made from poly(3,4-ethylenedioxythiophene) and polyurethane elastomers. *Advanced Functional Materials*, 2007. (Cited on page 30.)

Y. Hattori, L. Falgout, W. Lee, S. Y. Jung, E. Poon, J. W. Lee, I. Na, A. Geisler, D. Sadhwani, Y. Zhang, Y. Su, X. Wang, Z. Liu, J. Xia, H. Cheng, R. C. Webb, A. P. Bonifas, P. Won, J. W. Jeong, K. I. Jang, Y. M. Song, B. Nardone, M. Nodzenski, J. A. Fan, Y. Huang, D. P. West, A. S. Paller, M. Alam, W. H. Yeo, and J. A. Rogers. Multifunctional skin-like electronics for quantitative, clinical monitoring of cutaneous wound healing. *Advanced Healthcare Materials*, 2014. (Cited on pages 19 and 20.)

G. J. Hayes, J. H. So, A. Qusba, M. D. Dickey, and G. Lazzi. Flexible liquid metal alloy (EGaIn) microstrip patch antenna. *IEEE Transactions on Antennas and Propagation*, 2012. (Cited on pages 35 and 36.)

A. Hirsch, H. O. Michaud, A. P. Gerratt, S. de Mulatier, and S. P. Lacour. Intrinsically Stretchable Biphasic (Solid–Liquid) Thin Metal Films. *Advanced Materials*, 2016. (Cited on pages 34, 35, 70, and 104.)

W. Honda, S. Harada, T. Arie, S. Akita, and K. Takei. Wearable, human-interactive, health-monitoring, wireless devices fabricated by macroscale printing techniques. *Advanced Functional Materials*, 2014. (Cited on page 20.)

Z. Hu, P. H. Cole, and L. Zhang. A method for calculating the resonant frequency of meander-line dipole antenna. In *2009 4th IEEE Conference on Industrial Electronics and Applications, ICIEA 2009*, 2009. (Cited on page 86.)

F. Hua, Y. Sun, A. Gaur, M. A. Meitl, L. Bilhaut, L. Rotkina, J. Wang, P. Geil, M. Shim, J. A. Rogers, and A. Shim. Polymer imprint lithography with molecular-scale resolution. *Nano Letters*, 2004. (Cited on page 49.)

X. Huang, Y. Liu, H. Cheng, W. J. Shin, J. A. Fan, Z. Liu, C. J. Lu, G. W. Kong, K. Chen, D. Patnaik, S. H. Lee, S. Hage-Ali, Y. Huang, and J. A. Rogers. Materials and designs for wireless epidermal sensors of hydration and strain. *Advanced Functional Materials*, 2014. (Cited on page 20.)

F. Ilievski, A. D. Mazzeo, R. F. Shepherd, X. Chen, and G. M. Whitesides. Soft Robotics for Chemists. *Angewandte Chemie International Edition*, 2011. (Cited on page 15.)

S. Imani, A. J. Bandodkar, A. M. V. Mohan, R. Kumar, S. Yu, J. Wang, and P. P. Mercier. A wearable chemical–electrophysiological hybrid biosensing system for real-time health and fitness monitoring. *Nature Communications*, 2016. (Cited on page 19.)

J. Je and J. Lee. Design, fabrication, and characterization of liquid metal microheaters. *Journal of Microelectromechanical Systems*, 2014. (Cited on page 47.)

S. H. Jeong, A. Hagman, K. Hjort, M. Jobs, J. Sundqvist, and Z. Wu. Liquid alloy printing of microfluidic stretchable electronics. *Lab on a Chip*, 2012. (Cited on pages 35 and 104.)

S. H. Jeong, K. Hjort, and Z. Wu. Tape transfer atomization patterning of liquid alloys for microfluidic stretchable wireless power transfer. *Scientific Reports*, 2015. (Cited on page 104.)

Y. R. Jeong, J. Kim, Z. Xie, Y. Xue, S. M. Won, G. Lee, S. W. Jin, S. Y. Hong, X. Feng, Y. Huang, J. A. Rogers, and J. S. Ha. A skin-attachable, stretchable integrated system based on liquid GaInSn for wireless human motion monitoring with multi-site sensing capabilities. *NPG Asia Materials*, 2017. (Cited on page 104.)

J. Ji, Z. Zhou, X. Zhao, J. Sun, and X. Sun. Electrochemical sensor based on molecularly imprinted film at Au nanoparticles-carbon nanotubes modified electrode for determination of cholesterol. *Biosensors and Bioelectronics*, 2015. (Cited on page 23.)

K. Jost, D. Stenger, C. R. Perez, J. K. McDonough, K. Lian, Y. Gogotsi, and G. Dion. Knitted and screen printed carbon-fiber supercapacitors for applications in wearable electronics. *Energy and Environmental Science*, 2013. (Cited on page 19.)

D. Kang, P. V. Pikhitsa, Y. W. Choi, C. Lee, S. S. Shin, L. Piao, B. Park, K. Y. Suh, T. I. Kim, and M. Choi. Ultrasensitive mechanical crack-based sensor inspired by the spider sensory system. *Nature*, 2014. (Cited on pages 19 and 20.)

H. Kawaguchi, T. Someya, T.and Sekitani, and T. Sakurai. Cut-and-paste customization of organic FET integrated circuit and its application to electronic artificial skin. 2005. (Cited on page 24.)

C. Keplinger, J. Y. Sun, C. C. Foo, P. Rothemund, G. M. Whitesides, and Z. Suo. Stretchable, transparent, ionic conductors. *Science*, 2013. (Cited on page 29.)

M. R. Khan, C. Trlica, J. H. So, M. Valeri, and M. D. Dickey. Influence of water on the interfacial behavior of gallium liquid metal alloys. *ACS Applied Materials and Interfaces*, 2014. (Cited on page 46.)

M. R. Khan, J. Bell, and M. D. Dickey. Localized Instabilities of Liquid Metal Films via In-Plane Recapillarity. *Advanced Materials Interfaces*, 2016. (Cited on page 104.)

D. Khodagholy, J. N. Gelinas, T. Thesen, W. Doyle, O. Devinsky, G. G. Malliaras, and G. Buzsáki. NeuroGrid: Recording action potentials from the surface of the brain. *Nature Neuroscience*, 2015. (Cited on page 30.)

S. Kholghi Eshkalak, A. Chinnappan, W. A. D. M. Jayathilaka, M. Khatibzadeh, E. Kowsari, and S. Ramakrishna. A review on inkjet printing of CNT composites for smart applications, 2017. (Cited on page 28.)

K. Khoshmanesh, S. Y. Tang, J. Y. Zhu, S. Schaefer, A. Mitchell, K. Kalantar-Zadeh, and M. D. Dickey. Liquid metal enabled microfluidics, 2017. (Cited on page 33.)

D. H. Kim, J. Song, W. M. Choi, H. S. Kim, R. H. Kim, Z. Liu, Y. Y. Huang, K. C. Hwang, Y. W. Zhang, and J. A. Rogers. Materials and noncoplanar mesh designs for integrated circuits with linear elastic responses to extreme mechanical deformations. *Proceedings of the National Academy of Sciences*, 2008. (Cited on pages 24 and 25.)

Do-Il Kim, Tran Quang Trung, Byeong-Ung Hwang, Jin-Su Kim, Sanghun Jeon, Jihyun Bae, Jong-Jin Park, and Nae-Eung Lee. A sensor array using multi-functional field-effect transistors with ultrahigh sensitivity and precision for bio-monitoring. *Scientific reports*, 2015. (Cited on pages 19 and 20.)

J. Kim, G. A. Salvatore, H. Araki, A. M. Chiarelli, Z. Xie, A. Banks, X. Sheng, Y. Liu, K. I. Lee, J. W.and Jang, S. Y. Heo, K. Cho, H. Luo, B. Zimmerman, J. Kim, L. Yan, X. Feng, S. Xu, M. Fabiani, G. Gratton, Y. Huang, U. Paik, and J. A. Rogers. Battery-free, stretchable optoelectronic systems for wireless optical characterization of the skin. *Science Advances*, 2016. (Cited on page 41.)

M. G. Kim, H. Alrowais, S. Pavlidis, and O. Brand. Size-Scalable and High-Density Liquid-Metal-Based Soft Electronic Passive Components and Circuits Using Soft Lithography. *Advanced Functional Materials*, 2017. (Cited on page 104.)

A. Koh, D. Kang, Y. Xue, S. Lee, R. M. Pielak, J. Kim, T. Hwang, S. Min, A. Banks, P. Bastien, M. C. Manco, L. Wang, K. R. Ammann, K. In Jang, P. Won, S. Han, R. Ghaffari, U. Paik, M. J. Slepian, G. Balooch, Y. Huang, and J. A. Rogers. A soft, wearable microfluidic device for the capture, storage, and colorimetric sensing of sweat. *Science Translational Medicine*, 2016. (Cited on page 41.)

H. J. Koo, J. H. So, M. D. Dickey, and O. D. Velev. Towards all-soft matter circuits: Prototypes of quasi-liquid devices with memristor characteristics. *Advanced Materials*, 2011. (Cited on page 36.)

R. K. Kramer, C. Majidi, R. Sahai, and R. J. Wood. Soft curvature sensors for joint angle proprioception. 2011a. (Cited on pages 32 and 37.)

R. K. Kramer, C. M. Majidi, and R. J. Wood. Wearable tactile keypad with stretchable artificial skin. *IEEE International Conference on Robotics and Automation*, 2011b. (Cited on page 39.)

M. Kubo, X. Li, M. Kim, C.and Hashimoto, B. J. Wiley, D. Ham, and G. M. Whitesides. Stretchable microfluidic radiofrequency antennas. *Advanced Materials*, 2010. (Cited on pages 35, 36, 63, and 64.)

S. P. Lacour, S. Wagner, Z. Huang, and Z. Suo. Stretchable gold conductors on elastomeric substrates. *Applied Physics Letters*, 2003. (Cited on page 24.)

Stéphanie P. Lacour, Joyelle Jones, Sigurd Wagner, Teng Li, and Zhigang Suo. Stretchable Interconnects for Elastic Electronic Surfaces, 2005. (Cited on page 25.)

R. J. Larsen, M. D. Dickey, G. M. Whitesides, and D. A. Weitz. Viscoelastic properties of oxide-coated liquid metals. *Journal of Rheology*, 2010. (Cited on page 47.)

C. Larson, B. Peele, S. Li, S. Robinson, M. Totaro, L. Beccai, B. Mazzolai, and R. Shepherd. Highly stretchable electroluminescent skin for optical signaling and tactile sensing. *Science*, 2016. (Cited on page 29.)

N. Lazarus, C. D. Meyer, S. S. Bedair, H. Nochetto, and I. M. Kierzewski. Multilayer liquid metal stretchable inductors. *Smart Materials and Structures*, 2014. (Cited on page 36.)

N. Lazarus, C. D. Meyer, and W. J. Turner. A microfluidic wireless power system. *RSC Advances*, 2015. (Cited on page 35.)

G. Li, X. Wu, and D. W. Lee. A galinstan-based inkjet printing system for highly stretchable electronics with self-healing capability. *Lab on a Chip*, 2016. (Cited on pages 23, 34, and 104.)

T. Li, G. Li, Y. Liang, T. Cheng, J. Dai, X. Yang, B. Liu, Z. Zeng, Z. Huang, Y. Luo, T. Xie, and W. Yang. Fast-moving soft electronic fish. *Science Advances*, 2017. (Cited on page 16.)

Y. T. Liao, H. Yao, A. Lingley, B. Parviz, and B. P. Otis. A 3-μW CMOS glucose sensor for wireless contact-lens tear glucose monitoring. *IEEE Journal of Solid-State Circuits*, 2012. (Cited on page 17.)

H. T. Lin, G. G. Leisk, and B. Trimmer. https://dx.doi.org/10.1088/1748-3182/6/2/026007. *Bioinspiration and Biomimetics*. (Cited on page 40.)

Y. Lin, S. Liu, S. Chen, Y. Wei, X. Dong, and L. Liu. A highly stretchable and sensitive strain sensor based on graphene-elastomer composites with a novel double-interconnected network. *Journal of Materials Chemistry C*, 2016. (Cited on pages 25, 33, and 44.)

N. Liu, A. Chortos, T. Lei, L. Jin, W. G. Kim, T. R.and Bae, C. Zhu, S. Wang, R. Pfattner, X. Chen, R. Sinclair, and Z. Bao. Ultratransparent and stretchable graphene electrodes. *Science Advances*, 2017. (Cited on page 26.)

R. Liu, G. Huskić, and A. Zell. Dynamic objects tracking with a mobile robot using passive UHF RFID tags. In *IEEE International Conference on Intelligent Robots and Systems*, 2014. (Cited on page 82.)

T. Liu, P. Sen, and C. J. Kim. Characterization of nontoxic liquid-metal alloy galinstan for applications in microdevices. *Journal of Microelectromechanical Systems*, 2012. (Cited on pages 31, 44, 45, and 46.)

X. Liu, L. P. B. Katehi, and D. Peroulis. Non-toxic liquid metal microstrip resonators. *IEEE Asia Pacific Microwave Conference*, 2009. (Cited on page 32.)

Z. F. Liu, S. Fang, F. A. Moura, J. N. Ding, N. Jiang, J. Di, M. Zhang, X. Lepró, D. S. Galvão, C. S. Haines, N. Y. Yuan, S. G. Yin, D. W. Lee, R. Wang, H. Y. Wang, W. Lv, C. Dong, R. C. Zhang, M. J. Chen, Q. Yin, Y. T. Chong, R. Zhang, X. Wang, M. D. Lima, R. Ovalle-Robles, D. Qian, H. Lu, and R. H. Baughman. Hierarchically buckled sheath-core fibers for superelastic electronics, sensors, and muscles. *Science*, 2015. (Cited on pages 26 and 36.)

M. Loepfe, C. M. Schumacher, U. B. Lustenberger, and W. J. Stark. An Untethered, Jumping Roly-Poly Soft Robot Driven by Combustion. *Soft Robotics*, 2015. (Cited on page 16.)

F. Lorussi, E. P. Scilingo, A. Tesconi, M.and Tognetti, and D. De-Rossi. Strain sensing fabric for hand posture and gesture monitoring. *IEEE Transactions on Information Technology in Biomedicine*, 2005. (Cited on page 24.)

T. Lu, L. Finkenauer, J. Wissman, and C. Majidi. Rapid prototyping for soft-matter electronics. *Advanced Functional Materials*, 2014. (Cited on page 104.)

Y. Lu, Q. Hu, Y. Lin, D. B. Pacardo, C. Wang, W. Sun, F. S. Ligler, M. D. Dickey, and Z. Gu. Transformable liquid-metal nanomedicine. *Nature Communications*, 2015. (Cited on page 46.)

W. Luo, T. Wu, B. Chen, M. Liang, and H. Zou. Highly Stretchable Conductors Based on Expanded Graphite Macroconfined in Tubular Rubber. *ACS Applied Materials and Interfaces*, 2017. (Cited on page 27.)

L. Ma, X. Shuai, P. Zhu, and R. Sun. A highly sensitive flexible pressure sensor based on multi-scale structure and silver nanowires. 2017. (Cited on page 26.)

C. Majidi, R. K. Kramer, and R. J. Wood. A non-differential elastomer curvature sensor for softer-than-skin electronics. *A non-differential elastomer curvature sensor for softer-than-skin electronics*, 2011. (Cited on pages 32, 37, 63, and 64.)

M. Malley, M. Rubenstein, and R. Nagpal. https://dx.doi.org/10.1109/iros.2017.8206563. In *IEEE International Conference on Intelligent Robots and Systems*. (Cited on page 40.)

K. Malzahn, J. R. Windmiller, G. Valdes-Ramirez, M. J. Schoning, and J. Wang. Wearable electrochemical sensors for in situ analysis in marine environments. *Analyst*, 2011. (Cited on page 19.)

M. S. Mannoor, H. Tao, J. D. Clayton, A. Sengupta, D. L. Kaplan, R. R. Naik, N. Verma, F. G. Omenetto, and M. C. McAlpine. Graphene-based wireless bacteria detection on tooth enamel. *Nature Communications*, 2012. (Cited on page 18.)

A. D. Marchese, R. K. Katzschmann, and D. Rus. A Recipe for Soft Fluidic Elastomer Robots. *Soft Robotics*, 2015. (Cited on pages 2, 40, and 41.)

G. Marrocco. The art of UHF RFID antenna design: Impedance-matching and size-reduction techniques. *IEEE Antennas and Propagation Magazine*, 2008. (Cited on page 88.)

N. Matsuhisa, M. Kaltenbrunner, T. Yokota, H. Jinno, K. Kuribara, T. Sekitani, and T. Someya. Printable elastic conductors with a high conductivity for electronic textile applications. *Nature Communications*, 2015. (Cited on page 26.)

N. Matsuhisa, X. Chen, Z. Bao, and T. Someya. Materials and structural designs of stretchable conductors, 2019. (Cited on page 29.)

R. M. McKenzie, T. W. Barraclough, and A. A. Stokes. Integrating Soft Robotics with ROS - A hybrid pick and place arm. *arXiv*, 2017. (Cited on page 15.)

Y. Mengüç, Y. L. Park, H. Pei, D. Vogt, P. M. Aubin, E. Winchell, L. Fluke, L. Stirling, R. J. Wood, and C. J. Walsh. Wearable soft sensing suit for human gait measurement. *International Journal of Robotics Research*, 2014. (Cited on page 37.)

K. P. Mineart, Y. Lin, S. C. Desai, A. S. Krishnan, R. J. Spontak, and M. D. Dickey. Ultrastretchable, cyclable and recyclable 1- and 2-dimensional conductors based on physically cross-linked thermoplastic elastomer gels. *Soft Matter*, 2013. (Cited on pages 32 and 44.)

V. Mitrakos, P. J.W. Hands, G. Cummins, L. Macintyre, F. C. Denison, D. Flynn, and M. P.Y. Desmulliez. Nanocomposite-based microstructured piezoresistive pressure sensors for low-pressure measurement range. *Micromachines*, 2018. (Cited on page 27.)

A. Miyamoto, S. Lee, N. F. Cooray, S. Lee, M. Mori, N. Matsuhisa, H. Jin, L. Yoda, T. Yokota, A. Itoh, M. Sekino, H. Kawasaki, T. Ebihara, M. Amagai, and T. Someya. Inflammation-free, gas-permeable, lightweight, stretchable on-skin electronics with nanomeshes. *Nature Nanotechnology*, 2017. (Cited on page 27.)

J. T. Muth, D. M. Vogt, R. L. Truby, D. B. Menguc, Y.and Kolesky, R. J. Wood, and J. A. Lewis. Embedded 3D printing of strain sensors within highly stretchable elastomers. *Advanced Materials*, 2014. (Cited on page 28.)

A. Nag, S. C. Mukhopadhyay, and J. Kosel. Wearable Flexible Sensors: A Review, 2017. (Cited on page 23.)

S. Nambiar and J. T. W. Yeow. Conductive polymer-based sensors for biomedical applications. *Biosensors and Bioelectronics*, 2011. (Cited on page 24.)

N. Naserifar, P. R. LeDuc, and G. K. Fedder. Material Gradients in Stretchable Substrates toward Integrated Electronic Functionality. *Advanced Materials*, 2016. (Cited on page 41.)

N. Naserifar, P. R. LeDuc, and G. K. Fedder. Drop casting of stiffness gradients for chip integration into stretchable substrates. *Journal of Micromechanics and Microengineering*, 2017. (Cited on page 41.)

M. P. Nemitz, P. Mihaylov, T. W. Barraclough, D. Ross, and A. A. Stokes. Using Voice Coils to Actuate Modular Soft Robots: Wormbot, an Example. *Soft Robotics*, 2016. (Cited on page 16.)

T. F. O'Connor, A. V. Zaretski, S. Savagatrup, A. D. Printz, C. D. Wilkes, M. I. Diaz, E. J. Sawyer, and D. J. Lipomi. Wearable organic solar cells with high cyclic bending stability: Materials selection criteria. *Solar Energy Materials and Solar Cells*, 2016. (Cited on page 30.)

J. Y. Oh, S. Kim, H. K. Baik, and U. Jeong. Conducting Polymer Dough for Deformable Electronics. *Advanced Materials*, 2016. (Cited on page 30.)

A. M. O'Mahony and J. Wang. Nanomaterial-based electrochemical detection of explosives: a review of recent developments. *Analytical Methods*, 2013. (Cited on page 17.)

A. P. O'Mullane, A. Mitchell, S. Tang, D. Abbott, K. Kalantar-zadeh, K. Khoshmanesh, P. Petersen, and V. Sivan. Liquid metal enabled pump. *Proceedings of the National Academy of Sciences*, 2014. (Cited on page 47.)

J. T.B. Overvelde, Y. Mengüç, P. Polygerinos, Y. Wang, Z. Wang, C. J. Walsh, R. J. Wood, and K. Bertoldi. Mechanical and electrical numerical analysis of soft liquid-embedded deformation sensors analysis. *Extreme Mechanics Letters*, 2014. (Cited on page 37.)

K. B. Ozutemiz, J. Wissman, O. B. Ozdoganlar, and C. Majidi. EGaIn–Metal Interfacing for Liquid Metal Circuitry and Microelectronics Integration. *Advanced Materials Interfaces*, 2018. (Cited on pages 104 and 107.)

J. K. Paik, R. K. Kramer, and R. J. Wood. Stretchable Circuits and Sensors for Robotic Origami. *IEEE/RSJ International Conference on Intelligent Robots and Systems*, 2011. (Cited on page 32.)

S. Palagi, A. G. Mark, S. Y. Reigh, K. Melde, T. Qiu, H. Zeng, C. Parmeggiani, D. Martella, A. Sanchez-Castillo, N. Kapernaum, F. Giesselmann, D. S. Wiersma, E. Lauga, and P. Fischer. Structured light enables biomimetic swimming and versatile locomotion of photoresponsive soft microrobots. *Nature Materials*, 2016. (Cited on page 16.)

C. Pang, J. H. Koo, A. Nguyen, J. M. Caves, M. G. Kim, A. Chortos, K. Kim, P. J. Wang, J. B.H. Tok, and Z. Bao. Highly skin-conformal microhairy sensor for pulse signal amplification. *Advanced Materials*, 2015. (Cited on pages 19 and 20.)

D. P. Parekh, C. Ladd, L. Panich, K. Moussa, and M. D. Dickey. 3D printing of liquid metals as fugitive inks for fabrication of 3D microfluidic channels. *Lab on a Chip*, 2016. (Cited on page 47.)

C. W. Park, Y. G. Moon, H. Seong, S. W. Jung, J. Y. Oh, B. S. Na, N. M. Park, S. S. Lee, S. G. Im, and J. B. Koo. Photolithography-Based Patterning of Liquid Metal Interconnects for Monolithically Integrated Stretchable Circuits. *ACS Applied Materials and Interfaces*, 2016. (Cited on page 41.)

J. Park, Y. Lee, J. Hong, M. Ha, Y. D. Jung, H. Lim, S. Y. Kim, and H. Ko. Giant tunneling piezoresistance of composite elastomers with interlocked microdome arrays for ultrasensitive and multimodal electronic skins. *ACS Nano*, 2014. (Cited on page 20.)

Y. L. Park, K. Chau, R. J. Black, and M. R. Cutkosky. Force sensing robot fingers using embedded fiber Bragg grating sensors and shape deposition manufacturing. 2007. (Cited on page 24.)

Y. L. Park, S. C. Ryu, R. J. Black, K. K. Chau, B. Moslehi, and M. R. Cutkosky. Exoskeletal force-sensing end-effectors with embedded optical fiber-bragg-grating sensors. *IEEE Transactions on Robotics*, 2009. (Cited on page 24.)

Y. L. Park, C. Majidi, R. Kramer, P. Brard, and R. J. Wood. Hyperelastic pressure sensing with a liquid-embedded elastomer. *Journal of Micromechanics and Microengineering*, 2010. (Cited on pages 37 and 104.)

Y. L. Park, B. R. Chen, C. Majidi, R. J. Wood, R. Nagpal, and E. Goldfield. Active modular elastomer sleeve for soft wearable assistance robots. In *IEEE International Conference on Intelligent Robots and Systems*, 2012a. (Cited on page 70.)

Y. L. Park, B. R. Chen, and R. J. Wood. Design and Fabrication of Soft Artificial Skin Using Embedded Microchannels and Liquid Conductors. *IEEE Sensors Journal*, 2012b. (Cited on pages 29, 32, 34, 38, 39, 63, and 64.)

M. Parrilla, R. Canovas, I. Jeerapan, F. J. Andrade, and J. Wang. A Textile-Based Stretchable Multi-Ion Potentiometric Sensor. *Advanced Healthcare Materials*, 2016. (Cited on page 17.)

M. Passlack, E. F. Schubert, W. S. Hobson, M. Hong, N. Moriya, S. N.G. Chu, K. Konstadinidis, J. P. Mannaerts, M. L. Schnoes, and G. J. Zydzik. Ga2O3 films for electronic and optoelectronic applications. *Journal of Applied Physics*, 1995. (Cited on page 46.)

N. Pekas, Q. Zhang, and D. Juncker. Electrostatic actuator with liquid metal-elastomer compliant electrodes used for on-chip microvalving. *Journal of Micromechanics and Microengineering*, 2012. (Cited on page 47.)

A. Piruska, I. Nikcevic, S. H. Lee, C. Ahn, W. R. Heineman, P. A. Limbach, and C. J. Seliskar. The autofluorescence of plastic materials and chips measured under laser irradiation. *Lab on a Chip*, 2005. (Cited on page 49.)

P. Polygerinos, Z. Wang, K. C. Galloway, R. J. Wood, and C. J. Walsh. Soft robotic glove for combined assistance and at-home rehabilitation. In *Robotics and Autonomous Systems*, 2015. (Cited on page 81.)

S. Pyo, J. Choi, and J. Kim. Flexible, Transparent, Sensitive, and Crosstalk-Free Capacitive Tactile Sensor Array Based on Graphene Electrodes and Air Dielectric. *Advanced Electronic Materials*, 2018. (Cited on pages 26 and 28.)

A. Qusba, A. K. Ramrakhyani, J. H. So, G. J. Hayes, M.D. Dickey, and G. Lazzi. On the design of microfluidic implant coil for flexible telemetry system. *IEEE Sensors Journal*, 2014. (Cited on page 36.)

M. Regan, H. Tostmann, P. Pershan, O. Magnussen, E. DiMasi, and B. Ocko. X-ray study of the oxidation of liquid-gallium surfaces. *Physical Review B - Condensed Matter and Materials Physics*, 1997. (Cited on page 46.)

M. Reynolds, M. Brown, K. McGill, P. Davidson, J. Lammerding, E. Minot, J. Goldberg, and P. McEuen. Kirigami Graphene Transistors for Biological Sensing. *APS March Meeting*, 2016. (Cited on page 23.)

S. I. Rich, R. J. Wood, and C. Majidi. Untethered soft robotics. *Nature Electronics*, 2018. (Cited on pages 16, 40, and 42.)

J. Rivnay, S. Inal, B. A. Collins, M. Sessolo, E. Stavrinidou, X. Strakosas, C. Tassone, D. M. Delongchamp, and G. G. Malliaras. Structural control of mixed ionic and electronic transport in conducting polymers. *Nature Communications*, 2016. (Cited on page 30.)

H. Rodrigue, W. Wang, D. R. Kim, and S. H. Ahn. Curved shape memory alloy-based soft actuators and application to soft gripper. *Composite Structures*, 2017. (Cited on page 16.)

J. A. Rogers, T. Someya, and Y. Huang. Materials and mechanics for stretchable electronics, 2010. (Cited on page 24.)

M. Rogoz, H. Zeng, C. Xuan, D. S. Wiersma, and P. Wasylczyk. Light-Driven Soft Robot Mimics Caterpillar Locomotion in Natural Scale. *Advanced Optical Materials*, 2016. (Cited on page 16.)

E. Roh, B. U. Hwang, D. Kim, B. Y. Kim, and N. E. Lee. Stretchable, Transparent, Ultrasensitive, and Patchable Strain Sensor for Human-Machine Interfaces Comprising a Nanohybrid of Carbon Nanotubes and Conductive Elastomers. *ACS Nano*, 2015. (Cited on pages 19 and 20.)

D. Rus and M. T. Tolley. Design, fabrication and control of soft robots. *Nature*, 2015. (Cited on page 16.)

T. Sanpechuda and L. Kovavisaruch. A review of RFID localization: Applications and techniques. In *5th International Conference on Electrical Engineering/Electronics, Computer, Telecommunications and Information Technology, ECTI-CON 2008*, 2008. (Cited on page 82.)

S. Savagatrup, E. Chan, S. M. Renteria-Garcia, A. D. Printz, A. V. Zaretski, T. F. O'Connor, D. Rodriquez, E. Valle, and D. J. Lipomi. Plasticization of PEDOT:PSS by common additives for mechanically robust organic solar cells and wearable sensors. *Advanced Functional Materials*, 2015. (Cited on page 30.)

A. Scidà, S. Haque, E. Treossi, A. Robinson, S. Smerzi, S. Ravesi, S. Borini, and V. Palermo. Application of graphene-based flexible antennas in consumer electronic devices. *Materials Today*, 2018. (Cited on pages 22 and 23.)

P. K. Sekhar and F. Wignes. Trace detection of research department explosive (RDX) using electrochemical gas sensor. *Sensors and Actuators B: Chemical*, 2016. (Cited on page 17.)

T. Sekitani, Y. Noguchi, K. Hata, T. Fukushima, T. Aida, and T. Someya. A rubberlike stretchable active matrix using elastic conductors. *Science*, 2008. (Cited on page 31.)

T. Sekitani, U. Zschieschang, H. Klauk, and T. Someya. Flexible organic transistors and circuits with extreme bending stability. *Nature Materials*, 2010. (Cited on page 23.)

V. Sencadas, R. Mutlu, and G. Alici. Large area and ultra-thin compliant strain sensors for prosthetic devices. *Sensors and Actuators, A: Physical*, 2017. (Cited on page 28.)

M. Sfakiotakis, A. Kazakidi, and D. P. Tsakiris. Octopus-inspired multi-arm robotic swimming. *Bioinspiration and Biomimetics*, 2015. (Cited on page 42.)

A. Shademan, R. S. Decker, J. D. Opfermann, S. Leonard, A. Krieger, and P. C.W. Kim. Supervised autonomous robotic soft tissue surgery. *Science Translational Medicine*, 2016. (Cited on page 81.)

R. F. Shepherd, F. Ilievski, W. Choi, S. A. Morin, A. A. Stokes, A. D. Mazzeo, X. Chen, M. Wang, and G. M. Whitesides. Multigait soft robot. *Proceedings of the National Academy of Sciences*, 2011. (Cited on pages 15 and 16.)

M. K. Shin, J. Oh, M. Lima, M. E. Kozlov, S. J. Kim, and R. H. Baughman. Elastomeric conductive composites based on carbon nanotube forests, 2010. (Cited on page 25.)

Xingtian Shuai, Pengli Zhu, Wenjin Zeng, Yougen Hu, Xianwen Liang, Yu Zhang, Rong Sun, and Ching Ping Wong. Highly Sensitive Flexible Pressure Sensor Based on Silver Nanowires-Embedded Polydimethylsiloxane Electrode with Microarray Structure. *ACS Applied Materials and Interfaces*, 2017. (Cited on pages 26 and 28.)

T. C. Shyu, P. F. Damasceno, P. M. Dodd, A. Lamoureux, L. Xu, M. Shlian, M. Shtein, S. C. Glotzer, and N. A. Kotov. A kirigami approach to engineering elasticity in nanocomposites through patterned defects. *Nature Materials*, 2015. (Cited on page 25.)

G. A. Snook, P. Kao, and A. S. Best. Conducting-polymer-based supercapacitor devices and electrodes, 2011. (Cited on page 30.)

J. H. So, J. Thelen, A. Qusba, G. J. Hayes, G. Lazzi, and M. D. Dickey. Reversibly deformable and mechanically tunable fluidic antennas. *Advanced Functional Materials*, 2009. (Cited on pages 34 and 36.)

J. H. So, H. J. Koo, M. D. Dickey, and O. D. Velev. Ionic current rectification in soft-matter diodes with liquid-metal electrodes. *Advanced Functional Materials*, 2012. (Cited on page 36.)

P. S. Sreetharan, J. P. Whitney, M. D. Strauss, and R. J. Wood. Monolithic fabrication of millimeter-scale machines. *Journal of Micromechanics and Microengineering*, 2012. (Cited on page 23.)

J. Y. Sun, C. Keplinger, G. M. Whitesides, and Z. Suo. Ionic skin. *Advanced Materials*, 2014. (Cited on page 29.)

Y. Sun, W. M. Choi, H. Jiang, Y. Y. Huang, and J. A. Rogers. Controlled buckling of semiconductor nanoribbons for stretchable electronics. *Nature Nanotechnology*, 2006. (Cited on page 24.)

P. Surmann and H. Zeyat. Voltammetric analysis using a self-renewable non-mercury electrode. *Analytical and Bioanalytical Chemistry*, 2005. (Cited on page 32.)

A. Tabatabai, A. Fassler, C. Usiak, and C. Majidi. Liquid-phase gallium-indium alloy electronics with microcontact printing. *Langmuir*, 2013. (Cited on pages 63, 64, and 104.)

M. Takiguchi and Y. Yamada. Improvement of radiation efficiencies by applying folded configurations to very small meander line antennas. In *2003 IEEE Topical Conference on Wireless Communication Technology*, 2003. (Cited on page 86.)

P. Tan, B. Chen, H. Xu, H. Zhang, W. Cai, M. Ni, M. Liu, and Z. Shao. Flexible Zn- and Li-air batteries: Recent advances, challenges, and future perspectives, 2017. (Cited on page 23.)

J. Tang, X. Zhao, J. Li, R. Guo, Y. Zhou, and J. Liu. Gallium-Based Liquid Metal Amalgams: Transitional-State Metallic Mixtures (TransM2ixes) with Enhanced and Tunable Electrical, Thermal, and Mechanical Properties. *ACS Applied Materials and Interfaces*, 2017. (Cited on page 104.)

S. Y. Tang, V. Sivan, P. Petersen, W. Zhang, P.D. Morrison, K. Kalantar-zadeh, A. Mitchell, and K. Khoshmanesh. Liquid metal actuator for inducing chaotic advection. *Advanced Functional Materials*, 2014. (Cited on page 47.)

L. Teng, K. Jeronimo, T. Wei, M. P. Nemitz, Geng. Lyu, and A. A. Stokes. Integrating Soft Sensor Systems Using Conductive Thread. *Journal of Micromechanics and Microengineering*, 2018a. (Cited on pages 4, 38, 46, and 113.)

L. Teng, K. Pan, M. P. Nemitz, R. Song, Z. Hu, and A. A. Stokes. Soft Radio-Frequency Identification Sensors: Wireless Long-Range Strain Sensors Using Radio-Frequency Identification. *Soft Robotics*, 2018b. (Cited on pages 4, 36, 37, and 114.)

L. Teng, K. Pan, L. Ting, X. Zhou, A. A. Stokes, and Z. Hu. Soft Wireless Battery-free UHF RFID Stretchable Sensor based on Microfluidic Technology. *IEEE Journal of Radio Frequency Identification*, 2019. (Cited on page 4.)

M. Y. Teo, N. Kim, S. Kee, B. S. Kim, G. Kim, S. Hong, S. Jung, and K. Lee. Highly stretchable and highly conductive PEDOT:PSS/Ionic liquid composite transparent electrodes for solution-processed stretchable electronics. *ACS Applied Materials and Interfaces*, 2017. (Cited on page 30.)

M. T. Tolley, R. F. Shepherd, B. Mosadegh, K. C. Galloway, M. Wehner, M. Karpelson, R. J. Wood, and G. M. Whitesides. A Resilient, Untethered Soft Robot. *Soft Robotics*, 2014. (Cited on pages 2 and 40.)

T. Q. Trung and N. E. Lee. Flexible and Stretchable Physical Sensor Integrated Platforms for Wearable Human-Activity Monitoringand Personal Healthcare. *Advanced Materials*, 2016. (Cited on pages 17, 19, and 28.)

L. Ukkonen, M. Schaffrath, D. W. Engels, L. Sydänheimo, and M. Kivikoski. Operability of folded microstrip patch-type tag antenna in the UHF RFID bands within 865-928 MHz. *IEEE Antennas and Wireless Propagation Letters*, 2006. (Cited on page 86.)

M. Varga, C. Ladd, S. Ma, J. Holbery, and G. Troster. On-skin liquid metal inertial sensor. *Lab on a Chip*, 2017. (Cited on pages 27 and 41.)

D. Vilela, A. Romeo, and S. Sánchez. Flexible sensors for biomedical technology. *Lab on a Chip*, 2016. (Cited on page 23.)

H. Wang, G. De-Boer, J. Kow, M. Ghajari, A. Alazmani, and P. Hewson, R.and Culmer. A Low-cost Soft Tactile Sensing Array Using 3D Hall Sensors. 2016. (Cited on page 29.)

K. Wang, Q. Liu, Q. Guan, J. Wu, H. Li, and J. Yan. Enhanced direct electrochemistry of glucose oxidase and biosensing for glucose via synergy effect of graphene and CdS nanocrystals. *Biosensors and Bioelectronics*, 2011. (Cited on page 23.)

Q. Wang, Y. Yu, J. Yang, and J. Liu. Fast Fabrication of Flexible Functional Circuits Based on Liquid Metal Dual-Trans Printing. *Advanced Materials*, 2015. (Cited on page 104.)

X. Wang, Y. Gu, Z. Xiong, Z. Cui, and T. Zhang. Silk-molded flexible, ultrasensitive, and highly stable electronic skin for monitoring human physiological signals. *Advanced Materials*, 2014a. (Cited on pages 19 and 20.)

Y. Wang, X. Su, Y. adn Zhu, G. Liu, and C. Fan. Development of electrochemical immunosensors towards point of care diagnostics. *Biosensors and Bioelectronics*, 2013. (Cited on page 17.)

Y. Wang, L. Wang, T. Yang, X. Li, X. Zang, M. Zhu, K. Wang, D. Wu, and H. Zhu. Wearable and highly sensitive graphene strain sensors for human motion monitoring. *Advanced Functional Materials*, 2014b. (Cited on pages 19 and 20.)

Y. Wang, C. Zhu, R. Pfattner, H. Yan, L. Jin, S. Chen, F. Molina-Lopez, F. Lissel, J. Liu, N. I. Rabiah, Z. Chen, J. W. Chung, C. Linder, M. F. Toney, B. Murmann, and Z. Bao. A highly stretchable, transparent, and conductive polymer. *Science Advances*, 2017. (Cited on pages 30 and 31.)

R. C. Webb, A. P. Bonifas, A. Behnaz, Y. Zhang, K. J. Yu, H. Cheng, M. Shi, Z. Bian, Z. Liu, Y. S. Kim, W. H. Yeo, J. S. Park, J. Song, Y. Li, Y. Huang, A. M. Gorbach, and J. A. Rogers. Ultrathin conformal devices for precise and continuous thermal characterization of human skin. *Nature Materials*, 2013. (Cited on pages 19 and 20.)

M. Wehner, R. L. Truby, D. J. Fitzgerald, B. Mosadegh, G. M. Whitesides, J. A. Lewis, and R. J. Wood. An integrated design and fabrication strategy for entirely soft, autonomous robots. *Nature*, 2016. (Cited on pages 2 and 16.)

T. Wei, A. A. Stokes, and B. Webb. Biomimetic and Biohybrid Systems - A Soft Pneumatic Maggot Robot. *Springer*, 2016. (Cited on pages 15, 57, and 58.)

W. Wei and S. Guo. A novel PDMS diaphragm micropump based on ICPF actuator. *IEEE International Conference on Robotics and Biomimetics*, 2010. (Cited on page 16.)

D. B. Weibel, W. R. DiLuzio, and G. M. Whitesides. Microfabrication meets microbiology, 2007. (Cited on page 50.)

N. Wettels, V. J. Santos, R. S. Johansson, and G. E. Loeb. Biomimetic tactile sensor array. *Advanced Robotics*, 2008. (Cited on page 24.)

E. L. White, M. C. Yuen, J. C. Case, and R. K. Kramer. Low-Cost, Facile, and Scalable Manufacturing of Capacitive Sensors for Soft Systems. *Advanced Materials Technologies*, 2017. (Cited on page 28.)

R. J. Whitney. The measurement of volume changes in human limbs. *The Journal of Physiology*, 1953. (Cited on page 33.)

J. Wirekoh and Y. L. Park. Design of flat pneumatic artificial muscles. *Smart Materials and Structures*, 2017. (Cited on page 15.)

D. Wirthl, R. Pichler, M. Drack, G. Kettlguber, R. Moser, R. Gerstmayr, F. Hartmann, E. Bradt, R. Kaltseis, C. M. Siket, S. E. Schausberger, S. Hild, S. Bauer, and M. Kaltenbrunner. Instant tough bonding of hydrogels for soft machines and electronics. *Science Advances*, 2017. (Cited on page 29.)

J. Wissman, M. D. Dickey, and C. Majidi. Field-Controlled Electrical Switch with Liquid Metal. *Advanced Science*, 2017. (Cited on page 104.)

H. A. Wurdemann, S. Sareh, A. Shafti, Y. Noh, A. Faragasso, D. S. Chathuranga, H. Liu, S. Hirai, and K. Althoefer. Embedded electro-conductive yarn for shape sensing of soft robotic manipulators. In *Proceedings of the Annual International*

Conference of the IEEE Engineering in Medicine and Biology Society, EMBS, 2015. (Cited on page 66.)

F. Xu and Y. Zhu. Highly conductive and stretchable silver nanowire conductors. *Advanced Materials*, 2012. (Cited on page 25.)

L. Xu, S. R. Gutbrod, A. P. Bonifas, Y. Su, M. S. Sulkin, N. Lu, H. J. Chung, K. I. Jang, Z. Liu, M. Ying, C. Lu, C. R. Webb, J. S. Kim, J. I. Laughner, H. Cheng, Y. Liu, A. Ameen, J. W. Jeong, G. T. Kim, Y. Huang, I. R. Efimov, and J. A. Rogers. 3D multifunctional integumentary membranes for spatiotemporal cardiac measurements and stimulation across the entire epicardium. *Nature Communications*, 2014. (Cited on page 25.)

T. Xu, Y. Ding, Z. Wang, Y. Zhao, W. Wu, H. Fong, and Z. Zhu. Three-dimensional and ultralight sponges with tunable conductivity assembled from electrospun nanofibers for a highly sensitive tactile pressure sensor. *Journal of Materials Chemistry C*, 2017. (Cited on page 27.)

T. Yamada, Y. Hayamizu, Y. Yamamoto, Y. Yomogida, A. Izadi-Najafabadi, D. N. Futaba, and K. Hata. A stretchable carbon nanotube strain sensor for human-motion detection. *Nature Nanotechnology*, 2011. (Cited on pages 19 and 20.)

C. Yang and Z. Suo. Hydrogel ionotronics, 2018. (Cited on page 29.)

D. Yang, M. S. Verma, J. H. So, B. Mosadegh, C. Keplinger, B. Lee, F. Khashai, E. Lossner, Z. Suo, and G. M. Whitesides. Buckling Pneumatic Linear Actuators Inspired by Muscle. *Advanced Materials Technologies*, 2016. (Cited on page 15.)

H. Yang, Y. Chen, Y. Sun, and L. Hao. A novel pneumatic soft sensor for measuring contact force and curvature of a soft gripper. *Sensors and Actuators, A: Physical*, 2017. (Cited on page 41.)

B. You, Y. Kim, B. K. Ju, and J. W. Kim. Highly Stretchable and Waterproof Electroluminescence Device Based on Superstable Stretchable Transparent Electrode. *ACS Applied Materials and Interfaces*, 2017. (Cited on page 26.)

C. Yuan, D. J. Roach, C. K. Dunn, Q. Mu, X. Kuang, C. M. Yakacki, T. J. Wang, K. Yu, and H. J. Qi. 3D printed reversible shape changing soft actuators assisted by liquid crystal elastomers. *Soft Matter*, 2017. (Cited on page 16.)

M. C. Yuen, H. Tonoyan, E. L. White, M. Telleria, and R. K. Kramer. Fabric sensory sleeves for soft robot state estimation. 2017. (Cited on page 28.)

Hyunwoo Yuk, Teng Zhang, Shaoting Lin, German Alberto Parada, and Xuanhe Zhao. Tough bonding of hydrogels to diverse non-porous surfaces. *Nature Materials*, 2016. (Cited on page 29.)

H. Zeng, O. M. Wani, P. Wasylczyk, and A. Priimagi. Light-Driven, Caterpillar-Inspired Miniature Inching Robot. *Macromolecular Rapid Communications*, 2018. (Cited on page 16.)

B. Zhang, Q. Dong, C. E. Korman, Z. Li, and M. E. Zaghloul. Flexible packaging of solid-state integrated circuit chips with elastomeric microfluidics. *Scientific Reports*, 2013. (Cited on pages 32, 63, and 64.)

Z. Zhang, K. Guo, Y. Li, X. Li, G. Guan, H. Li, Y. Luo, F. Zhao, B. Wei, Q. Pei, and H. Peng. A colour-tunable, weavable fibre-shaped polymer light-emitting electrochemical cell. *Biosensors and Bioelectronics*, 2015. (Cited on pages 17 and 23.)

S. Zhu, J. H. So, R. Mays, S. Desai, W. R. Barnes, B. Pourdeyhimi, and M. D. Dickey. Ultrastretchable fibers with metallic conductivity using a liquid metal alloy core. *Advanced Functional Materials*, 2013. (Cited on pages 31, 32, 33, and 44.)

Z. Zhu, T. Liu, G. Li, T. Li, and Y. Inoue. Wearable Sensor Systems for Infants. *Sensors*, 2015. (Cited on page 17.)

Appendices

APPENDIX A

Poster: Towards Hard and Soft Packaging for Die-scale ICs

Conference: MicroTech 2016 - Sensors, MEMS and Advanced Packaging

Authors: Lijun Teng, Onur Zirhli, Burcin Ustbas, Dilek Sezer, Amin Hodaei, Ozge Akbulut, and Adam A. Stokes

Online access to poster: Towards Hard and Soft Packaging for Die-scale ICs

TOWARDS HARD AND SOFT PACKAGING FOR DIE-SCALE ICS

Lijun Teng[1*], Onur Zirhli[2^], Burcin Ustbas[3^], Dilek Sezer[4^], Amin Hodaei[5^], Ozge Akbulut[6^], and Adam A. Stokes[7*]

1- Ph.D. Candidate, *Stokes Research Group, University of Edinburgh, (L.Teng@ed.ac.uk)

2- Research Assistant, ^Sabanci University, (onurzirhli@sabanciuniv.edu)

Sabanci Universitesi
SABANCI UNIVERSITY

THE UNIVERSITY OF EDINBURGH
THE UNIVERSITY OF EDINBURGH

INTRODUCTION

HARD PACKAGING

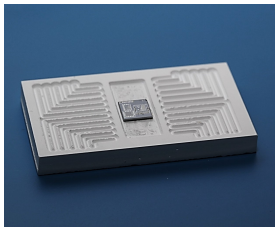

Fig 1.1 Hard packaging

For hard packaging, we use machinable ceramics with steel or platinum wire interconnect.
We use a rheology modifier to control the viscosity. We can adjust the particle loading in ceramic suspensions to increase the toughness of the material, which allowed us to engrave interconnect channels for an example integrated circuit.

SOFT PACKAGING

For soft packaging, We use an LPKF laser micro-machining system to fabricate soft lithography masters for breakout connections for VQFP chip packages.

We used soft lithography to make a polymeric package (PDMS) and an eutectic liquid metal (EGaIn) for the interconnects.

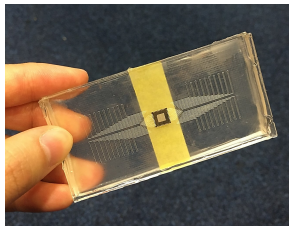

Fig 2.1 Soft packaging

FABRICATION PROCESS



Fig 1.2 Pure alumina powder



Fig 1.3 Superplasticizer

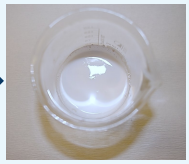

Fig 1.4 Alumina suspensions

The superplasticizer is a type of poly(carboxylate ether) based powder that enables us to machine green bodies which are solid cast from aqueous suspensions of alumina.

We established that an alumina loading of 35 vol% with 1.25 wt% superplasticizer resulted in a green body that was suitable for machining by lathe or mill.

By using superplasticizer we were able to demonstrate machining of solid cast green bodies. This superplasticizer provided sufficient mechanical strength such that the green bodies could withstand machining operations with no formation of visible cracks and flaws.

We demonstrated pattern printing and via formation in the same piece of green body, which means we can avoid complicated and inaccurate stacking processes.

Also, taking advantage of the shrinkage of the ceramic, we can machine vias with excellent sealing around metallic wires.



Fig 1.5 Engraved green body



Fig 1.6 Drilled green body

NOVELTY: Our process shows potential for prototyping highly customized or one-off ceramic packages and avoids alignment in the stacking process used in conventional ceramic packaging methods

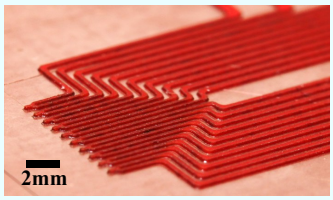

Fig 2.2 Channels mould in detail

The material we used to make the mould is self adhesive vinyl.
The minimum channel width of our design is 100 μm.
The profile can be cut very precisely by our high resolution laser micro-machining system.

The chip is MSP430FR5739, an ultra-low-power microcontroller.
Chip dimensions:
6.15 x 6.15 x 0.95mm
Pad size: 0.3 x 0.18mm

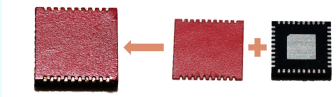

Fig 2.3 Chip and pad cover

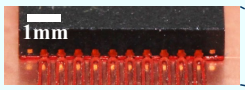

Fig 2.5 Alignment detail

Alignment can be easily achieved by positive location of the cut vinyl. We use a small droplet of wax to fix the chip in position.

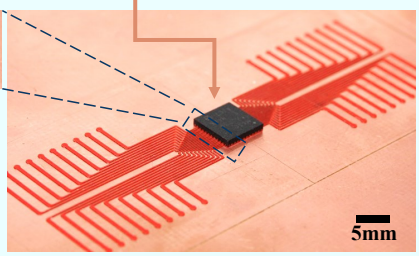

Fig 2.4 Whole mould for PDMS

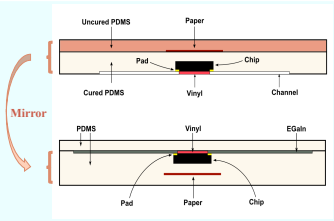

Fig 2.6 Overall cross-section diagram

A piece of paper is embedded to stiffen the PDMS in the vicinity of the chip, and prevent voids opening under strain.
To seal the channels we bond another blank PDMS to the structure with a plasma oven.
We inject eGaIn with a syringe and needle, with a second needle to vent air.

NOVELTY: Very short fabrication time (less than 5mins to make the mold)
Easy to change the mold design (doesn't require a mask and photoresist)

APPLICATION



The ceramic packaging has desirable characteristics of durability in tough thermal and physical conditions.
It would find utility in harsh, high-temperature and pressure environments such as: oil and gas exploration; undersea cabling; and aerospace.



HEAT RESISTANCE



ANTI-PRESSURE



Conventional Packaging



FLEXIBILITY



STRETCHABILITY

Soft encapsulation has desirable characteristics of mechanical compliance.
It holds great potential for many applications such as: wearable wireless health monitors; spatiotemporal cardiac measurements; environmental monitoring; soft robots; and smart lenses.



CONCLUSION

Integrated Circuit packaging provides the link between silicon microsystems and the wider environment. These two methods show that the choice of materials for an IC package is entirely dependent on the use-case for that chip. Flexible wearable electronics require a completely different set of mechanical and material properties than when the same IC is used in harsh, high temperature and pressure environment. We can think of this study as an exploration of Application Specific Integrated Circuit Packaging (ASICP).

Reference: 1. Zhang, B., Dong, Q., Korman, C. E., Li, Z. & Zaghloul, M. E. Flexible packaging of solid-state integrated circuit chips with elastomeric microfluidics. *Scientific reports* **3,** (2013).
2. G. Avci, et al., A PCE-based rheology modifier allows machining of solid cast green bodies of alumina, Ceramics International (2015), http://dx.doi.org/10.1016/j.ceramint.2015.11.004
3. Lizhi Xu, et al. "3D multifunctional integumentary membranes for spatiotemporal cardiac measurements and stimulation across the entire epicardium." Nature Communications 5, Article number: 3329 DOI: 10.1038/ncomms4329.

3- Ph.D Candidate, ^Sabanci University, (Burcinustbas@sabanciuniv.edu)
4- Graduate Student, ^Sabanci University, (Dileksezer@sabanciuniv.edu)
5- Graduate Student, ^Sabanci University, (aminhodaei@sabanciuniv.edu)
6- Assistant Professor, ^Sabanci University, (ozgeakbulut@sabanciuniv.edu)
7- Principal Investigator, *Stokes Research Group, University of Edinburgh, (adam.stokes@ed.ac.uk)

APPENDIX B

Flexible and Stretchable Soft electronic systems

Conference: The University of Edinburgh Research Conference 2017 - Sensors, School of Engineering

Authors: Lijun Teng and Adam A. Stokes

FLEXIBLE AND STRECHABLE SOFT ELECTRONIC SYSTEMS

Lijun Teng[1*] and Adam A. Stokes[2*]

SCOTTISH MICROELECTRONICS CENTRE

THE UNIVERISTY OF EDINBURGH

1. INTRODUCTION

Flexible and stretchable electronics, which are gaining more and more attention nowadays, have some advantages over traditional solid-state electronics: (i) Deformable structures can deal with uncertainty, highly dynamic tasks. (ii) Soft compositions can touch living cells and human bodies. (iii) The use of materials, such as silicone, plastic, fabric, rubber, or compliant mechanical parts, are usually cheaper than metal parts and high-torque servos employed in traditional hard electronic systems.[1]

The soft electronic systems we made are mainly based on silicone material, such as Ecoflex and PDMS (polydime-thylsiloxane), and conductive liquid, such as Gallium-based eutectic alloy.These soft systems have a lot of potential to be applied in soft robots, wearable devices, rescue, exploration, industry, military, and medicine.[2]

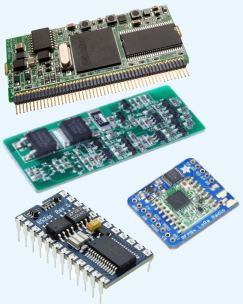

Fig 1.1 Solid electronic devices

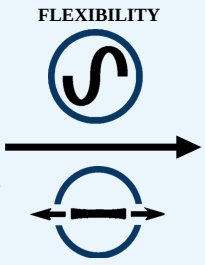

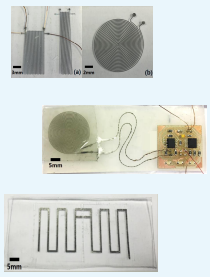

Fig 1.2 Soft electronic devices

2. AIMS AND OBJECTS

The ultimate aim of my Ph.D. is to achieve soft systems that have independent data acquisition, data transmission, self-control functions. This research needs the background of micro-fabrication, electronics, and material science. In order to meet the project's aim and the requirement of PhD study, the project is divided into three parts:

- Soft sensors and soft encapsulation
- Integrate the soft sensors into soft electronic systems
- Improve the soft electronic systems

3. SOFT ENCAPSULATION

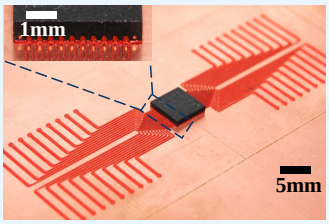

Fig 3.1 Photolithograpy mould for casting PDMS

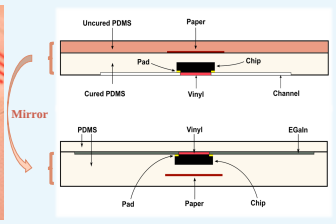

Fig 3.2 Cross-section diagram of a chip in soft encapsulation

For soft packaging, We use an LPKF laser micro-machining system to fabricate soft lithography masters for breakout connections for VQFP chip packages.We used soft lithography to make a polymeric package (PDMS) and an eutectic liquid metal (EGaIn) for the interconnects.[3]

Novelty: Very short fabrication time (less than 5mins to make the mold). Easy to change the mold design (doesn't require a mask and photoresist)

4. SOFT SENSORS

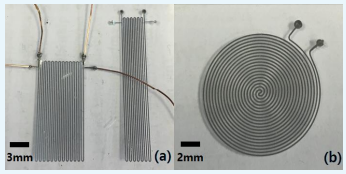

Fig 4.1 Soft sensors based on resistance change. (a) Tensile sensors. (b) Pressure sensor

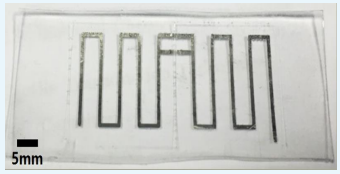

Fig 4.2 Soft sensor based on capacitance change

Different types of sensors can be made with proper designed microfluidic channels, such as stretch sensors, curvature sensors, and pressure sensors.

The liquid alloy we use is a deformable conductive material, its length and cross-sectional area will change when the channels are stretched and pressed. Electrical properties of the material will change according to the geometry change of the channels.

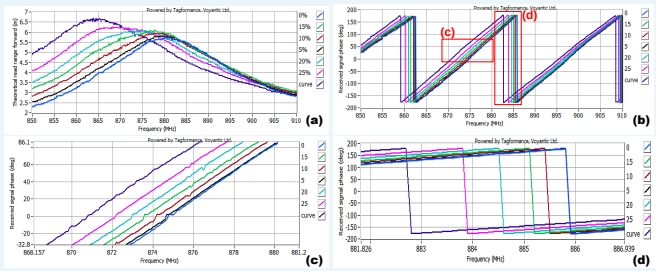

Fig 4.3 Frequency response curves of the tensile sensor in Fig 4.2. (a) Reading range. (b) Received signal phase. (c-d) Partial enlarged details of phase curves.

Novelty of the tensile sensor based on capacitance change:

- Don't need to connect power suppliers
- Ultra-low power consumption
- Large reading range (5~6 m)
- Intrinsically stretchable
- Completely wireless

5. FUTURE WORK

- Flexible and Stretchable Soft Electronic System with Microfluidic Device and Conductive Thread Internal Connection.
- Sensor Arrays Embedded as Electronic Skin in Soft Robot.
- Force sensing sphere for analysing force distribution problem in granular materials.
- Wireless soft curvature and strain sensing system based on RFID technology.

REFERENCE

[1] P. S. Sreetharan, J. P. Whitney, M. D. Strauss, and R. J. Wood, "Monolithic fabrication of millimeter-scale machines," Journal of Micromechanics and Microengineering, vol. 22, no. 5, p. 055027, 2012.

[2] C. Majidi, "Soft Robotics:A Perspective—Current Trends and Prospects for the Future". Soft Robotics. July 2013, 1(1): 5-11. doi:10.1089/soro.2013.0001.

[3] L. Teng, O. Zirhli, O. Akbulut, and A. Stokes7, "Towards hard and soft packaging for die-scale Ics," Micro Tech, 2016

1- Ph.D. Candidate, *Stokes Research Group, University of Edinburgh, (L.Teng@ed.ac.uk)
2- Principal Investigator, *Stokes Research Group, University of Edinburgh, (adam.stokes@ed.ac.uk)

INTEGRATED MICRO AND NANO SYSYRM IMNS

APPENDIX C

Presentation: From Hard To Soft Systems: Using Soft Materials To Encapsulate Off-the-shelf Electronic Components

Conference: ASME IMECE 2017

Topic: 11-7 Material Processing of Flexible Electronics, Devices, and Sensors

Authors: Lijun Teng and Adam A. Stokes

Online access to abstract: From Hard To Soft Systems: Using Soft Materials To Encapsulate Off-the-shelf Electronic Components

From Hard To Soft Systems: Using Soft Materials To Encapsulate Off-the-shelf Electronic Components

Lijun Teng & Adam A. Stokes

In the last decade, people are gradually beginning demand flexible electronic devices. Consumer electronics are trending toward wearable devices which would benefit from the removal of hard and non-deformable blocks. We want to have more smart-wearable-devices to monitor our health condition and record our motion and sport. Also, we want the wearable devices to be more comfortable, or even not able to be felt. More than that, flexible electronics are also related to a lot of cutting-edge technologies, such as, soft robotics, medical instrument, and in-body health monitoring. Making electronic systems flexible is important and an inevitable trend in the future.

At present, many flexible electronic devices have been developed. Nevertheless, there is still a long way to go if we want to make electronic systems completely flexible whilst retaining the same functionality as conventionally-packaged electronic systems. Currently, the vast majority of electronic components are packaged using plastic, ceramic or other solid materials. The printed circuit boards, which are used to link these components, are usually made of copper tracks and a hard-composite substrate (such as FR4).

In the transition from hard electronics to flexible electronics, making changes to the conventional materials used to fabricate printed circuit board is an efficient way to achieve flexible systems. That is to say: making soft package and connections for conventional chips and other components by using flexible conductors (such as liquid alloy and metal fibre thread) and soft substrates (such as silicone rubber and hydrogel) as substitutes for copper and plastic in conventional printed circuit boards. In the poster, we present three methods to fabricate both soft packaging and flexible electronic systems.

We use an LPKF micro-machining system to fabricate soft-lithography masters which are designed to produce breakout connections, using soft-interconnect, for off-the-shelf surface-mount chip packages. We used soft-lithography to make a soft silicone encapsulation (Ecoflex) and a eutectic liquid metal (Galinstan) for the interconnects.

We use the laser micro-machining system to cut the profile of a circuit on a flexible conductive layer to make flexible electronic systems. We use two different methods to make the conductive layer: i) Using silver pen to draw on a piece of paper; ii) Spraying graphene ink on a piece of paper. One reason for using paper is that it can be permeated by uncured Ecoflex, and this permeation creates strong adhesion after curing. Next, we use Z-axis conductive tape (Z-tape) to bond chips and components at the correct position on the circuit. Z-tape is a sticky material which is only conductive in the z-direction. Then we place the circuit on a piece of blank Ecoflex and apply another Ecoflex layer on the top of it to encapsulate the interconnect and electronic-packages into a monolithic flexible electronic system.

APPENDIX D

Integrating Soft Sensor Systems Using Conductive Thread

Journal: Journal of Micromechanics and Microengineering

Authors: Lijun Teng, Karina Jeronimo, Tianqi Wei, Markus P. Nemitz, Geng Lyu, and Adam A. Stokes

Online access to paper:

https://iopscience.iop.org/article/10.1088/1361-6439/aaaca8

Journal of Micromechanics and Microengineering

PAPER

Integrating soft sensor systems using conductive thread

To cite this article: Lijun Teng *et al* 2018 *J. Micromech. Microeng.* **28** 054001

View the article online for updates and enhancements.

This content was downloaded from IP address 129.215.4.178 on 20/05/2018 at 19:30

IOP Publishing Journal of Micromechanics and Microengineering
J. Micromech. Microeng. **28** (2018) 054001 (10pp) https://doi.org/10.1088/1361-6439/aaaca8

Integrating soft sensor systems using conductive thread

Lijun Teng[1], Karina Jeronimo[1], Tianqi Wei[1,2], Markus P Nemitz[1,3], Geng Lyu[2] and Adam A Stokes[1,4]

[1] The School of Engineering, Institute for Integrated Micro and Nano Systems, The University of Edinburgh, The King's Buildings, Edinburgh, EH9 3LJ, United Kingdom
[2] Institute of Perception Action and Behaviour, School of Informatics, The University of Edinburgh, Informatics Forum, 10 Crichton St, Edinburgh, EH8 9AB, United Kingdom
[3] Department of Computer Science and Engineering, University of Michigan, 2260 Hayward St. BBB3737, Ann Arbor, MI 48109, United States of America

E-mail: Adam.Stokes@ed.ac.uk

Received 28 September 2017, revised 8 January 2018
Accepted for publication 2 February 2018
Published 26 February 2018

Abstract

We are part of a growing community of researchers who are developing a new class of soft machines. By using mechanically soft materials (MPa modulus) we can design systems which overcome the bulk-mechanical mismatches between soft biological systems and hard engineered components. To develop fully integrated soft machines—which include power, communications, and control sub-systems—the research community requires methods for interconnecting between soft and hard electronics.

Sensors based upon eutectic gallium alloys in microfluidic channels can be used to measure normal and strain forces, but integrating these sensors into systems of heterogeneous Young's modulus is difficult due the complexity of finding a material which is electrically conductive, mechanically flexible, and stable over prolonged periods of time. Many existing gallium-based liquid alloy sensors are not mechanically or electrically robust, and have poor stability over time.

We present the design and fabrication of a high-resolution pressure-sensor soft system that can transduce normal force into a digital output. In this soft system, which is built on a monolithic silicone substrate, a galinstan-based microfluidic pressure sensor is integrated with a flexible printed circuit board. We used conductive thread as the interconnect and found that this method alleviates problems arising due to the mechanical mismatch between conventional metal wires and soft or liquid materials.

Conductive thread is low-cost, it is readily wetted by the liquid metal, it produces little bending moment into the microfluidic channel, and it can be connected directly onto the copper bond-pads of the flexible printed circuit board. We built a bridge-system to provide stable readings from the galinstan pressure sensor. This system gives linear measurement results between 500–3500 Pa of applied pressure.

We anticipate that integrated systems of this type will find utility in soft-robotic systems as used for wearable technologies like virtual reality, or in soft-medical devices such as exoskeletal rehabilitation robots.

Keywords: sensors, soft systems, wearable technologies, soft robotics, conductive thread, system integration

S Supplementary material for this article is available online

(Some figures may appear in colour only in the online journal)

[4] Author to whom correspondence should be addressed.

 © 2018 IOP Publishing Ltd Printed in the UK

1. Introduction

1.1. Why do we need integrate liquid-metal microfluidic devices with conventional electronic systems?

Soft systems research is a burgeoning field which includes research into components such as sensors and actuators, as well as the integrations of these components to make, for example, locomoting robots and wearable exoskeletons. These devices are built from soft materials including silicone elastomers and hydrogels [1, 2]. These materials have bulk-properties such as low Young's modulus and low hysteresis elasticity. These properties mean that the soft systems show great potential for a wide variety of applications, such as: compliant robotic grippers [3], locomoting soft robots that can navigate through narrow spaces [4], artificial skin with multidimensional sensors [5], skin-like large-area strain and pressure sensor [6], graphene–ZnO nanofiber for UV sensing [7], soft curvature sensors for joint angle proprioception [8, 9], deformable and mechanically tuneable fluidic antennas [10], and many more.

The community is striding toward integrating more functionality into complex systems which include soft-components. Integrated circuit (IC) microelectronics packages—such as microcontrollers, amplifiers, voltage regulators—are made from hard materials such as epoxy and high-modulus metals. These ICs provide a means for delivering practical functionality to soft-systems, including: (i) procedural control; (ii) amplification and feedback; and (iii) digital communications. The ability to deliver robust, integrated, soft electronics systems will make an important step in the evolution of soft devices.

1.2. Challenges in integrating Gallium-based microfluidic devices into electronic systems

Gallium-based microfluidic electronic devices usually consist of a soft silicone substrate with embedded liquid metal channels formed using soft-lithography. Conventional copper wires, which are commonly used to connect sub components in hard electronic devices by soldering, are not suitable for interconnecting eutectic liquid-metal microfluidic devices. Copper wires have a high bending moment, meaning that any mechanical reaction force acting upon the surrounding soft material can cause delamination, and device failure. Figure 1(a) provides a schematic of the mechanical displacement of a copper wire inside the fluidic channel. Delamination of the silicone, or movement of the wire, can cause a poor and unstable connection or a leak of eutectic liquid metal from the channels. Gallium-based liquid alloys are covered by a thin film of gallium-oxide [11]. This oxide forms a solid oxide 'skin' which affects the wetting dynamics of this complex fluid [12]. Gallium-oxide film is a semiconducting material [13] which means if a wire does not connect to the bulk-liquid, but is in-contact with the surface of the liquid, it is is likely to form a rectifying junction. Figure 1(d) shows the condition when a metal wire is inserted into a micro-channel and is wetted by highly conductive Galinstan, this configuration results in a stable connection. Figure 1(c) shows an unstable connection between the metal wire and the Galinstan, where the displaced wire only makes electrical-contact with the gallium-oxide skin. The displacement shown by figure 1(c) is often irreversible due to the surface tension of the oxide. In summary, single-core copper-wire is a poor material for making strong-and-stable connections between printed circuit boards and eutectic liquid-metal sub-systems. Therefore, there is a need of a material used for connections with high conductivity and mechanical flexibility.

Several studies have been focused on making soft microfluidic sensors, but little work has been conducted into finding suitable materials for making robust interconnect. In 2015, Lessing *et al* [14] proposed a solution to the interconnect problem by using a composite of metal wool embedded in a silicone elastomer. Metal-wools usually have centimetre-scale size and need to be soaked in the pre-polymer and degassed. Due to the amorphous structure of the steel-wool, and the soaking step, it is difficult to imagine how one would use this interconnect system to integrate a sensor with a small form-factor microcontroller, for example.

Park *et al* designed a soft artificial skin [5] which uses multiple layers of microfluidic channels embedded in an elastomeric substrate. These channels are filled with eutectic gallium indium (eGaIn). The system is used to detect multi-axial strain and normal pressure. The researchers used thin single-core copper wire as interconnect to an external data-logger. Similar connection methods have also been used in other research work, such as Vogt *et al* [15], Tabatabai *et al* [16], Park *et al* [17], Majidi *et al* [9], and Kubo *et al* [18]. Zhang *et al* reported on a novel method for integrating solid-state ICs directly eGaIn microfluidics in an elastomer package, by including the package at the casting-step [19]. Zhang *et al* used steel needles to inject the eGaIn into the microchannels and then left these needles in-place to act as the external electrical-connection. Each of these systems has drawbacks in the interconnection to other devices, and these limitations hinder the uptake of the soft-sensor devices into integrated systems.

1.3. Conductive thread can be used as an interconnect material for integrated soft systems

Our approach to solve the interconnection-problem is to use conductive thread. This thread is a low-cost commodity material made of steel fibre which is commonly used to make electrically conductive smart-textiles. We used this material to fabricate interconnect for an integrated electronics system. Figure 2 shows the integrated system which contains a sensor, interconnect, and a flexible printed circuit board. The printed circuit board provides a bridge, an amplifier, a microcontroller and LED outputs. The conductive thread lies in a serpentine shape (shown by figure 2(b)) and form a mechanically, and electrically, robust connection between the soft microfluidic pressure sensor and the flexible printed circuit board (PCB). We made the pressure sensor via soft-lithograpy using a silicone substrate (Ecoflex 00-50), and we filled the channel with a gallium-indium-tin eutectic alloy (Galinstan) that contains 68.5% gallium, 21.5% indium, and 10% tin. We made this alloy from the constituent metals, and we chose the proportions

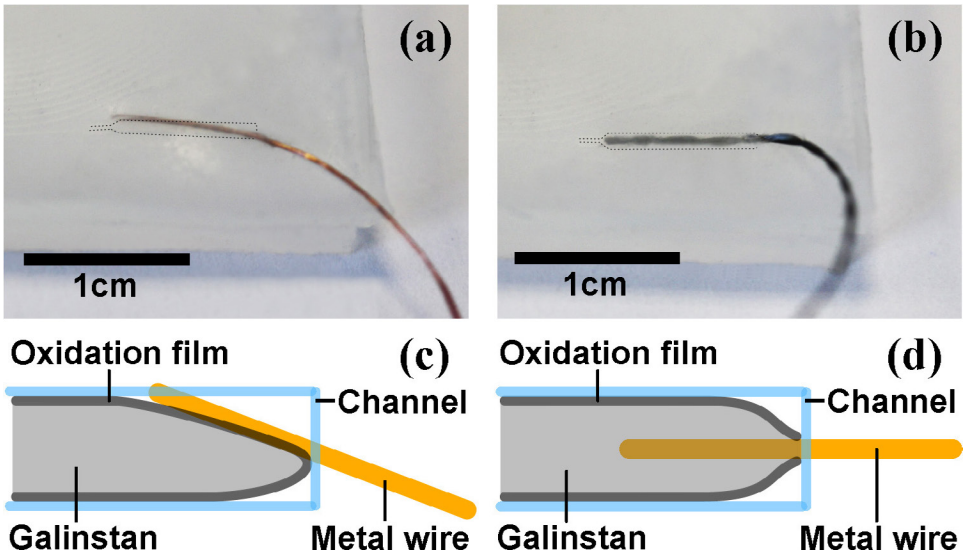

Figure 1. (a) A single-core copper wire inserted into a microfluidic channel in an Ecoflex substrate. Due to the high-bending moment and rigidity of the wire, when the external part of the wire moves it causes movement inside the channel. This movement can lead to delamination and degradation of the device. (b) When conductive thread is inserted into a microfluidic channel in an Ecoflex substrate then external movement does not affect the position of the wire inside the channel. (c) Schematic showing a poor connection between the wire and the liquid metal. The copper wire has moved out of the bulk-liquid and only touches the semi-conducting gallium-oxide film. (d) Schematic showing a good connection between the liquid-metal and a wire. The wire is wetted by the eutectic, and makes an electrical connection to the conductive bulk-liquid.

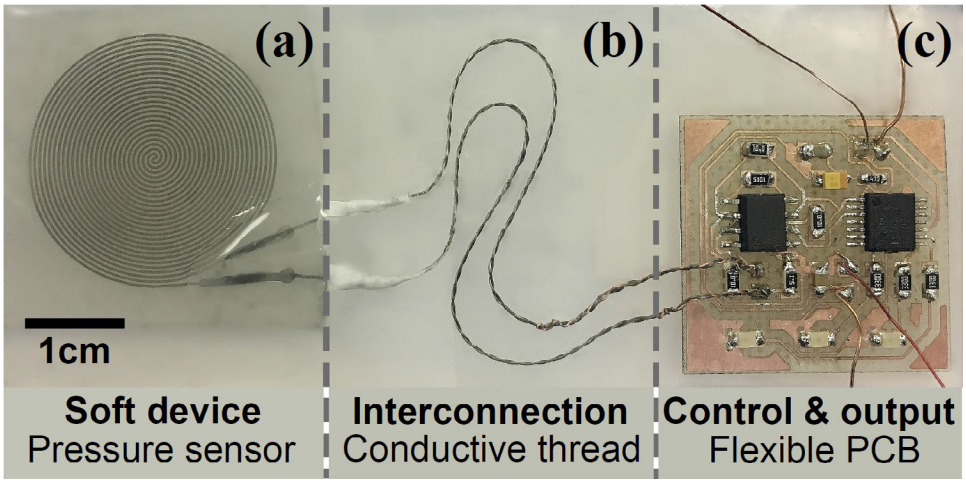

Figure 2. Top view of the integrated soft pressure sensing system. (a) Normal-force pressure sensor made with a Galinstan-filled microfluidic-channel encapsulated in an Ecoflex substrate. (b) Conductive thread is used as interconnection between the pressure sensor and the flexible PCB. The serpentine shape provides strain-relief. (c) A flexible PCB consisting of hard electronic components, including a bridge circuit, an amplifier, a microcontroller, and LEDs.

to ensure that the eutectic was liquid at room temperature, it has a melting point of −19 °C [11]. The PCB is 18 μm (0.5 Oz) copper based on a 200 μm flexible FR4 substrate.

We chose conductive thread as the best candidate for the connection between the pressure sensor and the flexible PCB due to the combination of its electrical and mechanical properties. Conductive thread can provide an electrically conductive path axially along the fibre bundle as well as it is flexible out-of-plane. As shown in figure 1, conductive thread presents mechanical stability within the channels when moved or deformed, providing a robust electrical connection.

We inserted one piece of conductive thread and one piece of copper wire (each of the same diameter) into two equal-volume droplets of galinstan. We observed the deformation of the complex-liquid surface as we withdrew the wires from the droplets. Figure 3 provides photographs taken immediately before the wires detached from the droplets. This figure shows that conductive thread (3(a)) is wetted more than the copper (3(b)).

2. Methods

2.1. Design and fabrication

2.1.1. Design of a rapid-prototyping technique for soft-lithography moulds. We developed a novel, rapid, and reliable way of making soft-lithography masters. Figure 4 illustrates the fabrication process: (i) we applied a piece of self-adhesive

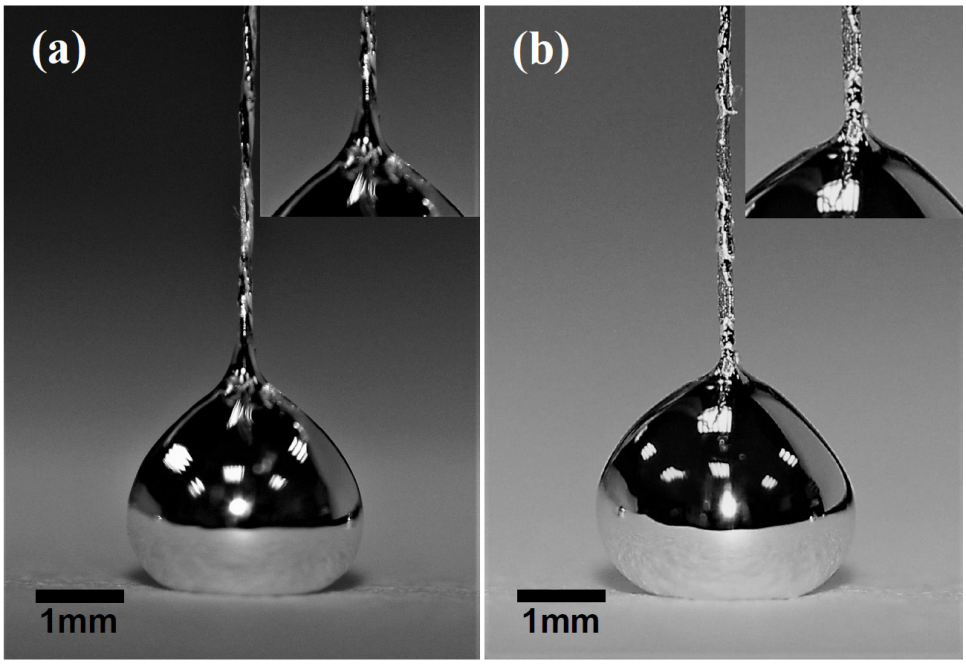

Figure 3. Photographs showing the withdrawal of (a) conductive thread and (b) copper wire from a galinstan droplet. The galinstan wets more onto the conductive thread than the copper wire.

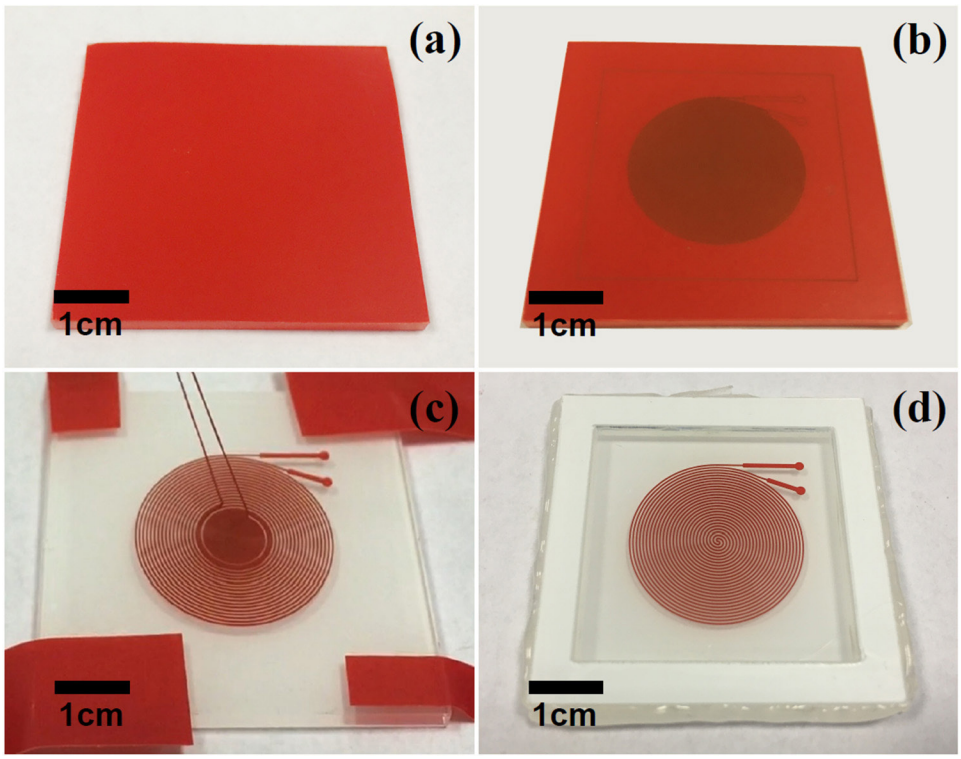

Figure 4. Illustration of fabrication process of the soft-lithography mould. (a) We stuck a piece of 0.15 mm thick self-adhesive vinyl onto an acrylic substrate; (b) we cut the vinyl using a laser micro-machining system. The channel width and the gap-width between channels are both 200 μm; (c) we weeded out the unwanted vinyl; (d) finally we glued a 2 mm-think acrylic frame onto the substrate to form a mould for soft-lithography.

vinyl (Brand: d-c-fix®, model number: CRAFTPK20) onto the surface of a 2 mm-thick acrylic board (2 mm Acrylic Cast, AMARI), and removed bubbles using a roller; (ii) we used an LPKF Protolaser U3 laser micromachining to cut out the designed channel profile on vinyl. The profile of the channels can be cut precisely since the laser system has an error rate less than 5%; (iii) we weeded out the unwanted parts of vinyl and no residue remained on the surface as this vinyl is designed to be removed without leaving residue; (iv) we glued another 2 mm-think acrylic frame onto the acrylic substrate as the final step of making a mould for soft-lithograpy.

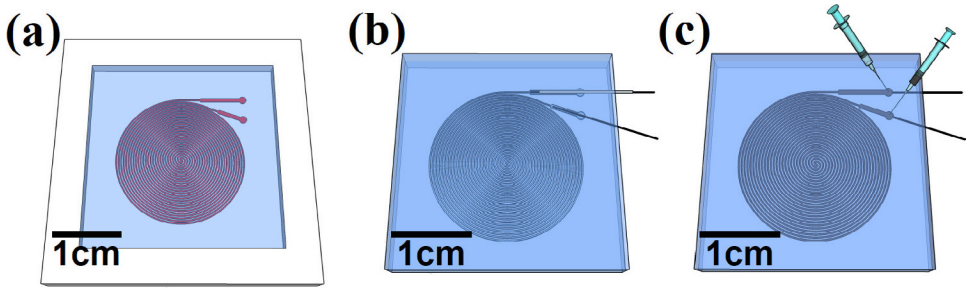

Figure 5. Fabrication process of the microfluidic pressure sensor. (a) We poured uncured Ecoflex into the soft-lithography mould; (b) we bonded another 2 mm blank piece of Ecoflex on to the patterned Ecoflex to seal the channel. We used a cannula to insert the conductive thread into the channels; (c) we injected galinstan into the channel with two needles, one to fill and one to vent. The syringes are not shown to scale.

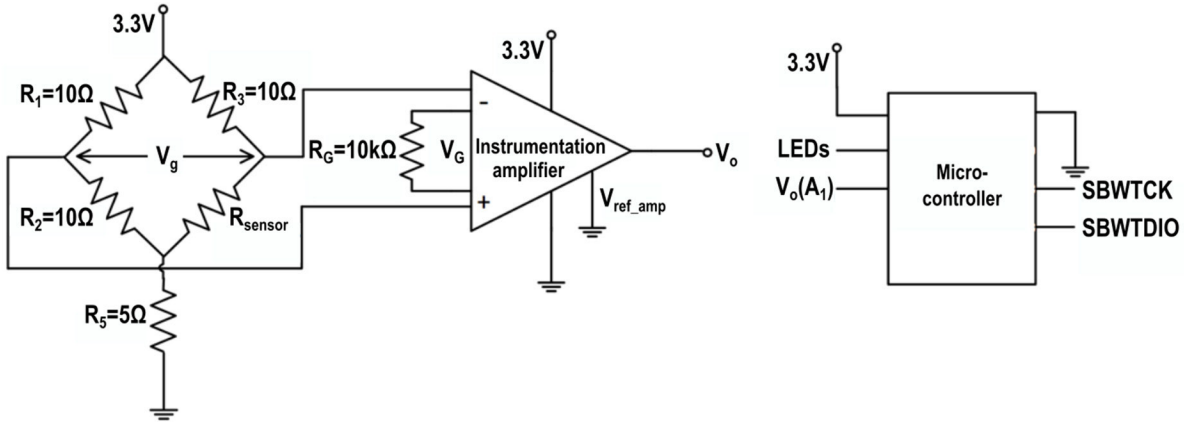

Figure 6. Circuit schematic of the system on the flexible PCB. The pressure sensor is a variable-resistance in the Wheatstone bridge network. The voltage output (V_0) from the instrumentation amplifier is the voltage input to the analog-to-digital (ADC) converter in the microcontroller (12-bit ADC on the Atmel SAM3X8E ARM Cortex-M3 or 10-bit ADC on the MSP430F2012 MCU). The MCU is programmed using 2-wire JTAG via SBWTCK (Spy-Bi-Wire Test Clock) and SBWTDIO (Spy-Bi-Wire Test Digital IO). The MCU outputs to three LEDs which light in-proportion to the applied normal pressure.

Using this new method, we can fabricate a custom-designed microscale soft lithography mould in just a few minutes. The smallest channel-width that we achieved using this method is 100 μm. The smallest linewidth that the laser micro-machining system can produce is 30 μm and the minimum distance between lines is 70 μm. Theoretically, we can fabricate any 2D structure with the fabrication procedure we proposed, as long as size of the design can fit the laser machine. When we produce a soft-lithography master with vinyl, we tend to get stable and reliable production results when the line width and space width are both equal or greater than 200 μm. This limit of 200 μm is limited by the physical removal of the vinyl, not the resolution of the laser system. This type of soft-lithography mould we fabricated can be used approximately 10 times before the vinyl loses adhesion to the acrylic substrate. This method is rapid and convenient for miocrofluidics and soft-systems researchers.

2.1.2. Design and fabrication of the microfluidic pressure sensor. The eutectic alloy we used consists of 68.5% gallium, 21.5% indium, and 10% tin, its bulk-resistance is $4.3 \times 10^{-6}\,\Omega\,\mathrm{cm}^{-1}$. We used this resistance value and the known dimensions of the vinyl film mould to design the length of the channel in the pressure sensor to be 10 Ω.

Figure 5 shows the fabrication process for this microfluidic pressure sensor. (i) We mixed a 1:1 volume ratio of Part A and Part B Ecoflex 00-50 (Reynolds Advanced materials), degassed the pre-polymer, poured the liquid into in the soft-lithography mould, and then placed the filled-mould into a convection oven at 65 °C for 20 min. (ii) We bonded another 2 mm-thick blank piece of Ecoflex to the casted piece of Ecoflex. We used a cannula to insert the conductive thread into the channels in the Ecoflex substrate. The resistance of the conductive thread is $27\,\Omega\,\mathrm{m}^{-1}$ (Smooth conductive stainless-steel thread bobbin, Sparkfun Electronics). (iii) We injected galinstan into the channels using a syringe and a needle, and we inserted a second needle into the outlet of the channel to vent air. To ensure that the conductive thread is fully wetted, we injected the galinstan 1 cm further into the channel than the protrusion of the embedded conductive thread. Finally, we used silicone epoxy to seal the holes that we created during the injection process. This seal prevents the wire being pulled out and prevents liquid metal-alloy leaks when the sensor is pressed.

2.1.3. Design of the electronic system. Figure 2(c) shows a top view of PCB in the integrated soft electronic system. In this flexible PCB, there is a Wheatstone bridge, an instrumentation amplifier, a microcontroller, and three LEDs as output. Figure 6

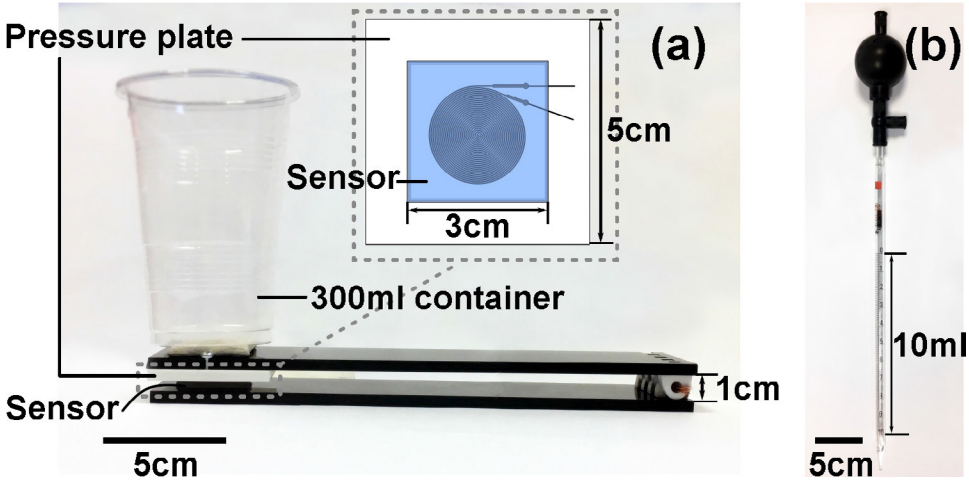

Figure 7. Experimental set-up. (a) A system for applying uniform pressure over the surface of the pressure sensor. The thickness of the pressure-plate is 6 mm and the thickness of the sensor is 4 mm, by designing the hinge to be 1 cm the plates are kept parallel; (b) we used a 10 ml-size pipette to dispense accurate volumes of water into the container shown in (a). We found this volumetric approach to be a convenient way to refine the increments of weight applied to the sensor.

shows the circuit design of the flexible PCB. The Wheatstone bridge is used to measure the variable resistance of the pressure sensor, and the instrumentation amplifier (INA 128, Texas Instruments®) is used to amplify the voltage difference from the bridge circuit. The output from the instrumentation amplifier is fed to the 10-bit analog-to-digital converter (ADC) in the microcontroller. The relationship between the resistance of the microfluidic sensor and the ADC value is shown by formulas (1)–(4). In these formulas, v_{ADC} is the ADC value measured by the microcontroller and V_{A1} is the voltage on pin $A1$ of the microcontroller, N is the number of bits in the ADC, and $V_{\mathrm{ref_MCU}}$ is the reference voltage of the ADC (3.3 V in this circuit). The bridge circuit consists of four resistors, R_1, R_2, R_3 and R_x, which is resistance of the microfluidic sensor. When the sensor is pressed, the cross-sectional area of the channel changes accordingly, and so does the value of R_x. The gain of the instrumentation amplifier is G, and this value depends on R_{G} in the circuit. Increasing the value of R_{G} can enhance the measurement sensitivity of the system while decreasing the value of R_{G} can improve measurement range of the system.

$$v_{\mathrm{ADC}} = \frac{V_{A1}}{2^N} \times V_{\mathrm{ref_MCU}} \tag{1}$$

$$V_{A1} = V_{\mathrm{g}} \times G \tag{2}$$

$$V_{\mathrm{g}} = \left(\frac{R_x}{R_3 + R_x} - \frac{R_2}{R_1 + R_2} \right) \times V_{\mathrm{s}} \tag{3}$$

$$G = 1 + \frac{50\,\mathrm{k\Omega}}{R_{\mathrm{G}}} \tag{4}$$

Many of the previously reported soft-sensors have been evaluated using external instrumentation such as a digital-multimeter, an LCR meter or four-point probes [17, 20, 21]. Including the Wheatstone bridge as an integral part of the system offers the following benefits: (1) The system can be powered with a low-voltage supply or even a 3.3 V button battery. (2) The Wheatstone bridge is based on the concept of a differential measurement which can be extremely accurate [22] and provides robustness to thermal-drift.

We used the MSP430F2012 microcontroller in this system as it offers a 10-bit ADC and is capable of low-power modes. We used three LEDs to visually demonstrate compression of the pressure sensor.

Table 1. Values of minimum load required to lose connection (detached wire/thread from the channel).

	Threads		Copper	
	Extension (mm)	Load (N)	Extension (mm)	Load (N)
1	10.003 23	1.505 69	8.67	1.124 97
2	10.17	1.347 25	7.836 69	1.002 57
3	14.169 96	1.8146	9.5033	1.106 32
4	7.170 11	0.934 95	9.836 57	1.302 65

2.2. Design of the experimental system and tests

To test the physical limitation of the pressure sensor and the mechanical robustness of the proposed conductive thread connection, we performed: (i) A tensile test on three batches of samples at a strain rate of 100 mm min^{-1} using an INSTRON 3367; (ii) A tensile test on two batches of samples with copper and conductive thread connections at a strain rate of 100 mm min^{-1} using an INSTRON 3367.

Figure 7 shows a photograph of the system we used to apply pressure for the pressure sensing system. In order to apply pressure uniformly, we made a flat clip with a pressure-plate which fully overlapped the sensor. As shown in figure 7(a), we placed the sensor at the centre of the pressure plate. We placed a 300 ml container on the top of the indenter. We used a pipette as shown in figure 7(b) to fill the container, and this volumetric approach allowed us to refine the applied weight in varying increments. At 25 °C, the weight of 1 ml water is 1 g, so 10 ml water results in a weight of 10 g, i.e. about 9.8 N on the pressure sensor. The distance between

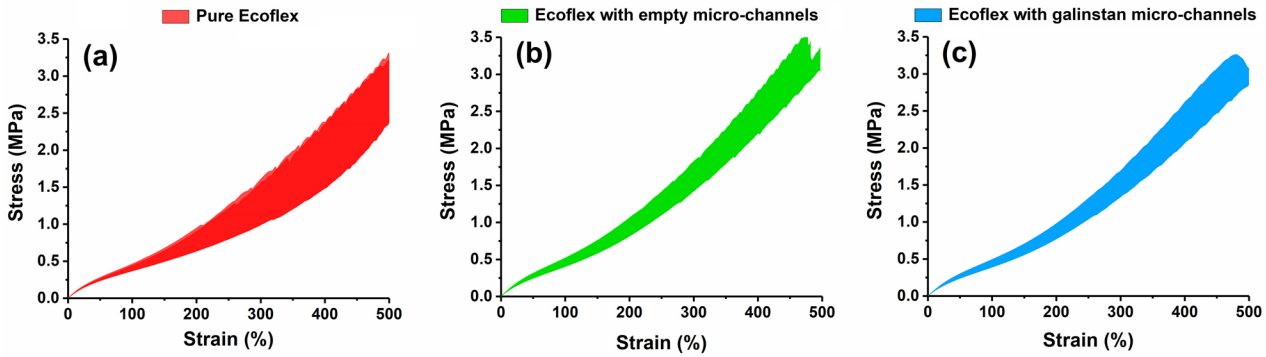

Figure 8. Stress versus strain curves of (a) pure Ecoflex; (b) Ecoflex with empty microchannels; and (c) Ecoflex with microchannels filled with Galistan. The red, green, and blue areas represent range of stress versus strain curves of four samples in each batch.

the parallel-plates of the clip is 1 cm, which is the sum of thickness of the pressure plate and the pressure sensor. The area of the pressure-plate is $5 \times 5\,\text{cm}^2$, and the area of the sensor is $3 \times 3\,\text{cm}^2$, which is the effective pressing area.

We designed five experiments using this system, to improve the resolution when characterising the pressure sensor we used a 12-bit ADC on an Atmel SAM3X8E ARM Cortex-M3 rather than the 10-bit ADC on the final integrated device, which used an MSP430F2012 MCU.

Experiment (1) To test the sensitivity and resolution of the pressure sensing system, we measured the change in the ADC value (ΔADC) when we varied the weight on the sensor from 0 g to 300 g with a step-size of 10 g.

Experiment (2) To test the hysteresis properties of the pressure sensor we increased the weight from 0 g to 300 g and then back from 300 g to 0 g.

Experiment (3) To measure the full-range, and get a calibration curve we increased the weight from 0 g to1080 g using weights.

Experiment (4) To test the reliability of the sensing system we powered on the sensing system at zero-applied load and recorded the change in the ADC value.

Demonstration To visually display the high resolution of our pressure sensing system we used coins as weights to press the sensor. The LEDs on the PCB were used to visually display the number of coins on the sensor.

3. Results

In order to investigate the mechanical properties of our system, a tensile testing was carried out using an INSTRON 3367 fitted with a 250 N load cell at a strain rate of 100 mm min^{-1}. We fabricated three sets of samples with the following dimensions: $50 \times 30 \times 4$ mm. Each set of samples were tested up to a strain of 500%, including neat Ecoflex, Ecoflex with empty microchannels and Ecoflex with microchannels filled of Galistan. Figure S1 (stacks.iop.org/JMM/28/054001/mmedia) in the supplementary information shows photographs in process of this experiment. Stress and strain curves of the three sets of samples were plotted as shown in figure 8.

In the results, the stress and strain curves of the three batches of samples do not show meaningful difference. The microchannel and the gallistan does not affect the overall mechanical behaviour in comparison to the pure Ecoflex. This might be due to the small size of the microchannel comparing to the thickness of the samples as well as the small amount of conductive-liquid within. In addition, each sample can be stretched to a strain up to 500% without failure. When the strain was higher than 500%, the samples slipped out from the clamps during the test. However, according to the datasheet of Ecoflex, elongation at break of Ecoflex 00-50 is 980% (tested with ASTM D-412). Therefore, we believe that the stretchability of the sensor is enough for our pressure sensing system.

An additional test was carried out in order to evaluate the mechanical robustness of the proposed connection. We fabricated two sets of samples. In each sample, copper wire or conductive thread was inserted into Ecoflex with a dimension of $30 \times 20 \times 4$ mm and then sealed with sil-epoxy, as shown in figure S2. In this experiment, the Ecoflex were clamped from the bottom and the thread or copper wire was clamped from the top. We used INSTRON 3367 fitted with a 250 N load cell to stretch the thread or copper wire at a strain rate of 100 mm min^{-1} until it detached. The minimum load and extension required to detach the thread/wire are shown in table 1.

As shown in table 1, although the fabrication errors may affect the experimental results, the conductive thread needs more load and extension to be pulled out of Ecoflex substrate than copper wire in general. An average minimum load of 1.40 ± 0.37 N and 1.13 ± 0.12 N is needed in order to detach the conductive thread and copper wire connections from the channel respectively. We believe this test demonstrates that the conductive thread exhibits a higher mechanical robustness than using a copper wire for our system.

Results from the four experiments that carried with the pressure applying system are shown by figure 9. From the perspective of an electronic system, it is the most intuitive to show the relationship between the value of the ADC read by the microprocessor and the pressure on the sensor. Therefore, ΔADC was used in our results instead of ΔR.

Figure 9(a) shows the sensitivity and resolution of the system by tracking the variation of the 12-bit ADC output—ΔADC—in the 0 Pa–300 Pa pressure range, with a step of ~100 Pa. Good linearity is observed when the load above 500 Pa and when the pressure is spread evenly. In the measured range, the value of the 12-bit ADC increased by 143

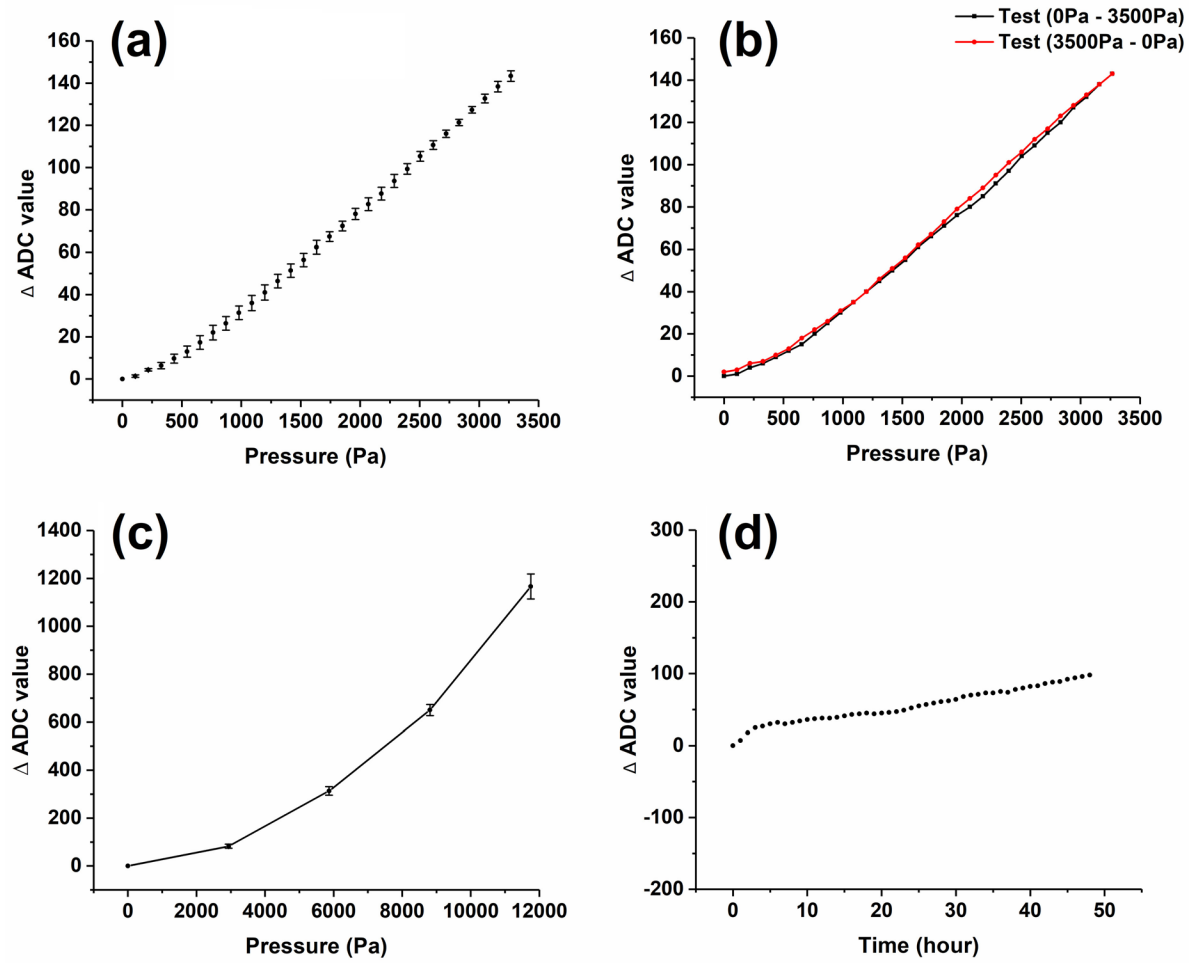

Figure 9. Results of four experiments to characterise the pressure sensor: (a) sensitivity and resolution test over a pressure range of 0 Pa–3500 Pa, with an increment of around 100 Pa. Points show the mean values of ΔADC and the error bar on the *Y*-axis shows one standard deviation $n = 7$; (b) hysteresis test. We increased the pressure on the sensor from 0 Pa to 3500 Pa (black curve) then decreased it from 3500 Pa to 0 Pa (red curve); (c) calibration curve of ΔADC when we increased the weight over a large range from 0 Pa to 12 kPa, using multiple 270 g weights; (d) reliability test. This curve shows the baseline change of the ADC from sample 1 at $t = 0$ to 48 h. This drift can be corrected by tracking the baseline value and taking the instantaneous ΔADC.

units. This experiment was conducted three times and the standard deviation of each point on the curve is less than 4.

Figure 9(b) shows the result of the hysteresis test. In this experiment, we increased (in ~100 Pa increments) the pressure on the pressure sensor from 0 Pa to 3500 Pa and then decreased it back to 0 Pa. The results show that the sensor is has little to zero hysteresis.

We tested a high-load range from 0 Pa to 12 kPa and the results are shown by figure 9(c). We conducted this experiment seven times. In the measured range, the value of the 12-bit ADC increased by around 1166 units. The results show that the larger loads give more spread in the data; the largest standard deviation is 52 at the last data point. The sensor shows a quadratic relationship between applied force and electronic output. The sensitivity increases as more pressure is added and this may warrant future investigation for a design with enhanced sensitivity.

We conducted an investigation into baseline-drift over a long period of time. Figure 9(d) shows the reliability test that we conducted for 48 h. The 12-bit ADC value in the no-load sensing system increased by 100 units in a linear fashion, but this drift is mitigated in the measurement system by taking instantaneous differential measurements.

To show, visually, the high sensitivity of our integrated pressure sensing system using the MSP430F2012 MCU: we used coins (UK £1) to weigh down the sensor. Figure 10(a)–(d) illustrates that when there was no weight on the sensor, no LED lights up, two coins light one LED and four coins light two LEDs. The weight of a one pound coin is 9.5 g, the diameter of the coin is 22.55 mm. Two coins, therefore, create 0.18 N force and ~200 Pa on the sensor.

4. Discussion

Our results clearly show that the proposed pressure sensing system has a high sensitivity in the low-Newtons of force range. Within the pressure range of 500–3500 Pa, the relationship between the 12-bit ADC value in the system and the weight on the sensor shows a linear relationship. Every 100 Pa increment in pressure causes an increment of five units in the 12-bit ADC value. After repeating three times the

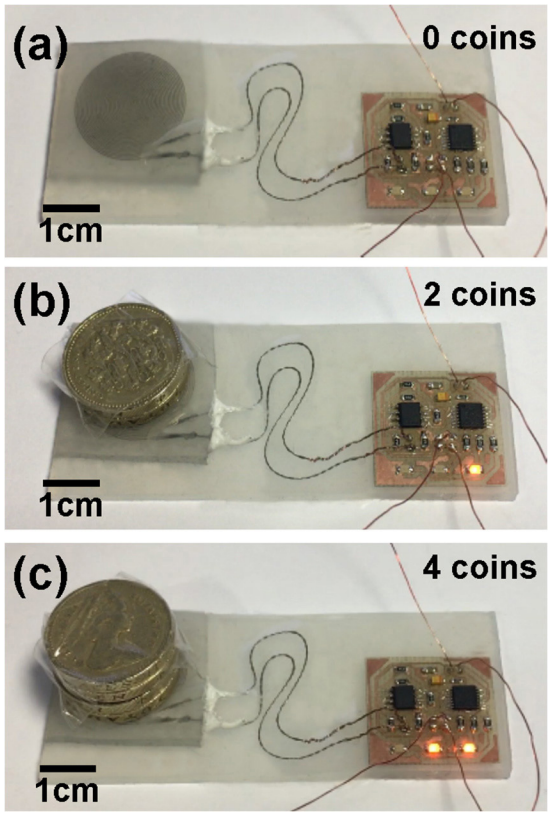

Figure 10. Demonstrating the sensitivity of the integrated soft system. We programmed the system to light LEDs in proportion to the applied force (a) no coins applied (b) two coins applied (c) four coins applied.

hysteresis experiment, we found out that the largest standard deviation is not higher than four (with a maximum 12-bit ADC variation of 143). However, when applying a high-load (12 kPa), the largest standard deviation goes up to 52 (with a maximum 12-bit ADC value of 1166). In 7 repeats of the high-load (12 kPa) experiment (with a maximum 12-bit ADC value of 1166) then the largest standard deviation is 52. These results show a good reliability and feasibility of our system. As show in figure 9(b), this pressure sensing system exhibits a low hysteresis. The test in figure 9(b) has proved this pressure sensing system has low hysteresis. In summary, we used conductive thread to integrate, robustly, a microfluidic sensor into an electronic system. This integration means that the resulting soft electronic system benefits from the functionality of conventional solid-state electronic system and exhibits the mechanical properties of soft and flexible materials.

We used a Wheatstone bridge and instrumentation amplifier in this system, the voltage that is measured by the microcontroller depends on both the voltage output of the Wheatstone bridge, and on the gain of the instrumentation amplifier. The gain of the amplifier depends on the choice of R_G. We do not discuss the influence of R_G to the sensing system as this is basic background electronics theory; increasing the gain of the instrumentation amplifier can give the sensing system higher resolution but will reduce the corresponding measurement range, and vice versa. The system we presented in the paper is supplied by 3.3 V, which means the instrument amplifier that connected to the bridge circuit has a maximum output of 3.3 V. When output voltage of the instrument amplifier reaches 3.3 V, even resistance of the sensor keeps increasing, the voltage output will not change. In conclusion, ADC value which can represent voltage at the analogue I/O port in the microcontroller, will increase when the sensor is pressed, then remain the same at its maximum value when the pressure reaches a boundary.

In the 48 h stability test, the ADC value in the system slightly and gradually increased. This increment indicates that the resistance of the microfluidic sensor was increasing. The resistance increase may be a result of temperature increase due to joule-heating or may be due to further oxidation of galinstan in the channel. To mitigate this drift, in future work, we could use a resistor which has ten or hundred times higher resistance than the microfluidic sensor before matching the Wheatstone bridge. This method will reduce the resolution in the system as it will reduce the current passing though the galinstan microfluidic pressure sensor.

5. Conclusions

In this study, we found that conductive thread is a good replacement for conventional metal wires to be used as interconnect in soft sensing systems based on liquid-metal microfluidic devices. We also presented a rapid and reliable method for fabricating soft-lithography moulds in the research laboratory. We built a pressure sensing system using conductive thread as the interconnection between microfluidic sensor and flexible PCB populated with solid-state electronic components. Using this integrated electronic system we demonstrated its ability to sense pressure with high resolution. Using these methods we hope that more researchers will be able to integrate soft devices with electronic systems. By enabling strong-and-stable electrical connections we hope to enable the community to be one-step-closer to developing fully integrated soft robotic, or wearable systems.

Acknowledgments

The authors acknowledge funding from the Engineering and Physical Sciences Research Council: Centre for Doctoral Training in Intelligent Sensing and Measurement EP/L016753/1, the Robotarium Capital Equipment and Robotics CDT Capital Equipment EP/L016834/1 and the UK Robotics and Artificial Intelligence Hub for Offshore Energy Asset Integrity Management EP/R026173/1.

ORCID iDs

Adam A Stokes https://orcid.org/0000-0002-6140-619X

References

[1] Wagner S and Bauer S 2012 Materials for stretchable electronics *MRS Bull.* **37** 207–13

[2] Suo Z 2012 Mechanics of stretchable electronics and soft machines *MRS Bull.* **37** 218–25

[3] Ilievski F, Mazzeo A D, Shepherd R F, Chen X and Whitesides G M 2011 Soft robotics for chemists *Angew. Chem., Int. Ed. Engl.* **123** 1930–5

[4] Shepherd R F, Ilievski F, Choi W, Morin S A, Stokes A A, Mazzeo A D, Chen X, Wang M and Whitesides G M 2011 Multigait soft robot *Proc. Natl Acad. Sci.* **108** 20400–3

[5] Park Y-L, Chen B-R and Wood R J 2012 Design and fabrication of soft artificial skin using embedded microchannels and liquid conductors *IEEE Sens. J.* **12** 2711–8

[6] Sahatiya P and Badhulika S 2017 Eraser-based eco-friendly fabrication of a skin-like large-area matrix of flexible carbon nanotube strain and pressure sensors *Nanotechnology* **28** 095501

[7] Sahatiya P and Badhulika S 2015 One-step *in situ* synthesis of single aligned graphene–ZnO nanofiber for UV sensing *RSC Adv.* **5** 82481–7

[8] Kramer R K, Majidi C, Sahai R and Wood R J 2011 Soft curvature sensors for joint angle proprioception *IEEE Int. Conf. Intell. Robot. Syst.* pp 1919–26

[9] Majidi C, Kramer R and Wood R J 2011 A non-differential elastomer curvature sensor for softer-than-skin electronics *Smart Mater. Struct.* **20** 105017

[10] So J, Thelen J, Qusba A, Hayes G J, Lazzi G and Dickey M D 2009 Reversibly deformable and mechanically tunable fluidic antennas *Adv. Funct. Mater.* **19** 3632–7

[11] Liu T, Sen P and Kim C J 2012 Characterization of nontoxic liquid–metal alloy galinstan for applications in microdevices *J. Microelectromech. Syst.* **21** 443–50

[12] Huang Y, Wang Y, Xiao L, Liu H, Dong W and Yin Z 2014 Microfluidic serpentine antennas with designed mechanical tunability *Lab Chip* **14** 4205–12

[13] Chiechi R C, Weiss E A, Dickey M D and Whitesides G M 2007 Eutectic gallium–indium (EGaIn): a moldable liquid metal for electrical characterization of self-assembled monolayers *Angew. Chem., Int. Ed. Engl.* **47** 142–4

[14] Lessing J, Morin S A, Keplinger C, Tayi A S and Whitesides G M 2015 Stretchable conductive composites based on metal wools for use as electrical vias in soft devices *Adv. Funct. Mater.* **25** 1418–25

[15] Vogt D, Menguc Y, Park Y and Wehner M 2013 Progress in soft, flexible, and stretchable sensing systems *Proc. of the Int. Workshop on Research Frontiers in Electronics Skin Technology at ICRA vol 13*

[16] Tabatabai A, Fassler A, Usiak C and Majidi C 2013 Liquid-phase gallium–indium alloy electronics with microcontact printing *Langmuir* **29** 6194–200

[17] Park Y L, Chen B, Majidi C and Wood R J 2012 Active modular elastomer sleeve for soft wearable assistance robots *IEEE Int. Conf. Intell. Robot. Syst.* pp 1595–1602

[18] Kubo M, Li X, Kim C, Hashimoto M, Wiley B J, Ham D and Whitesides G M 2010 Stretchable microfluidic radiofrequency antennas *Adv. Mater.* **22** 2749–52

[19] Zhang B, Dong Q, Korman C E, Li Z and Zaghloul M E 2013 Flexible packaging of solid-state integrated circuit chips with elastomeric microfluidics *Sci. Rep.* **3** 1098

[20] Hirsch A, Michaud H O, Gerratt A P, de Mulatier S and Lacour S P 2016 Intrinsically stretchable biphasic (solid–liquid) thin metal films *Adv. Mater.* **28** 4507–12

[21] Chossat J B, Park Y L and Wood R J 2013 A soft strain sensor based on ionic and metal liquids *IEEE Sensors J.* **13** 3405–14

[22] Giordano J 1997 On the sensitivity, precision and resolution in DC wheatstone bridges *Eur. J. Phys.* **18** 22–7

Supplemental Information

In order to investigate the mechanical properties of our system, a tensile testing was carried out using an INSTRON 3367 fitted with a 250 N load cell at a strain rate of 100 mm min^{-1}. Figure S1 shows photographs in experimental process. All the samples we used in this tensile test has a dimension of $50 \times 30 \times 4$ mm.

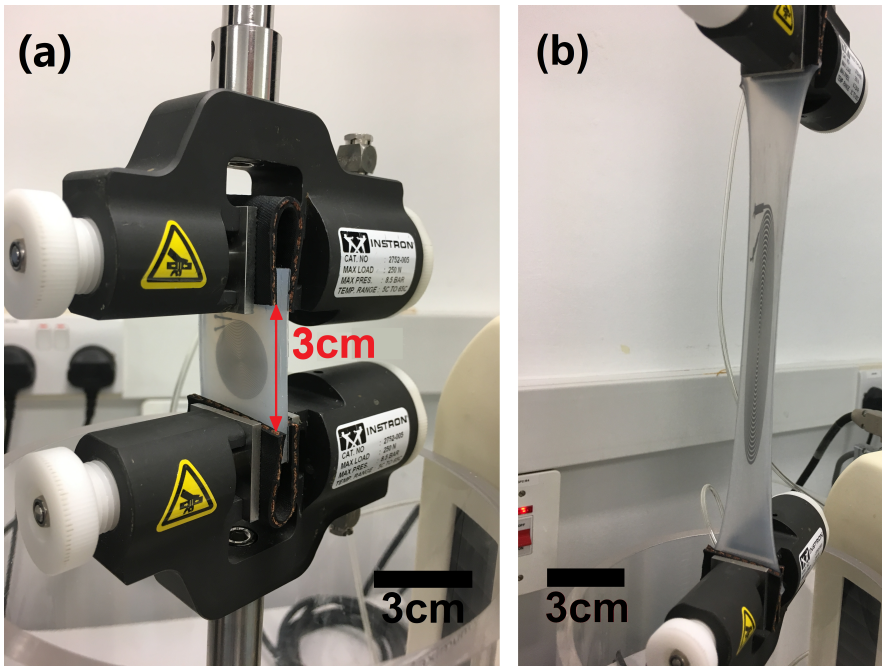

Figure D.1.: *Ecoflex pressure sensor under tensile test.* A $50 \times 30 \times 4$ mm Ecoflex substrate with micro-channels filled of galinstan was under a tensile test with an INSTRON 3367 fitted with a 250 N load cell.

Supplemental Information

In order to evaluate the mechanical robustness of the proposed connection, we fabricated two sets of samples. In each sample, copper wire or conductive thread was inserted 1 cm into Ecoflex with a dimension of $30 \times 20 \times 4$ mm and then sealed with sil-epoxy, as shown in Figure D.2.

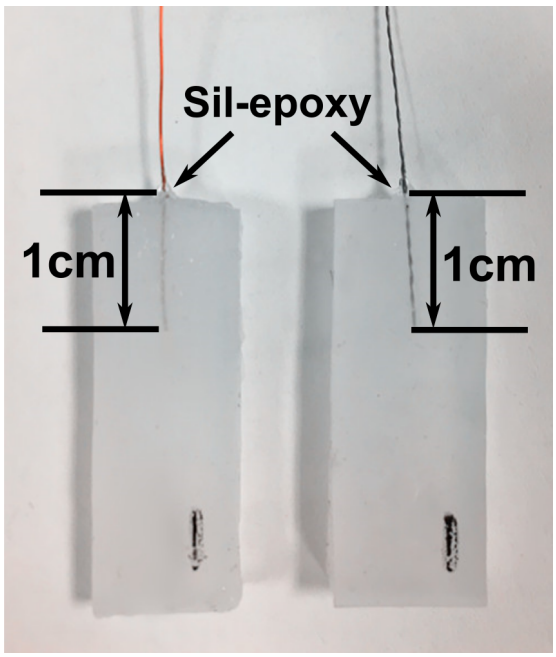

Figure D.2.: *Samples used to test mechanical robustness of the connection* between Ecoflex substrate and copper wire or conductive thread.

APPENDIX E

Soft RFID Sensors: Wireless Long-range Strain Sensors Using Radio-frequency Identification

Journal: Soft Robotics

Authors: Lijun Teng, Kewen Pan, Markus P. Nemitz, Rui Song, Zhirun Hu, and Adam A. Stokes

Online access to paper:

https://doi.org/10.1089/soro.2018.0026

SOFT ROBOTICS
Volume 00, Number 00, 2018
Mary Ann Liebert, Inc.
DOI: 10.1089/soro.2018.0026

SoRo
Soft Robotics

Soft Radio-Frequency Identification Sensors: Wireless Long-Range Strain Sensors Using Radio-Frequency Identification

Lijun Teng,[1,*] Kewen Pan,[2,*] Markus P. Nemitz,[1,3] Rui Song,[1] Zhirun Hu,[2] and Adam A. Stokes[1]

Abstract

Increasing amounts of attention are being paid to the study of *Soft Sensors* and Soft Systems. *Soft Robotic Systems* require input from advances in the field of *Soft Sensors*. Soft sensors can help a soft robot to perceive and to act upon its immediate environment. The concept of integrating sensing capabilities into soft robotic systems is becoming increasingly important. One challenge is that most of the existing soft sensors have a requirement to be hardwired to power supplies or external data processing equipment. This requirement hinders the ability of a system designer to integrate soft sensors into soft robotic systems. In this article, we design, fabricate, and characterize a new soft sensor, which benefits from a combination of radio-frequency identification (RFID) tag design and microfluidic sensor fabrication technologies. We designed this sensor using the working principle of an RFID transporter antenna, but one whose resonant frequency changes in response to an applied strain. This new microfluidic sensor is *intrinsically stretchable* and can be reversibly strained. This sensor is a *passive* and *wireless* device, and as such, it does not require a power supply and is capable of transporting data without a wired connection. This strain sensor is best understood as an RFID tag antenna; it shows a resonant frequency change from approximately 860 to 800 MHz upon an applied strain change from 0% to 50%. Within the operating frequency, the sensor shows a standoff reading range of >7.5 m (at the resonant frequency). We characterize, experimentally, the electrical performance and the reliability of the fabrication process. We demonstrate a pneumatic soft robot that has four microfluidic sensors embedded in four of its legs, and we describe the implementation circuit to show that we can obtain movement information from the soft robot using our wireless soft sensors.

Keywords: soft sensing, RFID, antenna, wireless, passive

Introduction

Soft sensors

Soft Sensors is an application-driven research field and has received much attention in recent decades. A soft sensor is a measuring tool that is made of a single polymer or a mixture of soft polymers. These soft polymers are usually *softer* than the materials they interact with, which make them inherently safe. One prominent example is electronic skin. Electronic skin is also called ''second skin'' referring to its softness; electronic skin is *softer* than human skin and makes it to an ideal substructure for sensor arrays.[1] A close relative of the field *Soft Sensors* is the field of *Soft Robotics*. One motivating factor for using *Soft Robotics* is the fact that the materials of the robots are *softer* than the environments with which they interact, and this compliance makes them ideal for applications involving human–robot interaction.[2–4]

[1]The School of Engineering, Institute for Integrated Micro and Nano Systems, The University of Edinburgh, The King's Buildings, Edinburgh, United Kingdom.
[2]Microwave and Communication Systems Group, School of Electrical and Electronic Engineering, University of Manchester, Manchester, United Kingdom.
[3]Department of Computer Science and Engineering, University of Michigan, Ann Arbor, Michigan.
*This is a joint article and these authors contributed equally to this work.

© Lijun Teng et al. 2018; Published by Mary Ann Liebert, Inc. This Open Access article is distributed under the terms of the Creative Commons License (http://creativecommons.org/licenses/by/4.0), which permits unrestricted use, distribution, and reproduction in any medium, provided the original work is properly cited.

Autonomous agents that *perceive* and act upon their immediate environment (robots) are influenced by sensor research. Sensor research impacts a robots' sensor modalities, sensor accuracy, or measurement range besides others. The concept of integrating sensing capabilities at low cost has also become increasingly important, especially for certain subgroups in robotics, namely soft robotics, modular robotics, and swarm robotics. In such cases, lower cost systems are motivated by *design for manufacturability* allowing one to commercialize or to scale a robot system. In the past decade, the community has started to make soft robotic actuators, such as (1) ionic actuators,[5–7] (2) pneumatic actuators,[8–11] or (3) dielectric actuators[12–14] to just name a few. These actuators can benefit from soft sensors from feedback force control.

Kim *et al.*[15] have proposed a stretchable sensor that is made of curvilinear silicon ribbons in an elastic substrate. This novel work allows high-precision complex active electronics to be densely integrated over a few square centimeters area while achieving high degrees of stretchability, bendability, and twistability. Park *et al.*[16] designed a soft artificial skin with multiple layers of microscale liquid metal channels embedded in an elastomeric substrate to detect multiaxial strain and normal pressure. Single-core copper wire was used in the above researches to interconnect an external data-logger. Other research work, such as Tabatabai *et al.*,[17] Park *et al.*,[18] and Majidi *et al.*[19] have also used similar connection methods.

Although the above-mentioned soft sensors show a promising future for stretchable electronics, they are active sensors that require a power supply and signal processing capabilities, such as a microcontroller with analog–digital converters. As reported in the study of Teng *et al.*,[20] each of these sensing systems has drawbacks in the interconnection to other devices, and these limitations hinder the uptake of the soft sensor devices into integrated systems. Embedding several such sensors in an untethered soft robotic system is difficult due to power consumption and practical considerations in wiring.

Stretchable antennas that have great potential to be used as wireless soft sensors have been reported in recent years. Stretchable liquid metal antennas have been presented by Cheng *et al.*,[21,22] Kubo *et al.*,[23] and So *et al.*[24] Although these antennas have shown fascinating electronic and mechanic properties, they require coaxial radio frequency (RF) connector or hardwiring to connect to external data processing equipment, which limits their capability of being implemented in sensing applications such as movement monitoring.

Huang *et al.*[25] mentioned the idea of integrating a measurement chip in stretchable antennas, but the researchers did not provide the solution of integration. Kim *et al.*[26] demonstrated epidermal electronics using near-field communication; this wireless sensor is biocompatible and achieves sensor reading ranges of a few centimeters. Cheng and Wu[27] also proposed a reversibly stretchable, large-area wireless strain sensor, which can work wirelessly >5 m with a strain limitation of 15%. These studies pave the way for making wireless stretchable antennas that can be used as soft sensors in soft robotic systems.

Design of a new soft radio-frequency identification sensor

In this article, we present the design, fabrication, and characterization of a long-range monitoring wireless strain sensor, which is capable of remotely detecting high tensile dynamic strain up to 50% at >7.5 m. This sensor benefits from a combination of radio-frequency identification (RFID) technology and microfluidic electronics fabrication technology. The proposed sensor is also a configurable RFID tag antenna. The RFID integrated circuit chip we integrated in the proposed sensor has very small dimensions ($0.4\,\text{mm} \times 0.4\,\text{mm} \times 0.2\,\text{mm}$), so it will not affect the deformability of the sensor.

The electronic properties of this antenna are highly sensitive to mechanical strains at the frequency of operation (800–860 MHz). This sensor can withstand repeated mechanical strain while retaining electrical functionality and can return to its original state after stretching. In comparison to existing stretchable sensors, our sensor is a completely passive and wireless device. This RFID sensor can be embedded into soft robots without requiring any power consumption from the original robotic device. The feature of wireless power extends the lifetime of the device, removing the need for changing batteries, or integrating an energy harvesting system.

Additionally, most of existing gallium-based liquid alloy sensors were designed based on measuring the resistance change of the liquid metal, but the long-time stability of these sensors will be affected by the oxidation of gallium (gallium-based liquid alloy is easily oxidized). Our proposed RFID strain sensor was designed based on resonant frequency change upon strain. Benefiting from the high electrical conductivity of Galinstan, the skin depth (a measure of how closely electric current flows along the surface of a material) of Galinstan under 800–860 MHz is only a few micrometers. Even though the Galinstan in the channels has a thin oxide layer at the surface, the oxide will not have a large effect on the resonant frequency of the sensor.

In this work, we describe the potential of integrating the proposed RFID sensor into soft robots, which have pneumatic actuators. Most of the existing soft sensors have a requirement to be hardwired to power supplies or to signal processing equipment. This dependence on electrical tethers limits the practical use of soft sensors in many promising applications in real-world conditions. Although, recently, researchers have presented some fully untethered soft robotic systems,[28–31] most of them require bulky onboard components, such as batteries, microprocessors, pumps, or motors. These onboard components add additional weight on the soft systems, and thereby, the systems need to carry more powerful actuators.

In this work, we intended to develop untethered soft sensors, which can work wirelessly by dispensing, entirely, with the need for onboard power and processors. The proposed sensor can be fully embedded into soft robots without adding any other devices or additional electrical tethers, so that one can eliminate the wire and weight pressures on soft robotic systems. The relatively long measurement working range can allow the soft robots to move freely in a reasonably large area.

Principles and Implementation

RFID technology

RFID is a low-cost technology that allows the passive wireless communication of data. In recent decades, RFIDs have been used in many projects such as in robot motion

sensors,[32] indoor localization,[33] and distributed sensor networks.[34] An RFID system usually consists of a transponder (sometimes called RFID tag) and the reader. The reader transmits electromagnetic waves to reach out to the RFID tag; if the RFID tag is within the operating range, it utilizes the energy of the incoming electromagnetic wave to transmit a new electromagnetic wave that contains RFID tag-specific information. The information usually contains a unique serial number. The reader receives and visualizes the information. RFIDs can be operated in different frequency bands. While the low-frequency (LF) (30–300 KHz) and high-frequency (HF) (3–30 MHz) bands use magnetic flux coupling, the ultra-high-frequency (UHF) (300 MHz–3 GHz) band uses electromagnetic wave coupling. The communication distance of the UHF band is >16 m, which outperforms the LF and HF bands. In this work, the proposed antenna operates in the UHF band.

Sensor constitutes

The sensor we present in this work consists of an RFID chip and a half-dipole antenna. The antenna consists of eutectic liquid alloy-filled microfluidic channels in an elastic silicone substrate. The eutectic alloy we used is Galinstan. Galinstan[35] is a family of room temperature liquid eutectic alloys consisting of gallium (Ga), indium (In), and tin (Sn, Stannum in Latin). Gallium-based room temperature liquid alloy has previously been used in strain,[16,36–38] pressure,[16,36,39] curvature,[19,40] and shear[41] sensors. It can be easily injected into channels of soft structures. The resistance of a channel can be approximated by $R = \frac{\rho}{A} * l$ (ρ is resistivity of the liquid metal and A and l are cross-section area and length of the channel, respectively); so the channel resistance changes through deformation.

The Galinstan we made consists of 68.5% Ga, 21.5% In, and 10% Sn; its melting temperature is –19°C; and its electrical conductivity is $3.46 \times 10^6\ \mathrm{S \times m^{-1}}$.[36] Galinstan indicates favorable properties as channel conductor. We observed reliable liquid distributions in the antenna channels despite extreme twisting, stretching, and folding.

We used Ecoflex as the elastic silicone substrate. This silicone material has a Young's modulus of ~ 69 kPa.[42] We chose Ecoflex to be the substrate due to its favorable properties; it is easy to synthesize, easy to handle, low cost, and biocompatible.[43] In tensile tests with the ASTM D412 system, the maximum elongation of Ecoflex 00-50 (type 00-50) is 980% (defined as the percentage change in length or $((l - l_0)/l_0) \times 100\%$).

Working principles

Figure 1a depicts a stretchable meandered half-wave dipole antenna. We embedded an RFID chip into the antenna design. Supplementary Figure S1 (Supplementary Data are available online at www.liebertpub.com/soro) indicates specific antenna dimensions.

The RFID chip is bonded on aluminum pads and inserted in between two Galinstan channels. The RFID chip consumes

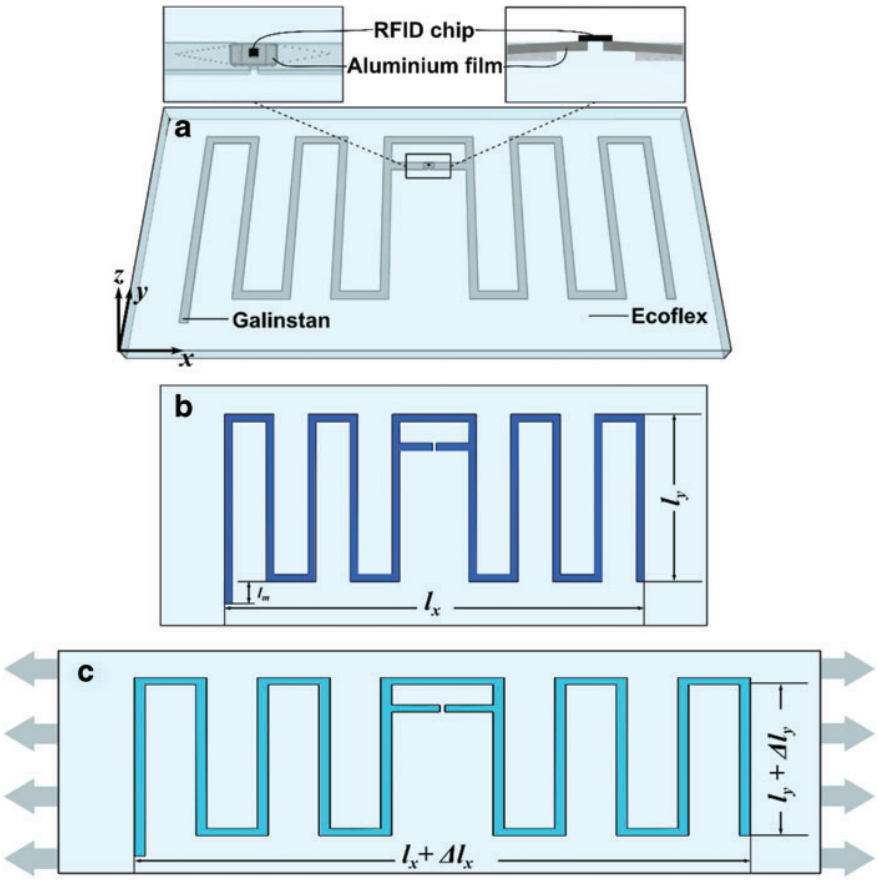

FIG. 1. **(a)** Schematic diagram of the stretchable microfluidic sensor. Galinstan is enclosed in Ecoflex substrate while an RFID chip is bonded on a piece of aluminum foil, which is inserted in the channels. Detailed and cross-section figures of the part near RFID chip are presented. Directions of x, y, and z axes are indicated. **(b)** Initial state of the antenna when it is not stretched. The effective antenna length on the x-direction and y-direction is defined as l_x and l_y, respectively. Notice: the electrical length of the entire antenna is $l_x + 10\ l_y + l_m$. The nonsymmetric part, l_m, is used for fine impedance matching between the antenna and the RFID chip. **(c)** When the soft antenna is stretched, the effective antenna length on the x-direction and y-direction is defined as $l_x + \Delta l_x$ and $l_y + \Delta l_y$, respectively. RFID, radio-frequency identification. Color images available online at www.liebertpub.com/soro

power from received signals and backscatters them without requiring an external power supply depicting a wireless *passive* soft sensor.

The results shown in Figure 1b and c indicate how deformation of an antenna can change its dimensions. If the channel dimensions change, the channel resistances change and therefore the entire antenna and its parameters change. The RFID chip backscatters signals with varying amplitude and phase based on the degree of stretching.

Implementation in soft robotics

Figure 2 shows the schematic diagram of our soft RFID sensor implementation. The implementation comprises a pneumatic soft robot with four embedded soft RFID tags, one tag on each robot leg, and the electronic circuitry to transceiver data. The *Controller* uses the *Signal Generator* to generate a HF carrier signal. An *Amplitude Shift Keying* (ASK) module modulates the amplitude of the carrier signal to decode information. A binary ''one'' consists of a fixed amplitude and frequency; a binary ''zero'' is a zero-voltage output.

The modulated signal is passed through a power amplifier preparing the signal for transmission. The signal lies on port 1 of a circulator circuit. Port 2 of the circulator outputs the signal to an antenna, therefore broadcasting the signal. The soft RFID tags receive the signal, utilize its energy, and transmit a new signal that incorporates their unique identification information. The antenna receives the signals from the soft RFID tags and outputs them to port 3 of the circulator. The circulator ensures that outgoing and incoming signals do not interfere with one another. The incoming signals from the soft RFID tags pass a low-noise filter, an ASK demodulator, and are ultimately inserted into an analog-to-digital converter. The controller analyses the various signals (distinguishable through their identification information) with regard to their amplitude and phase.

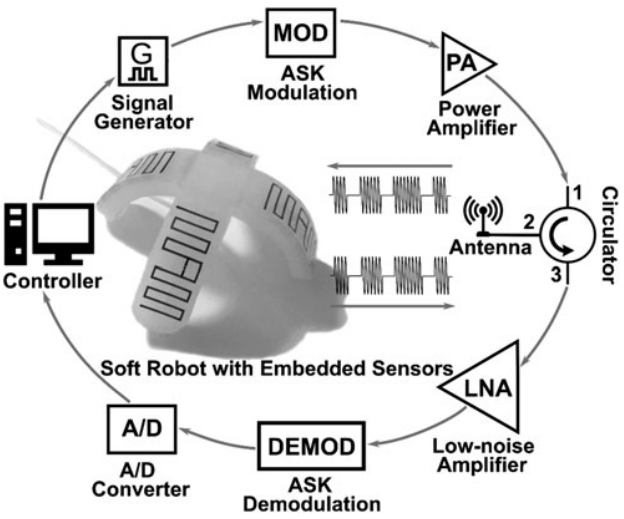

FIG. 2. The electronic system for measuring data from a pneumatic soft robot that contains four embedded microfluidic strain sensors.

Antenna design

Selection and design of the antenna. The antenna design of our soft RFID sensor is different from other antenna designs because of power and size requirements. The antenna powers the RFID chip with incoming signals; we do not require a power supply. We decided to design the soft RFID sensor as small as possible to attach the RFID tags to even small objects making our sensor more applicable. Since the soft RFID sensors can be attached in any arbitrary orientation, we ensured 360° or *omnidirectional* readouts by using a half-wave dipole antenna design. The effective electrical length of a half-wave dipole antenna is half the wavelength of the operating frequency of the system. This antenna design is commonly used in RF systems with omnidirectional radiation patterns perpendicular to the antenna axis.

In previous work, small antenna sizes were accomplished by using microstrips.[44] However, they suffered directional readout constraints and low efficiency. Our design uses a meander line antenna (MDA) to achieve long reading ranges and small antenna size. MDA is a derivative of the dipole antenna and achieves high efficiencies[45] for small antenna sizes.[46,47]

Stretching the soft half-wave dipole antenna as illustrated in Figure 1b causes a change in the dimensions if the antenna is in both the x and y directions. An increase in strain in the x-direction decreases the thickness of the soft polymer, due to the Poisson effect, and also decreases its height by Δl_y. Therefore, stretching the soft RFID tag changes the electric length of the antenna; each infinitely small change in electric length shifts the resonant frequency. Now, if we send signals to RFID tags, the frequency of the carrier signal can be changed to the specific resonant frequency of the antenna's current electric length. The backscattered signals from the RFID tags will indicate phase and amplitude changes due to the resonant frequency.

Antenna matching. As mentioned in the previous section, the RFID antenna utilizes power from the incoming electromagnetic waves to supply power to the RFID chip. *Impedance matching* between the RFID chip and the antenna is paramount in RFID antenna design because it affects how much power the antenna is able to reflect, hence determines the antenna's operational range.

Figure 3 indicates how to match impedances. The best impedance matching for maximum power transmission is to conjugate impedance matching, which means $R_a = R_c$ while $X_a = -X_c$. The RFID chip we used (Monza R6, Impinj) possesses an impedance of $Z_c = (13.5 - j\ 126)\Omega$ at 860 MHz. Therefore, we designed the transporter antenna to match the impedance of this RFID chip.

The theoretical impedance of a half-wave dipole antenna in free space is $73 + j42.5$ Ohms,[48] which makes it impossible to match the impedance of the RFID chip. Therefore, we used the T-match method[49] to match the impedance between transporter antenna and RFID chip. The results shown in Figure 3b and c indicate that a half-wave dipole antenna can be changed through a centered short-circuit stub. The antenna *source* is connected to a small dipole of length $a \leq l$ and is placed at a close distance b from the first and larger dipole. The electric current distributes along the two main radiators according to the size of their transverse sections. The impedance Z_a at the source points is given by Equation 1:

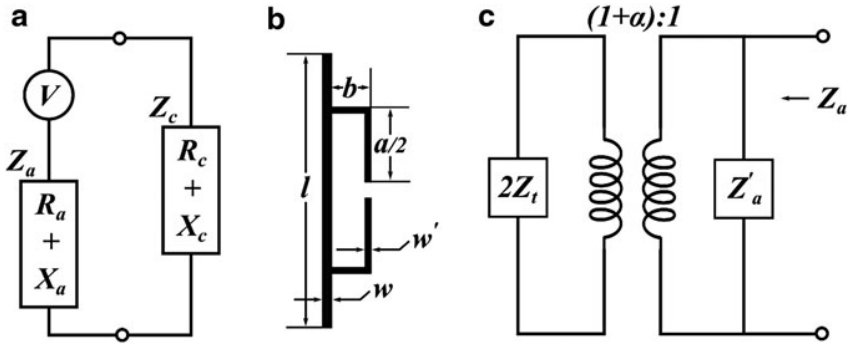

FIG. 3. **(a)** Equivalent circuit of the RFID chip and the transporter antenna. Z_a is the total impedance of the transport antenna, whereas Z_c is impedance of the RFID chip. **(b)** Schematic diagram of T-matching for a dipole antenna. The l represents the length of the original dipole antenna. This antenna is connected at the center to a short second dipole. The close distance between matching stub and the original antenna is b, whereas w and w' are the widths of the original dipole antenna and the mating stub, respectively. **(c)** Equivalent circuit at the source point of the dipole antenna after T-matching. Z'_a is the impedance of the first dipole antenna without T-matching, whereas Z_t is the impedance that the matching stub created. The α in the ratio is the current division factor between the two connectors.

$$Z_a = \frac{2Z_t(1+\alpha)^2 Z'_a}{2Z_t + (1+\alpha)^2 Z'_a}. \quad (1)$$

In Equation 1, Z'_a is the original dipole impedance taken at its center in the absence of a T-match connection, whereas Z_t is the impedance created by the matching stubs. α is the current division factor between the two connectors, $\alpha = \ln(b/re')/\ln(b/re)$. *re* and *re'* are the equivalent radii of the initial dipole and the matching stub.

We performed impedance calculation with finite element method (FEM) simulations with Computer Simulation Technology (CST) Microwave Studio. FEM includes the use of mesh generation techniques for dividing a complex structure into a large number of small elements. Calculations are made for every single element, and combining the individual results can give us the conclusive results of the structure. We modified the edge of the antenna to be asymmetric, so that created l_m in Figure 1a, for a final fine matching step.

Materials and Fabrication Methods

Figure 4 shows the soft-lithography fabrication process of our stretchable antenna (photographs of the fabrication process are shown in Supplementary Figure S2). We designed and fabricated an antenna mould with a laser micromachining system (Protolaser U3; LPKF) and a self-adhesive vinyl film (CRAFTRKZO; d-c-fix®), as shown in Figure 4a. A piece of vinyl film was attached to an acrylic substrate (2 mm Acrylic Cast; AMARI). The channel profiles were cut with the LPKF laser system. We peeled the vinyl residuals (negative) from the substrate and laid a 2 mm-thick acrylic frame along the mould edges as indicated in Figure 4b.

We synthesized Ecoflex 00-50 (Reynolds Advanced Materials; 1:1 ratio), degassed it in a vacuum chamber, and poured the soft polymer into the mould as illustrated in Figure 4c. We put the mould into a convection oven at 65°C for 20 min and then removed the soft structure from the mould and flipped it over. A 150 μm-thin Ecoflex 00-50 layer was fabricated with spin coater to seal the unfolded channels, as shown in Figure 4d.

We made small incisions in the center of the thin Ecoflex layer to embed the RFID chip; the RFID chip (Monza R6; Impinj) was bonded on an Aluminum film with a bonding machine (FB-300 manual RFID wrapping machine) and inserted in the channels. During the bonding process, the chip was aligned to the substrate with a vacuum sucker, microscopes, and cameras in the bonding machine, an adhesive material was dispensed between the chip and the aluminum film, then the chip was firmly bonded on the aluminum film with hot-pressing for 10 s.

We inserted two injection needles into the soft structure, as illustrated in Figure 4e. One needle was used to inject the Galinstan into the channel, and the other needle was used to release air pressure. The Galinstan made contact with the aluminum pads of the RFID chip without leaking to the surface. At the end, we applied a thin film of uncured Ecoflex on top of the device to seal the open holes created by chip insert and liquid metal injection.

Experimental Design

The permittivity of Ecoflex 00-50 and the resistivity of Galinstan are parameters that are required to simulate S_{11}; S_{11} is the input reflection coefficient or input return loss. S_{11} indicates the radiation efficiency of the antenna and reaches its maximum value at resonant frequency. We used an Agilent 85070E dielectric probe kit to measure the permittivity variations of Ecoflex 00-50 in a frequency range from 200 MHz to 1.2 GHz, as shown in Figure 5b. We simulated changes in resonant frequency and radiation efficiency under strain variations between 0% and 50% and a step size of 5%.

We used a Voyantic Tagformance system to measure the characteristics of our antenna design; namely the frequency modulation of our soft RFID sensor due to strain variations, as indicated in Figure 5a and c. This setup allowed us to determine the resonant frequency, the theoretical RFID reading range, and the phase changes of the backscattered signals for every applied strain in the range from 0% to 50% with a step size of 5%.

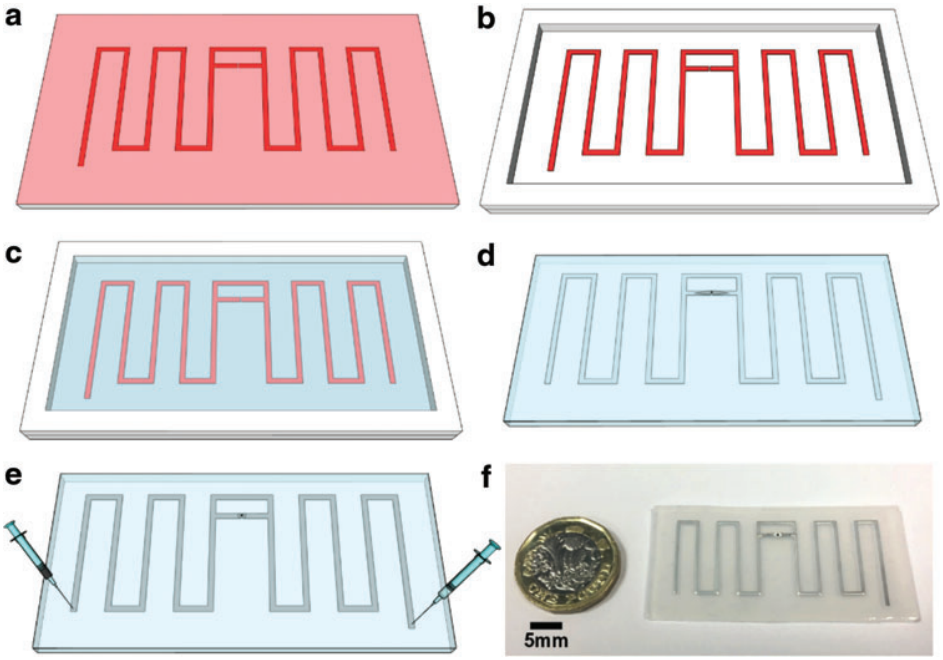

FIG. 4. Fabrication process and prototype of the stretchable microfluidic sensor (RFID tag antenna). **(a)** Cut the sensor profile on a piece of self-adhesive vinyl attached on an acrylic substrate. Notice: the *red* and *pink* parts are a same piece of vinyl. Two different colors are used here to show the laser-cut profile clearer. **(b)** The unwanted part of vinyl was peel off, a 2 mm-thick acrylic frame was stuck on the substrate to form a soft-lithography mold. **(c)** Uncured Ecoflex with a controlled height of 2 mm was poured into the soft-lithography mould. **(d)** The casted piece of Ecoflex was sealed with another 0.15 mm Ecoflex film, and the RFID chip bonded on aluminum film was inserted into the channels. **(e)** Two needles were used to inject Galinstan into the channel. **(f)** Photograph of the final prototype. Color images available online at www.liebertpub.com/soro

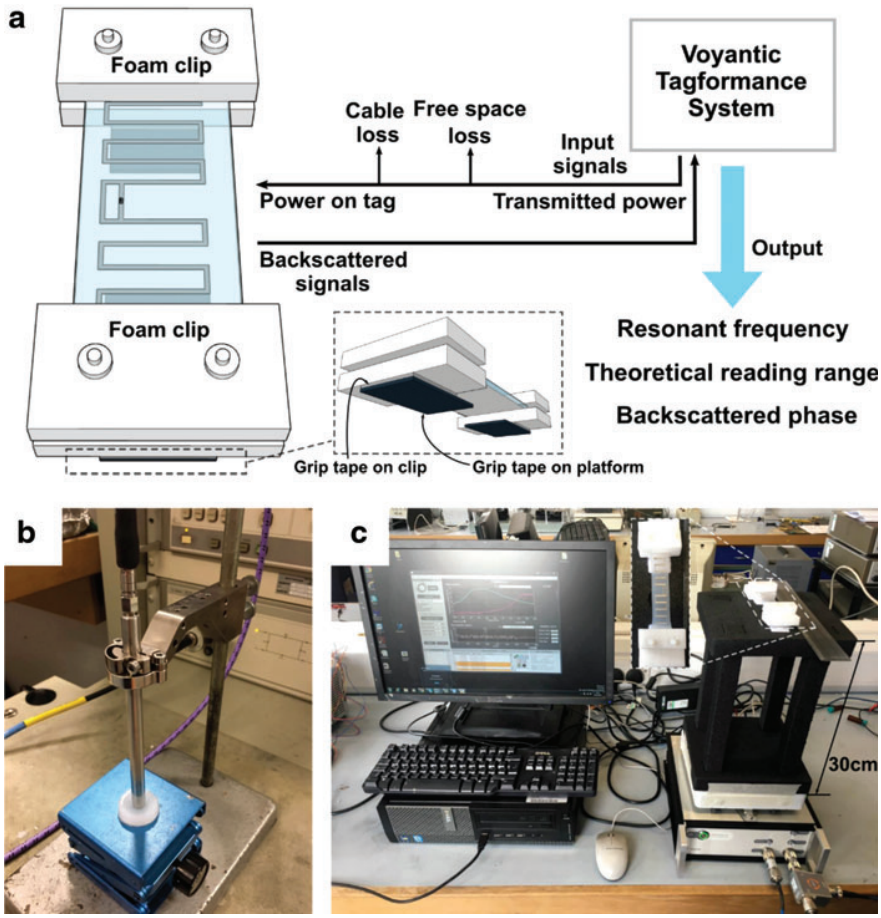

FIG. 5. **(a)** We used the Voyantic Tagformance system to measure characteristics of the proposed antenna. This measurement system sends input signals to the tag antenna with transmitted power. The power received on tag is the transmitted power minus cable loss and free space loss. RFID chip in the tag antenna receives the input signals, absorbs energy in the signals, and then sends backscattered signals back to the measurement system. According to the results of the measurement system, we can know the resonant frequency and the theoretical reading range of the tag antenna, as well as the phase of the backscattered signals. We affixed the two edges of the tag antenna with clips made of rigid foam. To stretch the tag antenna and hold its position for measurement, we stuck grip tape on the surface of the foam clips and on the measurement platform. **(b)** Experimental setup for measurement of the permittivity of Ecoflex 00-50 with the Agilent 85070E dielectric probe kit system. **(c)** Photograph of the experimental setup of the soft antenna and the Voyantic Tagformance system. Color images available online at www.liebertpub.com/soro

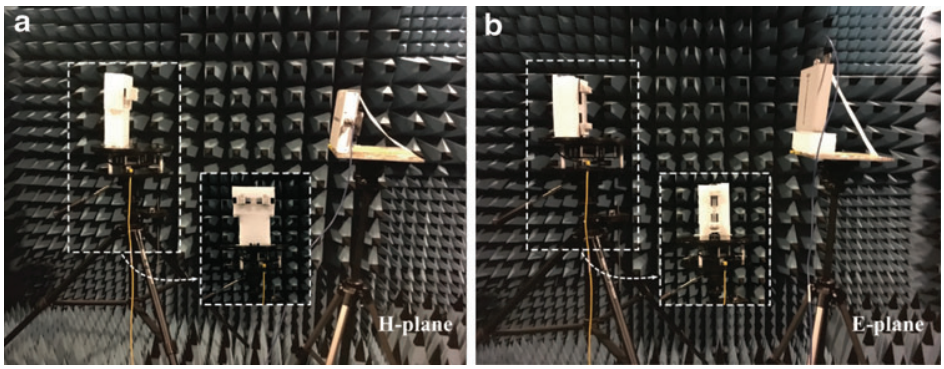

FIG. 6. Radiation pattern measurement in the **(a)** H-plane and the **(b)** E-plane in an anechoic room with Diamond Engineering Automated measurement system and an automatic turntable. In the measurement, the reader antenna holds its position while the strain sensor (transporter antenna) turns with the turntable. Color images available online at www.liebertpub.com/soro

We repeated each measurement seven times to indicate the soft polymer's reversibility. We fabricated three sensor samples to enable us to evaluate the repeatability of our fabrication process. We did a cyclic stretching test to prove the reliability of the proposed sensor when it is stretched to 50% for 240 times. It is worth mentioning that we calculated the strain value in all the experiments with $\left(\left(\frac{\Delta l_x}{l_x}\right)\times 100\%\right)$, l_x and Δl_x are shown in Figure 1. The length we used in calculation is the effective antenna length in the x-direction, not the distance between the foam clips. We also tested the soft RFID sensors when we applied twists of 0°, 45°, and 90°.

We used a diamond engineering automated measurement system and an automatic turning table in an anechoic room to measure the radiation patterns of our soft RFID sensor in the H- and E-planes (Fig. 6). An anechoic room absorbs reflections from acoustic and electromagnetic waves. We analyzed the directivity of the antenna (in the H- and E-planes) when subjected to strains of 0%, 25%, and 50%.

Results

Permittivity of Ecoflex 00-50

According to the results in Figure 7, the relative permittivity (ε_r) of Ecoflex 00-50 is nearly stable at 3 in the range of 500 MHz–1.2 GHz, as shown in Figure 7. The operating frequency range of our sensor is 800–860 MHz, which is covered in this stable range. Thus, we can take ε_r of Ecoflex as a constant in calculation and simulation.

Simulation of antenna efficiency

When our soft RFID sensor is stretched, its antenna parameters such as resonant frequency and radiation efficiency change. Below, we analyze, analytically, the antenna parameters due to strain variations and we apply an ideal folded half-wave dipole antenna model.

The resonant frequency of a half-wave dipole antenna[50] is given by

$$f_r = \frac{c}{2l_e\sqrt{\varepsilon_e}}\times r, \tag{2}$$

where l_e is the effective electrical length of the antenna; f_r is the resonant frequency; ε_e is the effective permittivity of the antenna substrate; and r is the correction factor of a folded half-wave dipole antenna. We can estimate the effective relative permittivity through the study of Jackson *et al.*[51]:

$$\varepsilon_e = 1 + \left(\frac{\varepsilon_r - 1}{2}\right)\frac{K_1}{K_2}, \tag{3}$$

where ε_r is the relative permittivity of Ecoflex, which is considered a constant here; $K_1 = \frac{K(k_1)}{K'(k_1)}$ and $K_2 = \frac{K(k_2)}{K'(k_2)}$ while $K(k)$ is a complete elliptic function of the first kind and $K(k')$ is its complimentary function.

In the K function, $k_1 = \frac{l_e}{l_e + 2s}$ and $k_2 = e^{-\frac{\pi s}{2h}}$, whereas l_e is effective electrical length of the antenna, s is the gap at the feed point, and h is height of substrate of the antenna. According to Equations 2 and 3, resonant frequency of a half-wave dipole antenna will change when its effective electrical length or its substrate height changes.

Equation 2 shows the resonant frequency of a half-wave dipole antenna changes with its effective electrical length, whereas Equation 3 indicates that the resonant frequency also changes with the substrate height of the antenna.

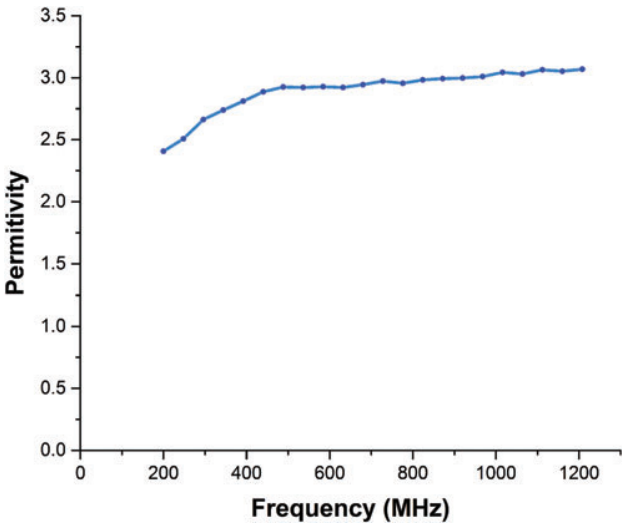

FIG. 7. Permittivity of Ecoflex type 00-50 in the frequency range of 200 MHz–1.2 GHz. Measured with Agilent 85070E dielectric probe kit system. Color images available online at www.liebertpub.com/soro

Rigid antennas possess a fixed effective electrical length, whereas our soft antenna's effective electrical length changes due to strain. Due to the Poisson effect, our antenna physically changes according to

$$\frac{\Delta l_y}{l_y} = 1 - \left(1 + \frac{\Delta l_x}{l_x}\right)^{-\nu}, \tag{4}$$

where l_x is the antenna length; Δl_x describes a change in antenna length; l_y is the antenna width; Δl_y describes a change in antenna width; and the initial (not stretched) electrical length of our antenna is $l_x + 10l_y + l_m$. Since $l_m \gg l_x + 10l_y$, we neglect the effect of l_m here. Figure 1 complements Equation 4.

We insert Equations 3 and 4 in Equation 2 and receive a new formulation for the resonant frequency for our soft antenna

$$f_r = \frac{c}{2\left(l_x\left(1+\frac{\Delta l_x}{l_x}\right)+10l_y\left(2-\left(1+\frac{\Delta l_x}{l_x}\right)^{-\nu}\right)\right)\times\sqrt{1+\left(\frac{\varepsilon_r-1}{2}\right)\frac{K_1}{K_2}}} \times k, \tag{5}$$

where ν is the Poisson ratio of Ecoflex type 00-50.

We performed an electromagnetic finite element simulation using CST to determine S_{11}, the input return loss, under a variety of strains. S_{11}'s maximum indicates the antenna's resonant frequency. Figure 8 indicates the simulation results; the soft antenna has been strained from 0% to 50% with a step size of 5%; the S_{11} peak values are all below −20 dB at resonance frequency for each strain condition indicating that 99% of the power from the input signal is scattered back from the soft RFID sensor. We successfully matched antenna to RFID chip resistance.

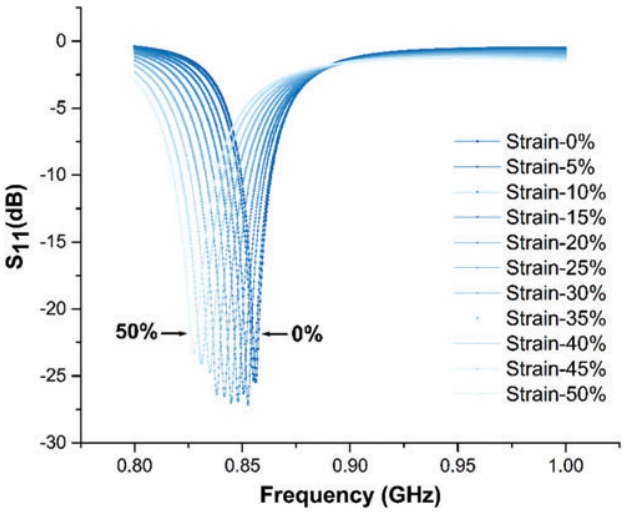

FIG. 8. Finite elements simulation results. Under 0% strain condition, simulated resonant frequency of the antenna is 856 MHz. The simulated resonant frequency continuously goes down to 827 MHz when the antenna is under 50% strain. Color images available online at www.liebertpub.com/soro

Resonant frequency upon strain

The Voyantic Tagformance measurement system controls the power of the signal that we transmit to the soft RFID sensor. First, we set the initial signal power to 25 dB. Second, we gradually decreased the signal power until we could not detect the backscattered signal from the soft RFID sensor anymore. Power of the input signal was recorded as Transmitted Power (P_t). We repeated this process for each sampling frequency in the frequency band of 800–880 MHz, with a step of 1 MHz.

As indicated in Figure 5a, the power received by the soft RFID tag antenna (P_{tag}) can be calculated as

$$P_{tag} = P_t - L_c + G_t - FSPL, \tag{6}$$

where L_c are cable losses; G_t is the Gain of the Voyantic Tagformance's transmitter antenna; and $FSPL$ are losses due to free space transmissions. $L_c, G_t, FSPL$ can be determined by calibrating the Voyantic Tagformance.

Figure 9a shows the minimum transmitted power (P_t) for each sample frequency to result in a detectable backscattered signal from the soft RFID sensor. Figure 9b indicates the power received on tag antenna (power on tag, P_{tag}) corresponding to the minimum P_t for each sample frequency.

The theoretical measurement reading range of the soft RFID sensor is frequency dependent and can be calculated by

$$R_r = \sqrt{\frac{P_{max,\,EIRP}}{P_{tag}}} \times \frac{c}{4\pi f}, \tag{7}$$

where $P_{max,\,EIRP}$ is the maximum signal power of the Voyantic Tagformance (default: 3.28 W). P_{tag} in this formula is related to the minimum transmitted power. Figure 9c depicts the reading ranges calculated with Equation 7 for the various frequencies; our soft RFID sensor has a reading range of ~7.5 m, whereas this range increases if the soft sensor is under strain. The reading range of the sensor increases to 10 m under a strain of 50%. The resonant frequency decreases from 862 MHz in idle state (no strain) to around 802 MHz under 50% strain. Figure 9d illustrates the backscattered signals from the soft RFID sensor under different strain conditions.

Repeatability and reliability test

We tested the reliability of our soft RFID sensor by performing seven strain experiments. We measured the resonant frequency under 0%–50% strain, with a step size of 5%. Figure 10a shows the average value and standard deviation of the resonant frequency for each strain. The resonant frequency dropped ~61 MHz (from 861 to 800 MHz) from 0% to 50% strain, whereas the maximum standard deviation did not exceed 2.6 MHz.

We performed a similar experiment in Figure 10c; once we reached 50% strain, we left the device stretched for 24 h in the laboratory before we gradually released the device to 0% strain. We also involved the simulation results of resonant frequency upon strain in Figure 10a as a comparison with the measurement results. In the simulation, the resonant

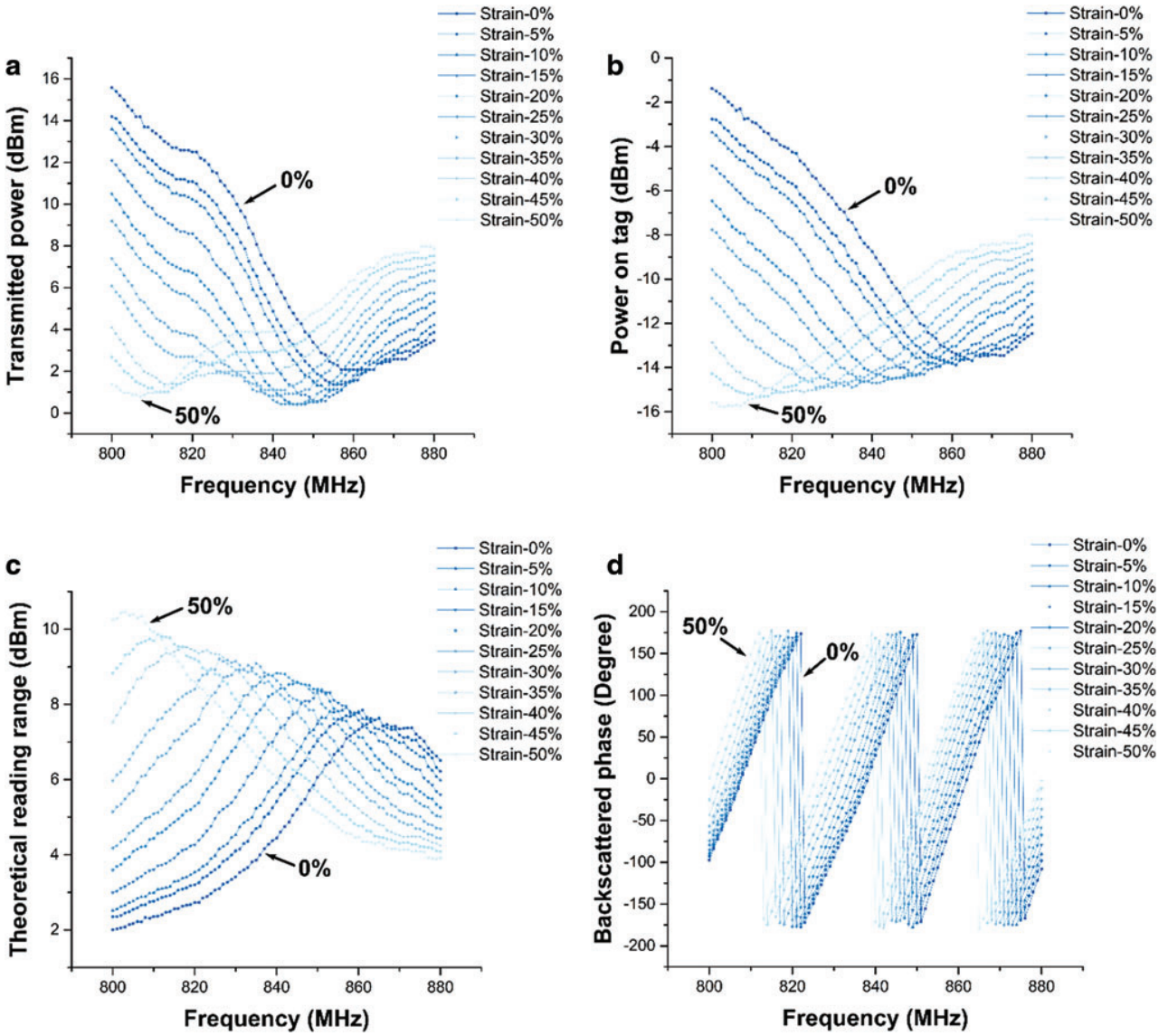

FIG. 9. **(a)** Transmitted power. The minimum transmitted power recorded for the sensor under 0%–50% strain, with a step of 5%. **(b)** The power received on tag, which was calculated based on the transmitted power and cable and free space loss. **(c)** Theoretical reading range forward, which was calculated based on the power received on tag. **(d)** Backscattered phase in the frequency band of 800–880 MHz (with a step of 1 MHz) when the sensor was under 0%–50% strain, with a step of 5%. Color images available online at www.liebertpub.com/soro

frequency changed 29 MHz in total (from 856 to 827 MHz) from 0% to 50% strain, which is smaller than the measurement results.

We fabricated another three prototypes of the same sensor design and again performed strain-resonant-frequency tests. Average value and standard deviation of the resonant frequency for each prototype are shown in Figure 10b. Figure 10b shows similar results than Figure 10a. Figure 10d depicts a cyclic s stretching test to prove the reliability of the proposed sensor when it is stretched 240 times.

As shown in the results, the resonant frequency of the sensor remains stable in the test (only dropped 2 MHz between 80 and 100 of iteration). We also measured resonant frequency response of a soft RFID sensor due to twist rather than strain and put the results in Supplementary Data. As shown in Supplementary Figures S3 and S4, three different twist angles were tested. According to the results, the electrical characteristics of our soft RFID sensor at frequency of operation are highly sensitive to mechanical strain while having no response to twisting.

Radiation pattern

We measured the theoretical reading range from our soft RFID sensor in the H- and E-planes with an antenna measurement system consisting of antenna measurement studio 5.5 and Diamond Engineering. The left subfigure of Figure 11 shows that omnidirectional radiation patterns were measured

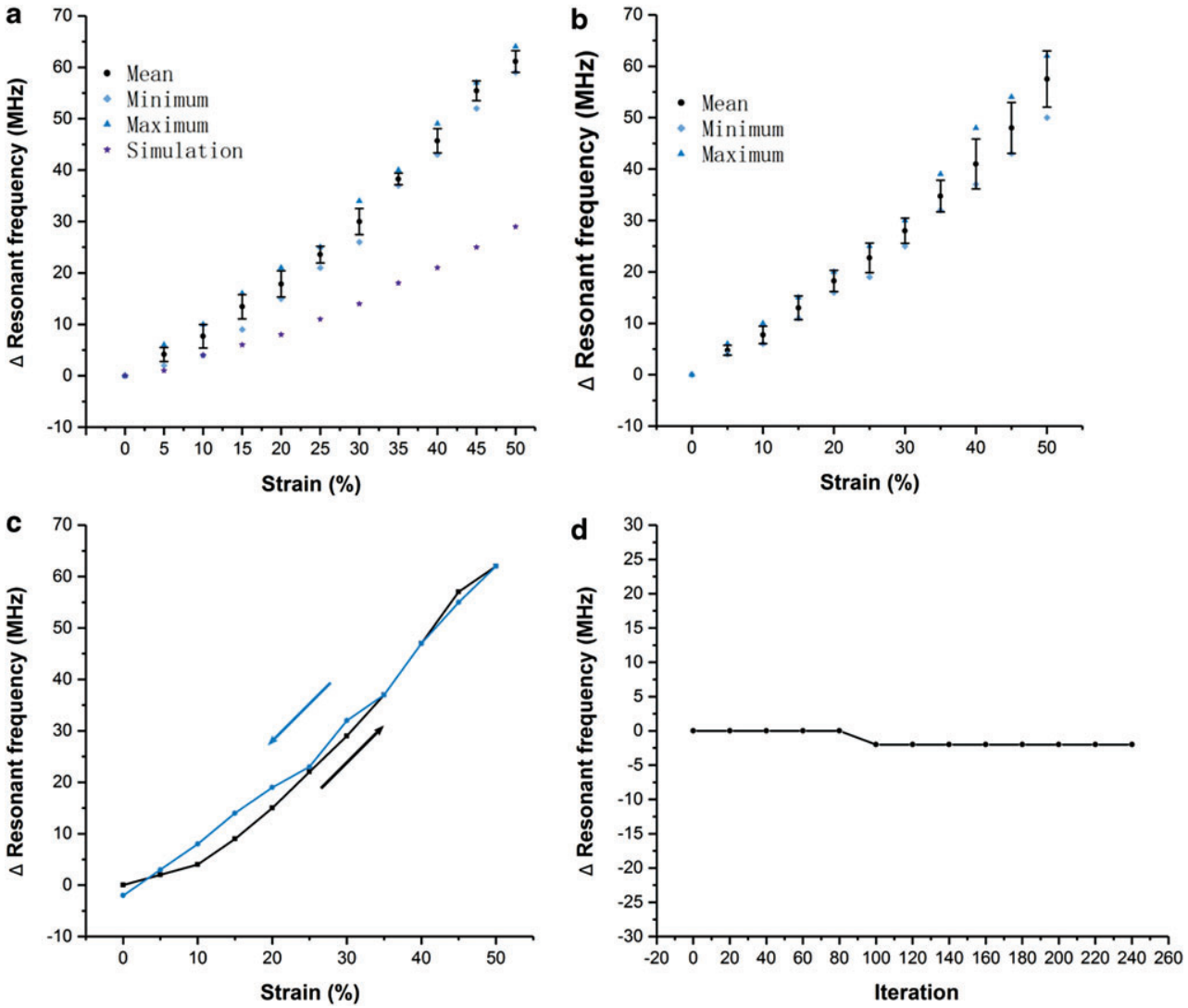

FIG. 10. **(a)** Resonant frequency change upon different strain conditions. In the experiment, we did seven tests on the same prototype. Error bars represent standard deviation. **(b)** Resonant frequency change upon different strain conditions. In the experiment, we did one test on three different prototypes with the same design and same fabrication method. Error bars represent standard deviation. **(c)** Hysteresis test. A prototype was tested from 0% to 50% of strain, leave for 24 h, then from 50% back to 0%. **(d)** Cyclic stretching test. The sample was stretched to 50% of strain and then back to 0% for 240 times. Resonant frequency of the sample was measured each 20 times of stretching. Color images available online at www.liebertpub.com/soro

in the H-plane. The right subfigure of Figure 11 indicates that the antenna is constrained in directions that are parallel to the sensor's x-axis ($60^\circ + n\pi < \theta < 120^\circ + n\pi$; n is an arbitrary integer). This constraint might have to be considered in certain applications. The different strain conditions have an impact on our soft RFID sensor's reading range *radius*; if strain is applied, the reading range radius increases.

Discussion

The results show that our soft RFID sensor changes its resonant frequency and the phase of its backscattered signal as function of strain.

Our measurements correlate with our simulations, the initial resonant frequency of all our sensor prototypes lies in the region of 860 MHz. In our simulation, the resonant frequency did not decrease as much under strain as in our experiments. This mismatch could be caused by the simplified model that we used for the Poisson effect or a potentially emerging resistance between the Galinstan channels and the RFID chip that might occur under strain.

We matched the resistances of the RFID chip and the antenna under 0% strain. Once we apply strain, the resistance of the antenna changes, hence the resistances of the RFID chip and antenna do not perfectly match anymore. Therefore, we expected a decrease in the measurement reading range

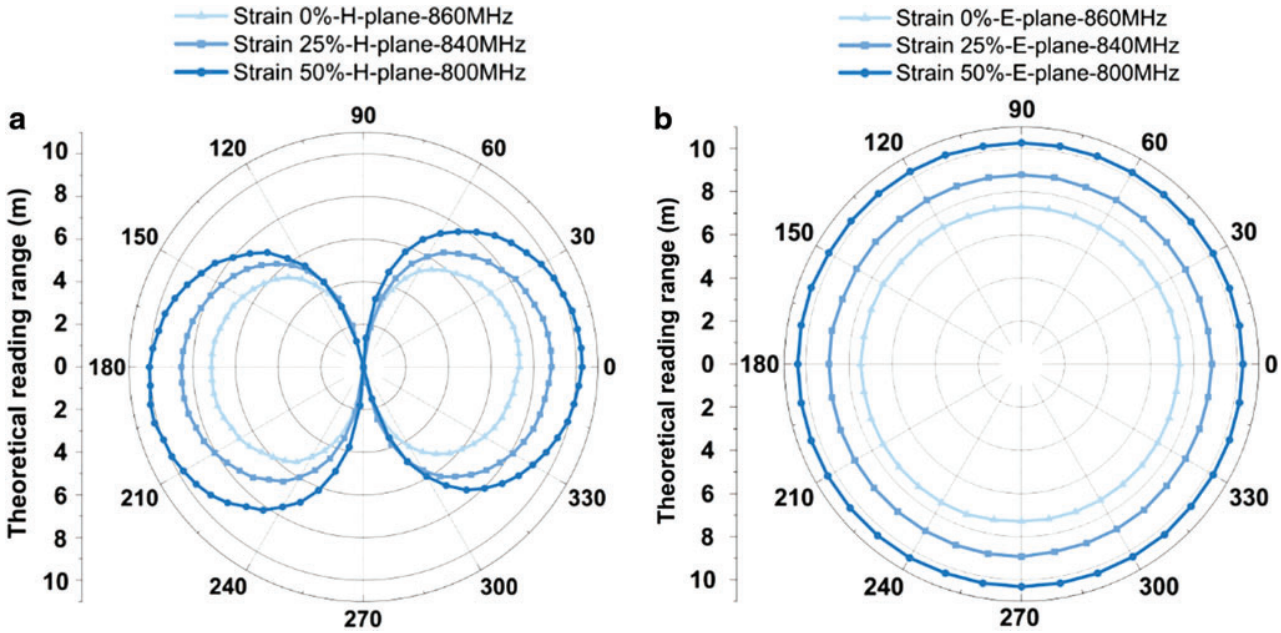

FIG. 11. Theoretical reading range of the antenna in the H-plane **(a)** and the E-plane **(b)** with 0%, 25%, and 50% length stretching in the *x*-direction. The data were recorded for every 5° rotation in the H-plane and every 10° rotation in the E-plane. Color images available online at www.liebertpub.com/soro

with an increase in strain. However, the measurement reading range increased with an increase of strain.

One explanation could be that a folded dipole antenna consists of conductors with opposite current flows; the opposing magnetic fields that are evoked through the currents might cancel each other out. Now, if we stretch the soft antenna, the conductors are being further separated and the magnetic fields might be too far away to interfere with one another. This may enhance the radiation efficiency of the antenna. An increase of the radiation efficiency might outperform an imperfectly matched antenna-RFID chip.

In this study, we investigated the resonant frequency response of stretchable soft RFID sensors due to strain. Future work might focus on the design of soft RFID sensors based on phase shift differences that occur in backscattered signals. We also want to increase the initial resonant frequency of our soft RFID sensors to increase the strain range. RFIDs usually operate in the range of 800 MHz–1 GHz, whereas, currently, our system operates in the 800–860 MHz range.

Conclusion

In this work, we designed and fabricated a stretchable strain sensor (soft RFID sensor) and tested a variety of its characteristics. The soft RFID sensor is a deformable folded half-wave dipole antenna. Its resonant frequency and backscattered signal phase changes under strain. We showed that our soft sensor is stable, reliable, and manufacturable. Our sensor consists of Ecoflex 00-50 and Galinstan, materials that are stretchable and withstand permanent deformation. The soft RFID sensor can be easily applied to for applications including wearable strain sensors or as part of soft robotic systems, as demonstrated in this study. The sensor does not require a power supply, indicates long measurement reading ranges (>7.5 m), and shows omnidirectivity.

Acknowledgments

The authors acknowledge funding from the Engineering and Physical Sciences Research Council: Centre for Doctoral Training in Intelligent Sensing and Measurement EP/L016753/1, the Robotarium Capital Equipment and Robotics CDT Capital Equipment EP/L016834/1 and the UK Robotics and Artificial Intelligence Hub for Offshore Energy Asset Integrity Management EP/R026173/1.

Author Disclosure Statement

No competing financial interests exist.

References

1. Yeo WH, Kim YS, Lee J, *et al.* Multifunctional epidermal electronics printed directly onto the skin. Adv Mater 2013; 25:2773–2778.
2. Shademan A, Decker RS, Opfermann JD, *et al.* Supervised autonomous robotic soft tissue surgery. Sci Transl Med 2016;8:337ra64.
3. Polygerinos P, Wang Z, Galloway KC, *et al.* Soft robotic glove for combined assistance and at-home rehabilitation. Rob Auton Syst 2015;73:135–143.
4. Alspach A, Kim J, Yamane K. Design of a soft upper body robot for physical human-robot interaction. In: 2015 IEEE-RAS 15th International Conference on Humanoid Robots (Humanoids), Seoul, South Korea, November 3–5, 2015, pp. 290–296.
5. Bahramzadeh Y, Shahinpoor M. A review of ionic polymeric soft actuators and sensors. Soft Robot 2014;1: 38–52.

6. Wei W, Guo S. A novel PDMS diaphragm micropump based on ICPF actuator. In: 2010 IEEE International Conference on Robotics and Biomimetics, ROBIO 2010, Tianjin, China, December 14–18, 2010, pp. 1577–1583.
7. Cho MS, Seo HJ, Nam JD, *et al.* An electroactive conducting polymer actuator based on NBR/RTIL solid polymer electrolyte. Smart Mater Struct 2007;16:S237.
8. Shepherd RF, Ilievski F, Choi W, *et al.* Multigait soft robot. Proc Natl Acad Sci USA 2011;108:20400–20403.
9. Wei T, Stokes A, Webb B. A soft pneumatic maggot robot. In: Lecture Notes in Computer Science (Including Subseries Lecture Notes in Artificial Intelligence and Lecture Notes in Bioinformatics), Volume 9793, Lepora N, Mura A, Mangan M, *et al*. (Eds). Springer, Cham, 2016, pp. 375–386.
10. Suzumori K, Endo S, Kanda T, *et al.* A bending pneumatic rubber actuator realizing soft-bodied manta swimming robot. In: Proceedings—IEEE International Conference on Robotics and Automation, Roma, Italy, April 10–14, 2007, pp. 4975–4980.
11. Ilievski F, Mazzeo AD, Shepherd RF, *et al.* Soft robotics for chemists. Angew Chem Int Ed Engl 2011;50:1890–1895.
12. Cianchetti M, Mattoli V, Mazzolai B, *et al.* A new design methodology of electrostrictive actuators for bio-inspired robotics. Sens Actuators B Chem 2009;142:288–297.
13. Pelrine R. Dielectric elastomer artificial muscle actuators: toward biomimetic motion. Proc SPIE 2002;4695:126–137.
14. Madden JDW, Vandesteeg NAAP, Madden JDW, *et al.* Artificial muscle technology: physical principles and Naval prospects. IEEE J Ocean Eng 2004;29:706–728.
15. Kim D-H, Ghaffari R, Lu N, *et al.* Flexible and stretchable electronics for biointegrated devices. Annu Rev Biomed Eng 2012;14:113–128.
16. Park Y-L, Chen B, Wood RJ. Design and fabrication of soft artificial skin using embedded microchannels and liquid conductors. IEEE Sens J 2012;12:2711–2718.
17. Tabatabai A, Fassler A, Usiak C, *et al.* Liquid-phase gallium-indium alloy electronics with microcontact printing. Langmuir Acs J Surfaces Colloids 2013;29:6194–6200.
18. Park YL, Chen B, Majidi C, *et al.* Active modular elastomer sleeve for soft wearable assistance robots. In: Proceedings of the IEEE/RSJ International Conference on Intelligent Robots and Systems (IROS'12), Vilamoura, Portugal, October 2012, pp. 1595–1602.
19. Majidi C, Kramer R, Wood RJ. A non-differential elastomer curvature sensor for softer-than-skin electronics. Smart Mater Struct 2011;20:105017.
20. Teng L, Jeronimo K, Wei T, *et al.* Integrating soft sensor systems using conductive thread. J Micromech Microeng 2018;28:054001.
21. Cheng S, Rydberg A, Hjort K, *et al.* Liquid metal stretchable unbalanced loop antenna. Appl Phys Lett 2009;94:144103.
22. Cheng S, Wu Z, Hallbjörner P, *et al.* Foldable and stretchable liquid metal planar inverted cone antenna. IEEE Trans Antennas Propag 2009;57:3765–3771.
23. Kubo M, Li X, Kim C, *et al.* Stretchable microfluidic radiofrequency antennas. Adv Mater 2010;22:2749–2752.
24. So JH, Thelen J, Qusba A, *et al.* Reversibly deformable and mechanically tunable fluidic antennas. Adv Funct Mater 2009;19:3632–3637.
25. Huang Y, Wang Y, Xiao L, *et al.* Microfluidic serpentine antennas with designed mechanical tunability. Lab Chip 2014;14:4205–4212.
26. Kim J, Banks A, Cheng H, *et al.* Epidermal electronics with advanced capabilities in near-field communication. Small 2015;11:906–912.
27. Cheng S, Wu Z. A microfluidic, reversibly stretchable, large-area wireless strain sensor. Adv Funct Mater 2011;21:2282–2290.
28. Tolley MT, Shepherd RF, Mosadegh B, *et al.* A Resilient, Untethered Soft Robot. Soft Robot 2014;1:213–223.
29. Marchese AD, Katzschmann RK, Rus D. A recipe for soft fluidic elastomer robots. Soft Robot 2015;2:7–25.
30. Bartlett NW, Tolley MT, Overvelde JTB, *et al.* A 3D-printed, functionally graded soft robot powered by combustion. Science (80-) 2015;349:161–165.
31. Wehner M, Truby RL, Fitzgerald DJ, *et al.* An integrated design and fabrication strategy for entirely soft, autonomous robots. Nature 2016;536:451–455.
32. Liu R, Huskic G, Zell A. Dynamic objects tracking with a mobile robot using passive UHF RFID tags. In: 2014 IEEE/RSJ International Conference on Intelligent Robots and Systems, Chicago, IL, September 14–18, 2014, pp. 4247–4252.
33. Sanpechuda T, Kovavisaruch L. A review of RFID localization: applications and techniques. In: 5th International Conference on Electrical Engineering/Electronics, Computer, Telecommunications and Information Technology, ECTI-CON 2008, Vol 2, Krabi, Thailand, May 14–17, 2008, pp. 769–772.
34. Choi B-S, Lee J-W, Lee J-J. Distributed sensor network based on RFID system for localization of multiple mobile agents. Wirel Sens Netw 2011;3:1–9.
35. Liu T, Sen P, Kim CJ. Characterization of nontoxic liquid-metal alloy galinstan for applications in microdevices. J Microelectromechanical Syst 2012;21:443–450.
36. Park YL, Majidi C, Kramer R, *et al.* Hyperelastic pressure sensing with a liquid-embedded elastomer. J Micromech Microeng 2010;20:125029.
37. Chossat JB, Park YL, Wood RJ, *et al.* A soft strain sensor based on ionic and metal liquids. IEEE Sens J 2013;13:3405–3414.
38. Adam Bilodeau R, White EL, Kramer RK. Monolithic fabrication of sensors and actuators in a soft robotic gripper. In: 2015 IEEE/RSJ International Conference on Intelligent Robots and Systems (IROS), Hamburg, Germany, September 28–October 2, 2015, pp. 2324–2329.
39. Kramer RK, Majidi C, Wood RJ. Wearable tactile keypad with stretchable artificial skin. In: Proceedings—IEEE International Conference on Robotics and Automation, Shanghai, China, May 9–13, 2011, pp. 1103–1107.
40. Kramer RK, Majidi C, Sahai R, *et al.* Soft curvature sensors for joint angle proprioception. In: 2011 IEEE/RSJ International Conference on Intelligent Robots and Systems, San Francisco, CA, September 25–30, 2011, pp. 1919–1926.
41. Vogt D, Park YL, Wood RJ. A soft multi-axis force sensor. In: Proceedings of IEEE Sensors, Taipei, Taiwan, October 28–31, 2012, pp. 1–4.
42. Case JC, White EL, Kramer RK. Soft material characterization for robotic applications. Soft Robot 2015;2:80–87.
43. Cheng S, Wu Z. Microfluidic electronics. Lab Chip 2012;12:2782.
44. Ukkonen L, Schaffrath M, Engels DW, *et al*. Operability of folded microstrip patch-type tag antenna in the UHF RFID bands within 865–928 MHz. IEEE Antennas Wirel Propag Lett 2006;5:414–417.

45. Takiguchi M, Yamada Y. Improvement of radiation efficiencies by applying folded configurations to very small meander line antennas. In: 2003 IEEE Topical Conference on Wireless Communication Technology, Honolulu, HI, October 15–17, 2003, pp. 96–97.
46. Hu Z, Cole PH, Zhang L. A method for calculating the resonant frequency of meander-line dipole antenna. In: 2009 4th IEEE Conference on Industrial Electronics and Applications, Xi'an, China, May 25–27, 2009, pp. 1783–1786.
47. Esa M. Electrically small High-temperature superconducting Y-Ba-Cu-O meander dipole antennas for space-limited applications. PhD thesis, University of Birmingham, 1996.
48. Balanis CA. Antenna theory: analysis and design. Electron Power 1982;28:267.
49. Antennas I, Magazine P, Politecnico V. The art of UHF RFID antenna design: impedance matching and size-reduction techniques. IEEE Antennas Propag Mag 2008;50: 66–79.
50. Abbosh A. Accurate effective permittivity calculation of printed center-fed dipoles and its application to quasi yagi-uda antennas. IEEE Trans Antennas Propag 2013;61:2297–2300.
51. Jackson DR, Alexopoulos NG. Analysis of planar strip geometries in a substrate-superstrate configuration. IEEE Trans Antennas Propag 1986;34:1430–1438.

Address correspondence to:
Adam A. Stokes
The School of Engineering
Institute for Integrated Micro and Nano Systems
The University of Edinburgh
The King's Buildings
Edinburgh EH9 3LJ
United Kingdom

E-mail: adam.stokes@ed.ac.uk

Zhirun Hu
Microwave and Communication Systems Group
School of Electrical and Electronic Engineering
University of Manchester
Manchester M13 9PL
United Kingdom

E-mail: z.hu@manchester.ac.uk

Supplemental Information

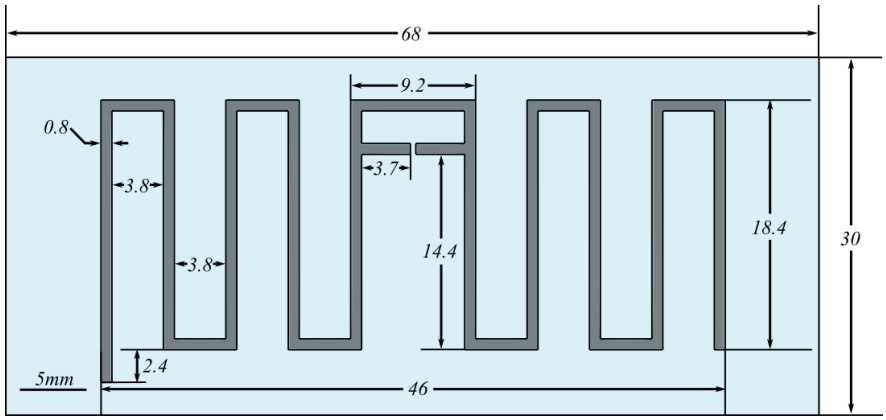

Figure E.1.: *Dimensional drawing of the meander line antenna.* The unit in this figure in milimetre. The height of the substrate is 2.15 mm in total.

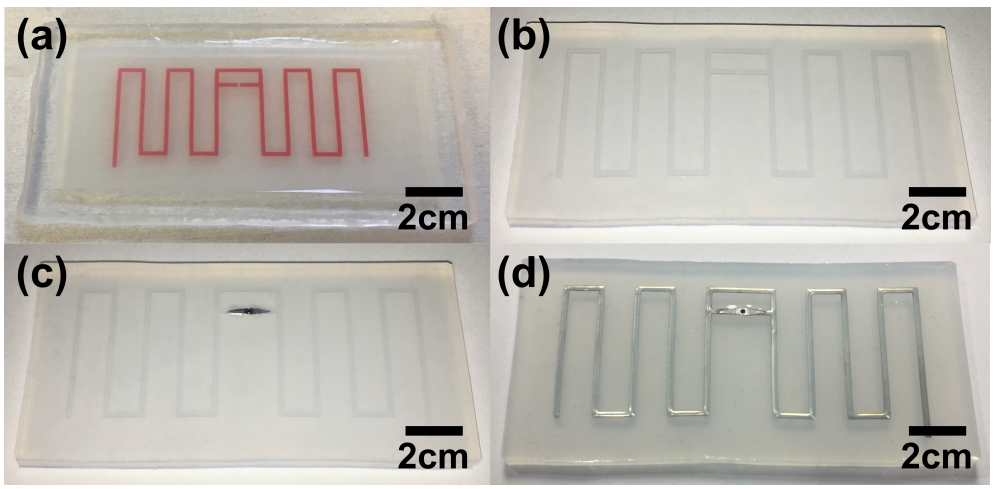

Figure E.2.: *Photographs of the fabrication process.*

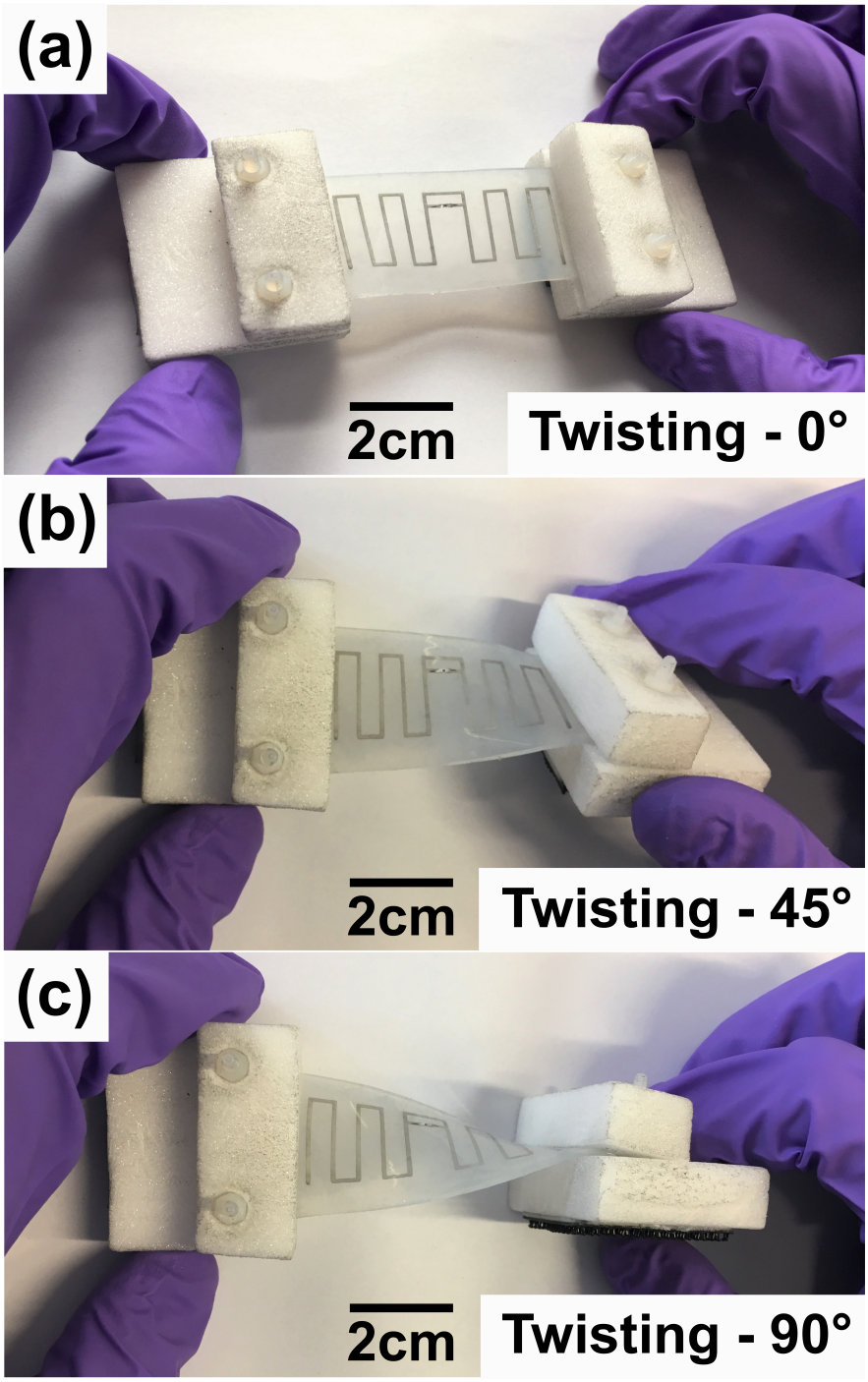

Figure E.3.: *Demonstration of three different test conditions in the twisting experiment.*

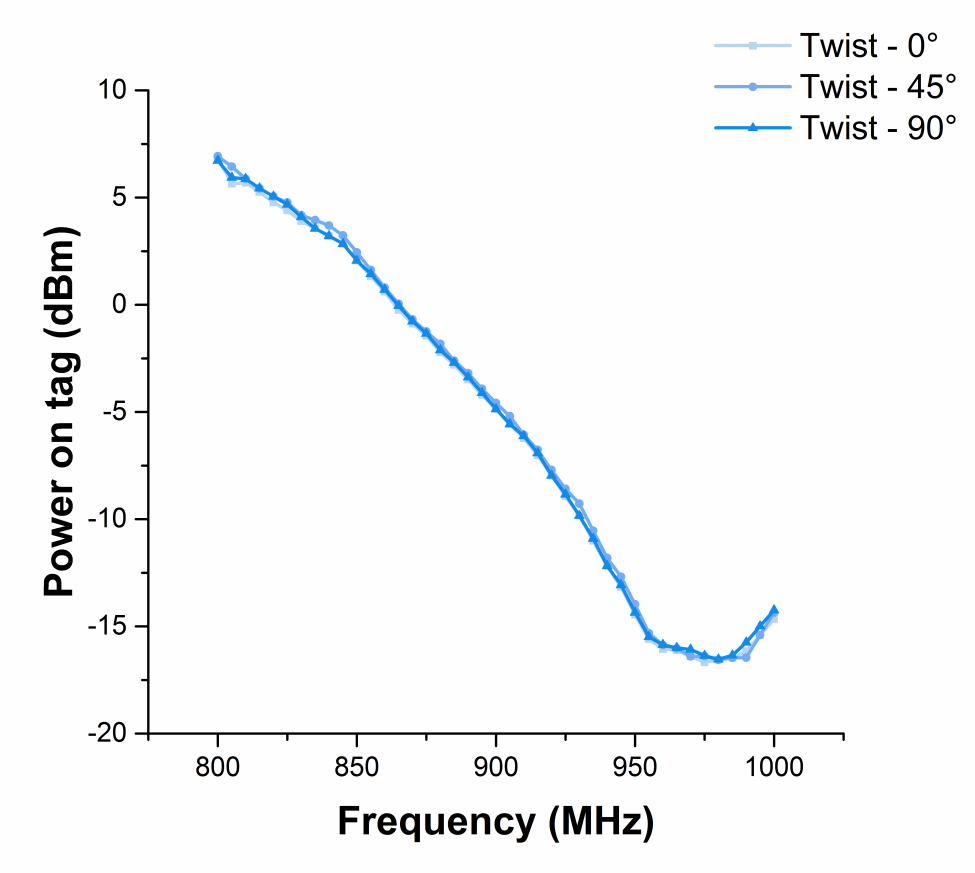

Figure E.4.: *A prototype was tested under three different twist angles:* 0°, 45°, *and* 90°.

APPENDIX F

Soft Wireless Battery-free UHF RFID Stretchable Sensor based on Microfluidic Technology

Journal: IEEE Journal of Radio Frequency Identification

Authors: Lijun Teng, Kewen Pan, Leng Ting, Xinyao Zhou, Adam A. Stokes, and Zhirun Hu

Online access to paper:

https://ieeexplore.ieee.org/abstract/document/8703088

This article has been accepted for publication in a future issue of this journal, but has not been fully edited. Content may change prior to final publication. Citation information: DOI 10.1109/JRFID.2019.2912959, IEEE Journal of Radio Frequency Identification

Soft Wireless Battery-free UHF RFID Stretchable Sensor based on Microfluidic Technology

Kewen Pan, Lijun Teng, Leng Ting, Zhou Xinyao, Adam A. Stokes and Zhirun Hu

***Abstract*—Stretchable microfluidic sensors have recently been developed and employed in many sensing applications. However, they are still in their early stage of development and facing considerable challenges, such as practical system integration due to the limitation of costs, wired connections and sensitivity. In this work, we present a compact soft wireless battery-free RFID stretchable sensor based on microfluidic technology. The proposed RFID sensor has high sensitivity and is able to be stretched to 160% of its original size. Moreover, the sensor is completely wireless powered and battery-free. It can be fully embedded into sensor carriers such as robots to eliminate wires, reduce the weight and increase the agility. Difference to known received signal strength indicator (RSSI) techniques for RFID sensing monitoring, resonance frequency shift is used in this work, significantly increasing the measurement accuracy, usefulness and reliability for many practical applications.**

***Index Terms*—Ecoflex, microfluidic antenna, stretchable sensor, metamaterilas, radio frequency identification (RFID).**

I. Introduction

Passive RFID technology in UHF band (860MHz-960MHz) utilizes RF signals to detect and identify specific objects [1]. Nowadays there is a growing interest in exploring the use of RFID technologies in sensing and monitoring [2]. Stretch monitoring using passive RFID technology was first demonstrated in [3] and further developed in [4], [5]. However, the deformable metal wire RFID tags in [5] have very limited lifetime and poor repeatability due to the fatigue of metal wire. E-textile works in [4] overcome the metal fatigue problem by using stretchable conductive polymers. However, the measurement depends on the received signal strength indicator (RSSI) which is not only affected by the antenna gain, but also varies with distance between the RFID tag and the reader antenna. Therefore, an additional reference tag located in a specific position is required to calibrate the distance effect. Furthermore, coupling and polarization effects between sensor and the reference tag have to be considered because they are not constant, especially when tags are bended or twisted.[1]

K. Pan, T. Leng, X. Zhou and Z. Hu are with the School of Electrical and Electronic Engineering, University of Manchester, Manchester M13 9PL, U.K. (Corresponding author: Z. Hu and e-mail: z.hu@manchester.ac.uk).

L.Teng and A. Stokes are with the School of Engineering, Institute for Integrated Micro and Nano Systems, The University of Edinburgh, The King's Buildings, Edinburgh, United Kingdom.

This is a joint article and these authors contributed equally to this work.

Benefiting from the development of microfluidic technology and the discovery of non-toxic, room-temperature liquid alloys made with gallium, indium (eGaIn) and tin (Galinstan), researchers have successfully fabricated liquid conductors and antennas without metal fatigue problem [22], [23]. Impressive works on deformable soft antennas, such as stretchable microfluidic antennas made with liquid metal and hybrid silicone [8], microfluidic serpentine antennas with reversible stretchability and mechanical frequency modulation ability [9] have been demonstrated. As the fabrication process becomes mature, mechanically tunable soft antenna was first reported using soft lithographic and rapid prototyping methods in [10]. After that, meandered dipole based stretchable RFID sensor has been reported in [11] and [12], where the measurement of stretch is based on RSSI and reference tag is still be required. In [13], a wireless stretchable RFID sensor which successfully converted the tensile elongation to frequency shift rather than signal strength was reported, significantly advanced the measurement reliability because the distance and angle between the tag and reader antennas are no longer relevant to the measurement accuracy. However, the antenna in [13] is a foot away from practical applications because of its lower Q factor, less sensitivity and nonlinearity.

In this work, the antenna structure is evolved from metamaterial inspired split ring resonator (SRR), operating at its second electric resonant mode [14], which overcomes the disadvantages of meandered dipoles as stretching sensing antennas in [11-13]. A T-matching network [15] was connected for conjugate matching with the RFID chip (Impinj Monza R6). The antenna has the size of $3.3 \times 3.5 \times 0.23$ cm^3 and the detection range of 6.7 m with the standard 3.28 W Equivalent Isotropic Radiated Power (EIRP).

Antenna design, fabrication process and measurement results will be presented in Section II, III and IV respectively, followed by discussions on the tests of antenna bending and rolling effects. Finally, a soft actuator monitoring system will be demonstrated.

II. Design of Metamaterial Inspired Liquid Metal Soft Antenna

SRR is one of the most commonly used metamaterial structures and was first proposed in 1999 [16]. The strong coupling effects between the rings make the structure very sensitive to the change of the ring length and gap width. Such

2469-7281 (c) 2018 IEEE. Personal use is permitted, but republication/redistribution requires IEEE permission. See http://www.ieee.org/publications_standards/publications/rights/index.html for more information.

This article has been accepted for publication in a future issue of this journal, but has not been fully edited. Content may change prior to final publication. Citation information: DOI 10.1109/JRFID.2019.2912959, IEEE Journal of Radio Frequency Identification

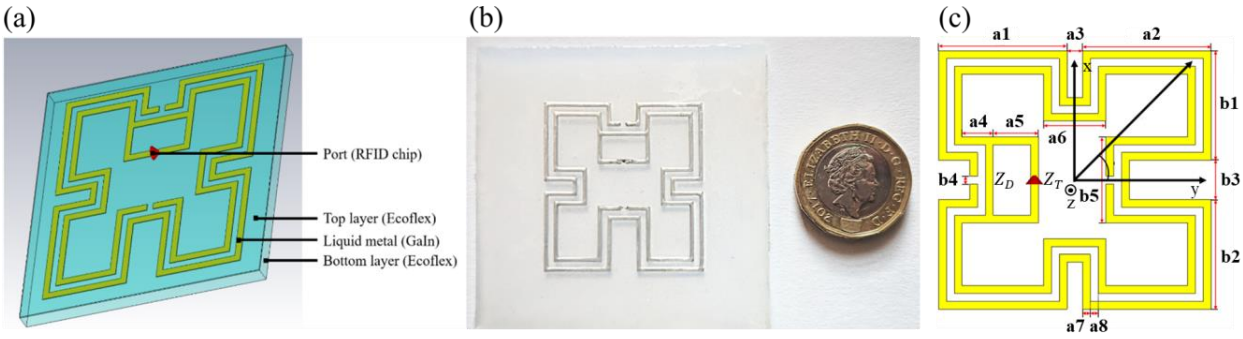

Fig. 1. SRR RFID stretchable sensor. (a) Antenna structure (red corn is feed port). (b) Fabricated device (3.3cm×3.5cm). (c) Geometrical parameters of the antenna.

characteristics provide higher sensitivity compared with those of the meandered line antennas [5]. A SRR inspired antenna can have multimode resonances. Its fundamental resonance mode has been proved having low radiation efficiency [14], [17]–[19]because the radii of the rings are much smaller than the corresponding free space wavelength, which leads to low radiation resistance and efficiency [18]–[20]. Therefore, second resonance mode was chosen in this work. The antenna consisted of an SRR radiator, T-matching network and a RFID chip, as shown in Fig. 1(a) and (b). The antenna and matching network were designed and simulated using commercial EM simulation software CST MWS [26]. In the simulation, the liquid alloy was modelled as metal with a conductivity of 2.3×10^6 S/m [20]. The geometrical parameters of the antenna are illustrated in Fig. 1(c): a_1=a_2=16.5 mm, a_3=2 mm, a_4=4 mm, a_5=5.8 mm, a_6=8 mm, a_7=a_8=1 mm, b_1=b_2=14 mm, b_3=5 mm, b_4=1 mm, b_5=11 mm. The thickness of bottom layer is 2.3 mm with 0.1 mm thick liquid channel. The upper layer is 0.2 mm thick for sealing purpose. The second resonance mode of the SRR antenna has been studied [21]. The radiation resistance in this resonance mode is approximately 7 times higher than that of the same half wave length dipole. The input impedance of the commercial RFID chip (Impinj, Monza R6) is 12-j120Ω at 915MHz. The T-matching network, which connects the chip to the inner ring of the SRR antenna, is required to provide a conjugate matching between the chip and antenna for maximum power efficiency. The input impedance of the antenna is [15]:

$$Z_{in} = \frac{2Z_t n^2 Z_a}{2Z_t + n^2 Z_a} \quad (1)$$

where Z_a is the input impedance of the SRR antenna itself, Z_t is the input impedance of T-matching network, n is current ratio between two arms. The overall input impedance Z_{in} can therefore be designed for conjugate matching with the RFID chip.

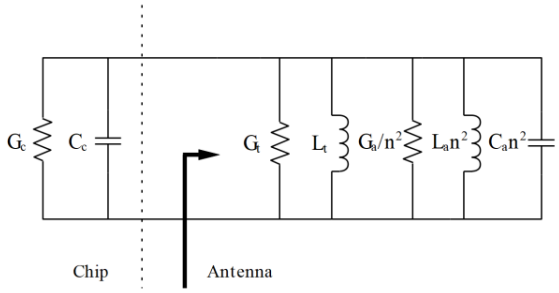

Fig. 2. Antenna equivalent circuit model (Left is RFID chip side and right is antenna side).

In the second resonance mode of SRR structure, the surface current distributions in both rings are of opposite directions and phase [14]. The resonance condition can be analysed using equivalent circuit model [19], as shown in Fig.2. G_c, G_t, and G_n are the conductance of RFID chip, T-matching network loss and SRR antenna (caused by loss and radiation) respectively. C_c and C_a represent the RFID chip input capacitor and SSR antenna parasitic capacitor where $C_a = \pi L_x C_{pul}$ [19] (L_x is the side length of antenna, C_{pul} is per unit length capacitor). L_t and L_a are the T-matching shorter arm equivalent inductor and antenna inductor. Resonance frequency f_0 can be expressed as:

$$f_0 = \frac{1}{2\pi\sqrt{L_{total} C_{total}}} \quad (2)$$

where $L_{total} = \frac{L_t L_a n^2}{L_a n^2 - L_t}$ and $C_{total} = C_c + C_a n^2$. It can be seen that the resonance frequency decreases significantly due to the transformation of T-matching network and RFID chip capacitor. Therefore, both T-matching network and SRR antenna behave inductively. Under stretched condition, L_t and L_a increase because of longer current path, resulting the resonance frequency move down to lower frequencies. The measurement results between different stretching levels and frequency shifts are discussed in the following sections.

III. Soft Antenna Fabrication

Galinstan is a generic name of a series of room-temperature eutectic liquid alloys which consist of gallium (Ga), indium (In), and tin (Sn). Galinstan has desirable properties such as low toxicity and low reactivity of its component metals. Therefore,

2469-7281 (c) 2018 IEEE. Personal use is permitted, but republication/redistribution requires IEEE permission. See http://www.ieee.org/publications_standards/publications/rights/index.html for more information.

This article has been accepted for publication in a future issue of this journal, but has not been fully edited. Content may change prior to final publication. Citation information: DOI 10.1109/JRFID.2019.2912959, IEEE Journal of Radio Frequency Identification

Galinstan is an excellent substitution for some conventional conductive liquid, such as toxic mercury and reactive sodium-potassium alloy. Galinstan used in this work has a typical composition of 68.5% Ga, 21.5% In, and 10% Sn with the electrical conductivity of 2.3×10^6 S/m. It also has a large surface tension and great wetting properties on the surface of Ecoflex or other silicone rubber materials. Galinstan, therefore, can afford stable and reliable connections in the elastic channels [10] as it tends to hold their position even when a device is twisted, stretched, or severely folded.

Ecoflex is one of the most commonly used substrate materials in fluidic devices due to its attractive high elasticity, uncomplicated fabrication, easy casting properties and excellent biocompatibility. In this work, we used Ecoflex type 00-50 to make elastic substrate of the SRR antenna. The elongation at break of Ecoflex 00-50 in tensile strength test with ASTM D412 system is 980% (defined as the percentage change in length or $\left(\frac{l-l_0}{l_0}\right) \times 100\%$, [22]).

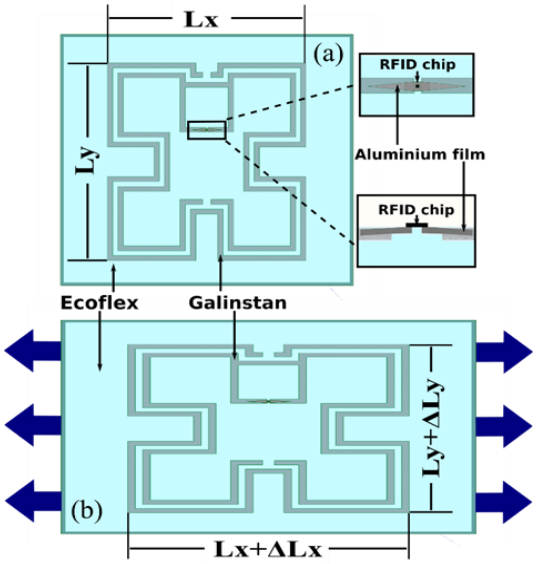

Fig. 3. (a) Top view of the Ecoflex liquid metal SRR antenna with detailed cross-section drawing of the RFID chip insertion. The initial length, width and thickness of the antenna are L_x=33 mm, L_y=35 mm and L_z=2.5 mm respectively. The channels with filled Galinstan in the Ecoflex substrate are 1 mm in the width. The RFID chip was bonded on an aluminum film then inserted in the fluidic channels to connect with Galinstan; (b) when the antenna is under stretching, the length in X direction, the width in Y direction and the thickness in Z direction become $L_x+\Delta L_x$, $L_y+\Delta L_y$ and $L_z+\Delta L_z$ respectively.

Fig. 3(a) and (b) show the structure of the antenna without and with stretching respectively. Deformation of the antenna under stretch is significantly influenced by Poisson's effect. For example, when the antenna is stretched in one direction, it becomes narrower and thinner in other directions. Such phenomenon changes the thickness of the antenna substrate and also affects its resonance frequency. The Poisson's ratio (v) of Ecoflex 00-50 is 0.49 which means this material is a nearly incompressible material which deforms elastically even under a very small strain. In Fig. 3(a), the original length, width and thickness of the antenna are represented by L_x, L_y and L_z respectively. When the antenna is stretched in X direction ($L_x + \Delta L_x$), as shown in Fig. 3(b), the thickness and width change to $L_y + \Delta L_y$ and$L_z + \Delta L_z$. Eq. (3) shows the relationship between $\Delta L_y/L_y$, $\Delta L_z/L_z$ and $L_x + \Delta L_x$ [22]:

$$\frac{\Delta L_y}{L_y} = \frac{\Delta L_z}{L_z} = (1 + \frac{\Delta L_x}{L_x})^{-v} - 1 \qquad (3)$$

It should be noticed when the length varies in X direction (L_x), not only the width in Y direction, but the thickness will also change simultaneously.

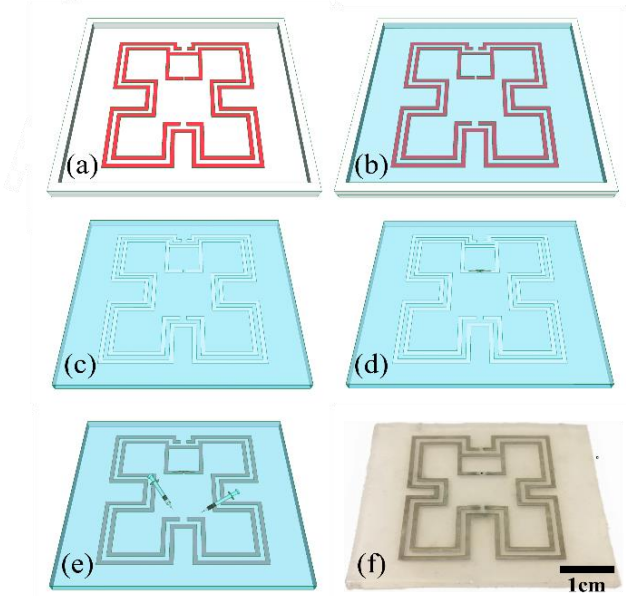

Fig. 4. Schematic illustration of the fabrication process and photograph of the stretchable fluidic antenna; (a) the soft-lithography mold made with 0.15 mm vinyl film (red) and 2 mm Acrylic substrate and frame (white); (b) uncured Ecoflex with height of 2 mm was poured into the soft-lithography mold; (c) the casted piece of Ecoflex was sealed with another 0.2 mm Ecoflex film; (d) the RFID chip bonded on an aluminum film was inserted into the channels in Ecoflex substrate; (e) two needles were used to inject Galinstan into the channels. (f) Photograph of the final prototype.

Fig. 4(a)-(e) illustrate the fabrication process of the stretchable sensor: (i) A soft-lithography mold to cast uncured Ecoflex with a 2 mm Acrylic board (Acrylic Cast, AMARI) and a piece of 0.15 mm self-adhesive vinyl film (CRAFTRKZO, d-c-fix®) were prepared. The Acrylic material, which was shaped with a laser cutter (Epilog Fusion), was used as the substrate and the frame in the mold. The vinyl film was used to form the structure of the channels in the mold. The profile of the antenna structure was cut on the vinyl film with a laser micro-machining system (Protolaser U3, LPKF) which contains an error rate less than 5%. (ii) Part A and part B of Ecoflex (type 00-50, Reynolds Advanced materials) were mixed at the ratio of 1:1. The uncured Ecoflex with a controlled height of 2 mm was degassed under vacuum for five minutes and then poured into the soft-lithography mold. In order to fasten the curing, the mold was put into a convection oven at 65 ℃ for 20 mins. (iii) The channels were sealed in the casted 2 mm Ecoflex layer with a piece of 0.2 mm Ecoflex film made with a spin coater. (iv) We made small incisions in the center of the thin Ecoflex layer to embed the RFID chip; the RFID chip (Monza R6; Impinj) was bonded on an Aluminum film with a bonding machine (FB-300 manual RFID wrapping machine) and inserted in the channels. (v) Two 0.3 mm-diameter needles

2469-7281 (c) 2018 IEEE. Personal use is permitted, but republication/redistribution requires IEEE permission. See http://www.ieee.org/publications_standards/publications/rights/index.html for more information.

This article has been accepted for publication in a future issue of this journal, but has not been fully edited. Content may change prior to final publication. Citation information: DOI 10.1109/JRFID.2019.2912959, IEEE Journal of Radio Frequency Identification

were used to inject Galinstan into the channels through positive pressure and remove air. (vi) In the end, a very thin film of uncured Ecoflex was coated on the surface of this antenna to seal all the holes.

IV. Antenna Measurement

Voyantic Tagformance measurement system was used for the RFID tag measurement as shown in Fig. 5. The RFID reader contains a signal generator, transmitter, power detector and receiver. The RFID antenna receives the signal and power from the reader and activates its chip which in turn modulates and backscatters the signal to the reader antenna.

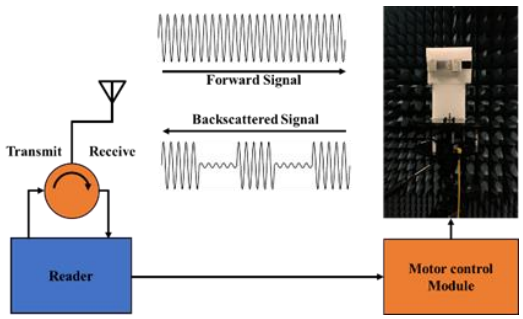

Fig. 5. RFID measurement set up with Voyantic Tagformance.

The minimum power that the RFID tag requires can be expressed as:

$$P_{tag} = \frac{P_{th}}{\tau G_{tag}} = [P_t - L_{cable} + G_t - FSPL]_{dB} \quad (4)$$

where P_t, G_t are the minimum transmitted power and gain of the reader antenna, L_{cable} and $FSPL$ represent cable loss and free space loss which can be calibrated by using a standard tag before measurement. P_{th} is the minimum threshold of the power required to activate the RFID chip, G_{tag} is the gain of the tag antenna. τ is the matching factor, which describes the conjugate impedance matching between the antenna and RFID chip.

P_{th} and τ are constant for a specific frequency, the minimum power that can power on the chip is inverse proportional to the antenna gain G_{tag}, which can be derived from measured P_t:

$$G_{tag} = [P_{th} - P_t + L_{cable} - G_t + FSPL]_{dB} \quad (5)$$

Considering the detection distance requirements in real applications, theoretical read range R_{max} can be calculated for given EIRP as:

$$R_{max} = \sqrt{\frac{P_{max,EIRP}}{P_{tag}}} \cdot \frac{c}{4\pi f} \quad (6)$$

where $P_{max,EIRP}$ =3.28W, c is light speed and f is the corresponded frequency.

V. Results and Discussions

The simulated antenna impedance variation with stretching is shown in Fig. 6(a). It can be seen that the peak values of both real and imaginary parts of the impedance shift to lower frequency when increasing the stretching, resulting in the decrease of resonance frequency.

The RFID antenna performance was measured in anechoic chamber. To measure the gain and resonance frequency of the antenna, the reader sweeps linearly from 800 MHz to 1 GHz with a 3 MHz step. The theoretical reading range is calculated using Eq. (6) and plotted in Fig. 6(b). It can be found that the resonance frequency without stretching is 938 MHz with 6.7 m read range and it drops to 818 MHz at 60% strain. Therefore, the sensitivity is 5.71 MHz/mm, doubled the previous result [13] (2.65 MHz/mm). When the antenna is stretched, its resonance frequency decreases whereas the read range increases due to longer electric length of the antenna and higher gain.

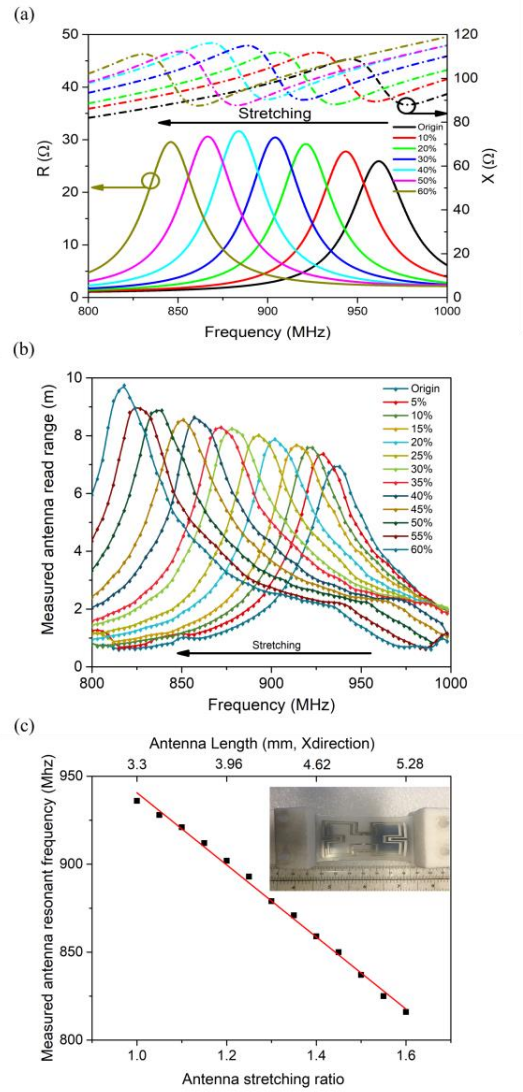

Fig. 6. (a) Simulated antenna impedance under different stretch conditions. (b) Measurement results of RFID tag read range and resonance frequency under different stretching conditions. (c) Antenna resonance frequency verses antenna stretching ratio (stretched length/ original length), the red line is linear fits of scatters.

2469-7281 (c) 2018 IEEE. Personal use is permitted, but republication/redistribution requires IEEE permission. See http://www.ieee.org/publications_standards/publications/rights/index.html for more information.

This article has been accepted for publication in a future issue of this journal, but has not been fully edited. Content may change prior to final publication. Citation information: DOI 10.1109/JRFID.2019.2912959, IEEE Journal of Radio Frequency Identification

Fig. 6(c) illustrates the relationship between the resonance frequency and antenna stretching ratio. Two holders, which consist of low permittivity and low loss foam (71 IG-F, MK), were used to hold and stretch the antenna in Y-axis (inset Fig. 6(c)). The distance between the RFID sensor antenna and reader antenna is 80 cm. To eliminate the influence of foam holders, calibration was performed every time when antenna length was changed. High stretchability up to 160% of the antenna length was tested with 5% per step. The antenna operates properly when being stretched to 160% and could be further stretched, yet, its resonance frequency will run out of the lowest allocated RFID frequency spectrum.

From Fig. 6(c), linear relationship between the resonance frequency and stretching length can be observed. Fitted formula of the relationship can be expressed as:

$$f_r = -205 \times r + 1145.6 \quad (7)$$

Eq. (7) can convert the stretching ratio r directly from the measured resonance frequency. However, it should be noticed that two sides of the antenna were clamped by foam holders and the width is fixed. The ratio of stretching at the edge would be different from the central part. The same problem would happen in real applications, which affects antenna's resonance frequency. Therefore, it is necessary to calibrate the frequency-stretching ratio relationship after installing the antenna.

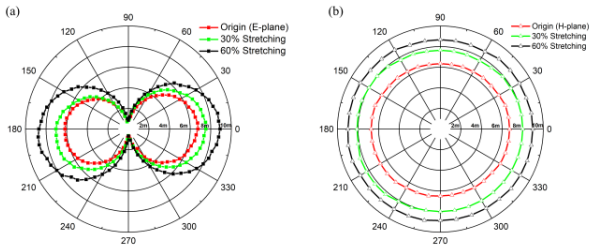

Fig. 7. Measured RFID antenna radiation pattern under different stretching length in E-plane (a) and H-plane (b) (0%, 30% and 60%).

The radiation patterns of the RFID antenna under different stretching conditions were measured in both E-plane and H-plane (Antenna Measurement Studio 5.5, Diamond Engineering). For more intuitionistic demonstration, the read range was plotted instead of antenna gain. The data were recorded every 5 degrees rotation, as shown in Fig. 7. The measured radiation pattern is similar with dipole antenna which means the antenna is omnidirectional at H-plane and weakly directional at E plane. The maximum read range is approximately 6.7 m, 7.4 m and 9 m with 0%, 30% and 60% stretching, respectively. Except the read range, there is no significant distortion of radiation pattern under stretching.

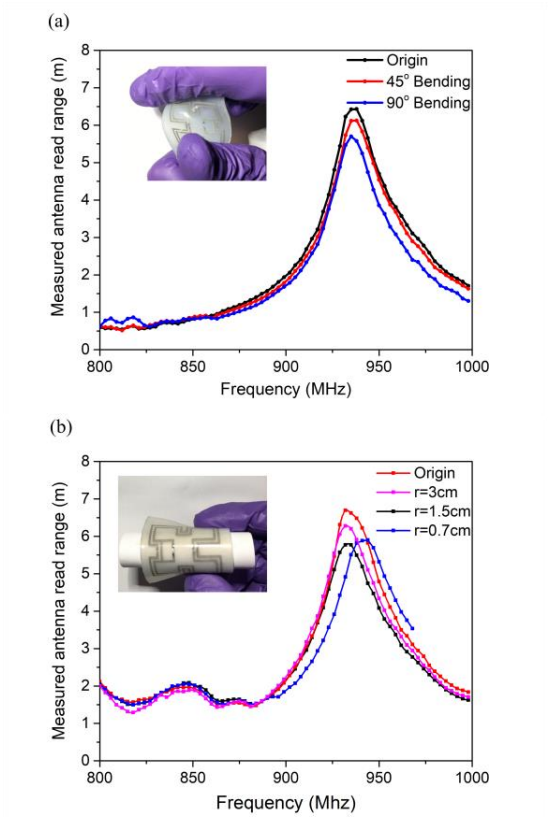

Fig. 8. (a) Antenna resonance frequency variation with different bending angle (0°, 45°, 90°). (b) Antenna resonance variation under rolling (r=0.7, 1.5, 3, ∞).

Having demonstrated the relationship between stretching length and resonance frequency of the RFID stretch sensor, we go further to investigate the effects of bending and rolling to the RFID sensor antenna resonance because most applications not only have plane stretching, but also get distortion and deformation in other directions. In Fig. 8(a), the antenna was bended from 0° to 90° (fixed by foam holders with different angles to ensure accuracy and reproducibility), the strong coupling between the inner and outer rings makes the antenna being less sensitive to the bending, no obvious frequency shift can be observed during bending. However, the maximum read range decreases by 1 metre when the antenna is bended to 90°. This is because the bending distorts the antenna's radiation pattern, i.e., the gain reduces. The same conclusion can be drawn from the rolling test in Fig. 8(b) (held by paper tubes with different radii), only when the radius is smaller than 1.5 cm, the resonance frequency starts to shift. It increases by only 15 MHz when the rolling radius reduces to 0.7 cm. At this point, the antenna touches itself from end to end. These experimental data verify that bending and rolling have little effects on the resonance frequency as the electric length of the antenna barely varies.

2469-7281 (c) 2018 IEEE. Personal use is permitted, but republication/redistribution requires IEEE permission. See http://www.ieee.org/publications_standards/publications/rights/index.html for more information.

This article has been accepted for publication in a future issue of this journal, but has not been fully edited. Content may change prior to final publication. Citation information: DOI 10.1109/JRFID.2019.2912959, IEEE Journal of Radio Frequency Identification

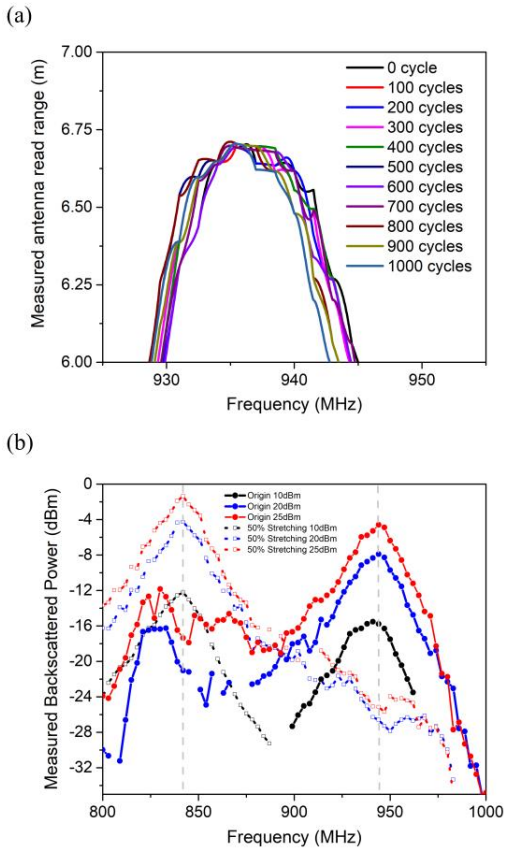

Figure 9: (a) Cyclability test of the RFID stretchable sensor. The sensor was stretched from its initial state to 200% of the original length (X direction) with 1000 cycles. (b) Demonstration of the measured backscattered power where the RFID stretchable sensor is placed in normal office environment with a fixed distance.

As the cyclability is another important criterion to evaluate stretchable sensor performance, the RFID sensor was stretched ($2L_x$) and released (L_x) 1000 cycles. Its resonance frequency was recorded every 100 cycles and plotted in Fig. 9(a). The resonance frequency is rather stable in the first 500 cycles and starts to decrease from 600 cycles. There is approximately 2 MHz frequency shift after 1000 cycles. Based on Eq. (7), the calculated distance error is 0.032 mm which confirms that the RFID sensor has an excellent cyclability.

In order to demonstrate that the proposed sensor can be used in practical environment, we moved the whole measurement set to office environment with tables, computers and people moving around. The measurement results are plotted in Fig. 9(b). In the original state, the peak value of the backscattered power varies with different radiating power whereas the resonance frequency has kept constant. After stretching the sensor of 50%, all peak values shift from 944 MHz to 842 MHz, indicating that the sensor works well under practical multipath interference environment.

Taking a step further to real applications, we have integrated the RFID stretchable sensor into a soft chamber which is made of silicone materials with pneumatic channels based on the structure described in [23] since it is compatible with soft lithography [24] technology. In the fabricated soft chamber, a series of pneumatic channels were embedded in an extensible Ecoflex layer and bonded to a relatively less extensible PDMS layer (Young's Modulus of Ecoflex is 69 kPa [13] whereas PDMS is 0.8-3MPa [25]). When compressed air is injected into the chamber, the chamber inflates like balloons. The difference in strain between the Ecoflex layer and the PDMS layer causes the structure to bend.



Fig. 10. Soft pneumatic actuator with RFID stretchable sensor attached on the Ecoflex side.

In Fig. 10, the fabricated actuator is flat and the RFID stretchable sensor antenna operates in its original state when air pressure is zero. Its resonance frequency is 917 MHz (this is lower than that of the antenna shown in Fig. 4(f) because of the increment of substrate thickness). With increasing air pressure, the Ecoflex grooves start to expand. However, the expansion rate of relatively rigid PDMS layer is much smaller. The different expansion rates lead to bending action of the actuator. Under such condition, the RFID stretchable sensor was stretched at both X and Y directions and bended from 0° to 90°. The resonance frequency with different bending angle is shown in Fig. 11. It can be seen that the average resonance frequency shift rate is >1.4 MHz/° at 0°~30° and >2 MHz/° at 30°~60° (exceed measurement range when bended over 60°).

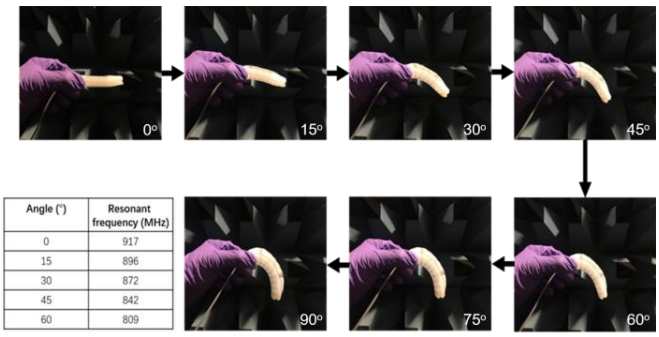

Angle (°)	Resonant frequency (MHz)
0	917
15	896
30	872
45	842
60	809

Fig. 11. Soft pneumatic actuator bending process when air pressure increasing (0°, 15°, 30°, 45°, 60°, 75° and 90°) and corresponded measured RFID antenna resonance frequencies.

2469-7281 (c) 2018 IEEE. Personal use is permitted, but republication/redistribution requires IEEE permission. See http://www.ieee.org/publications_standards/publications/rights/index.html for more information.

This article has been accepted for publication in a future issue of this journal, but has not been fully edited. Content may change prior to final publication. Citation information: DOI 10.1109/JRFID.2019.2912959, IEEE Journal of Radio Frequency Identification

VI. Conclusion

In this paper, we have demonstrated a metamaterial inspired soft wireless battery-free UHF RFID liquid metal stretchable sensor. The operation principle is based on the resonance frequency detection of the RFID sensor antenna, which can convert physical parameter variations to its resonance frequencies. This technique has advantages over the RSSI: it doesn't need reference antenna and has high sensitivity. First a compact SRR UHF RFID antenna which is highly sensitive to the mechanical stretch has been designed and fabricated. Secondly the performance of the RFID sensor under different stretching length, including backscattered powers, read ranges and radiation patterns, has been measured, verifying that the resonance frequency of the RFID antenna can be altered efficiently during stretching. Thirdly, bending and rolling of the antenna have been tested and discussed. Fourthly, the reliability test reveals that the sensor maintains good performance up to 1000 stretching cycles. Finally, a prototype of RFID stretching sensor enabled soft pneumatic actuator has been fabricated and demonstrated, illustrating the potential applications of the reported soft wireless battery-free UHF RFID stretchable sensor.

References

[1] H. Stockman, "Communication by means of reflected power," *Proc. IRE*, vol. 36, no. 10, pp. 1196–1204, 1948.

[2] J. Landt, "The history of RFID," *IEEE potentials*, vol. 24, no. 4, pp. 8–11, 2005.

[3] S. Merilampi, P. Ruuskanen, T. Björninen, L. Ukkonen, and L. Sydänheimo, "Printed passive UHF RFID tags as wearable strain sensors," in *Applied Sciences in Biomedical and Communication Technologies (ISABEL), 2010 3rd International Symposium on*, 2010, pp. 1–5.

[4] X. Chen, L. Ukkonen, and T. Björninen, "Passive e-textile uhf rfid-based wireless strain sensors with integrated references," *IEEE Sens. J.*, vol. 16, no. 22, pp. 7835–7836, 2016.

[5] C. Occhiuzzi, C. Paggi, and G. Marrocco, "Passive RFID strain-sensor based on meander-line antennas," *IEEE Trans. Antennas Propag.*, vol. 59, no. 12, pp. 4836–4840, 2011.

[6] Y. Lin, C. Cooper, M. Wang, J. J. Adams, J. Genzer, and M. D. Dickey, "Handwritten, soft circuit boards and antennas using liquid metal nanoparticles," *Small*, vol. 11, no. 48, pp. 6397–6403, 2015.

[7] M. D. Dickey, "Emerging applications of liquid metals featuring surface oxides," *ACS Appl. Mater. Interfaces*, vol. 6, no. 21, pp. 18369–18379, 2014.

[8] M. Kubo *et al.*, "Stretchable microfluidic radiofrequency antennas," *Adv. Mater.*, vol. 22, no. 25, pp. 2749–2752, 2010.

[9] Y. Huang, Y. Wang, L. Xiao, H. Liu, W. Dong, and Z. Yin, "Microfluidic serpentine antennas with designed mechanical tunability," *Lab Chip*, vol. 14, no. 21, pp. 4205–4212, 2014.

[10] J. So, J. Thelen, A. Qusba, G. J. Hayes, G. Lazzi, and M. D. Dickey, "Reversibly deformable and mechanically tunable fluidic antennas," *Adv. Funct. Mater.*, vol. 19, no. 22, pp. 3632–3637, 2009.

[11] S. H. Jeong, A. Hagman, K. Hjort, M. Jobs, J. Sundqvist, and Z. Wu, "Liquid alloy printing of microfluidic stretchable electronics," *Lab Chip*, vol. 12, no. 22, pp. 4657–4664, 2012.

[12] S. H. Jeong, K. Hjort, and Z. Wu, "Tape transfer printing of a liquid metal alloy for stretchable RF electronics," *Sensors*, vol. 14, no. 9, pp. 16311–16321, 2014.

[13] L. Teng, K. Pan, M. P. Nemitz, R. Song, Z. Hu, and A. A. Stokes, "Soft Radio-Frequency Identification Sensors: Wireless Long-Range Strain Sensors Using Radio-Frequency Identification," *Soft Robot.*, 2018.

[14] J. García-García, F. Martín, J. D. Baena, R. Marques, and L. Jelinek, "On the resonances and polarizabilities of split ring resonators," *J. Appl. Phys.*, vol. 98, no. 3, p. 33103, 2005.

[15] J. Choo, J. Ryoo, J. Hong, H. Jeon, C. Choi, and M. M. Tentzeris, "T-matching networks for the efficient matching of practical RFID tags," in *Microwave Conference, 2009. EuMC 2009. European*, 2009, pp. 5–8.

[16] J. B. Pendry, A. J. Holden, D. J. Robbins, and W. J. Stewart, "Magnetism from conductors and enhanced nonlinear phenomena," *IEEE Trans. Microw. Theory Tech.*, vol. 47, no. 11, pp. 2075–2084, 1999.

[17] R. Marqués, F. Mesa, J. Martel, and F. Medina, "Comparative analysis of edge-and broadside-coupled split ring resonators for metamaterial design-theory and experiments," *IEEE Trans. Antennas Propag.*, vol. 51, no. 10, pp. 2572–2581, 2003.

[18] B. Sauviac, C. R. Simovski, and S. A. Tretyakov, "Double split-ring resonators: Analytical modeling and numerical simulations," *Electromagnetics*, vol. 24, no. 5, pp. 317–338, 2004.

[19] R. Marqués, F. Medina, and R. Rafii-El-Idrissi, "Role of bianisotropy in negative permeability and left-handed metamaterials," *Phys. Rev. B*, vol. 65, no. 14, p. 144440, 2002.

[20] T. Liu, P. Sen, and C.-J. Kim, "Characterization of nontoxic liquid-metal alloy galinstan for applications in microdevices," *J. Microelectromechanical Syst.*, vol. 21, no. 2, pp. 443–450, 2012.

[21] S. Zuffanelli, G. Zamora, P. Aguilà, F. Paredes, F. Martín, and J. Bonache, "On the radiation properties of split-ring resonators (SRRs) at the second resonance," *IEEE Trans. Microw. Theory Tech.*, vol. 63, no. 7, pp. 2133–2141, 2015.

[22] J.-B. Chossat, Y.-L. Park, R. J. Wood, and V. Duchaine, "A soft strain sensor based on ionic and metal liquids," *IEEE Sens. J.*, vol. 13, no. 9, pp. 3405–3414, 2013.

[23] F. Ilievski, A. D. Mazzeo, R. F. Shepherd, X. Chen, and G. M. Whitesides, "Soft robotics for chemists," *Angew. Chemie*, vol. 123, no. 8, pp. 1930–1935, 2011.

[24] D. Qin, Y. Xia, and G. M. Whitesides, "Soft lithography for micro-and nanoscale patterning," *Nat. Protoc.*, vol. 5, no. 3, p. 491, 2010.

[25] Y. Fouillet *et al.*, "Stretchable Material for Microfluidic Applications," in *Multidisciplinary*

2469-7281 (c) 2018 IEEE. Personal use is permitted, but republication/redistribution requires IEEE permission. See http://www.ieee.org/publications_standards/publications/rights/index.html for more information.

This article has been accepted for publication in a future issue of this journal, but has not been fully edited. Content may change prior to final publication. Citation information: DOI 10.1109/JRFID.2019.2912959, IEEE Journal of Radio Frequency Identification

Digital Publishing Institute Proceedings, 2017, vol. 1, no. 4, p. 501.

[26] CST (Computer Simulation Technology). https://www.cst.com/

2469-7281 (c) 2018 IEEE. Personal use is permitted, but republication/redistribution requires IEEE permission. See http://www.ieee.org/publications_standards/publications/rights/index.html for more information.

APPENDIX G

Copyright

Copyright Clearance Center RightsLink

Help Email Support

Publisher: Mary Ann Liebert, Inc.

Copyright © 2019, Mary Ann Liebert, Inc.

Creative Commons

This is an open access article distributed under the terms of the Creative Commons CC BY license, which permits unrestricted use, distribution, and reproduction in any medium, provided the original work is properly cited.

You are not required to obtain permission to reuse this article.

Mary Ann Liebert, Inc., offers reprint services for those who want to order professionally produced copies of articles published under the Creative Commons Attribution (CC BY) license. To obtain a price quote, email Reprints@liebertpub.com. Please include the article's title or DOI, quantity, and delivery destination in your email.

© 2020 Copyright - All Rights Reserved | Copyright Clearance Center, Inc. | Privacy statement | Terms and ConditionsComments? We would like to hear from you. E-mail us at customercare@copyright.com